Investigation of a semiconductor waveguide optical routing devic

Green, M. R.

Award date:
1996

Awarding institution:
University of Bath

INVESTIGATION OF
A SEMICONDUCTOR WAVEGUIDE OPTICAL ROUTING DEVICE

Submitted by:

M.R. Green

for the degree of Ph.D. of the University of Bath

1996

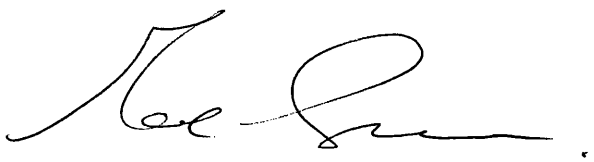

M.R. Green

ProQuest LLC
789 East Eisenhower Parkway
P.O. Box 1346
Ann Arbor, MI 48106-1346

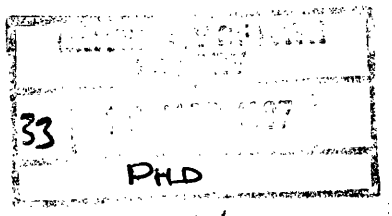

5109694

Abstract

Optical communications systems using reliable semiconductor lasers and detectors with ultra low loss fibre interconnections are in widespread use, but optical switching and routing nodes are not as commonplace, since the available optical routing devices are complicated in operation and are large (10's mm) compared to the laser and detector (<1mm). Routing is, therefore, achieved by demodulating the optical signal into the electrical domain, where it is identified, routed accordingly and remodulated onto optical frequencies. As the demand for data rate increases beyond the multi-gigabit per second standards that exist, e.g. OC192 standard ≈ 10Gbit/s, there is a need for optical routing devices to be developed before the electronic systems become incompatibly slow. In addition to the replacement of electronics, photonic technology offers the possibility to save weight and power.

This thesis describes the design and fabrication of an integrated semiconductor optical routing device, which utilises electrically controlled waveguide couplers for its operation. Each individual component of the switch design is analysed and optimised to achieve efficient operation of the complete optical switch. The study of the effects of fabrication processes and submicron fabrication tolerance on the performance of the switch have been given considerable attention here. The results and conclusions from this study are presented.

Detailed measurements of guiding, carrier diffusion, and variable coupler operation have been made and compared to developed theoretical models. The effect of material damage from ion beam etching is shown, and operation of variable couplers by thermal and free carrier variation of refractive index is demonstrated theoretically and experimentally, illustrating that the device is not restricted to one method of operation.

Measurements of speed and on-off ratio of the switch element are shown to be as expected, i.e. 10ns and 6-15dB respectively, demonstrating that the device is a viable structure for use in optical switching matrices.

Acknowledgements

Thanks must go to my supervisor Dr. J. Sarma for the *jing bang thing*, various *levels of fish*, his encouragement and wisdom. My gratitude goes to Dr. I. Middlemast for his scepticism, and to Trevor Ryan for teaching me infinite patience and other fabrication techniques.

My gratitude goes to Mr. Malcolm Pate at the Sheffield Central Facility for reactive ion etching of the mirrors, and to Dr. John Roberts for supply of the semiconductor material.

My thanks also go to all my other friends and colleagues at Bath who have had to put up with me and put me up!!

My thoughts go to those who I have lost and gained during this work.

"Happiness is not a mathematical concept"

J. Sarma, September 1993.

Contents

Chapter 1.

Introduction

1.1 Optical Communication

Optical communication in the form of hilltop fires was used many centuries ago, and modern adaptations using powerful light sources and lenses have also been tried, but since the invention of both the laser and the glass fibre guide, development and usage of optical signalling has radically increased.

The first laser used a gas for the lasing medium and was built in 1960. This was closely followed by the semiconductor laser in 1962, and the first room temperature CW semiconductor laser was demonstrated in 1970. The concept of using glass fibres as light guides was proposed in 1966, but with unusable attenuation. By 1975 losses had been reduced to less than 2dB/km, and presently available single mode commercial fibres have attenuation figures of 0.1-0.2 dB/km.

With the ability to send optically modulated signals over very long distances, and a potential bandwidth well into terahertz regions, fibre optic communications systems are now used for a wide range of applications from local data exchange systems, to intercontinental transmission. There does, however, still remain the task of efficiently routing these signals. Currently, trunk telephone calls are sent from exchange to exchange on fibre optic cables, but demodulated into electronic signals at the exchange in order to be identified and routed correctly. They are then converted back to optical signals for the next part of their journey. This is not only a costly process from a hardware viewpoint, but also creates a bottleneck in the data stream as the electronics do not share the same high bandwidth as the optical system. With the increasing demand for higher data rates, there is an increasing need for fast and efficient routing techniques. It is because of this, that there is a great deal of research being undertaken in the field of optical switching and routing.

Optical signalling is not only limited to data communication but can also be applied to control. Highly accurate synchronization can be obtained by optical clock distribution, and RF feeds over fibre are useful, for example, in active phased array beamforming antennae as the fibre is more lightweight than microwave guides, and offers the possibility of less phase distortion for complex routing applications. Optical control of microwave signals can also be used in photonic/microwave MMIC devices[1]. High electromagnetic immunity, and lightweight, compact devices make opto-electronic integrated circuits (OEIC's) ideally suited for use in satellite and space applications. Taken to its full conclusion, optical routing devices would complement all- optical logic arrays, and all-optical computing circuitry.

There exist a number of switching possibilities identified by the property that is used for routing. These are for time division multiplexing (TDM), wavelength division multiplexing (WDM), space division multiplexing (SDM) and code division multiplexing (CDM). This report is only concerned with the development of switching devices for space division multiplexing where a signal is routed from one input channel to one or more specified output channels. Although space division switches may be used to demultiplex time or code division multiplexed signals from a single signal path to their own respective outputs, the space division switch can also be used to route signals that still contain forms of multiplexing without adversely affecting the multiplexing of the input signal. Under this type of operation the device is required to be insensitive to wavelength (over the range of WDM signal) and bit rate, and in some cases also polarisation insensitive.

1.2 Current Designs in Optical Switching

Space division switches are broadly divided into three main categories. The first consists of those that employ an array of light shutters in a plane perpendicular to the direction of the optical signal. An example of this is the liquid crystal spatial light modulator,[2] which is an effective device, but has switching speeds of the order of milli-seconds. The second category employs movement of reflecting surfaces to direct the free space signal beam to the required detectors or outputs. This is usually by means of piezoelectric crystals[3], and is again a slow device due to its mechanical nature. The last category uses the advanced planar technology learned from the silicon electronics fabrication industry, to make semiconductor, or dielectric devices that are in the same plane as the signal direction. This not only saves space, but in some materials can have the advantage that the laser sources can be fabricated in the same material as the routing device. This is not the case with $LiNbO_3$ or Silica but is possible with the common III-V compounds such as GaAs, InP etc. It is this planar type of spatial switch that this investigation will consider. GaAs is used here as the demonstrating material, but the concept is also applicable to other similar materials.

Many parameters have to be considered in the design of an optical switch. Losses, crosstalk, on-off ratios, speed, and channel symmetry are common factors that the performance of a device are measured by, and their relative importance is dictated by what application the device is intended for.

$LiNbO_3$ switches have so far had the advantage that they can be made to exhibit very low loss (0.25-1dB) and also very good crosstalk figures (35-20dB).[4] Semiconductor devices, however, can be made to have gain at certain wavelengths, removing the problem of losses, but this does introduce extra noise to the signal in the form of spontaneous emission at the same wavelength. The large electro-optic effect in $LiNbO_3$ has the advantage of low switching power requirement, and devices of 16×4 are commercially available. The device power and speed are largely dominated by its capacitance, however

good device design can minimise this. These devices operate by bringing two waveguides close together to form a directional coupler. The coupler can be tuned and detuned by electro-optic variation of the refractive index in the guides, resulting in coupling being permitted or not. The coupling length in this type of device is of the order of 1-2mm, with each guide being of the order of 3-7μm in width with similar separation between them. Larger multichannel arrays become very long and thin, and a 16×16 device has been reported[5] being 2.5mm in width and 69mm long, using 56 directional couplers. This design of routing array would become considerably longer for a greater number of inputs, and so very difficult to fabricate with standard lithography and etching techniques.

A drawback of having the guides in close proximity to each other, is that the signals from each are difficult to separate, as the modes from each guide are overlapped. This can lead to poor figures for crosstalk performance. As a fibre optic guide is of the order of 250μm in diameter, methods are needed to separate the two signal paths. Ways of doing this are diverging guides, curved guides and reflecting mirrors, all of which have an associated loss.

There also exists the disadvantage that the silica and $LiNbO_3$ devices cannot themselves be used for generation of light, which requires the integration of laser sources into their structure. (Erbium doped silica devices exist, which generate light at a certain wavelength, but require pumping from another source). As many optical signals are generated with semiconductor laser devices, it would be very convenient to have routing from the source, with laser and routing device all on one substrate. Similar device structures to the $LiNbO_3$ directional couplers can be made in semiconductor material, but the electric field effects on refractive index (Appendix 3) are much weaker, resulting in poorer performance in bulk material[6], and so other techniques have to be found for semiconductor devices. Popular methods used in semiconductor optical routing devices are now briefly described.

1.2.1 Attenuation Switched Devices

This type of device relies on the input signal being divided amongst a number of different output channels in the highly absorbing material. The required output is obtained by pumping the selected path, introducing gain, thus allowing the signal to propagate. The other paths are left unpumped, which will attenuate the signals in them. The advantage of this type of device is that it can have lossy components such as curved guides or mirrors to direct the path across the substrate and still remain lossless, as a whole, due to the gain. A disadvantage to this method is that the signal wavelength has to be the same energy as the bandgap of the material. This leads to any spontaneous emission from the pumped regions, being the same wavelength as the signal, being amplified and appearing as noise. There is a limit to the number of these devices that can be cascaded, as the spontaneous noise is

amplified at each stage resulting in lower signal to noise ratios as the signal progresses across the matrix.[7]

This type of device will also consume more power than those described below as the whole path length has to be energised for the signal to appear at the output. This problem can be overcome by regrowing the waveguide regions in a material with a wider bandgap and therefore lower propagation loss. Only the gain regions now have to be pumped, as shown in Figure 1.1.

Performance of these devices in small matrices is very good as any losses associated with the signal paths can be overcome by optimising the gain. On-off ratios in excess of 45dB can be attained[8] with the configuration shown in Figure 1.1, but switching speed is limited by the gain modulation rate.

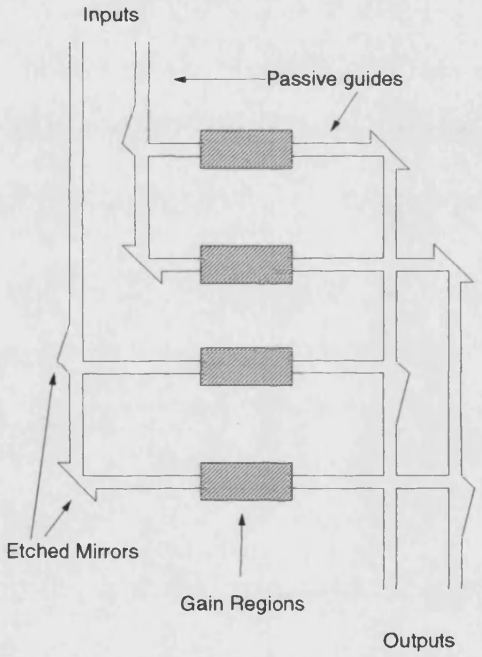

Figure 1.1. Attenuation Controlled Switching.
(After Sherlock *et al.* Ref. 7)

1.2.2 Y-Junction Switches

Instead of splitting the power from one guide into two other guides and producing gain in one of the two paths, the 'y' junction uses suppression of the refractive index to alter the mode shape of the incoming signal so that most of the power is guided into either one or the other arm of the 'y'. Successful devices have been made[9] with a crosstalk of 20dB, employing carrier injection or reverse bias to realise the index changes. (Figure 1.2). As there are no couplers or gain regions in this design the devices can be made comparatively short, depending on the angle of the 'y' and the required guide separation at the output.

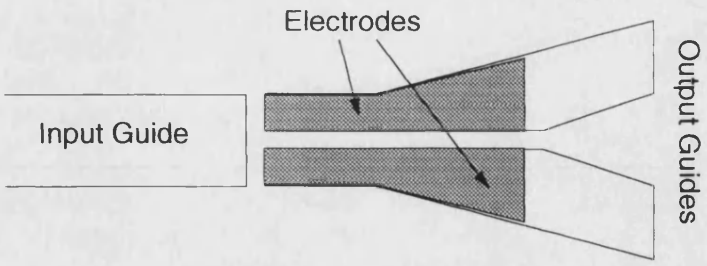

Figure 1.2. Y-junction Switch (after Cavailles *et al.* ref. 8).

1.2.3 Directional Couplers

The idea of detuning a directional coupler, as in the case of $LiNbO_3$ devices, can be implemented in other ways. The devices mentioned earlier have their guides mounted next to each other, and are about 3-5μm in width with similar spacing. Figure 1.3. This results in long coupling lengths in excess of 1000μm. With the small linear electro-optic (LEO) effect in semiconductors, longer guide lengths are needed to achieve enough phase shift to properly detune the coupler. The stronger effect of carrier injection has been used,[10] but it does increase the loss of the device with increased carriers.

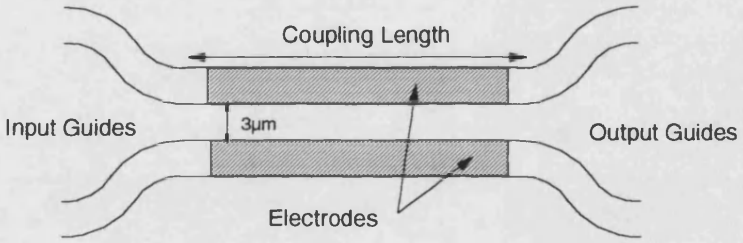

Figure 1.3. Plan View of a typical Directional Coupler.

The quantum confined stark effect (QCSE) is another phenomenon that produces a large refractive index change, but it also gives a large change in absorption and so is not suitable for longer devices. If the guides are made much smaller, however, and placed closely on top of each other, the coupling length is reduced. This can be done by growing high index MQW layers in the material and using them as slab guides, giving a coupling length of as little as 30μm. Figure 1.4a. These can then be detuned by QCSE[11], with the absorption having less effect on the total loss. The total power output of this type of device is still affected, being reduced by approximately half when the device is under reverse bias. Attempts to reduce this problem have been made[12] by placing a lower index MQW region between the coupled guides instead of within them, as in Figure 1.4b. This has the advantage of being in a position where there is less power throughput, and so affects the total power loss to a lesser extent. The vertical coupler arrangement will suffer from a need for very stringent manufacturing tolerances because of the smaller nature of the guide core layers and separation.

Care has to be taken in using directional couplers as they can be strongly wavelength dependent, and so do not always appear transparent to a WDM signal.

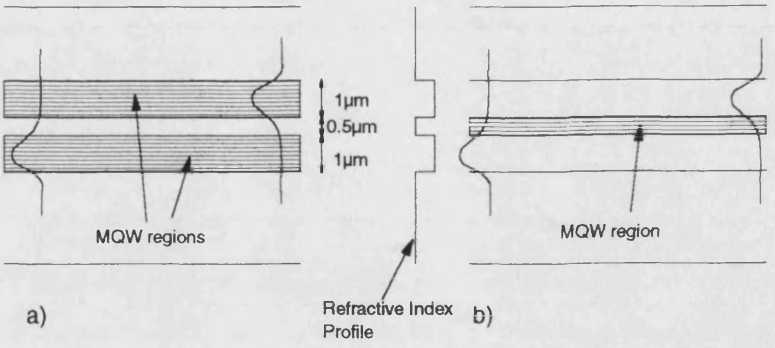

Figure 1.4. Vertical Couplers showing a) MQW regions as guides and b) MQW between guides.

1.2.4 Multi-Mode Interference Couplers

A more recent attempt to use the linear electro-optic effect in bulk semiconductors[13] employs multimode interference guides. These consist of a number of input waveguides coming together to form a very wide multimode guide, and then after a certain length being split back into the original guide configuration, as in Figure 1.5.

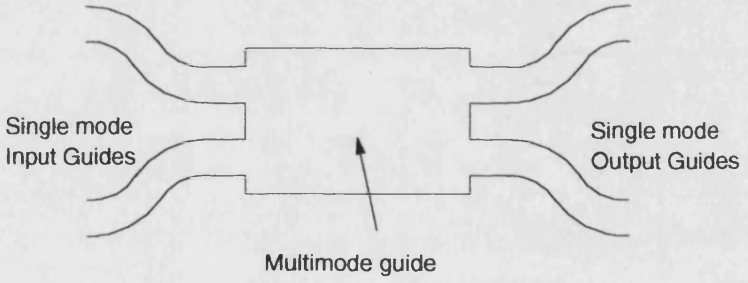

Figure 1.5. Multimode Interference Coupler.

Depending on the phase of the input signal in each input guide, the modes in the wide guide can be made to constructively interfere at the start of one output guide and not at the others. A successful example of this uses 6mm electro-optic phase shifters before the multi mode interference (MMI) coupler to achieve a 10dB crosstalk figure and 12dB of loss for a 10×10 array 13mm long. Individual 2×2 MMI couplers can be as short as 130µm[14] which compares favourably with the 1-2mm long twin guide couplers.

1.2.5 Intersectional Guides

Two guides that cross each other in the form of an 'x' give rise to the possibility of having two inputs and two outputs, but this configuration is usually only used with one input, and at very small angles, typically 1-8°. Figure 1.6. There are a variety of methods for controlling which way the light travels at the crossing. As a passive structure, most of

the light will go straight through, with very little leaking into the other arm. To alter this the refractive index of one side of the crossing point is changed, producing an index step off which the incident mode can reflect. Because of the very small change in index, the angle of intersection of the guides has to be very small to obey the laws of total internal reflection. This is usually between 1° and 8° and the technique has been realised using carrier injection[15], reverse bias[16], and QCSE[17]. The small angle implies that a larger switching matrix using this method is very long and thin.

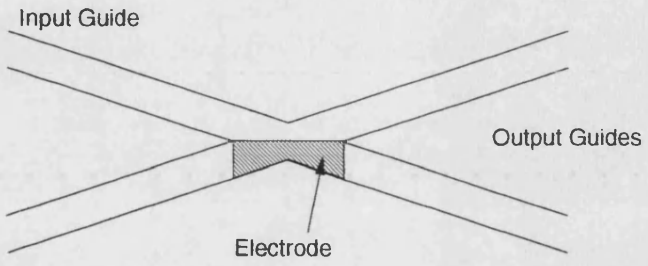

Figure 1.6. Intersectional Guides.

There is some argument over the true operation of these devices as it can be said that it operates in the same way as the MMI device. This is backed up by a working device that alters the refractive index symmetrically at the centre of the device.[18]

A slightly different form of intersectional guide with an induced mirror is one where, instead of one index step to act as a mirror, the process is repeated many times giving a periodic variation of the refractive index at the intersection to produce a Bragg grating. Because of the higher efficiency of the periodic structure the waveguide angles do not have to cross at such a shallow angle. Attempts at fabricating this arrangement of device have been made, but have not proved to be very successful.[19]

1.2.6 Fixed Mirror

Previous designs of switches have either had closely spaced guides causing difficulty in separating the different signals, or have used weakly induced mirrors to separate the signal paths. The fixed mirror, although not in itself a switching element, is a feature that can enhance the performance of the switching device. The use of the mirror for signal distribution has already been illustrated in Figure 1.1, but other configurations are also able to use a mirror. An example of this is a switch which uses a controllable directional coupler, to route the signal, closely followed by a permanently etched mirror to separate the output paths. The mirror surface being of a fixed, passive nature and usually between the semiconductor and air, gives the possibility of having large angles in the switch design, thereby giving large switching arrays a better length to width ratio. This has been accomplished with vertical directional couplers using QCSE for detuning[20] and, theoretically, with carrier injection,[21] in 8° intersections and a right angle configuration

respectively. Because of the vertical coupler arrangement the signals are still difficult to separate, and crosstalk is still a problem being 4-6dB in the practical QCSE device, but 20-25dB in the theoretical injection device. Losses are still a problem, as the injection of carriers is into a region through which the optical signal has to pass.

Curved waveguides could also be used in place of the mirrors, as shown in Figure 1.3, but to obtain low loss bends, very strong guides with very smooth side walls and large bending radii are needed. Curved waveguides are not an ideal choice for a compact device, and the strength of guide needed can lead to multimode operation which would be detrimental to signal dispersion. It will also be shown in Chapter 2, that fabrication of smooth sidewalls is not an easy task in semiconductor devices.

1.2.7 Mach-Zehnder Interferometers

The interferometer by itself is not a space division switch, but a modulator that can be operated at very high speed if necessary. The interferometer splits the signal into two paths and then recombines it after an appropriate distance. Figure 1.7. If the length of the two separate paths is identical then the signal will add in phase, but the optical path length of one of the arms is changed by altering the refractive index, so that the two signals add up in anti phase. The index may be changed by a number of methods, e.g. electrically, thermally etc.

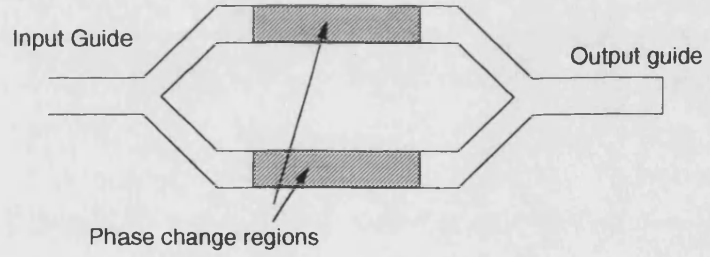

Figure 1.7. Mach-Zehnder Interferometer.

Very short pulses can be generated by altering the optical length of one arm to give a changed state at the output. The other arm is then changed in the same way almost immediately afterwards, thus removing the phase difference between the two arms caused by the initial change. This has been implemented in bulk GaAs/GaAlAs[22] guides to give a pulse width of less than 8ps.

1.2.8 All-optical Switching

All-optical switching uses light to control the switching mechanism. This often requires high power pulses to change the carrier profile within the device, either at bandgap or half bandgap wavelength. This can be used to de-multiplex, separate and route a signal with a high power, from one at a lower power. Very high speed operation, of the

order of 50ps, can be obtained, but at the cost of high power signals requiring critical power levels in the region of 170W/cm^2, which is demonstrated in a structure similar to the twin MQW vertical coupler of Figure 1.4a.[23]

Optical latches have also been demonstrated using the generated photo current to keep the device in the prescribed state. A strong reference beam is used to set or reset the device. [24] The fastest all-optical switch reported to date is a free space device that employs a semiconductor slab to act as a mirror. In the passive state the signal hits the mirror at the Brewster angle and passes through the semiconductor. When the mirror is illuminated with light of higher energy than the bandgap a shortlived large free carrier concentration is generated at the surface giving the semiconductor a different refractive index and thus Brewster angle, allowing the signal to be reflected. The device is reported[25] to have switching times of 1ps turn off time and 100fs turn on time.

1.3 The CGCPS

The switching device under study in this thesis is the Coupled Guide Cross Point Switch, (CGCPS). The proposed structure for the CGCPS consists of a number of orthogonally placed (main) input and output guides. Figure 1.8. At each intersection of two guides there is a switching element that enables the signal in the input guide to be diverted through 90 degrees and placed into the output guide. The right angled structure of this device offers the most compact arrangement for large N x N routing arrays. An etched mirror facet, rather than a curved waveguide, is used to effect the 90° turn, which makes for a very compact configuration.

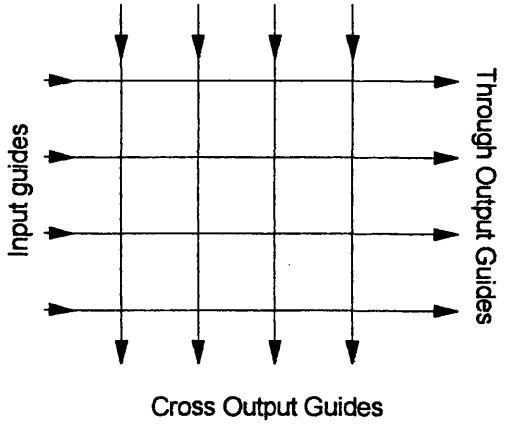

Figure 1.8. Optical Routing Array.

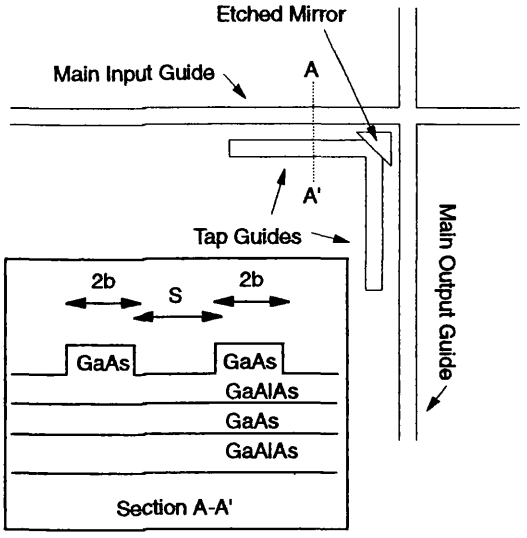

Figure 1.9. One Element of the CGCPS.

The use of a semiconductor material which is transparent at the signal wavelength does, ideally, allow for unattenuated signal propagation in the matrix without any need for

pumping to achieve transparency. Spontaneous emission generation is then at a different wavelength and can be easily filtered out. For a structure where the laser source is fabricated in the same material, transparency could be achieved by shifting the absorption energy (bandgap) of the material in the routing areas by, for example, quantum well intermixing or material regrowth. For developmental purposes, an independent laser source has been used, so that spontaneous emission and signal wavelengths can be separated.

The mechanism for operation of the switching element is to employ electrically variable planar couplers[26]. These consist of secondary tap guides that are placed alongside the main guide, Figure 1.9. In the 'On-state' the light from the main input guide couples across into the tap guide. The signal then reflects from the suitably placed etched facet mirror and is turned through 90° into a corresponding orthogonally positioned tap guide. The signal then couples from this tap guide into the main output guide. In the 'Off-state' the tap guides are 'annihilated' so that the signal progressing along the main input guide is not affected by the suitably displaced mirror position and hence no switching occurs at that junction. This is in contrast to the 'detuning' of the coupled guide structure normally employed, and should be more tolerant to wavelength variation as the coupler is annihilated in the off state, thereby giving a very tolerant off condition. Control of the tap guide is achieved in this case by carrier injection, which depresses the refractive index in the region below the tap guide rib. The reduction of the effective index and thus the guiding strength of the tap guide is such that its presence is no longer felt by the main guide, and therefore (temporarily) destroys the coupler.

In the case where the injection current is not large enough to destroy the tap guide, and therefore some coupling remains, some of the optical signal will be directed to the mirror, and the remainder left to propagate straight on to the through output. In this situation the device allows a distribution of the optical signal with the signal appearing at more than one output.

Several operational advantages that follow from the CGCPS structure are:-

1. Minimised power requirements. Since the actual switching mechanism occurs close to the junction points of two (main) guides, only this area needs to be energised.
2. A single electrode is needed for each switching point.
3. Compact structure.
4. The flexibility that permits signal from one input to be simultaneously distributed to more than one selected output (multicast).
5. Simultaneous operation of multiple inputs and outputs.
6. Increased fabrication tolerance.

1.4 Thesis Layout

The CGCPS is made from a number of individual components, namely, the basic wafer of material, the guides, the couplers and the mirrors. The theory, design, fabrication and operation of each of these items are discussed in a separate chapter. Although considerable time has been spent in fabricating the devices, the description of fabrication has not been given a chapter of its own. Instead, the fabrication processes for each component have been described in the relevant chapter. This is because it is felt that as the fabrication technology has such an impact on the design of a device that its limitations and advantages are an integral part of the design process. Details and settings for the fabrication process and the order of the whole device fabrication process have been given in Appendix 4, as the fine detail of the processing is needed for reference in future fabrication, but is unnecessary in the discussion of the requirements for each component.

One possible arrangement would be to arrange the order of the chapters in accordance with the degree of importance of the component parts of the switch, i.e. starting with semiconductor material, then discussing the guides etc., and ending with the results of the whole device. This layout is, however, not chosen as the material design is, in part, dictated by the requirements of the guides and couplers, and therefore it is advantageous to discuss these aspects first. The material design chapter is placed after those of the guides and couplers as they are so closely linked, but it could equally come between the results from devices in the old and new materials. In addition to the material design, results and operating characteristics from the material are presented.

Chapter 5 gives calculations for the expectations of the etched mirror and the measured results from those fabricated.

The first chapter to give results from the CGCPS as a whole is Chapter 6, and shows the performance of the devices from the old material. Theoretical expectations of the device are detailed first, followed by a description of the development of the fabrication process, and the measurements from the resulting device.

Chapter 7 presents a number of improvements to the design and fabrication process that could be made, and presents results from the CGCPS made from the material designed in Chapter 4, implementing some of the fabrication improvements discussed.

The conclusions inferred from the work so far, together with an outline for continuation of the work are given in Chapter 8.

References

[1] D.H. Auston. "Picosecond optoelectronic switching and gating in silicon." Applied Physics Letters, Vol. 26, No. 3, pp101-103. February 1975.

[2] A.E. Chiou, P. Yeh, "2x8 photorefractive reconfigurable interconnect with laser diodes." Applied Optics, Vol. 31, No. 26, pp5536-5541. September 1992.

[3] K.J.Strozewski *et al.* "Characterisation of a micro-mechanical Spatial light modulator." J. Applied Physics, Vol. 73, No. 11, pp7125-7128. June 1993.

[4] D.K. Hunter, D.G. Smith. "New architectures for optical TDM switching." J. Lightwave Technology, Vol. 11, No. 3, pp495-511. March 1993.

[5] P.J. Duthie. M.J. Wale. "16×16 single chip optical switch array in $LiNbO_3$." Electronics Letters, Vol. 27, No. 14, p126. September 1991.

[6] J.C. Shelton. F.K. Reinhart. R.A. Logan. "Rib waveguides switches with MOS electrooptic control for monolithic integrated optics in GaAs GaAlAs." Applied Optics, Vol. 17, No.16, pp2548-2555. August 1978.

[7] J.J.O. Pires, M. O'Mahony. "Photonic switch size limitations imposed by phase noise from semiconductor optical amplifier gates." Electronics Letters, Vol. 31, No. 18, pp1582-1585. August 1995.

[8] G.Sherlock, J.D. Burton, P.J. Fiddyment. "Integrated 2×2 optical switch with gain." Electronics Letters, Vol. 30, No. 2, pp137-138. January 1994.

[9] J.A. Cavaillès, M. Renaud, J.F. Vinchant, M. Erman. "First digital optical switch based on InP/GaInAsP double heterostructure waveguides." Electronics Letters, Vol. 27, No. 9, pp699-700. April 1991.

[10] B. Acklin, M. Schienle, B. Weiss, L. Stoll, G. Müller. "Novel optical switches based on carrier injection in three and five waveguide couplers." Electronics Letters, Vol. 30, No. 3, pp217-218. February 1994.

[11] J.A. Cavaillès, M. Erman, K. Woodbridge. "Experimental study of switching in a p-i(MWQ)-n vertical coupler." IEEE Photonics Technology Letters, Vol. 1, No. 11, pp373-375. November 1989.

[12] M. Cada, B.P.Keyworth. "Electro-optical switching in GaAs multiple quantum well directional coupler." Applied Physics Letters, Vol. 54, No. 25, pp2509-2511. June 1989.

[13] R.M. Jenkins, J.M. Heaton, D.R. Wight, J.C.H. Birbeck, G.W. Smith, K.P. Hilton. "Novel 1×n and n×n integrated optical switches using self imaging multimode GaAs GaAlAs waveguides." Applied Physics Letters, Vol. 64, No. 6, pp684-686. February 1994.

[14] L.H. Spiekman, Y.S. Oei, E.G. Metaal, F.H. Groen, I. Moerman, M.K. Smit. "Extremely small multimode interference couplers and ultrashort bends on InP by deep-etching." IEEE Photonics Technology Letters, Vol.6, No.8, pp.1008-1010. 1994.

[15] O. Mikami, N. Nakagome. "Waveguide optical switch in InGaAS/InP using free-carrier plasma dispersion." Electronics Letters, Vol. 20, No. 6, pp228-229. March 1984.

[16] T.C. Huang, T. Hausken, K. Lee, N. Dagli, L.A. Coldren, D.R. Myers. "Depletion edge translation waveguide crossing optical switch." IEEE Photonics Technology Letters, Vol. 1, No. 7, pp168-170. July 1989.

[17] H. Yamamoto, M. Asada, Y. Suematsu. "Theory of refractive index variation in quantum well structure and related intersectional optical switch." J. Lightwave Technology, Vol. 6, No. 12, pp1831-1840. December 1988.

[18] R.G. Ravikumar *et al.* "Switching operation in intersectional type field effect MQW optical switch." Electronics Letters, Vol. 24, No. 7, pp415-416. March 1988.

[19] L.B. Aronson, L. Hesselink. "Integrated optical switch arrays in GaAs based on electrically controlled dynamic free carrier gratings." Applied Physics Letters, Vol. 62, No. 5, pp449-451. February 1993.

[20] S. Baba, K. Shimomura, S. Arai. "A novel integrated twin guide optical switch with built in TIR region." IEEE Photonics Technology Letters, Vol. 4, No. 5, pp486-488. May 1992.

[21] R. Maciejko, A. Champagne, B. Reid, H. Mani. "Analysis of an InGaAsP/InP twin overlayed waveguide switch." IEEE Journal of Quantum Electronics, Vol. 30, No. 9, pp2106-2113. September 1994.

[22] S. Nakamura, K. Tajima, Y. Sugimoto. "Experimental investigation on high speed switching characteristics of a novel symmetric Mach-Zender all-optical switch." Applied Physics Letters, Vol. 65, No. 3, pp283-285. July 1994.

[23] P.R. Berger, Y. Chen, P.K. Bhattacharya, J. Pamulapati. "Demonstration of all-optical modulation in a vertical guided-wave nonlinear coupler." Applied Physics Letters, Vol. 52, No. 14, pp1125-1127. April 1988.

[24] R.T. Sahara, S.G. Hummel, W.H. Steier, P.D. Dapkus. "GaAlAs waveguide optically controlled directional coupler latch." Journal Lightwave Technology, Vol. 11, No. 10, pp1533-1538. October 1993.

[25] A.Y. Elazzabi, J. Meyer, "All-optical time division demultiplexing using semiconductor switching" Applied Optics, Vol. 33, No. 17, pp3635-3641. June 1994.

[26] J.Sarma, I. Flint. "Electrically variable couplers for integrated optical circuits." IEE Proceedings part J, Vol. 135, No. 3, pp268-275. June 1988.

Chapter 2.

Semiconductor Optical Waveguides

This chapter describes the waveguides used for the CGCPS and the details of the material from which they are fabricated. It also introduces the mathematical models used for calculating the guided mode shape, and the attenuation of the propagating light. Different fabrication methods for the waveguides are described, together with their effects on the guiding. Techniques for measuring guiding parameters are given, and the practical results are compared with the theoretically predicted values.

2.1 Material Parameters

The material used for the guides is a GaAlAs/GaAs/GaAlAs double heterostructure (DH) wafer, illustrated in Figure 2.1. The GaAlAs semiconductor alloy is used here as it is readily available, although the concept and operation of the devices would also apply for other DH semiconductors. Appendices 1 and 2 give the calculations for finding the guiding conditions and mode shape of the light. The propagating mode is centred about the core GaAs layer, as the GaAs is of a higher refractive index than the GaAlAs. The wafer also has a GaAs substrate and a capping layer for initial growth, and for good ohmic contact to metal contacts respectively. The high index substrate is far enough away not to affect the guiding, and the capping layer thin enough and so placed that the structure does not (vertically) guide more than one mode at the signal wavelength. Lateral guiding is achieved by etching away the top of the material to form a rib, under which the effective index, described in Appendix 1, is higher than in the surrounding regions. The lateral guiding is symmetric, and can easily be calculated using the cosine/exponential formula in Appendix 1.

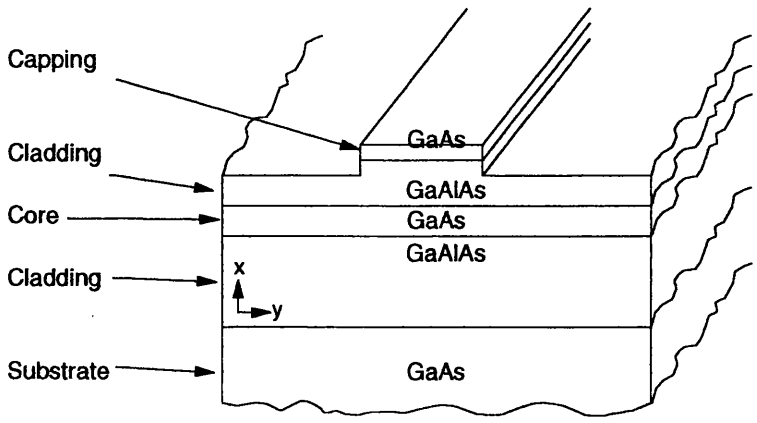

Figure 2.1 General Diagram of Rib Waveguide Structure

The vertical guiding condition is difficult to calculate analytically because of the five different layers of material so the transverse resonance method is employed as described in Appendix 2.

The refractive index of the GaAlAs depends on the wavelength of light and the aluminium content. At least two analytic expressions for the index of the ternary alloy can be found in the literature. Adachi's model[1] covers the spectrum above and below the bandgap, but as our studies only use wavelengths below bandgap energies, where both models are in close agreement, the simpler Afromowitz model[2] is used. The refractive index, n, is then given by:-

$$n^2 - 1 = \frac{E_d}{E_o} + \frac{E^2 E_d}{E_o^3} + \frac{E^4 E_d}{2E_o^3\left(E_o^2 - E_\Gamma^2\right)} \ln\left(\frac{4\left(E_o^2 - E_\Gamma^2\right) - E^2}{\left(E_\Gamma^2 - E^2\right)}\right) \qquad [2.1]$$

where

$E_d = 36.1 - 2.45x$

$E_o = 3.65 + 0.871x + 0.179x^2$

$E_\Gamma = 1.424 + 1.266x + 0.26x^2$

E = incident light energy (eV)

x = Aluminium Content

It was mentioned in Chapter 1 that a very desirable configuration of the CGCPS would be the fabrication of the switch and laser signal source on the same material; thus the layers are doped to allow injection of current into the device, so that the material can be made to lase. The outer GaAs layers have to be highly doped so that good ohmic contact is formed with the metal of the electrical contacts. Further discussion of the effects of doping concentrations is given in Chapter 4. The wafers available for this study are grown by the University of Sheffield by MOVPE, and their parameters are given in Appendix 6 for comparison.

2.2 Signal Attenuation

Losses in a waveguide are a fundamental drawback to the operation of a guided wave device structures. With optical fibres having losses in the region of 0.2dB/km it is a great contrast to find that the best semiconductor waveguides have a similar attenuation per centimetre. Careful fabrication procedure[3] can however reduce this to 0.1dB/cm. Even with quite a high propagation loss coefficient, the typically short length of an individual semiconductor device has a total loss that is usually very small. With larger integrated optic device sizes, however, the attenuation over the whole chip will be significant, and different routing options within the device will exhibit varying signal loss.

There are many sources of loss within a semiconductor waveguide which are shown in Figure 2.2. This section describes the major causes of attenuation, and give methods for calculating their contribution to the total signal loss.

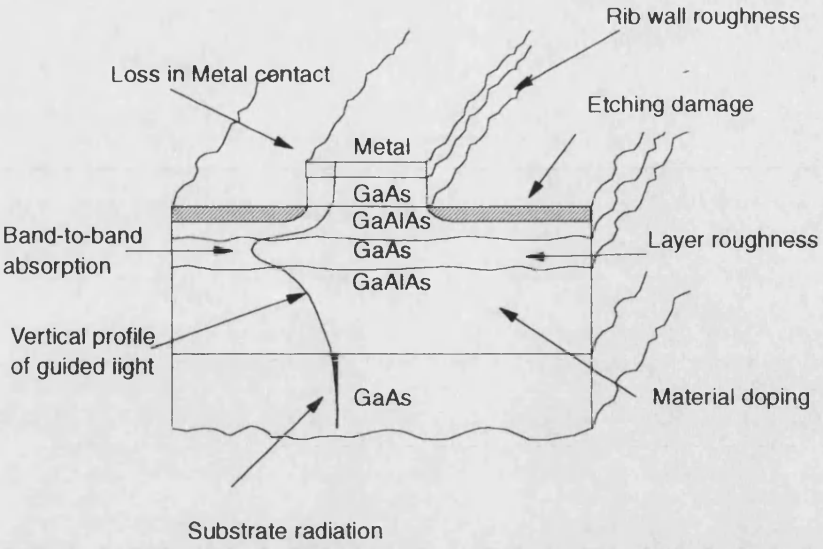

Figure 2.2. Sources of attenuation in semiconductor rib waveguides.

2.2.1 Band-to-Band

Band-to-Band absorption occurs when the wavelength of the propagating light has enough energy to raise electrons from the valence to conduction band. The consequent signal attenuation can be overcome since, at this wavelength, gain can be introduced in subsequent regions through which the signal propagates. The wavelength of light used for this study is of lower energy than the bandgap, hence this form of absorption can be ignored.

2.2.2 Free carrier loss

Free carrier loss is due to intra-band transitions absorbing the incident light. This is most prevalent for long wavelength light. If the power in the material P(z) is attenuated from its original value P_o as it travels in the z direction as:-

$$P(z) = P_o \exp(-\alpha z) \qquad [2.2]$$

then classical theory[4] gives the loss to be:-

$$\alpha = \frac{N_{e,h} q^2 \lambda^2}{m^*_{e,h} 8\pi^2 n c^3 \tau} \qquad [2.3]$$

where $N_{e,h}$ is the density of carriers (electrons or holes), m* is the carrier effective mass, n is the refractive index of the material, and τ is a relaxation term governed by the scatterers in the crystal lattice, which will vary according to the element used as a dopant. q is the electron charge, λ the free space wavelength and c the speed of light in a vacuum.
For GaAs there is some evidence to suggest that a higher power of λ would be a better approximation, but the exact power of λ to be used in equation [2.3] is dependent on the element used for the doping. For GaAs the attenuation is approximately[5]:-

$$\alpha = 3\times10^{-18} n + 7\times10^{-18} p \quad cm^{-1} \qquad [2.4]$$

There appears to be very little information on free carrier loss in GaAlAs but from the experimental data of Hibbs *et al.*[6] the loss can be assumed to be the same as that in GaAs. Free carrier loss is particularly noticeable in metals which are highly degenerate. As the number of carriers is generally not specified in a metal, the loss figure can be obtained from the complex refractive index, **n**. **n**=0.14-i 8.52 for Gold[7] at 1.3μm giving a plane wave power loss of $\alpha=2k_o\times 8.52$ cm $^{-1}$, which is very large (as expected for a metal). In a guided wave device consisting of a number of differently doped layers, the free carrier loss is calculated by taking the power confinement factor of the vertical mode profile multiplied by the loss for each layer. This is an approximation that is reasonably valid within the semiconductor devices under consideration in this work. For a metal contact the approximation has to be improved to[8]:-

$$\alpha_{metal} = \frac{2nkk_o^2}{\beta}\Gamma_{metal} \qquad [2.5]$$

where the refractive index is **n**=n-ik, Γ_{metal} is the power confinement in the metal layer, and β is the modal propagation constant. It is reassuring to note that the larger the k becomes the lossier the metal, but an increased k makes the real part of the dielectric constant, Re (n^2), more negative, and so confining the guided mode more in the semiconductor and reducing Γ_{metal}. The effect on confinement can be larger than the increase in loss from the metal, i.e. an incremental change in absorption from the bulk metal would not give the same increase in loss for the guided wave structure. This is true for the material structure used here, but this beneficial effect on confinement does continue for the cases of the metal contact being taken to extremes of loss or transparency, as here, modal confinement due to the semiconductor structure will dominate.

2.2.3 Roughness Loss

Roughness loss originates from variation in the width of the guide, in the form of roughness, causing some of the signal power to couple into continuum modes. Roughness takes two forms. Firstly there is the roughness between the material layers called epilayer roughness, and depends on the growth technique used. MBE grown samples have increasing roughness with thickness of the grown layer.[9] The samples used here are MOCVD grown, and offer better layer flatness and reduced losses. As the roughness is random in amplitude and spatial frequency it cannot be absolutely defined, only a mathematical approximation can be used. Tien[10] used the Rayleigh scattering theory to estimate losses in rough film surfaces to be:-

$$\alpha = \frac{4\sigma^2 h^3}{\beta n_c^2 (t + 2/p)} \qquad [2.6]$$

where σ is the roughness magnitude, h and p are the transverse propagation constants for core and cladding respectively, and β is the longitudinal modal propagation constant.

The other roughness loss comes from the corrugations in the walls of the etched rib guide, and again this is dependent on the fabrication technique. The Tien formula has been used to estimate this loss, but is inaccurate because only a small part of the mode is in contact with the perturbation, compared to the epilayer roughness that is present all through the lateral mode shape. Other approximations have been made[11] by using a formula that takes into account only the field present at the rough edge. This gives:-

$$\alpha = \frac{a^2\left(k_2^2 - k_1^2\right)K_3^2\left\{\int_{-h}^{0} E_0 dy\right\}^2}{4\beta} \qquad [2.7]$$

$$K_3 = k_3^2 - (\chi - \beta)^2$$

where k_1 k_2 and k_3 are the plane wave propagation constants in the upper cladding, guiding and lower cladding layers respectively. a is the amplitude of the wall roughness, β is the modal propagation constant, and χ the spatial frequency of the corrugations. E_o is the field at the rough wall, normalised so that $\iint E^2 dxdy = 1$.

2.2.4 Substrate loss.

Guiding is achieved when there is a central region of higher index than the surroundings. It is customary, however, to mount the guiding material onto a substrate of high index, using a cladding layer of between 1.5-3μm to separate the slab guide from the mount to allow guiding to occur. As some of the guided mode still extends into the high index mount, some of the power must couple into the substrate, and away from the active layer. The attenuation coefficient, α, from this effect has been calculated as[12]:-

$$\alpha = \frac{\lambda_o^3 h p^2 \sin^2(hd_a)\exp(-2pd_c)}{\pi^3 n_s \Delta n^2 d_a} \qquad [2.8]$$

where h and p are the transverse propagation constants of the mode for core and cladding respectively. d_a and d_c are core and cladding thicknesses. This formula is for slab waveguides, but can be applied to rib guides if the lateral guiding is very weak.

2.2.5 Other Losses.

There are other causes of optical loss in semiconductors, such as trap states from bad material structure, and interface states at heterojunctions and contact layers. The preferred method for fabrication of rib guides at Bath is Ion Beam Etching (IBE) which makes a layer on the top surface of the crystal become amorphous, and therefore must contribute to the loss of the guide. This is, however, considered very small compared to other sources of attenuation.

2.2.6 Evaluation

The losses described in the section above are here evaluated for the materials detailed in Appendix 6.

Material	loss in CB34		loss in CB536		parameters
Loss Mechanism	cm^{-1}	dB/cm	cm^{-1}	dB/cm	λ=1.3μm
Metal Contact	11.35	49.31	1.46	6.34	gold contact
Free Carrier	2.323	10.1	4.79	20.8	
Epilayer Roughness	0.08	0.37	0.076	0.33	5nm roughness
Wall Roughness	18	78	6	26.2	50nm roughness
Substrate Leakage	0.01	0.047	0.77	3.37	

Table 2.1. Comparison of Loss for different materials

For the above calculations for wall roughness the field integral along the rough wall in equation [2.7] was estimated using the EDC method. This will not be accurate for general cases, but as the guides under consideration are very weak, the assumption is adequate for the first order approximation. The wall roughness figures are very large as the corrugation in the wall is assumed to be the same periodicity as the propagation constant, giving a maximum figure. In practice, this would not be the case, and some statistical measurement of the range of corrugation periodicity would have to be made.

Table 2.1 shows that the optical losses for the materials shown are dominated by the doping and the rib wall roughness, followed by the effect of using a gold contact on the top of the rib. Material CB34 has a very thin cladding layer, which allows a larger proportion of the vertically guided mode to propagate through the capping and metal layers. This leads to the high values of contact and rib wall losses. The presence of aluminium in the active layer of CB536 reduces the refractive index and creates a weaker guide, resulting in more of the mode to pass through the higher doped cladding layers, giving higher loss. CB34 has almost 70% of the mode confined to the undoped active layer, compared to 50% for CB536.

2.3 Fabrication

2.3.1 Effects on Attenuation

Before discussing the measurements and results of the guides it is worth describing the methods by which they are made to appreciate the effects that fabrication can have on the losses and guiding of the material. The three factors that can be altered to achieve a lower loss guide are the doping, layer design to minimise substrate and epilayer losses, and fabrication technique. Having material already supplied, the first two options are not open to us at this stage, but are analysed in Chapter 4. Fabrication technique, however, can be improved upon.

The preferred method of fabricating guides at Bath is to use Ion Beam Etching (IBE) where a beam of high energy argon ions are accelerated toward the sample and knock off

the surface atoms of the semiconductor sample. This method is used because it is easily controllable and consistent in etch rate. The area that is not to be etched is covered with a protective mask, which is usually made from photoresist. If positive resist is used, the whole sample is coated, and the unwanted resist areas exposed with UV and washed away. Under certain conditions and types of etching, for example chemical and reactive ion etching (RIE), it is either not convenient to use a photoresist mask, or the photoresist is not durable enough to withstand the etching process and becomes etched away itself. In this case it is common to make a mask out of a harder substance using the liftoff technique. With liftoff, the photoresist is exposed such that the areas to be etched are left covered. The whole sample is then coated in the harder material, which for our use is usually gold or silica. The resist is then washed off, taking with it the gold that was laying over it, but leaving the gold that is directly in contact with the sample. The result is the same pattern as in the mask made from resist only, but in gold or silica. The disadvantage of this method is that when the unwanted coating is lifted off, it is ripped away from that which stays behind, leaving a jagged edge. In making a rib guide this way, the mask has rough edges before the etching has begun, so does not help in loss reduction, however, liftoff is sometimes more convenient to use in non-critical stages such as contacts and isolation layers.

Edge roughness in the resist mask can also occur if the resist is not exposed or developed properly. Bad contact between the master pattern and the resist when exposing will allow the UV light to diffract around the mask and expose areas that should be masked. Diffraction patterns can then be seen on the developed resist, and these enhance any defects that exist on the master pattern. Developing the sample for a longer time can reduce this but at the expense of accurate pattern size. A typical 3μm wide stripe for a rib guide can be reduced to 2μm by bad contact and developing.

Spot defects in the patterning can also arise from contamination of the resist. Small pieces of resist that have been exposed or hardened to a greater or lesser extent than the rest, can leave extra lumps or holes in the exposed pattern. Position and application affect whether these defects are acceptable.

Having achieved an adequate mask, the sample is then ion beam etched to form the rib guides. The IBE process does not, however, result in smooth sidewalls, but leaves striations on the edges of the rib, not only from the ions directly, but also from the progressive wearing of the mask. These marks are generally of the order of 50nm as seen in Figure 2.3, and this is the figure used in the theoretical calculations above.

To produce smoother side walls, chemical etching can be employed. Chemical etching of GaAs is achieved with a combination of H_2O_2, acid and water. The hydrogen peroxide reacts with the material to produce an oxide layer on the surface which is then dissolved by the acid. It is clear therefore that etching will not occur with either acid or peroxide alone. A mixture of the two (in water) will etch, with a maximum rate when the proportions are in the region of 55:35:10 of H_2O_2:H_2SO_4: H_2O.[13] The proportions of each

chemical also affect the manner in which the etch occurs, and there are two regimes in chemical etching that are available for our purposes.

Reaction Rate Limited (RRL) etching is the usual manner for etching simple structures. The reaction is limited by the rate at which the chemical reactions can occur. This can be slowed by dilution with water. This etching method is anisotropic, and also produces etch pits if any form of contamination is present. Figure 2.3. Typical concentrations are 1:8:40 of H_2O_2:H_2SO_4:H_2O.

Diffusion Rate Limited (DRL) etching differs in that the reaction is limited by the diffusion of fresh reagent to the material surface. This has the advantage that any irregularities will have a greater surface area to diffuse to and so be etched preferentially, resulting in very smooth etched surface[14]. The etch rate is reduced by diluting the peroxide solution with more acid, resulting in a very thick solution. Typical concentrations are 1:20:1 of H_2O_2:H_2SO_4:H_2O. Diffusion limited etching is isotropic, but does not accurately preserve the delineation of the mask due to the under cutting and rounding off of mask detail.[15] Figure 2.3 shows SEM photographs of IBE, reaction rate limited etch and diffusion rate limited etches. Clearly the DRL etch gives the best sidewall smoothness, but is difficult to control, as for the 0.2µm etch required in the material shown the sample is etched for 15 seconds with the solution at 17°C. Etch rate slows down as the etchants are exhausted, but can be accelerated if metal is present close to the sample. Preparation of the etchant is given in Appendix 4.

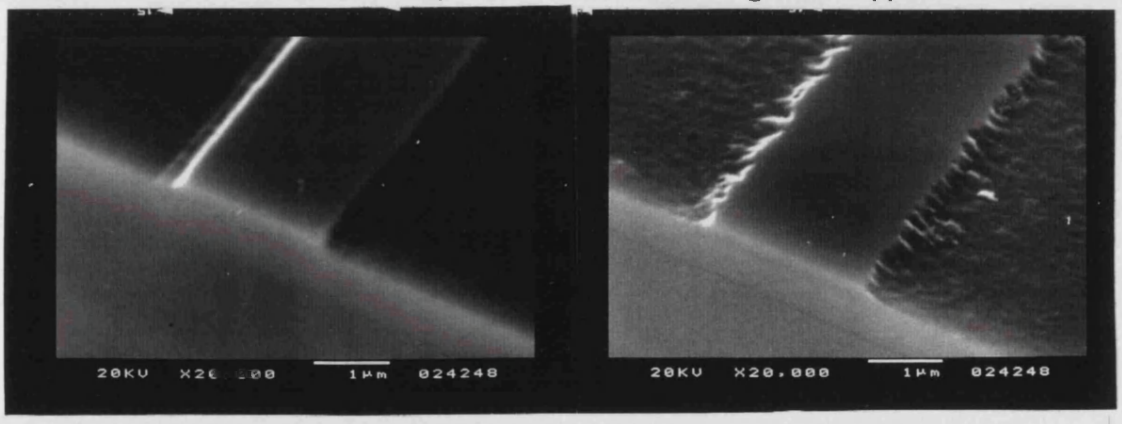

a) Ion beam etch

b) Reaction rate limited etch

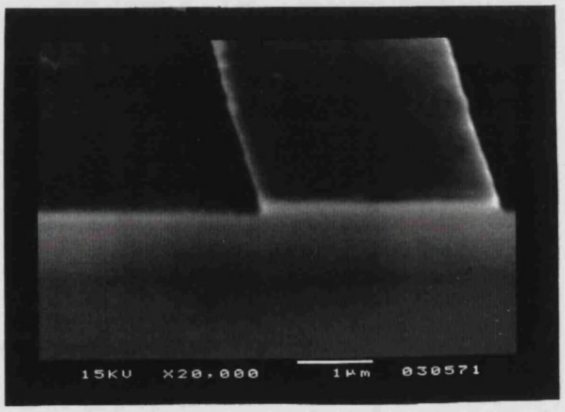

c) Diffusion rate limited etch

Figure 2.3. SEM of IBE, wet etched RRL and DRL guides

2.3.2 Effects on Mode Shape

Because ion beam etching relies purely on the kinetic energy of the incident ions breaking the gallium and arsenic atoms from the GaAs crystal, it is inevitable that damage to the underlying lattice will occur. The incident ions do not penetrate very far into the lattice, normally in the region of 10nm[16], but the damage to the lattice can diffuse down to a depth of 200nm[17]. Many studies have been made of the damage profile in the lattice using photoluminescence[18], cathodoluminescence[19], and Schottky barriers[20], but only one source of reference has been found to mention effects on optical guiding of the ion etching,[21] but this is with plasma etching, and not ion beam damage. Electron Cyclotron Resonance etching techniques have been shown to produce very little damage[22], but this technique is not available to us.

The resulting damage from ion beam etching is split into two layers. The top layer is an amorphous layer approximately 100Å thick, and usually highly conductive. As an amorphous layer should be highly resistive the anomaly is thought to be due to preferential etching of the arsenic, leaving a gallium rich layer.[23] Below the amorphous layer is the damage diffused region. Here, the lattice defects increase refractive index from disordering and also form trap states, which can reduce the free carrier concentration[24] again increasing the refractive index. The defects also increase optical absorption.

Experiments have been made to evaluate the effect of the IBE machine at Bath. Guides were fabricated by wet etching and IBE with etch depths of 0.1μm 0.15μm and 0.2μm. Etch depths were measured with an interferometer to an accuracy of ±100Å. IBE was made using the usual settings for the gun, at an angle of 45° to the plane of the rotating sample. This is the angle for which the best etch rate is achieved. Ions are generated with a B21 saddle source with a 5kV applied voltage. The energy of the ions, however, cannot be determined due to the shape of the accelerating field in the ion gun.

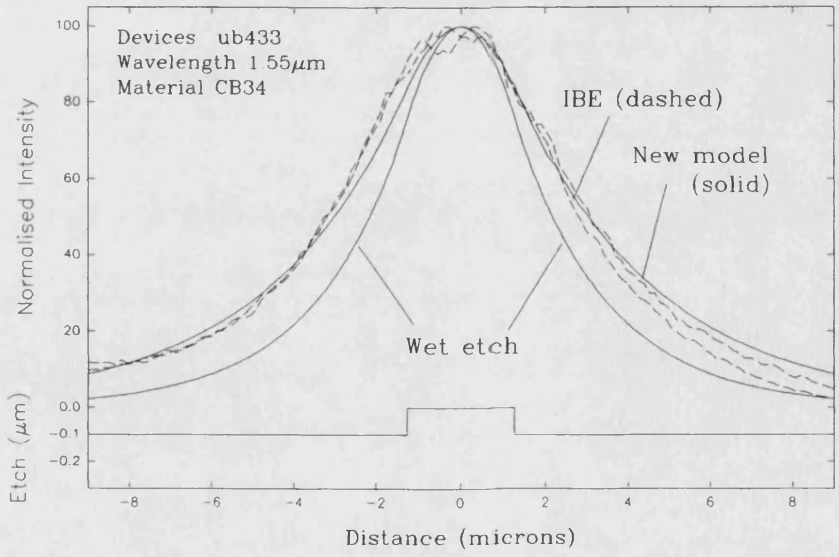

Figure 2.4a. Near field profiles of IBE and wet etched guides.
The two dashed lines are near field profiles from two similar devices.

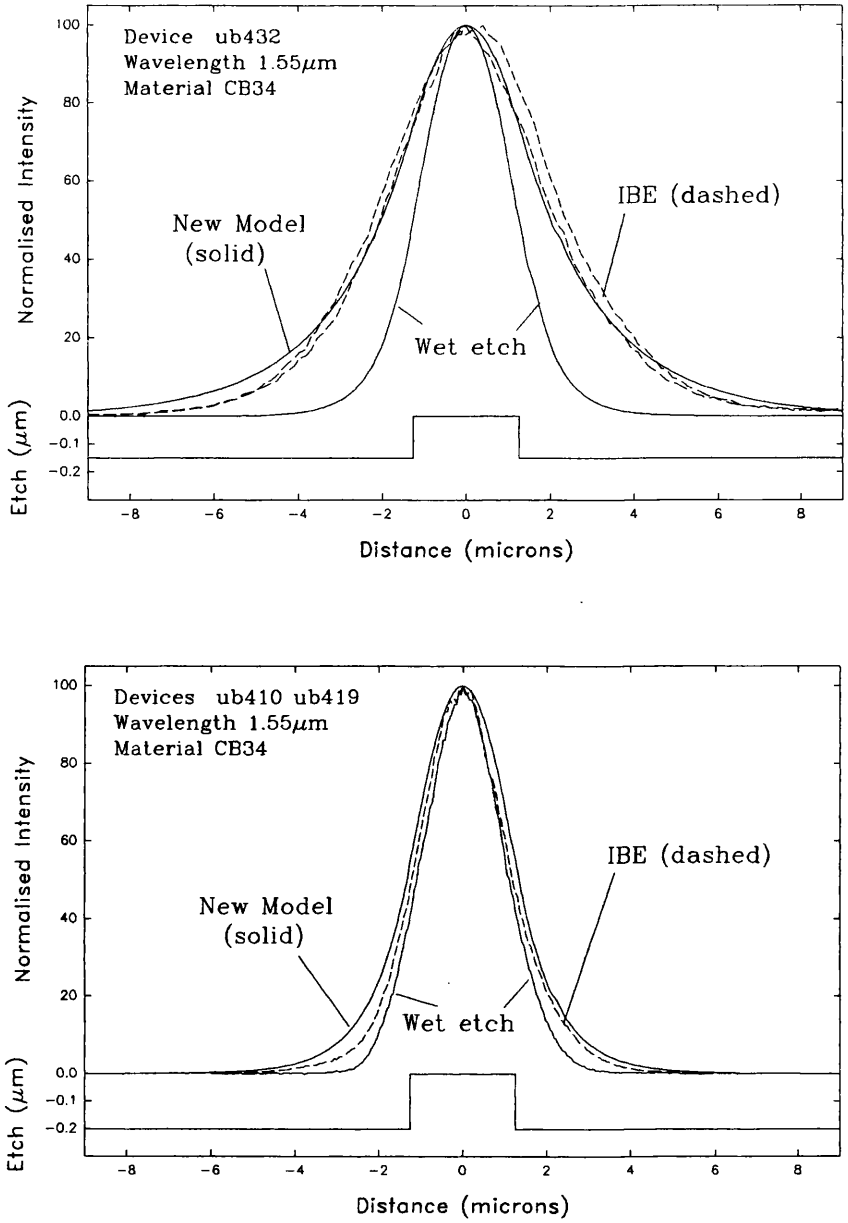

Figure 2.4b. Near field profiles of IBE and wet etched guides.
The two dashed lines are near field profiles from two similar devices

Comparisons between guiding in wet chemical etched guides and IBE guides are shown in Figure 2.4 for sets of guides with different etch depths. The chemical etched guides have the narrower near field shapes, and these fit the theoretical mode profile very well. The IBE mode shapes are considerably wider, especially for the 0.15μm deep etch. As the two types of etch are liable to different degrees of undercut in processing there lies a possibility that some of the effect is due to guide width variation. Figure 2.5, however, gives plots of the near field intensity for a 2μm and 3μm wide guide, showing that the theoretical mode shapes are comparatively insensitive to width at this etch depth.

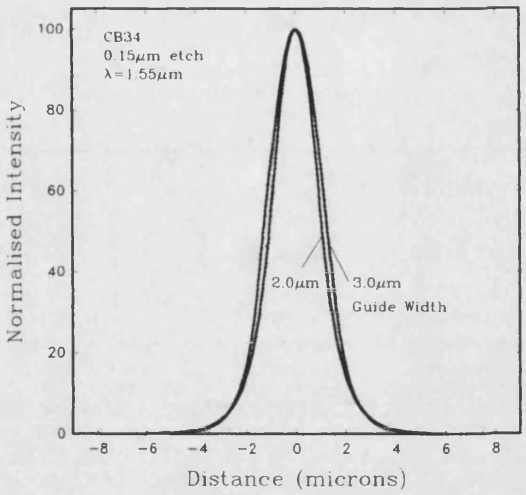

Figure 2.5. Near field profiles of a 2μm and 3μm rib etched 0.15μm deep.

An approximate model has been developed to account for the index change due to IBE induced damage in the top layer. Figure 2.6 shows the basic layout of the damaged material. The damaged depth is assumed to be rectangular, and below the etched region. The index in the damaged region is then increased by a fixed amount. In practice the damage would exponentially reduce with depth from the surface, giving a decaying effect on the index. As the depth and index variation depend to a great extent on the etching conditions, and we have no accurate means of measuring the damage profile, the simple model will suffice for the present.

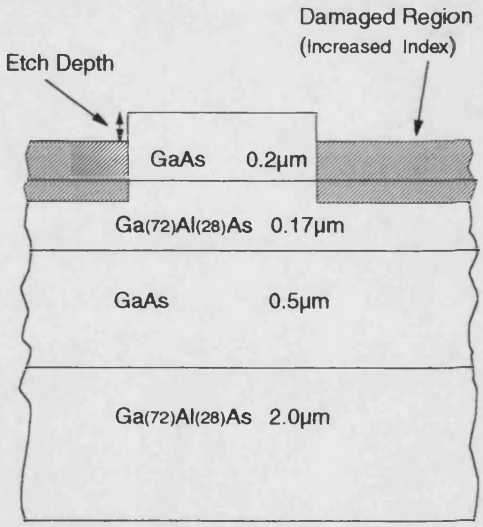

Figure 2.6. Material Structure showing damaged region for block model.

The influence of the index change and the depth to which the change takes effect is shown by the results in Figure 2.7. These curves are used to find the best fit for the experimental results of Figure 2.4, and the following figures for each case are found to give a good representation of the output mode shape.

Etch Depth	Damage Depth	Index Change
0.1μm	0.2μm	+0.09
0.15μm	0.21μm	+0.09
0.2μm	0.2μm	+0.09

Table 2.2 Damage parameters used in block model.

Table 2.2 uses a reduced increase in index compared to the work of Kwun *et al.*[25], who found an increase of 0.49 when measuring damage of Be bombarded GaAs. It could be thought that as the etching ions are aimed at 45° to the sample, the diffusion of damage would spread into the rib as ions are directly hitting the exposed rib wall. Extending the numerical model to account for this results in much widened mode profiles even for a diffusion depth (laterally) of 0.1μm. This shows that either damage does not diffuse far in this direction of the lattice, or that damage is not as great. A possible explanation is that, according to the work of Germann *et al*[26], the damage diffusion is anisotropic and prefers to be channelled along the <111> and <110> axes. Because of the symmetry of the crystal, there are more of these axes running alongside and away from the rib edge than underneath it so damage under the rib edge is less prevalent. Another factor is that the device is rotated while being etched, and therefore the rib wall will only be exposed to the ion beam for half the time, thus less damage can be caused.

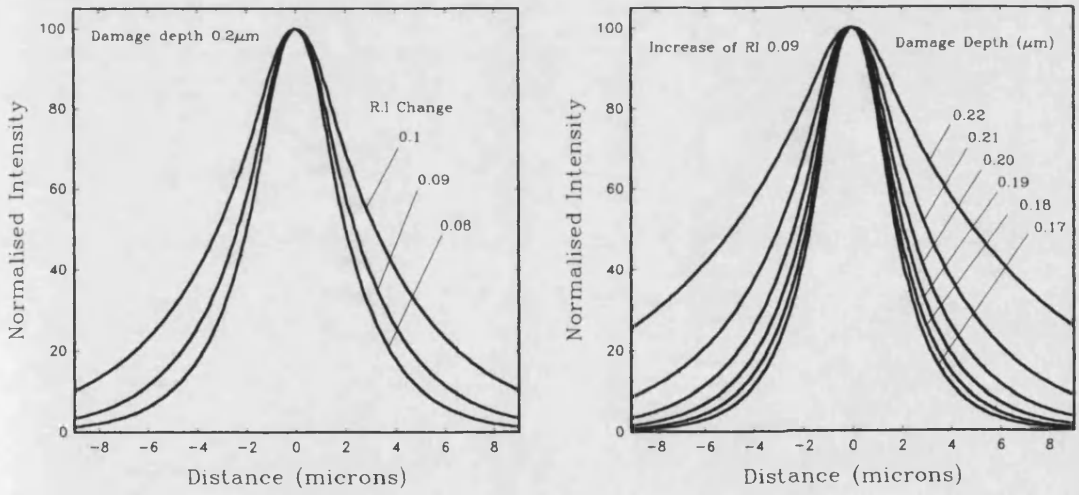

Figure 2.7. Illustrations of how different parameters affect the near field profile.

Without the use of more sophisticated electron microscopes it is not possible to determine exactly what the damage region for the fabricated rib guides is, but a clear result of the effect it has on the guiding has been shown. Lattice damage can be removed in some cases by annealing, but in the experiments carried out here, using a 430°C bake for 15 minutes in hydrogen gas, failed to have any appreciable effect on the mode shapes. Previous work already cited above shows variable results depending on ion energy, and the

work of Kwan *et al.*[20], suggests that annealing material etched by ions over 400eV makes the damage worse.

2.4 Measurement Techniques

2.4.1 Wavelength Tuning

Wavelength tuning is a reliable method for measuring the loss and uses the guide as a Fabry-Perot etalon. As the wavelength of light is varied, the output from the guide changes due to the change in resonance condition within the guide. The contrast ratio between the maximum output and the minimum output gives a measure of the attenuation of the guide. The input optical power to the guide must remain constant over the wavelength tuning range, but the advantage of this method is that the guide under test is not moved, so constant coupling can be assured. Tunable lasers, however, may not have constant power output over their tunable range, but this can be accounted for in calibration. Variation of optical input from guide to guide when testing many devices is not important as it is the ratio of output variation that is used. The wavelength variation required for each cycle can be calculated as follows.

For a 1000μm device, the round trip path length is 2000μm, which at a signal wavelength of 1.3μm in an effective refractive index of approximately 3.37, this gives 5184.61 wavelengths in the device.

For one Fabry-Perot resonance to take place the number of wavelengths has to increase by half a wavelength. Therefore, for 5184.61+0.5 wavelengths in the 2000μm round trip gives a wavelength of 1.299876μm. This is a wavelength variation of 1.25×10^{-10}m.

It is essential that the linewidth of the laser source is much less than this, so that the resonances are clear. As the DFB laser used has a linewidth of 7×10^{-13}m, the resonances are clear and unaffected by the laser linewidth. The wavelength variation technique requires the guide to be single moded.

The loss of the guide is calculated as[27]:-

$$\alpha = \frac{1}{L}\ln\left(\frac{R\left(\sqrt{K}+1\right)}{\left(\sqrt{K}-1\right)}\right) \qquad [2.9]$$

where K is the ratio between the maximum intensity to the minimum intensity from the device facet as shown in Figure 2.9. R is total field reflectivity at the facets (i.e. $R=r_1r_2\approx0.3$) L is length. Using different lengths of the same device, both reflectivity and attenuation can be found.

This method has been used successfully to measure losses in in-house fabricated devices made from the semiconductor materials above. The launching apparatus is shown in Figure 2.8 using a tunable CW laser. Wavelength tuning is achieved by moving a grating

in an external cavity semiconductor laser. A 60V ramp fed to a piezo-electric crystal was used to do this, giving a linear wavelength response, but slightly varying in power. The output power is measured with a photodetector coupled to a PC driven ADC, that also follows the laser tuning driver.

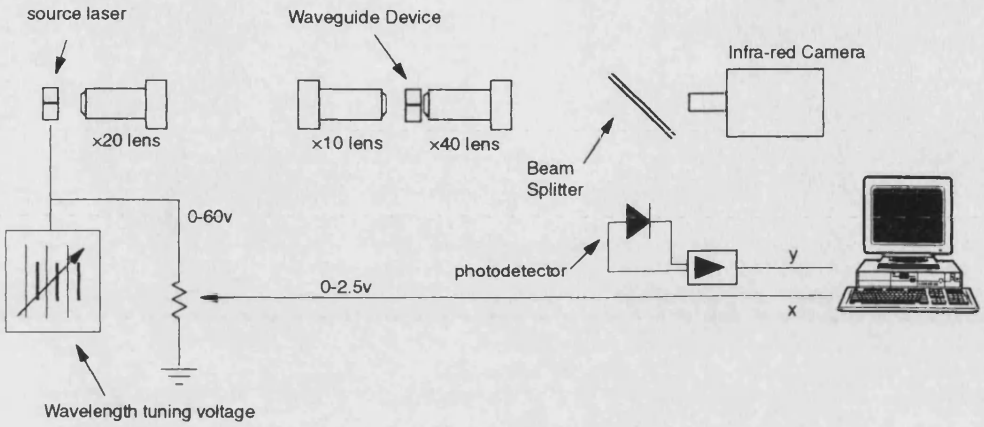

Figure 2.8. Experimental setup for wavelength tuning method

With this setup, although the exact wavelength is not known, a graph of wavelength offset *vs.* output power can be obtained, (Figure 2.9). Noise can be present in the output power signal, but this was found to be due to extra Fabry-Perot resonances from the etalon formed between the facet of the launching fibre (the source laser in Figure 2.8 was pigtailed) and the facet of the device. As launching angle is not critical, slewing the device under test prevented the unwanted resonances. It was also found that in some parts of the laser output spectrum, the output power was zero. However, these null points were not over a wide enough wavelength range to be a significant problem.

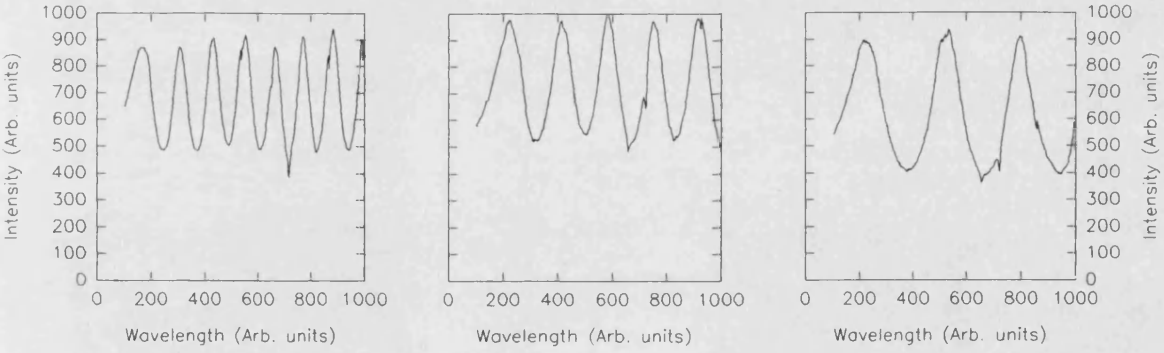

Figure 2.9 Graphs of output intensity *vs.* wavelength offset.

Graphical methods of finding the ratio of maxima to minima were used initially, but it was found more efficient to automate the process. To do this, and remove the noise in the signal, the data are taken and smoothed by using a least squares polynomial fit over a selected window in the data. The number of points in the window, and the order of polynomial have to be chosen depending on the finesse of the guide and its length. The

maxima and minima are then found easily from the smoothed data, and the ratio calculated for each peak-trough pair. This is done to account for variations in total power over the wavelength scan. The final answer is gained by taking an average from a number of ratios.

A possible error may be introduced from the input light from the source laser travelling to the output facet as radiation modes. The extra light from these modes would introduce an offset in the total received power at the detector, and thereby reduce the contrast ratio, and increase the apparent waveguide loss. To avoid this, the waveguides can either be made very long, to attenuate the radiation modes to a negligible power, or to place the waveguide at an angle, such that the unguided light appears at the output facet away from the waveguide output. The latter technique is often applied, as the waveguides are quite short, and the angled facets prevent unwanted resonances with the equipment as already discussed.

Having obtained the values of contrast ratio for these guides, a graph of loss *vs.* reflectivity can be drawn, to find both the end facet reflectivity, and the guide loss, where the curves intersect. This is shown in Figure 2.10, and it can be seen that there is a wide variation in crossing points. As the devices were measured 'fresh', i.e., newly cleaved so that there is not time to form an oxide layer on the facet or to acquire other contamination, the reflectivity is unlikely to vary greatly, so it can be concluded that the propagation losses are different from guide to guide for the same reasons as in the cutback experiments, to be described. From the graphs of IBE and wet etching shown in Figure 2.10, it can be seen that the reflectivity appears to be slightly lower in the wet etch case. Facet reflectivity is normally estimated as 30-33%, but this lower value is probably due to the guides having been etched at a small angle to the facet normal. Reflectivity is likely to vary between the IBE and wet etched batches as they are fabricated separately.

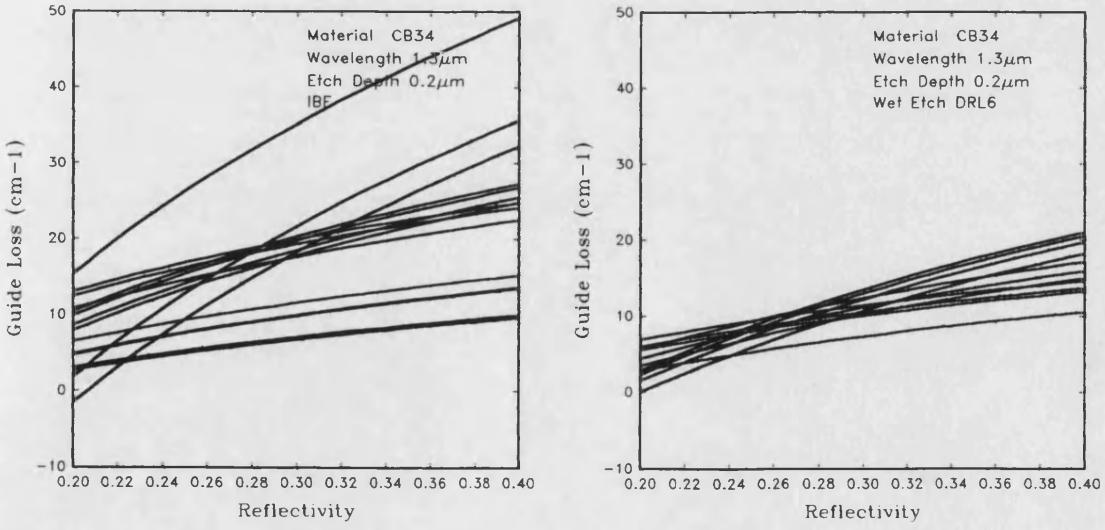

a) IBE fabricated guides b) Wet etched guides

Figure 2.10. Graphs of loss *vs.* reflectivity for a range of guides

The wavelength variation method gives an averaged value of loss of 17 cm^{-1} (73dB/cm) for the IBE guides and 9 cm^{-1} (40dB/cm) for the DRL etch guides in the CB34 material. The use of chemical etching can be seen to improve greatly the losses of the guide. CB536 has a slightly lower loss of 13.8 cm^{-1} (60dB/cm) for the IBE guide, which from the calculations in Section 2.3 is to be expected. In trials where a metal contact is added, the losses appear to become very high, as the contrast in the resonances is small. A loss figure for CB536 with gold contact is estimated as 150dB/cm, which from the earlier calculations is dramatically high, but only 2 samples have yielded results. The small number of results is due in part to the number of samples available but also to the high loss of the guides making the measurement technique less reliable. It is thought that the excess losses are due to bad mask contact and processing rather than the effect of the gold directly.

Samples contacted with indium tin oxide (ITO) give a loss of 95dB/cm. ITO is a material that is conducting at DC, with a measured resistance of 1.2×10^{-3} Ω cm, but is transparent at optical frequencies. This material should therefore offer a low loss contact material to replace the gold, and has been used successfully in making transparent contacts for vertical cavity lasers.[28] The loss figure is surprisingly high, but as the real part of refractive index of ITO is approximately 2, there will be a smaller increase in the amount of mode propagating in the ITO layer than if metal were there. The ITO layer can also be very absorptive, as the carrier concentration can be as high as 8×10^{20} cm^{-3}, and the band-band absorption edge as low as 1.3μm.[29] Without a measurement of the complex refractive index of ITO, it is not possible to say whether it would be lossier than a metal for use as a contact for planar guides.

Other techniques for measuring the guide attenuation were investigated:

2.4.2 Prism launching.

This method uses two prisms, one placed on the top surface of the waveguide to launch light into the guide, and another to remove it. If the prisms are moved apart from each other while measuring the power taken from the guide, a figure for the loss in the guide can be determined. This method is more suitable for surface guides where the active layer can be made to come into contact with the prism directly. The materials shown above have a capping layer, and often a metal contact on which the prism coupling would not work.

2.4.3 Temperature Variation

Temperature variation can be used to change the length of the waveguide, and the refractive index. Similar to the wavelength variation method, if highly coherent light is coupled into one end of the guide, the variation in optical path length from one end of the guide to the other due to heating the device will cause the light output to vary as the structure goes through Fabry-Perot cavity resonances. The heat applied to the device may

cause movement and change the coupling into the device. Experiments were undertaken using devices mounted on the edge of 0.5mm thick copper sheet, but the heat from a 60W bulb placed 10cm from the device was enough to move the device 10-20μm due to copper expansion, reducing the input coupling to zero, and making this method unusable. Other device supports were tested including stiff paper bridges, to reasonable effect. The method, however, was found not to be useful because of the waveguide lengths of the study. Devices in the range of 300μm to 1000μm were used. Using the equations for expansion and increase of index with temperature, the number of expected maxima and minima can be calculated. For one maximum to minimum output variation, the round trip length of the device must increase from N wavelengths to N+1/2 wavelengths in the material. Given that

$$\frac{1}{n}\frac{\partial n}{\partial T} = 4.5\times10^{-5} = \alpha_n \qquad [2.10]$$

$$\Delta L = L_o(\Delta T \times \alpha_L) \qquad \alpha_L = 5.6\times10^{-6} \qquad [2.11]$$

where L_o is the length, n the refractive index and T the temperature, then the change in number of wavelengths in the device (round trip) is:-

$$\Delta N = 2\frac{Ln}{\lambda}\left(1-(1+\alpha_L\Delta T)e^{\alpha_n\Delta T}\right) \qquad [2.12]$$

which gives $\Delta N \approx 2.5$ for 1000μm device over a 10°C temperature variation. This implies at least two maxima and two minima in intensity output.

The device temperature was measured with a thermocouple, and with the aid of the light from a microscope illuminator focussed to a 2mm diameter spot, temperature variations of 20°C were possible, but with the variation in input coupling and the small number of resonances it was decided that this method was unsuitable for our devices.

2.4.4 Cutback

Cutback is a simple method where light is coupled into the waveguide, and the guide's output power is measured. The guide is then cut shorter, and the output measured again for the same input power. This is repeated, and from the results the coupling losses and lens losses can be eliminated to obtain the guide propagation loss. The difficulty with this method is the repeatability of power coupling into the guide, as the device has to be de-mounted, cleaved, and repositioned in exactly the same orientation. Guides with a very narrow far field have to have the angular positioning controlled very tightly to give reasonable results. Using freshly cleaved devices, it can be assumed that the facet losses remain constant. This method must not be used with a strongly coherent laser such as a DFB. The Fabry-Perot effects discussed above will then distort the results. A broad spectrum Fabry-Perot laser, with a cavity length less than that of the device was used for this application.

The cutback method has been used with in-house fabricated devices. A variation of the method is used, in that instead of cutting back one device and re-measuring, a single long device is cut into 5 shorter lengths. This makes alignment faster, but does assume constant loss along the whole length. Repeatability of facet alignment is achieved by reflecting a visible laser beam off the top of the device, and off the front facet. The output power is measured with a vidicon camera. As the response of the camera is liable to drift, a reference beam, driven from the same source as the guiding laser is used as a comparison, as shown in Figure 2.11. The relative intensity of the two beams is used as the measured result. The intensity of the beams has to be corrected for the non-linearity in the response of the camera. The calibration of the camera is described in Appendix 5.

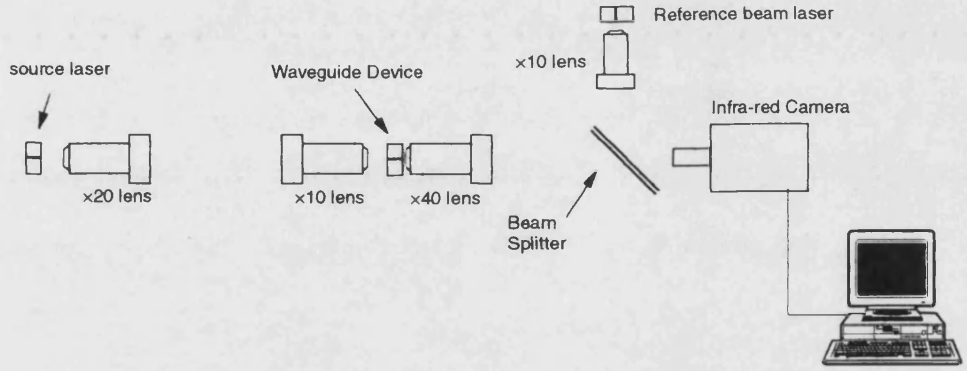

Figure 2.11. Schematic diagram of experimental setup

The results from the cutback method are shown in Figure 2.12. This gives an averaged loss of 34dB/cm. This value is far less than the 73dB/cm loss that the wavelength scanning technique measured. As the number sources of error in the cutback method is greater than that of the wavelength method, the latter is taken to be a more reliable figure.

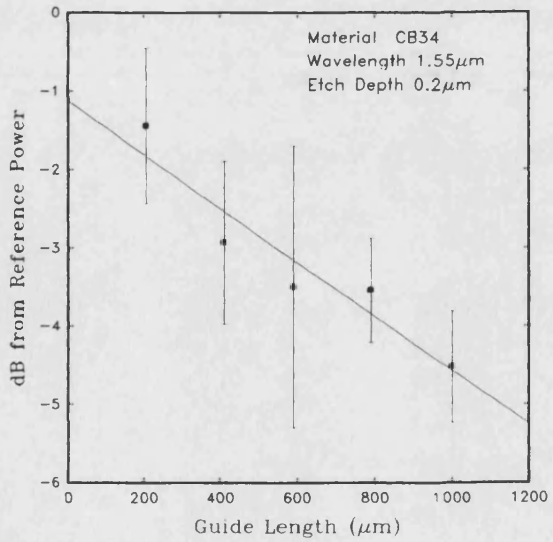

Figure 2.12. Results of Cutback Loss Measurement on IBE Guides

For the cutback measurement 40 guides were used. For each of the 5 lengths used, 8 guides were measured. It can be seen by the spread in the error bars that the measured values across similar devices are not consistent. The spread in the data for the 600µm devices is almost as wide as the whole data range. (Error bars represent the standard deviation of data samples.) Some of the error will arise from experimental inaccuracy, but there must also be a component from device to device differences. This can be from variation of material parameters across the original wafer, but as has already been mentioned, another major component of the error is due to guide defects in fabrication. Generally, the wall roughness is caused by ion beam etching, or pit formation if wet etched. These causes of roughness are small and can be considered even along the guide length. Occasionally, there can arise a situation where the lithography mask does not contact well, or a piece of the photoresist has hardened. After the developing of the photoresist, perturbations can exist in the width of the guide in the form of cutouts or lumps. As this is a random and discrete occurrence, it can affect the loss of one particular guide only. The considerable difference between the loss results from the two methods is, however, surprising given that the sample range is so large for the cutback method. In future work the guide to guide variation could be eliminated by doing experiments measuring the loss in the same guide with the Fabry-Perot technique as it is cutback, thus incorporating both methods. Using the above method the plot of loss against end facet reflection could be plotted for each individual guide. However, reliable cleaving of the device is required for this method, from 1mm to 250µm, which would only give 4 lengths of device.

References

[1] S. Adachi. "Optical Properties of AlGaAs alloys." Phys. Rev. B, Vol. 38, No. 17, pp12345-12352. December 1988.

[2] M.A. Afromowitz. "Refractive index of GaAlAs." Solid State Communications, Vol. 15, No. 1, pp59-63. February 1974

[3] E. Kapon, R. Bhat. "Low-loss single mode GaAs / GaAlAs optical waveguides grown by OMVPE." Applied Physics Letters, Vol. 50, No. 23, pp1628-1630. June 1987.

[4] Pankove J.I. "Optical Process in Semiconductors." Prentice Hall, p75. 1975.

[5] H.C. Casey and M.B. Panish "Heterostructure Lasers Pt. A, Fundamental Principles." Academic Press, p175. 1978.

[6] M.K. Hibbs-Brenner, C.T. Sullivan, "Low loss AlGaAs optical rectangular waveguides at 830nm." Applied Physics Letters, Vol. 56, No. 16, pp1529-1531. April 1990.

[7] S.J. Al-Bader H.A. Jamid, "Metal clad ridge waveguide modes." IEE Proceedings Part J. Vol.135, No. 1, pp79.-84. 1988.

[7] S.J. Al-Bader H.A. Jamid, "Metal clad ridge waveguide modes." IEE Proceedings Part J. Vol.135, No. 1, pp79.-84. 1988.

[8] A. Yariv, P. Yeh. "Optical Waves in Crystals." Wiley Interscience, p428. 1984.

[9] F. Alexandre, L. Goldstein, G. Leroux, M.C. Joncour, H. Thibierge, E. Rao. "Investigation of surface roughness of MBE GaAlAs layers and its consequences on GaAs / GaAlAs heterostructures." Journal of Vacuum Science and Technology B, Vol. 3, No. 4, pp950-955. July 1985.

[10] P.K. Tien. "Light waves in Thin films and Integrated optics." Applied Optics, Vol. 10, No. 11, pp2395-2413. November 1971.

[11] R.C. Hewson-Brown, P.C. Kendall, D.A. Quinney. "Roughness scattering into substrate radiation modes of rib waveguides." IEE Proceedings Part J, Vol. 136, No. 5, pp281-286. October 1989.

[12] Elsa Gamire in "Integrated Optics." T Tamir ed. 2nd edition. Springer Verlag, p253. also D. Marcuse, Journal of Quantum Electronics, Vol. 8, p661. 1972

[13] R.E. Williams. "GaAs Processing Techniques", Artech House. p110.

[14] M.K. Hibbs-Brenner, C.T. Sullivan, "Low loss AlGaAs optical rectangular waveguides at 830nm." Applied Physics Letters, Vol. 56, No. 16, pp1529-1531. April 1990.

[15] R.E. Williams. "GaAs Processing Techniques", Artech House. p113.

[16] K. Akita, M. Taneya, Y. Sugimoto, H. Hidaka. "Evaluation of the stopping depth of non-radiative recombination centres in AlGaAs by Ar^+ ion beam sputtering." Journal Vacuum Science Technology A, Vol. 8, No. 4, pp3274-3278. July 1990.

[17] Y. Yuba, T. Ishida, K. Gamo, S. Namba. "Characterisation of ion beam etching induced defects in GaAs." Journal Vacuum Science Technology B, Vol. 6, No. 1, pp253-256. February 1988.

[18] H. Hidaka, K, Akita, Mtaneya, Y. Sugimoto. "Damage depth in GaAs processed by Ar plasma etching." Electronics Letters, Vol. 26, No. 15, pp1112-1113. July 1990.

[19] A.C. Papadopoulo, C. Dubon-Chevalier, J. Bresse, A.M. Duchenois, F. Heliot. "Etching procedures of GaAs: Cathodoluminescence study of the induced damages and of the recovery techniques." Journal Vacuum Science Technology B, Vol. 8, No. 3, pp407-412. June 1990.

[20] P. Kwan, K.N. Bhat, J. Borrego. "Ion cleaning damage in 100 GaAs and its effects on schottky diodes." Solid State Electronics, Vol. 26, No. 2, pp125-129. February 1982.

[21] C. Thirstrup, S.W. Pang, O. Albrectsen, J. Hanberg. "Effects of reactive ion etching on optical and electro-optical properties of GaInAs/InP based strip loaded waveguides." Journal Vacuum Science Technology B, Vol. 11, pp1214-1221. July 1993.

[22] A.H. Bensaoula, A. Freundlich, "Effects of ion beam and electron cyclotron resonance etch-induced damage on the optical properties of MQW structures." Journal Applied Physics, Vol. 75, No. 6, pp2818-2822, March 1994.

[23] S.J. Pearton, U.K. Chakrabarti, A.P. Perley. "Ion Milling damage in InP and GaAs." Journal Applied Physics, Vol. 68, No. 6, pp2760-2768. September 1990.

[24] T.R. Hayes, M.A. Dreisbach, P.M. Thomas. "Reactive ion etching of InP using CH_4/H_2 mixtures-mechanisms of etching and anisotropy." Journal Vacuum Science Technology B. Vol. 7, No. 5, pp1130-1140. June 1989.

[25] S.K. Kwun, M.H. Lee, "Solid state regrowth of low temperature Be-implanted GaAs." Journal Applied Physics, Vol. 57, No. 4, pp1022-1028. February 1985.

[26] R. Germann, A. Forchel, M. Bresch. "Energy dependance and depth distribution of dry etching induced damage in III/V semiconductor heterostructures", Journal Vacuum Science Technology B, Vol. 7, No. 6, pp1475-1477. November 1990.

[27] R.G. Walker. "Simple and accurate method for loss measurement in semiconductor optical waveguides." Electronics Letters, Vol. 21, No. 13, pp581-583. June 1985.

[28] M.A. Matin *et al*, "Optically transparent ITO ohmic contacts in the fabrication of vertical cavity surface emitting lasers." Electronics Letters, Vol. 30, No. 4, pp318-320. February 1994.

[29] S.B. Lee, J.C. Pincenti, A. Cocco, D.L. Naylor. "Electronic and Optical properties of room temperature sputter deposited indium tin oxide." Journal Vacuum Science Technology A, Vol. 11, No. 5, pp2742-2746. September 1993.

Chapter 3.

Coupled Waveguide Structures.

This chapter will show the basic operation of the directional coupler and different techniques for designing the passive device to be insensitive to fabrication errors. Electrically variable couplers operating in both forward and reverse bias are discussed, and their modes of operation analysed. Modelling and fabrication of the variable couplers are used to verify the mode of operation and measure the diffusion coefficient of carriers in the material.

3.1 Passive Directional Coupler

Waveguide directional couplers can be used for frequency selection, polarisation selection, modulation and power division, but in the context of the CGCPS the purpose of the directional coupler is to transfer the signal power from one waveguide to another. The purpose of this section is to detail the design of the couplers that can be made in the materials available, and show how they can be optimised to be tolerant to errors in fabrication.

Various analyses have been made on couplers giving approximations for coupling lengths and propagation constants,[1,2] but the original work on electrically variable couplers was carried out by Sarma and Flint[3] using the analytical solutions for individual coupled guides. Their work described the calculation of the optimum operating point for the guide structure to be most tolerant to changes in guide parameters, and also the considerations for achieving a large on off ratio for the variable coupler. The variation of the coupler in the analysis was considered as the tap guide being present or not, with this result being effected by injection of carriers into the guiding layer directly below the ridge of the tap waveguide, and nowhere else.

In the analysis presented here the transverse resonance method is used, and is described in Appendix 2. The advantage of using the transverse resonance method is that it is easy to change layer thicknesses and indices once the initial framework of the software is in place. The method is also useful in that it can be used on any arbitrary index profile provided that it can be approximated by a discrete number of constant index portions. In the modelling used here, the coupler only requires 5 sections, but as will be seen later, in the variable coupler discussions, the method can be used for over 500 sections without any significant loss of accuracy. Care has to be taken, however, as the calculations rely on the effective index method, and the effective index of the regions under consideration vary

with the wavelength and etch depth used (Figure 2.6.) to create the rib waveguide. Thus an extra variable is added into the design of the structure.

Generally, for a coupler to function, two waveguides must be in reasonable proximity to each other. All types of coupling theory predict that maximum power transfer is achieved if the two guides are identical, and so this is enforced during the following analyses for the passive device. For definition of terms, the layout of the coupler is given in Figure 3.1.

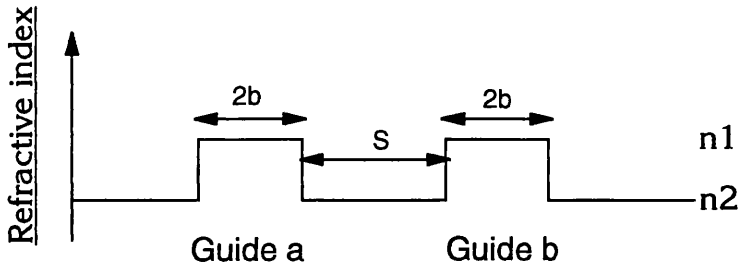

Figure 3.1. Definition of Coupler Terms.

With the transverse resonance solution method, the coupled guide structure is regarded laterally as a whole and the mode solutions for the horizontal 5 layer index profile are found. The general field solutions for the structure are shown in Figure 3.4. If light is coupled into one of the guides, then the input field to the coupled structure will be a super position of the two modes adding in phase. Coupling is then seen as the two modes, which propagate at different phase velocities β_1 and β_2 , adding in anti-phase, after the coupling length, to make the output intensity profile to be mainly contained in the other guide. The coupling length is the length of guide it takes for the modes to have changed their relative phases by π. i.e. coupling length = $\pi/\Delta\beta$. Using this method it is possible to evaluate the power at any point more accurately than using the two individual guide modes, as the field shapes are known accurately over the whole structure.

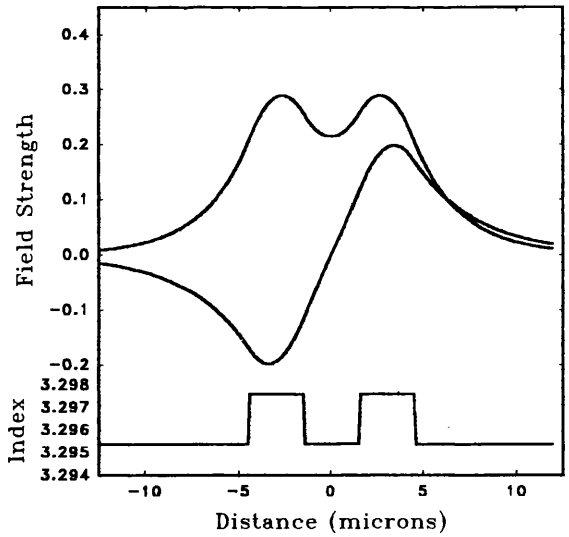

Figure 3.4. Modes of the coupled guide structure.

In the design of a coupler many factors have to be taken into account. Physical size in both coupling length and guide width, together with ease of coupling light into the device, have to be considered. With the fabrication facilities available the minimum workable linewidth is 2μm. Although the linewidth of the mask exposure machine is capable of going to less than 1μm, using 2μm as a minimum leaves a margin for the width to reduce from developing variation of the photoresist masks, and wear from etching. Guide width is important, as the light has to be coupled from the twin guide structure to single guides for routing across the device. These single guides must be single moded, but also strong enough to keep the light well confined.

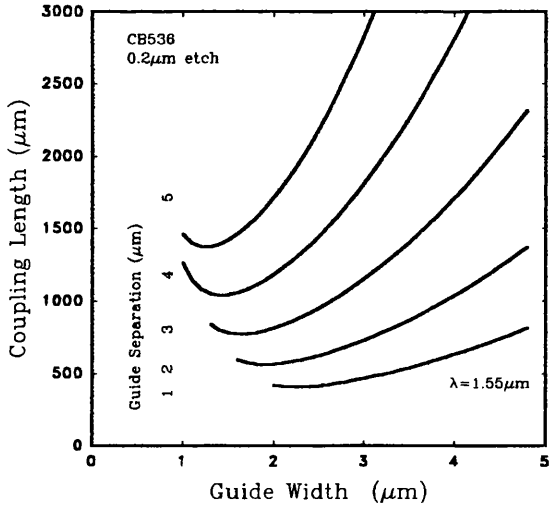

Figure 3.5. Coupling lengths for twin rib couplers.

Figure 3.5 gives an illustration of the expected coupling length for different guide widths and separations. Separation here is the gap between the guides, not the centre to centre distance. The lines are plotted for an etch depth of 0.2μm in the existing material

CB536 (see Appendix 6.) when the device only supports two modes, as one mode will not exhibit coupling and three modes becomes more complicated. The etch depth of 0.2μm has been chosen here as it is a depth that is easily made, and is governed partly by the application of the forward bias variable coupler to be detailed in the next section.

Choosing the guide width is arbitrary at this stage, but bearing in mind that the wider the guide the easier it is to fabricate accurately, and the more confined the light will be in the single guide, a figure of 3μm has been chosen, with 3μm separation. This keeps the coupling length low (≈1mm) with a reasonably strong single moded guide (Normalised frequency w≈π/3). Closer spacing of the guides would reduce the coupling length, but for use in an optical switch, it is easier to separate the signals from each output with the guides further apart, resulting in a better crosstalk figure.

The parameters chosen from Figure 3.5 are used to make the mask pattern for the device which is made using electron beam lithography, so are not subject to appreciable fabrication errors at this stage. The errors from fabrication appear during the processing where etch depth and over-development of the pattern affect the results, and are shown in Figure 3.6. It can be seen here that the etch depth can be set to minimise the variation of coupling length with etching error, and advantageously minimise the coupling length itself. The influence of over-development of the pattern from the mask, which narrows the guides from both sides equally, is also shown. The variation of coupling length is less for the 0.2μm etch and the variation becomes less for more reduction in guide width. With a 0.15μm etch the width of guide has more effect, but the 3μm wide guide is on the shallowest part of the curve gradient, giving it the least change in coupling length with guide width.

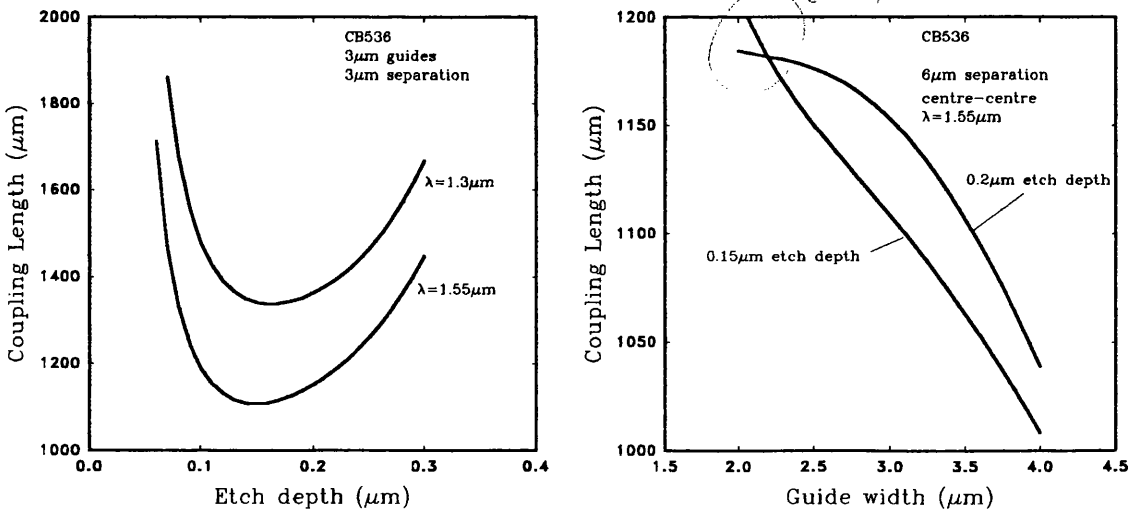

Figure 3.6. Impact of processing errors on coupling length.

3.2 *Forward Bias Variable Couplers*

3.2.1 Injection Methods

From the available methods for varying the refractive index given in Appendix 3, it is clear that the injection of carriers produces the largest index change. The large reduction of index is required as the design of the CGCPS requires one of the guides of the coupler to be effectively created or removed by reducing the effective index step, that makes the lateral guide, to zero. There are two ways of making a coupler operate by carrier injection, and these are illustrated in Figure 3.7. The first method is to inject carriers to create the lower index cladding areas of the guide, and the second is to start with an etched rib guide and inject the rib to reduce the index of the core region.

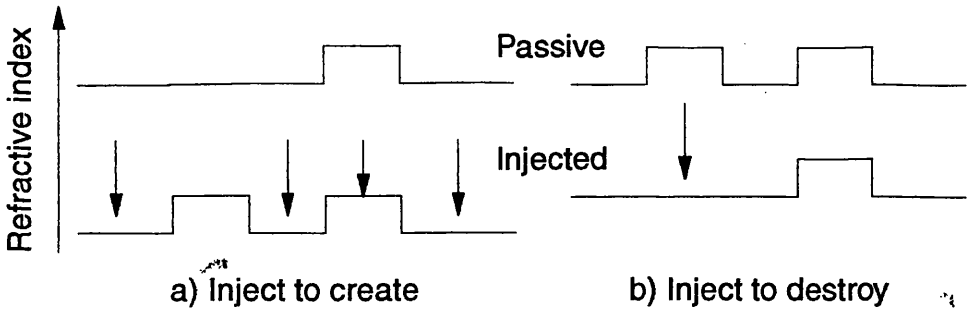

Figure 3.7. Methods of variable coupler operation with current injection.

Method a) suffers from a number of disadvantages. The current is injected into the main guide rib as well as the surrounding etched cladding regions. This means that a large proportion of the optical signal power has to travel through a lossy guide with many carriers in it. A smaller source of signal reduction would be due to the signal coming from a passive single guide into an injected guide. The waveguides would have the same index step but the passive guide, being un-injected, would be at a higher index overall giving a different propagation constant, β, and less efficient coupling. The third problem with the design is that in fabrication, the contacts would have to be laid onto areas that would have been etched. This, although not insurmountable, is a considerable problem with the facilities to hand, due to the etch damage discussed in Chapter 2. A variation of the first method is to have a flat index profile in the passive case and inject either side of the rib areas to create both guides. A device of this type has been fabricated, but did not exhibit good guiding behaviour. Reasons for this failure are due to the effective index being lowered beneath the metal contacts because of the low dielectric constant of the metal capping, and the strain imposed onto the GaAs material by the metallisation.[4] Carrier spreading may also lead to the weakening of the required guides, and this is discussed later in this chapter. Because of these reasons the 'inject to create' possibilities have not been pursued further

and the emphasis of the analysis has been on the 'inject to destroy' regime of variable coupling.

3.2.2 Method of operation

The ' inject to destroy' mode of injected coupler takes advantage of some of the disadvantages discussed above for the 'inject to create' method. When injected, the output signal is required to go through the uninjected guide only, and so avoids the lossy injected guide, and the signal is coupled from a guide that is of exactly the same refractive index profile. Also, only one metal contact is required.

The theoretical modes of a coupler in material CB536 with 3μm guides, 3μm apart, are shown in Figure 3.8. for injected and non injected cases. The operation of the coupler requires that the second (injected) guide be destroyed by the injection reducing its index. The coupler, while being injected, becomes asymmetric and this has advantages for the operation of the device. In Figure 3.8 it can be seen that the modes appear symmetric in the passive state, but when injected become asymmetric. The first order mode now has most of its power in the passive guide, while the second order mode shifts toward the injected rib. The input signal to the coupler is aligned to the passive guide, resulting in the majority of the power coupling into the first order mode, and a little going into the second mode. The second order mode also suffers more free carrier loss than the first as it has a larger percentage of power in the injected guide. These two factors help to reduce the influence of the second mode, which with further injection becomes cutoff as the injected rib is effectively destroyed.

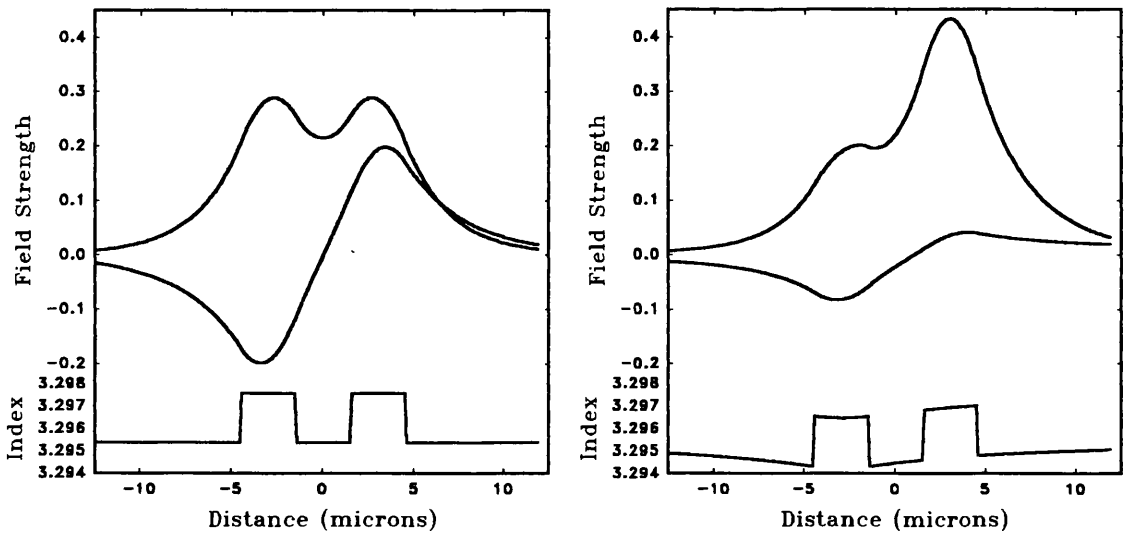

a) Passive Case. b) Injected.

Figure 3.8. Mode profiles of passive coupler and injected coupler.

The method of operation described above can be verified by measuring the Fabry-Perot resonances of each mode. Careful selection of the length of the coupler has to be

made for the test because; if the device is too long, the losses will make the resonant peaks too wide to see the peaks of the individual modes. If the device is too short, then too few peaks will be seen to verify the results. It is also advantageous to select the length so that most of the light appears in one of the guides, and a stronger signal can be measured. The tuneable laser used for measurement has an output of 1.3μm, so the coupling length is approximately 1400μm. A device length of 400μm is chosen, as this will give a higher 'Q' resonance, as the device is shorter, thus less lossy, and very little coupling across the guides.

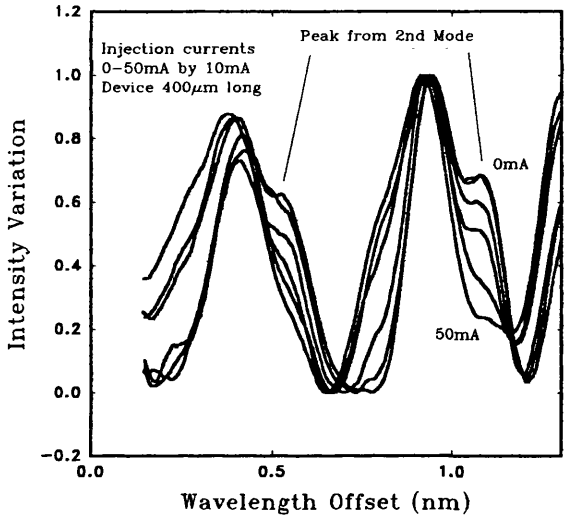

Figure 3.9. Fabry Perot Resonances of Coupled Guide Structure showing reduction of 2nd mode with increasing injection.

The results of Figure 3.9 show the reduction of the second mode resonance with injection of current. The second mode resonance is the smaller of the two, as less light is coupled into this mode. It is not possible to determine from Figure 3.9 whether the decrease is due to the reduced coupling into the second mode or the increased attenuation it suffers, as the resonances are too close together to determine whether the amplitude of the second peak is reduced alone or increases in width due to increased attenuation. Theoretically, both effects should be taking place.

3.2.3 Carrier Distribution

So far it has been assumed that injection of carriers reduces the refractive index below the metal contact through which it is applied. The material used is double heterostructure material similar to that used for lasers, so the carriers are confined in the active GaAs layer until they recombine with carriers of the opposite type in the same layer. The heterojunction barriers, which prevent the carriers of each type going further than the active layer, will be discussed further in Chapter 4.

The carriers are injected through the doped cladding layers which makes little difference to the total number of free carrier in these regions, so an increase of carriers only occurs in the active layer. Calculating the reduction of index in the active layer from both electrons and holes, the effect this has on the lateral effective index compared to the etched rib, is shown in Figure 3.10. These calculations show that the index reduction from an etch depth of 0.15μm can be equalled by a carrier concentration of just over 10^{18} cm^{-3}. Thus, the etch depth for the passive coupler design is set between 0.15-0.2μm.

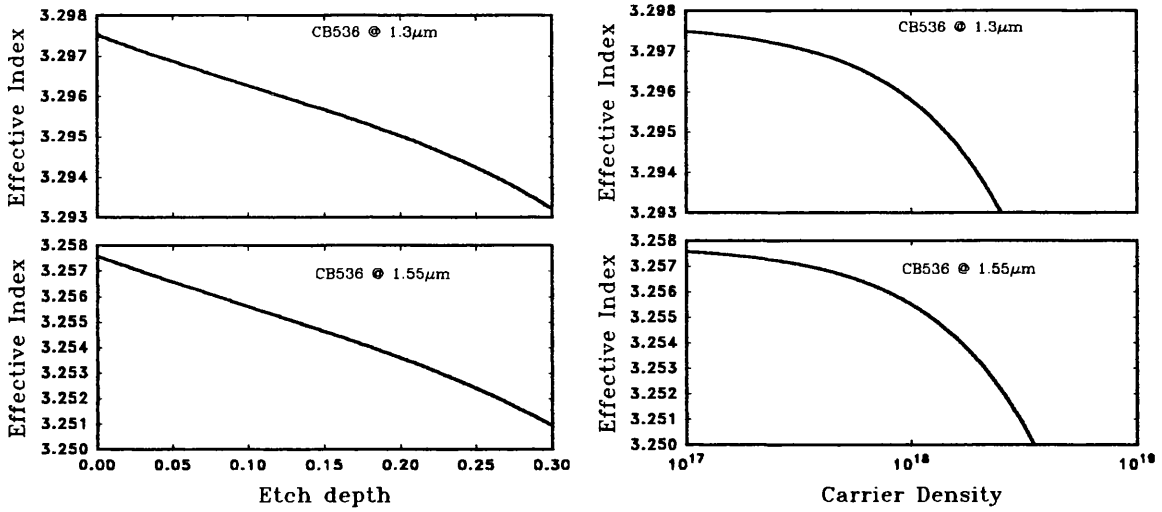

Figure 3.10. Effective index of CB536 with etch depth and carrier injection.

As the top contact is much narrower than the bottom contact, the current spreads out from top to bottom, increasing the area over which the carriers are injected into the active layer, and decreasing the current density. The carrier density in the active layer is further reduced as the increased concentration of carriers in the (undoped) active layer diffuses laterally along the layer. These effects can be modelled so that their effects can be more closely understood, by using Poisson's equation in the cladding layer, and a diffusion equation in the active layer.[5]

For the current spreading in the cladding layer it is fortunate that the guides are typically etched such that the top GaAs layer, which is highly conducting, is only present at the rib, thus we can start the modelling from the cladding layer, and assume that the voltage is constant across the cladding/capping interface, (Figure 3.11). This is not strictly true, as the current across the rib is not uniform, and in a rib of finite resistance, there will be a voltage change across the width. The slight voltage drop vertically across the rib can be neglected, as it is the current that is of interest. Having no GaAs capping to consider, and assuming charge neutrality in the doped cladding, the Poisson equation reduces from:-

$$\nabla.(\varepsilon\nabla\varphi) = -q(N_a - N_d - p + n)$$

to: $$\nabla^2\varphi = 0 \qquad [3.1]$$

where the ∇ operator is considered to be in x and y only, and $\varphi(x,y)$ is the voltage within the cladding layer. The boundary conditions around the cladding layer allow for current to flow into the cladding layer from the rib, and from the cladding into the active layer through the cladding/active layer boundary. On these boundaries the voltage, φ, is defined as $\varphi=\varphi_t$ at the cladding/capping interface, and $\varphi=\varphi_j(y)$ at the cladding/active layer boundary, where φ_t is the voltage applied to the rib, and $\varphi_j(y)$ is the voltage across the heterojunction. Current does not flow out from the device across any other boundaries as they are insulated, thus the boundary conditions of $\frac{\partial\varphi}{\partial y}=0$ at the device edges, $\frac{\partial\varphi}{\partial x}=0$ at the device surface outside the rib region are used.

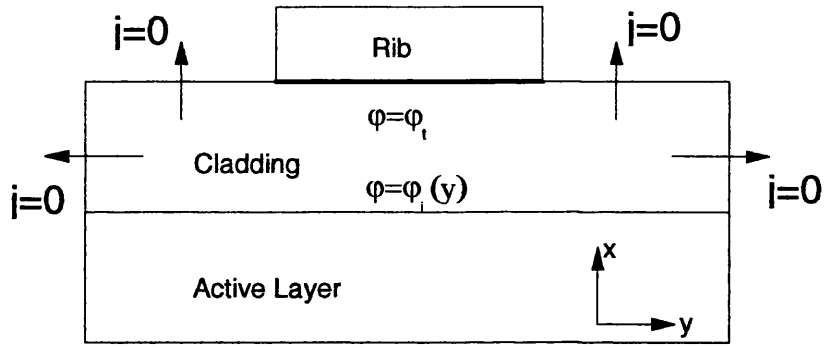

Figure 3.11. Boundary Conditions for Cladding Layer.

Initially $\varphi_j(y)$ is set to a constant value for the first solution. The voltage distribution is then found by a finite difference routine, and from this, an injection current, j(y) into the active layer can be found using [3.2]. This is also done for the current into the top of the cladding layer, as the voltage at the cladding/capping layer interface is an initial estimate, and it is the current that is finally of interest.

$$j(y) = -\sigma\frac{\partial\varphi}{\partial x} \qquad [3.2]$$

The value of cladding layer conductivity, σ, is only important to keep the voltage values realistic, as it is the current into the rib, and into the active layer that are required, and current has to be conserved, so that the total current into the active layer equals that entering the rib contact. The conductivity is chosen as 5 mho/cm in line with the literature.

In the active region, the dominant carrier distribution process is diffusion. Given this injected current distribution, j(y), the diffusion equation [3.3] can be solved to find a distribution of carriers n(y). Since the active layer thickness, d, is smaller than a diffusion length, the diffusion equation may be taken in y alone, *i.e.* n(x,y)=n(y). As signal wavelength energies are below that of bandgap, stimulated recombination need not be considered. In GaAs, Auger recombination can also be thought as negligible, leaving

spontaneous recombination as the carrier loss term. N_o is the initial carrier concentration before injection, due to impurities. This is set low (10^{14} cm^{-3}) as the active layer in this case is undoped.

$$D\frac{d^2N(y)}{dy^2}+\frac{J(y)}{qd}-B_r(N(y)+N_o)N(y)=0 \qquad [3.3]$$

The diffusion coefficient, D, is held constant for these calculations, although strictly speaking, D should be carrier concentration dependent. The diffusion coefficient is also dependent on the type of carrier. Here, the ambipolar diffusion coefficient is assumed, and, for this particular semiconductor material, measured by the method discussed in the next section. Solution methods for Poisson's equation, and the diffusion equation are given in Appendix 7.

Given a solution for the carrier distribution, the voltage at the heterojunction can be calculated [3.4] from the quasi Fermi levels, and substituted into the current spreading analysis as a boundary condition. This iterative process converges to an adequate degree of accuracy within 10 iterations.

$$V_j(y)=\frac{kT}{e}(v_1(n)+v_2(p))+E_g \qquad [3.4]$$

$v_1(n)$ and $v_2(p)$ are the quasi Fermi levels of conduction and valence bands given by[6]:-

$$v_1(n)=\ln\left(\frac{n}{N_C}\right)+3.5355\times10^{-1}\left(\frac{n}{N_C}\right)-4.95009\times10^{-3}\left(\frac{n}{N_C}\right)^2 +1.48386\times10^{-4}\left(\frac{n}{N_C}\right)^3-4.42563\times10^{-6}\left(\frac{n}{N_C}\right)^4 \qquad [3.5]$$

and similarly for the valence band, $v_2(p)$ is calculated with n/N_c replaced by p/N_v. N_c,N_v, are the density of states for the bands, and n=p can be assumed. For active layers with a percentage of aluminium, the bandgap energy, and Fermi levels are adjusted by standard formulae.[7] Equation [3.5] assumes parabolic bands, and so will not be valid for large amounts of aluminium in the GaAlAs.

Having found a lateral distribution of carriers in the active layer, the effect on the refractive index is calculated from Appendix 3, and the guiding properties of the device are found using the effective dielectric constant (EDC) method across the structure. Appendix 2. The optical signal from a single guide is coupled into the two modes of the coupler structure, and the resulting intensity profile is calculated at the other, output, end of the injected device. The resultant refractive index profile is shown in Figure 3.12. The effect of the carrier distribution is clearly seen, and the initial index step is preserved, but suppressed by a wider index depression. The index profile of the coupler becomes sufficiently asymmetric to cause the second order mode to cut off, while still leaving a small peak in the first mode in the tap guide. The size of this residual peak affects the on-off ratio of the coupler when used as a switch, but it can be reduced with further injection.

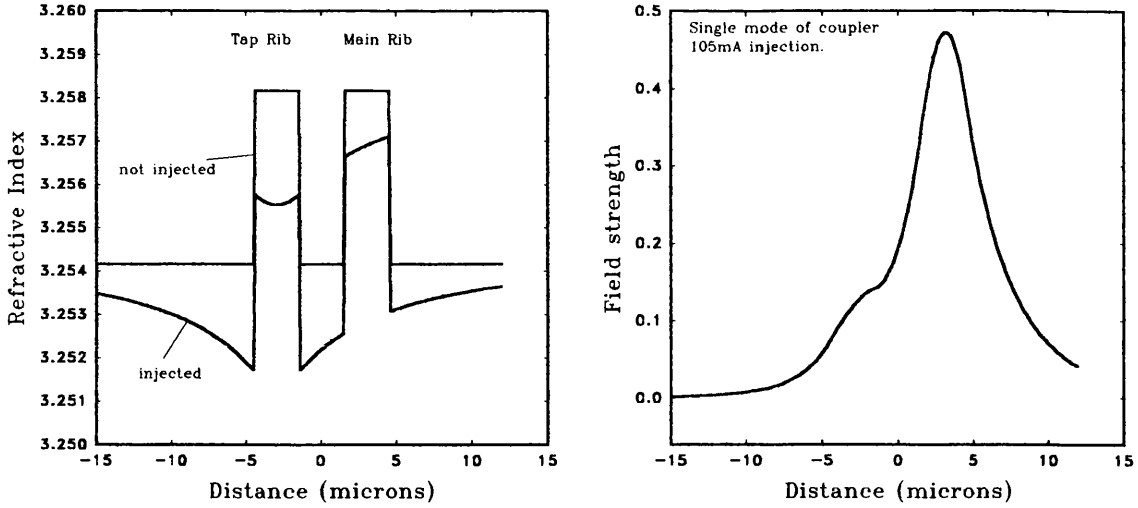

Figure 3.12. Refractive index profile of injected coupler and resulting guided mode shape.

3.2.4 Calibration

Because of the variability of parameters in different samples of semiconductor[6], the diffusion coefficient and recombination rate have to be measured to calibrate the model. To measure the diffusion coefficient the profile of the spontaneous emission from the injected guide is measured. As spontaneous emission will only occur where there are injected carriers present, the intensity profile of the emission gives a profile of the carrier distribution within the active layer. The carrier distribution from the theoretical calculations is compared to the experimental result, and the values of diffusion coefficient, D, and recombination term, B_r are adjusted until the calculated carrier profile matches the measured profile.

It is not easy to match the experiments with results with two variables, but an adequate match can be obtained since the two terms affect the carrier profile differently. Changing the recombination term has a small effect on the shape of the carrier distribution, but has a larger effect on the overall carrier density as expected. The diffusion term however has a greater effect on the spread of carriers, so by adjusting the two variables a good match can be obtained. The diffusion term is altered until an approximate match in shape is achieved. The recombination term can then be adjusted so that the correct concentration of carriers is present. This can be checked by comparison of the total current required to prevent guiding in experimental single guides. Fine tuning of the diffusion constant is then made to achieve better shape match with the carrier distribution.

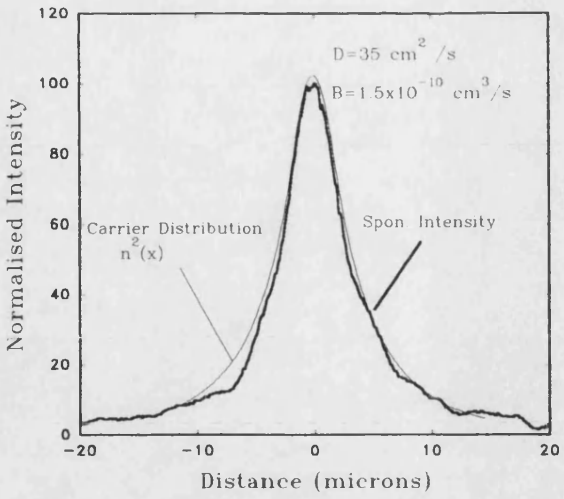

Figure 3.13. Match of spontaneous intensity to square of carrier distribution.

The spontaneous intensity is measured with an IR camera focussed onto the end facet of the guides while they are injected. As it is a guide that is being viewed, it is likely that the structure will guide the spontaneous light, and give a distorted intensity profile at the facet. To reduce this, the observed light is strongly filtered, so that only the shortest wavelengths are measured. Short, high energy, wavelengths that are generated at the far end of the guide suffer a very large absorption as they travel along the guide, and their intensity is negligible at the viewed facet. The intensity recorded should, therefore, be only from the spontaneous light generated very close to the facet. This light has not been guided, thus gives the position of the carriers in the active layer, not a guided mode profile.

As the intensity from the spontaneous emission is proportional to $B_r N(N_o+N) \sim B_r N^2$, comparisons of the experimental intensity distribution and N^2 are made. This is shown in Figure 3.13 for the given values, at a current of 80 mA showing a good match. Accuracy for the diffusion constant measurement is of the order of $\pm 5 cm^2/s$, as changes in the diffusion coefficient smaller than this, have a negligible effect on the carrier profile.

3.2.5 Experimental Results

Figure 3.14 shows the comparisons of the results from the fabricated coupler and the model, and illustrates that optical switching has been achieved. The theoretical profiles for switching, however, do not operate as efficiently as the practical prototype, with the values of diffusion and recombination given above, and the theoretical structure only becomes truly single moded at 100mA. The lateral shift in output power at low currents is due to detuning of coupling and deformation of the guided mode from the effect of the carriers on the refractive index. The required annihilation of the tap guide is only achieved at the higher values for injection, (80mA experimental, 100mA theoretical). The

experimental result appears better than the theory, and this is thought to be due to the loss from the higher number of free carriers in the tap guide affecting the output in that region.

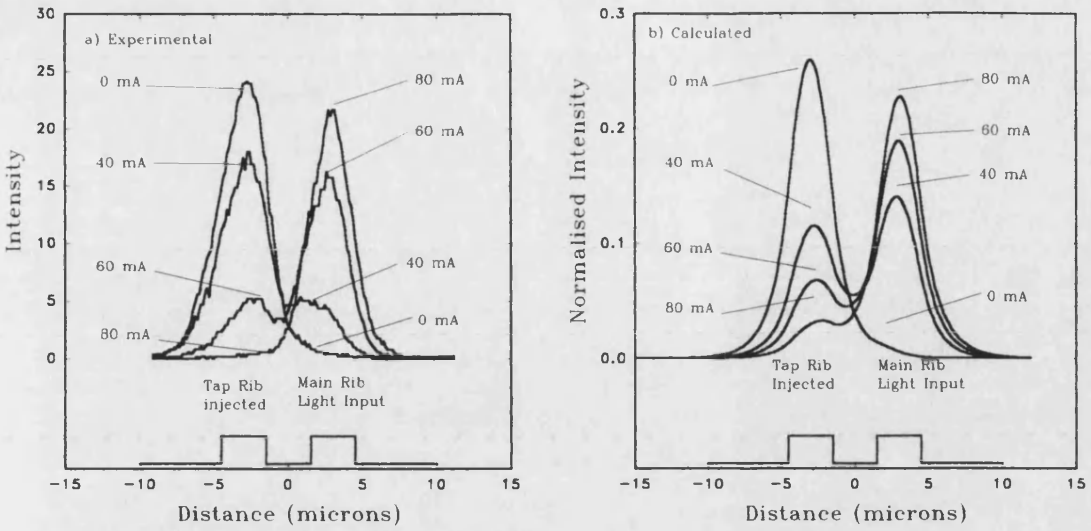

Figure 3.14 Experimental and Theoretical near field profiles of twin ridge couplers of device UB348 at1.55μm signal wavelength.

Measuring the amount of power that is present in each side of the coupled structure gives a figure for the signal crosstalk and on-off ratio for the device. The power levels are too low to be measured with photodetectors, so an integral of the near field profile is used. Taking the power either side of the centre line, the on-off ratio and crosstalk are 14.5 dB in the experimental device. The theoretical device has a poorer performance of 10-10.5dB.

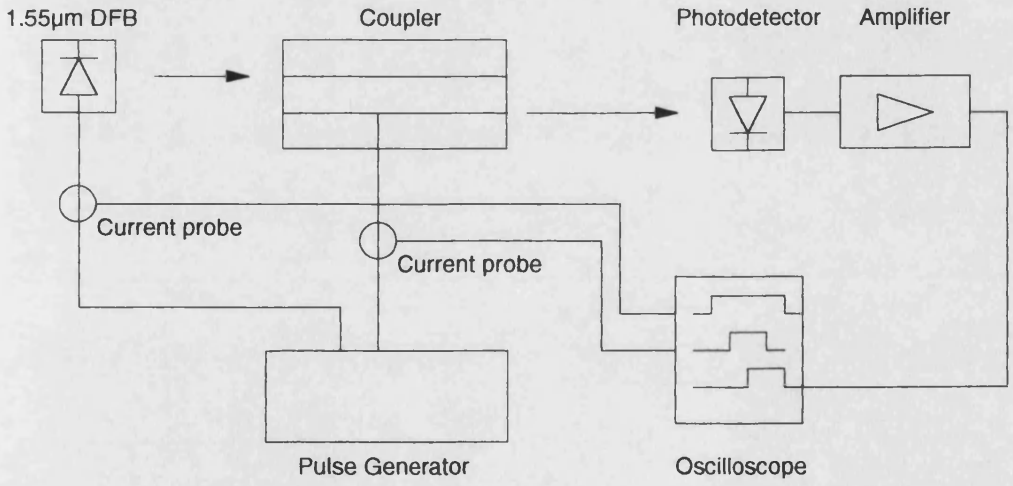

Figure 3.15. General set-up for speed measurement.

3.2.6 Speed

The switching speed of the above coupler has been measured using a photodetector and a fast amplifier. The outline of the apparatus is shown in Figure 3.15. Care has to be taken in measuring high speeds in the devices as each element of the measuring equipment has its own intrinsic delay. The coaxial cable used for all signals has a

propagation speed of 5ns/m measured by time domain reflectometry. The amplifier has a delay of 10ns when the photodetector is illuminated with a 1.55μm DFB laser. This does assume that the laser has an instantaneous turn on, which may introduce an error. The current probes are rated to over 1GHz so do not cause an appreciable rise time delay. The source laser is turned on in a quasi CW state so that only the effects of injecting the coupler are measured.

Taking into account the cable lengths and other delays the coupler has a turn on time of 6ns, and a recovery time of approximately 12ns. It is very difficult to see the recovery time, as the signal to be measured is very small (0.1mV). The transition is sharper when turning on the device, and so more visible. When turning off, the slope of the waveform makes it difficult to see the end point.

3.3 Reverse Bias Variable Couplers

The principle behind the reverse bias coupler is to achieve a refractive index change utilising the depletion of carriers due to the reverse biassing of a pn junction. The material forming the pn junction is adequately doped, so that the free carriers reduce its refractive index. In the depletion region, where the carriers are displaced, the refractive index can be considered un-affected, and so, varying the width of the depletion region varies the width of the higher index layer. The large electric field in the depletion region also affects the refractive index of the material through the Pockels, or linear electro-optic effect (LEO), but this effect is much smaller than the carrier effect and has different effects for polarisation of light, and crystallographic direction. The LEO effect is, therefore, not considered further.

By locally altering the guiding properties of the slab material, a lateral guide can be induced by the applied voltage. If this is done close to an existing guide, then an electrically controllable coupler can be made, which is useful in the construction of the optical switch. This method will also have an advantage over the forward bias designs in that the reverse biassing does not require continuous current to flow, thus reducing the power requirement to that needed to move the charge from the depletion region. To create a lateral guide, the bias must be confined to the central, core region of the guide. Confining the bias to a particular region is a problem. If a single contact is placed above the guide region, the applied voltage would appear over the whole capping layer as its resistance is very low. Side contacts, of a constant potential, are required to restrict the reverse biassing to the central region, but to have a different voltage in different regions would result in lateral voltage gradients. The resistance of the doped layers would make any currents induced very high, and lead to heating problems. A solution to this would be to bombard the region between the core and outer contacts. This increases the material resistance due to the lattice damage it creates, and will in turn reduce the lateral current flow. The effect of this lattice damage, and the strain from the applied contacts will affect the index of the material, but this is not considered at this stage.

The following is a description of the considerations taken in evaluating the concept.

3.3.1 Optimisation of Material

3.3.1.1 pn Junction.

The amount by which the carriers reduce the refractive index in the material is given in Appendix 3 for n and p type doping. These equations are for GaAs with-in the 1μm-1.55μm wavelength band, but other references give slightly different values taken from experimental results. The refractive index of GaAlAs has not been extensively studied and it is tempting to replace the effective carrier masses in the above equations with those for GaAlAs. It has been shown, however,[9] that the free carrier loss, which has a similar dependency on effective mass, is similar in GaAlAs to that in GaAs, so here we assume that the reduction in index due to free carriers is the same in each material.

The depletion width for an abrupt pn junction can be approximated by:-

$$w_n = \sqrt{\frac{2\varepsilon(V_{bi}+V)}{qN_D}\left(\frac{N_A}{N_A+N_D}\right)} \qquad [3.6]$$

$$w_p = \sqrt{\frac{2\varepsilon(V_{bi}+V)}{qN_A}\left(\frac{N_D}{N_A+N_D}\right)} \qquad [3.7]$$

where w_n is the depletion width in the n-type region, and w_p is the depletion width in the p-type region. V is the applied reverse bias, and V_{bi} is the built in voltage across the junction given by the difference in fermi levels in the n and p doped materials.

$$V_{bi} = E_g - E_{fp} - E_{fn} \qquad [3.8]$$

$$E_{fn} = \ln\left(\frac{n}{N_C}\right) + 3.353\times10^{-1}\times\left(\frac{n}{N_C}\right) - 4.95009\times10^{-3}\times\left(\frac{n}{N_C}\right)^2 + 1.48386\times10^{-4}\times\left(\frac{n}{N_C}\right)^3 - 4.42563\times10^{-6}\times\left(\frac{n}{N_C}\right)^4 \qquad [3.9]$$

N_c is the density of states, and n is the free carrier density. A similar expression is used for E_{fp} using the hole density and density of states for the conduction band. If it is assumed that all the donors and acceptors are fully ionised, and the minority carriers are negligible, then the depletion width can be calculated easily.

Since the dimensions and refractive indices of all the layers in the material are now known, the multi-layer waveguide program can be used to find an effective dielectric constant (EDC) for the material for guiding in the vertical direction for various applied voltages. Then, using the EDC method with and without reverse bias, the lateral guiding strength can be evaluated given a central core region with the bias applied, and the outer regions with no bias. This does, however, assume that the applied voltage can be confined abruptly, and the confinement methods have no effect on the vertical effective indices.

The free carrier effect on refractive index is very small, typically <1%, so the material parameters have to be chosen so as to optimise the effect on the guiding properties. It can be seen intuitively for a symmetrical slab guide that when the core width is small, the propagation constant for the guide, β, will be unaffected by small changes in the width. Similarly, β will not be greatly affected by changes in guide width if the core region is very large. There must, therefore, be an optimum core dimension for which the slab guide propagation constant, and thus effective index, is most sensitive to variation in core width, which in this case is the depletion width.

As it is the vertical effective index that needs to be varied, the optimisation of the material structure is achieved by finding the core width for maximum change in β for the slab guide. For the symmetric guide:-

$$\frac{\partial\beta}{\partial b} = \frac{h^2\left(\frac{pb}{1+pb}\right)}{b\beta} \qquad [3.10]$$

where the field profile is described by

$$E_y(x) = \begin{cases} A\cos(h)|x| & \text{for } |x| < b \\ B\exp(-p)|x| & \text{for } |x| > b \end{cases} \qquad [3.11]$$

where 2b is the guide core width, and h, p and β are taken for the first symmetric mode. Given that the guide normalised frequency, w, is obtained from:

$$w^2 = b^2\left(h^2 + p^2\right) \qquad [3.12]$$

the sensitivity of β to variation in guide width can be found (graphically) to be maximum approximately when w=0.54 for a wide range of guide widths and index steps. As the depletion width is very narrow, and the effect of the carrier removal very small, guiding with the depletion layer alone is very weak, and the optimum operating point cannot be reached. Increasing the doping, to increase the carrier effect, decreases the depletion width according to [3.6] and [3.7]. There is advantage in doing this but the returns are proportional to the square root of carrier density, and even with doping of 10^{19}, which would result in very lossy material, we can only reach a value of w=0.025 assuming a symmetric effect on index in n and p types. This is not strictly true as shown in Appendix 3.

3.3.1.2 PIN Structure

The calculations above show that the depletion layer alone forms a very weak guide that is insensitive to increases in the depletion width. A stronger guide that is also more sensitive to core width variation is, therefore, required. Two methods are possible for increasing w; increasing the guide width, (depletion layer), or increasing the index step between outer regions and the core. Use of a PIN structure is considered here, (Figure 3.16) using the 'I' region as an artificially increased depletion layer width, and has the advantage that the wider, undoped, active layer will reduce losses dramatically in the material. The introduction of the undoped layer does, however, mean that the voltage drop

across the depletion layer alone in the PN device is now across the 'I' region as well. The reduction of electric field reduces the depletion regions at either end of the 'I' region, and the effect of extra applied bias is reduced. The p-type depletion width for a PIN structure is given by:-

$$W_p = \frac{-N_A i + \sqrt{N_A^2 i^2 + 2\frac{N_A}{N_D}(N_A + N_D)\frac{\varepsilon}{q}(V_{bi} + V)}}{\frac{N_A}{N_D}(N_A + N_D)} \qquad [3.13]$$

where i is the 'I' region width. It can be seen that if i is zero, this reduces to the PN equation given in [3.7], otherwise, [3.13] will always be smaller than [3.7] as [3.13] takes the form:-

$$W_p(\text{pin}) = -q + \sqrt{q^2 + W_p^2(\text{pn})} < -q + q + W_p(\text{pn}) \qquad [3.14]$$

The applied bias will also create a change in depletion width at the ends of the 'I' region, where the optical field is smaller. This results in a reduced change in effective index compared to the PN case where a bigger effect is achieved as the confinement factor of the varying region is higher. Reduction of depletion regions and confinement factors within them make the PIN type structure less attractive for a field induced waveguide.

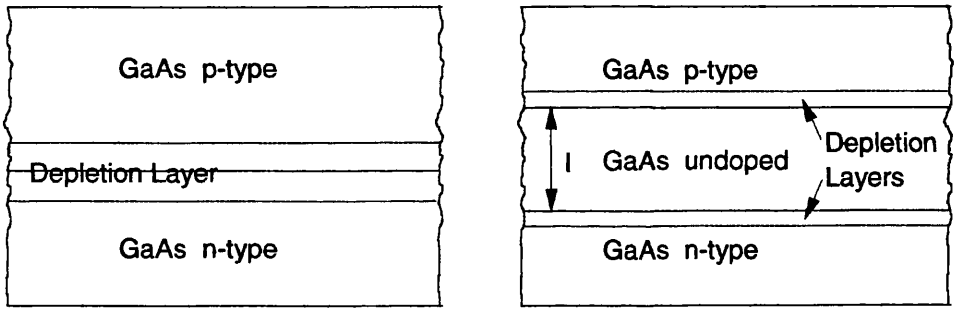

Figure 3.16. PN structure and PIN structure.

3.3.1.3 Heterostructure Devices

From the above, it is clear that extra layers of lower index must be introduced into the material to increase the vertical confinement of the mode in the depletion region, and thus the effect of applied bias on the effective index. Analysis of this is not easily undertaken analytically, therefore optimisation is carried out using the multi-layer waveguide program described in Appendix 2.

For the structure shown in Figure 3.17, the n type and p type active GaAs layers have been optimised using a doping of 10^{18} and 10^{19} cm^{-3} (Figure 3.18), using the carrier effects on index given in Appendix 3. The structure is, for the present, assumed symmetric with infinite p and n type GaAlAs cladding layers. The results shown are for the change in effective dielectric constant from no applied bias to an applied bias of 5 volts. It is assumed that the applied voltage is across the depleted region only, and no voltage is dropped

across the cladding layers, or heterojunctions. The cladding aluminium content of 28% is chosen as this is a well used concentration, allowing a high index change, but without the added problems of the semiconductor band structure becoming predominantly indirect, or the lattice being overly strained.

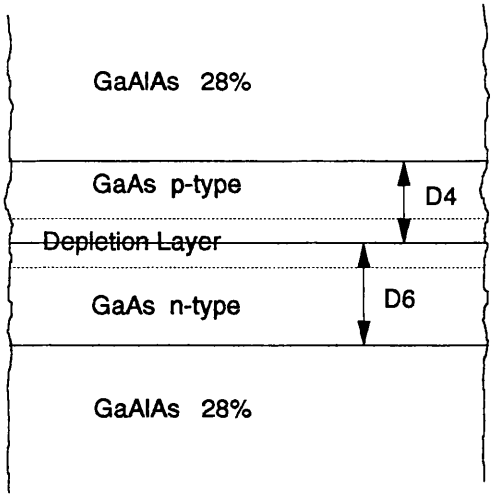

Figure 3.17. Multilayer Material.

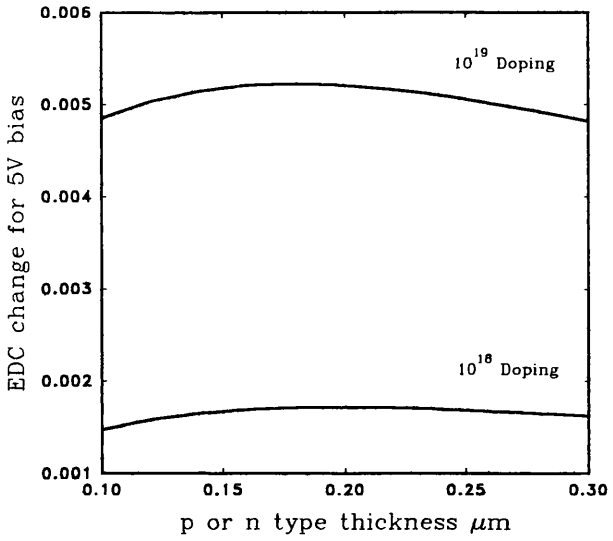

Figure 3.18. EDC Change with GaAs layer thickness.

The active layer width for maximum effect of bias shown in Figure 3.18 varies slightly for the different doping concentrations. The variation is due to the fact that the index change for n and p types is different, resulting in an asymmetric guide. The index reduction for p-type is much less than for n-type, so the layer thickness for maximum effect is such that the maximum amount of the guided mode is carried in the n-type depletion region.

The n and p type doping is chosen to be equal as the depletion region is required to be large in the n-type material. If the p-type doping is reduced, it will reduce the depletion depth in the n-type material. To increase the p-type doping would increase the carrier effect in this region and also increase the n-type depletion width. This is beneficial to the operation of the device, but at the expense of increased free-carrier loss. It is therefore decided to consider equal doping levels at present.

For a practical device, top and bottom contacts have to be connected to the material, which puts a limit on the thicknesses of the cladding layers. The contact also has to be made to a highly doped GaAs layer for adequate ohmic contact to be made. Metal contact is not made to GaAlAs because good ohmic contact cannot be made to this material.

Assuming a 0.1μm and 0.2μm capping layer of GaAs, the effect of a finite cladding layer thickness is shown in Figure 3.19 for 10^{18} cm^{-3} doping. The active n and p type layers are both 0.2μm thick, and light wavelength is 1.55μm.

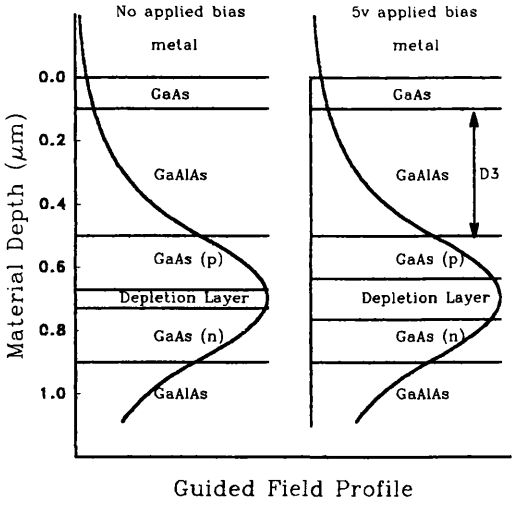

Figure 3.19. Field profiles for material with finite cladding with and without bias.

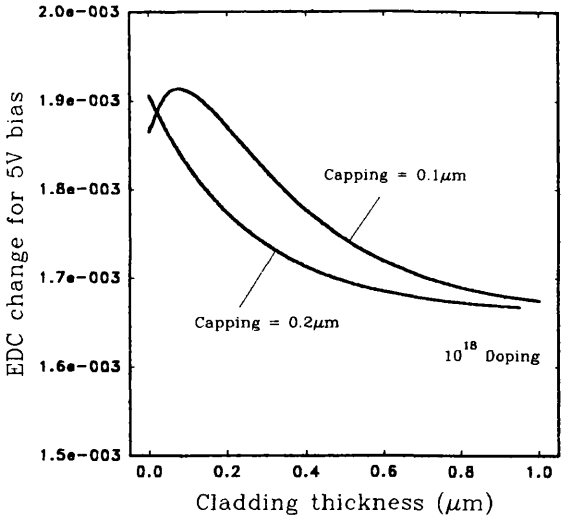

Figure 3.20. EDC change with 5V bias for different material thickness.

It is clear from Figure 3.20 that the effect of the bias is dependent on both cladding and capping layer thicknesses. As expected, the change in effective dielectric constant reflects exactly the amount of power there is in the depletion region for the particular layer thicknesses. The initial rise in the case of the 0.1μm capping is caused by the high index capping being close to the active layer, making the structure appear as a very broad active layer with a GaAlAs bottom cladding and metal top cladding. This arrangement will reduce the amount of modal power in the variable depletion layer, as the depletion region will appear to be to one side of the whole active (high index) layer. As the cladding becomes thicker, the influence of the capping is lessened, and the depletion region confinement factor is now reduced because the large index step between the semiconductor and the air is moved further away from the core region. The guide will eventually become dominated by the GaAlAs GaAs index step, which is much weaker, thus reducing the confinement factors in the core regions.

Although the required effect of large EDC change occurs for a 0.1μm cladding, the proximity of the top metal layer must also be taken into account. It can be seen from Figure 3.19 that even for 0.4μm thick cladding thickness there is a significant portion of the guided mode in the contact layer. From equations [2.5], the resulting attenuation from metal losses alone (assuming Gold) is 554dB/cm for every 1% of power in the metal. For the 0.4μm cladding shown above the power in this metal is 0.02% of the total guided mode, leading to 11 dB/cm of lost power. This is clearly an undesirable factor.

Increasing the cladding layer thickness reduces the loss, and with 1μm of GaAlAs the loss is reduced to 5dB/cm, but the induced effects on the guiding properties are clearly not at their optimum working point. Other disadvantages also result from a thick cladding layer, namely: increased voltage drop across the layer, increased lateral spreading of the

reverse bias, and further difficulty in confining the lateral effects (e.g. H^+ bombardment would have to be deeper).

3.3.2 Induced Waveguide for Variable Coupler

To create a coupler for use as an electrically variable device, it is advantageous to have two guides of similar strengths to achieve 100% power transfer from one to the other. It is also desirable to vary one of these guides, leaving the other unchanged. To achieve these requirements the induced guide strength must be equal to the strength of a rib guide, and both must have adequate guiding ability on their own to support a clearly defined mode. The requirement, therefore, is to find the rib height required to create the same change in effective index as that given by the reverse biassing. As the rib will be in addition to the material so far discussed, it will have to be made from a locally increased thickness of the GaAs capping layer. In practice the rib thickness would be the original material thickness, and the surrounding areas would have to be etched away, then contacts evaporated on where the reverse bias guides are to be induced. (It is difficult to put contacts on etched material, as they create very high resistance contacts.) The GaAs cannot be completely etched away as contact has to be made to GaAs not GaAlAs, Figure 3.21.

Assuming a cladding thickness of 1.0μm, and a capping thickness of 0.2μm the rib height would have to be 0.15μm to mimic the reverse bias induced guide. For the case where the capping is 0.1μm thick the rib height has to be 0.2μm. Ribs between 0.1μm and 0.15μm in height are practical to fabricate, due to the cladding being so thick, and the rib loading having only a slight effect. If the cladding is reduced to 0.5μm, the required rib height in both cases is less than 0.02μm, which is impractical.

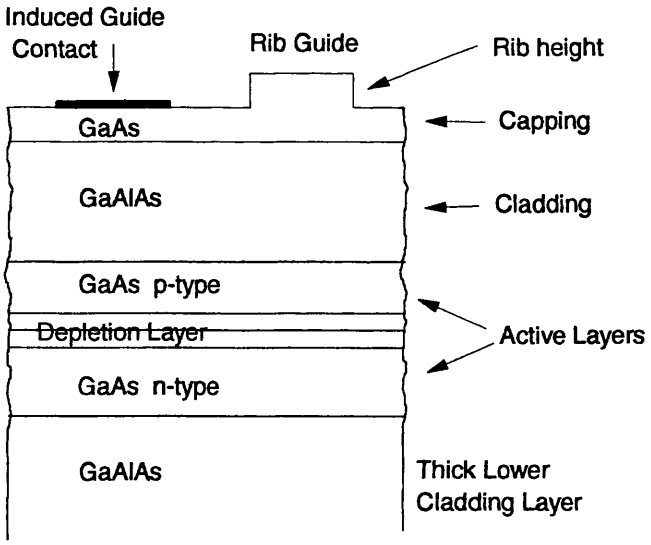

Figure 3.21. Reverse biassed induced coupler structure.

Another consideration is the coupling length between the two guides. For this analysis we shall assume that the induced guide has sharply defined edges, as does the rib loaded guide, and that the strength of the two guides is equal. For the material discussed

above the effective dielectric constant change laterally from core, rib loaded material, to cladding with no rib loading, is 0.00167. This is a very small change, and for a guide to have a practical guiding ability, the rib and induced guide areas will have to be wide. As an initial starting point we chose the guide strength (normalised frequency) of $w=\pi/3$. This allows a single mode guide, with reasonable confinement for a single guide on its own. At a wavelength of 1.55μm, this gives a guide width of 12.6μm. Figure 3.22 below shows the coupling length for two such guides with varying separation.

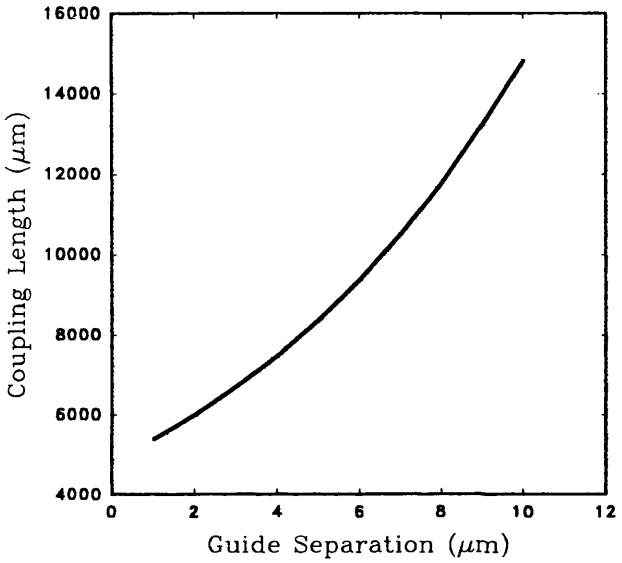

Figure 3.22. Coupling length for coupler with 12.6μm wide guides of $w=\pi/3$ with increasing guide separation.

These coupling lengths are clearly far too large for a realistic device, as the device would not only be very long, but losses over this magnitude of length would be intolerable. In considering the fabrication of the device it is noted that the induced guide would need space for the side contact and proton bombardment between it and the rib guide. This would require a separation of at least 5μm, giving a coupling length of 8mm. Weaker guides could be used to give lesser coupling lengths, but loss of mode confinement will result in more difficulty in separating the output from the individual guides, resulting in signal crosstalk. These disadvantages would be compounded by the extra problems of confining the reverse bias to the required areas and overcoming the added index variation from metal contacts. The LEO effect has not been taken into account, nor the voltage drops across the hetero-interfaces, both of which would make the device less effective, so the method of inducing waveguides with reverse bias has not been considered any further in this thesis.

3.4 Conclusions

This chapter has studied the variable coupler from the robustness of the passive device to the finer points of the operation of different types of variable structures. Mathematical modelling has lead to the optimisation of device structure, and in modelling of the carrier diffusion lead to measurement of the diffusion coefficient. The important factors in the requirements of the device have been discussed and compromises between conflicting ideals have been explained.

The calculations and experimentation show that out of the different types of variable coupler devices, the injected coupler gives the best operating characteristics for use in the CGCPS.

References.

[1] A. Yariv, "Optical Electronics." 3rd Edn., Holt-Sanders, p437. 1985.

[2] D. Marcuse, "Light Transmission Optics." New York, Van Nostrand, p415. 1972.

[3] J. Sarma, I. Flint. "Electrically Variable Couplers for Integrated optics." IEE proceedings pt J, Vol. 135, No. 3, pp268-275. June 1988.

[4] L.D. Westbrook, P.N. Robson, A. Majerfeld. "Strain induced optical waveguiding in GaAs epitaxial layers at 1.15μm." Electronic Letters, Vol. 15, No. 3, pp99-100. February 1979.

[5] G. Lengyel, P. Meissner, E. Patzak, K. Zschauer. "An analytical solution of the lateral current spreading and diffusion problem in narrow oxide stripe GaAlAs/GaAs DH lasers." IEEE Journal of Quantum Electronics, Vol. 18, No. 4, pp618-625, April 1982.

[6] W.B. Joyce, R.W. Dixon, "Analytic approximations for the Fermi energy of an ideal Fermi gas." Applied Physics Letters, Vol. 31, No. 5, pp354-356. September 1977.

[7] H.C. Casey, M.B. Panish, "Heterostructure Lasers pt A." Academic Press, p194.

[8] P.J. Poole, C.C. Phillips, M. Henini, O. Hughes, "All-optical Measurement of the Giant Ambipolar Diffusion Constant in a Hetero-nipi Reflection Modulator." Semiconductor Science and Technology, Vol. 8, pp1750-1754. July 1993.

[9] M. K. Hibbs-Brenner C.T. Sullivan. "Low-loss AlGaAs optical rectangular waveguides at 830nm." Applied Physics Letters, Vol. 56, No. 16, p1529-1531. April 1990.

Chapter 4

Semiconductor Material Design

Previous chapters have concentrated on materials that had already been supplied, and it was clear that these materials were not ideal for use in the CGCPS due to excessive losses and the high current needed to make electrically variable couplers. This chapter describes the design of a new semiconductor material structure and composition, covering the design aspects needed for loss reduction, coupler design and carrier injection. The results from the grown material are presented and show excellent reduction in losses, and good coupling that is electrically controllable. The mechanism for coupler variation in one material is not as expected, and discussion and theoretical analysis of its mechanism is given.

4.1 Material Composition

Chapter 2 showed that a major source of propagation loss was due to the doping of the material causing free carrier absorption. For this reason, the doping is to be as low as possible in the design of the new material. A compromise has to be made, however, in that the doping is required to keep the resistance of the device low enough to make current flow easily through the material layers, and in part, to help with the confinement of the carriers in the active layer. The carriers are also confined by the heterojunction barriers, which are due to the aluminium content of the cladding layers. The aluminium also has an effect on refractive index, and helps to confine the guided mode in the active region. The unconfined carriers will be free to flow across the device, and although they will contribute to the reduction of index, they will increase the current that has to be injected into the device. This section evaluates the amount of carriers that are not confined in the active layer, and studies the influence of reduced doping on the confinement.

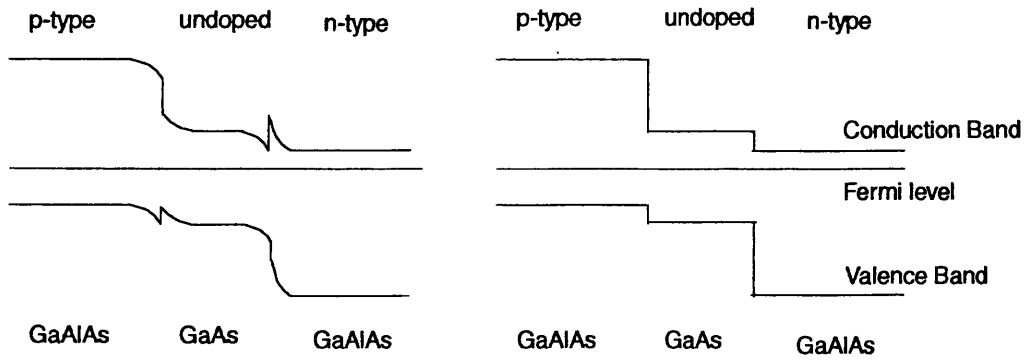

a) Band Structure with discontinuities. b) Assumed Band Structure

Figure 4.1. Double heterojunction with no applied bias showing band structure assumptions.

To estimate the required doping concentrations for efficient device operation, the double heterostructure band discontinuities, ΔE_c , ΔE_v can be evaluated. Some simplifying assumptions are made here, in that the junctions are sufficiently graded to be able to discount the interfacial spikes in the bands, as shown in Figure 4.1.

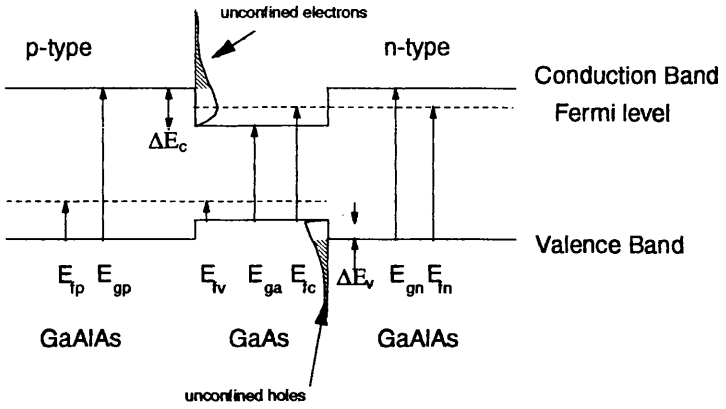

Figure 4.2. Double Heterojunction With Applied Bias.

Figures 4.1 and 4.2 show the general double heterostructure in unbiassed and forward biassed states, with the quantities shown and the unconfined carriers shaded. In the forward biassed state, the Fermi levels in the 3 layers do not align together, but the p-type fermi level aligns with the hole quasi-fermi level in the active layer, and the fermi level in the n-type material becomes level with the active layer electron quasi fermi level. Once all the fermi levels have been calculated, the band discontinuities are found easily.[1]

$$\Delta E_C = (E_{gp} - E_{fp}) - (E_{ga} - E_{fv}) \qquad [4.1]$$

$$\Delta E_v = E_{fn} - E_{fc} \qquad [4.2]$$

Calculation of the fermi levels is complicated in the GaAlAs layers, as the indirect X and L bands in AlAs are lower than the Γ band, so have to be considered in the GaAlAs ternary alloy. Using the density of states for each band separately the equation for number of free carriers in the conduction band, n, and valence band, p are:-

$$n = N_c^{\Gamma} f_{1/2}\left(\frac{E_f - E_c}{kT}\right) + N_c^{X} f_{1/2}\left(\frac{E_f - E_c - \Delta X}{kT}\right) + N_c^{L} f_{1/2}\left(\frac{E_f - E_c - \Delta L}{kT}\right)$$
$$p = N_v f_{1/2}\left(\frac{E_V - E_f}{kT}\right) \qquad [4.3]$$

where ΔX and ΔL are the difference between the X and L bands and the conduction band edge E_c. The density of states for all bands is calculated from:-

$$N_c = 4.83 \times 10^{15} (m^* T)^{3/2} \ \text{cm}^{-3} \qquad [4.4]$$

and m^* for the aluminium content, $x<0.4$ for each band is given as

$$m^{\Gamma} = 0.067 + 0.083x$$
$$m^{X} = 0.85 - 0.07x \qquad [4.5]$$
$$m^{L} = 0.55 + 0.642x$$

For the valence band, as the light hole and heavy hole bands are at the same level, the effective masses can be combined, and taken as:-

$$m_p = 0.48 + 0.31x \qquad [4.6]$$

The material band gaps can also be expressed, taking the valence band as the reference, as:-

$$\begin{aligned} E_g^{\Gamma} &= 1.424 + 1.247x \\ E_g^{X} &= 1.9 + 0.125x + 0.143x^2 \\ E_g^{L} &= 1.708 + 0.642x \end{aligned} \qquad [4.7]$$

The fermi integral $F_{½}$ is given by:-

$$F_j(\eta) = \frac{1}{j!}\int_0^{\infty} \frac{x^j}{\exp(x-\eta)+1} dx \qquad [4.8]$$

and cannot be expressed in an exact closed analytical form. Various approximations have been made for the outer regions of η, and here the following are used[2]:-

$$F_{½}(\eta) \approx \exp(\eta) \qquad \text{for } \eta<-4 \qquad [4.9]$$

$$F_{½}(\eta) \approx \frac{4\eta^{3/2}}{3\sqrt{\pi}} + \frac{\pi^{3/2}}{6\sqrt{\eta}} \qquad \text{for } \eta>1.5 \qquad [4.10]$$

To evaluate the integral for $-4<\eta<1.5$ a ninth order polynomial has been fitted to the tabulated data using the least squares method. This is found to be more than 99% accurate over the range and better than other polynomial approximations that cover larger ranges.

$$\begin{aligned} F_{½}(\eta) = 0.76587 &+0.60657\eta + 0.18851\eta^2 \\ &+0.18393\times10^{-1}\eta^3 - 0.30522\times10^{-2}\eta^4 \\ &-0.46054\times10^{-3}\eta^5 + 0.84350\times10^{-4}\eta^6 \\ &+0.70103\times10^{-5}\eta^7 + 0.12377\times10^{-5}\eta^8 \end{aligned} \qquad [4.11]$$

As the aim of the calculation is to find the lowest doping necessary, we shall assume that all the dopants are ionised, and the total carrier density is the same as the net dopant concentration.

In the active layer, which is nominally undoped, the required injected carrier density is used to calculate the quasi fermi levels. Quasi fermi levels are used here as the material layer is no longer in equilibrium. The required number of carriers to reduce the refractive index by an amount large enough to wipe out the guides so far fabricated has been approximately 2×10^{18} cm^{-3}, which is the value used for these calculations. Having found the number of carriers, the fermi level can be found numerically from [4.3], for each material layer, thus the band discontinuities can be calculated.

The unconfined electrons in the active layer are those at a higher energy level than the electron barrier, $E_{ga}+\Delta E_C$, and in the valence band, the holes of lower energy than the hole barrier, ΔE_V. These carriers can be quantified by an expression similar to [4.3], but with the fermi integral taken from the edge of the carrier barrier, instead of the conduction or valence band edge. Therefore the unconfined holes are given by:-

$$p_{unconfined} = N_v F_{1/2}\left(\frac{E_v - E_{fv} - \Delta E_v}{kT}\right) \qquad [4.12]$$

where the valence band energy is usually taken as the reference, so E_v=0. Similar calculations are done for the conduction band with all three conduction minima.
The results from these calculations are shown below in Figures 4.3 and 4.4, and illustrate how the two types of carrier are affected. The holes are less confined because of the position of the quasi fermi levels in the active layer. At a carrier concentration of 2×10^{18} cm^{-3} the conduction band quasi fermi level is outside the bandgap, while the hole quasi fermi level remains inside, which leads to ΔE_c being greater than ΔE_v. These calculations show that for less than 1% of carriers to flow over the barriers the doping has to be in excess of 10^{15} cm^{-3} for n-type and p-type, with a 35% aluminium content, which puts the restriction for doping on the layer resistance that can be tolerated for the device. As the device layers under consideration are generally very thin (<1-2μm), the overall device resistance is low, even for low doped layers. (The device is supported by at least a 100μm thick substrate layer which is heavily doped and much wider than the device, so contributes very little to the device resistance.) Doping of 10^{15} cm^{-3} in p-type GaAs has a resistance[3] of 20 Ω cm which for a 3μm by 1000μm device, 1μm thick gives a resistance of 66Ω. N-type GaAs has a resistance 10 times less for the same doping so is not considered. This resistance is a little high, so the doping has to be increased slightly. Resistivity is approximately proportional to carrier concentration, so 10^{16} cm^{-3} doping reduces the resistance to 6Ω which is easily low enough for successful operation.

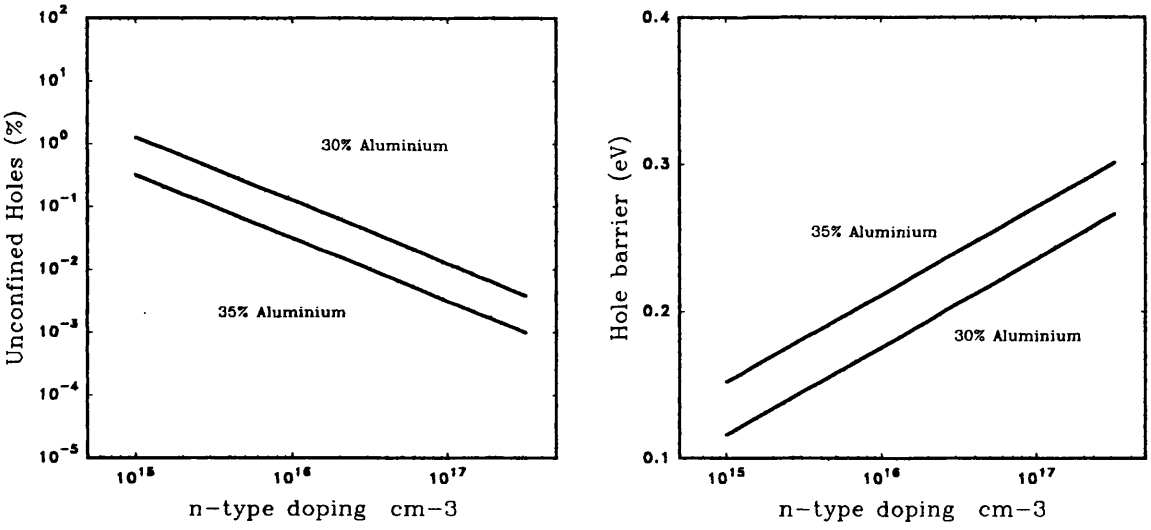

Figure 4.3. Percentage of injected holes confined by the valence band hole barrier with doping for 30% and 35% aluminium in the GaAlAs layer.

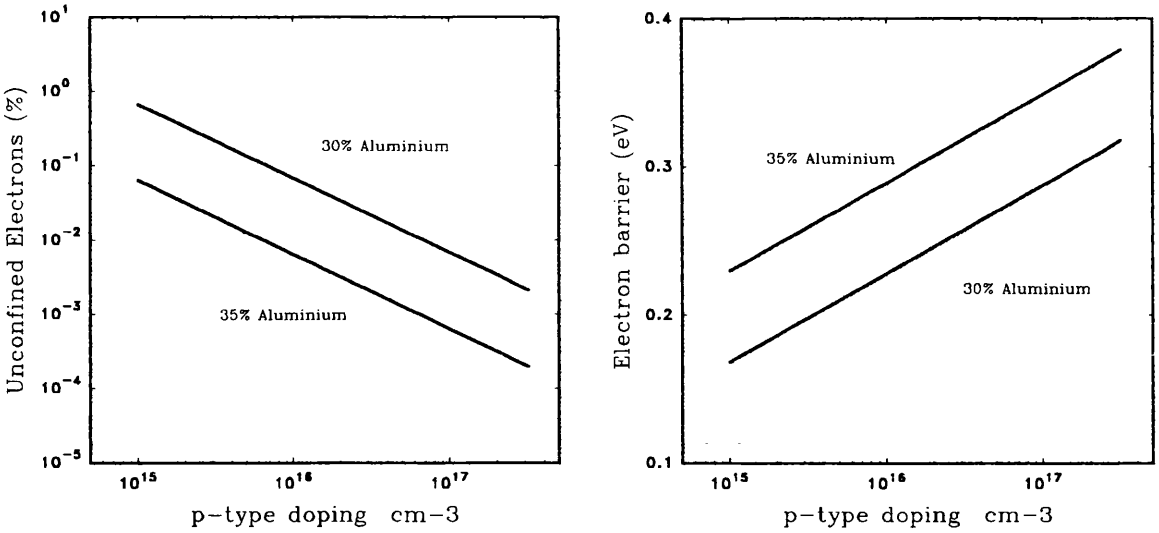

Figure 4.4. Percentage of injected electrons confined by the conduction band electron barrier with doping for 30% and 35% aluminium in the GaAlAs layer.

As an example of the effect of further injection, the percentage of unconfined carriers is plotted for increasing active layer carrier concentration. Figure 4.5, below, shows the effect with 30% aluminium cladding layers doped to 10^{16} cm^{-3}. At 1.3×10^{19} cm^{-3} the hole barrier becomes zero.

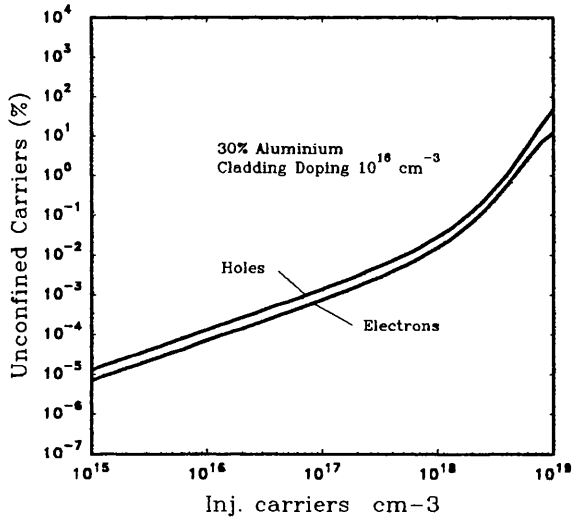

Figure 4.5. Effect of further injection on carrier confinement.

4.2 Layer Structure

In the design of the directional couplers of Chapter 3, the material was already supplied and therefore could not be altered. In this chapter we have the freedom to change the layer structure to improve the performance of the material as a guiding medium. A number of factors have to be considered in the design of the material structure,

both for vertical and lateral guiding. The most important of these are loss reduction, effect of injection, and lateral coupling. It is difficult to consider each layer individually in the material design as they all have an effect on the requirements of each other.

The basic structure of the material shall remain the same as previous samples as they perform well and there is no need at present to go to MQW or other more complicated material structures. The material structure is shown in Figure 4.6. The substrate is made from GaAs as this is the standard crystal from which all GaAs based samples are grown. The GaAlAs can then be grown on top with a specified aluminium content to form the lower cladding layer. The active layer is next, with the upper cladding GaAlAs layer above. A GaAs layer then has to be present for the top metal contact, as contact to GaAlAs is difficult due to oxidation of the aluminium during the metal deposition.

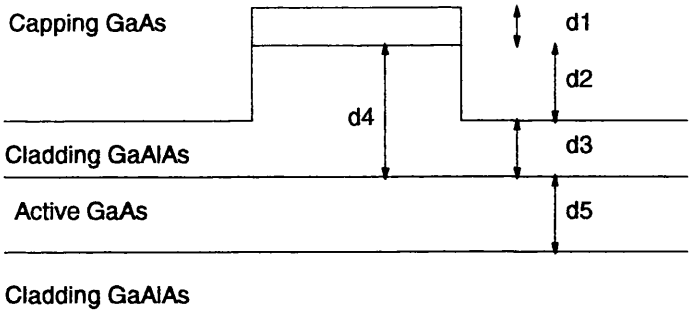

Figure 4.6. Material structure and rib dimensions.

As mentioned in Section 4.1, the aluminium content of the cladding layers forms the barrier to the carriers in the active layer, and also the index step for the vertical guiding. Increasing the aluminium content increases the confinement of the carriers and guided mode which is beneficial to both, but the increase is subject to the limit that above 40% aluminium the background doping is high and difficult to compensate[4]. Below 40% aluminium, the background doping is usually p-type 5×10^{15} cm^{-3}. Because of this the aluminium content is chosen to be 38% to allow for errors in composition, but have maximum benefit from the index and energy band changes.

Section 4.1 dealt with the doping of the material, and concluded that with over 30% aluminium, there was no disadvantage to carrier confinement with reduction of doping. Resistance has to be considered still, but to a lesser degree. Metal contacts, however, require a high doping for a good ohmic contact, and they have to be on both top and bottom layers in GaAs. The amount of guided light in these layers has to be minimised to reduce the losses. The lower GaAlAs layer can be made very thick to push the highly doped substrate away from the guided mode shape, and this also reduces substrate leakage losses. However, increasing the thickness of the lower GaAlAs layer does degrade the quality of the layers above it. The top capping layer is not so easy to move as the upper cladding layer affects the guiding properties quite strongly. The doping in the capping layer can be reduced slightly, and the layer thickness reduced, in order to minimise the power in

the layer. The capping layer, however, has to be thick enough not to be etched away by mechanical cleaning processes. A capping layer thickness of 500Å is therefore decided upon, with a doping of 8×10^{17} cm^{-3} as this is the lowest doping previously used for contact layers.

Active layer thickness is important as it is the nominally undoped region, and also the region that undergoes index change with carrier injection. Both the propagation loss and the free carrier effect will benefit from there being a larger amount of the mode in the active layer, so a strong vertical guide is required. The thickness of the active layer is also important in the amount of light that can be coupled into it from a fibre or lens. This is not a prime consideration as the CGCPS is meant to be used as an array, possibly with the source laser grown in the same substrate. A laser would have a narrower active layer, so would couple easily into a wider guiding layer of the switch. The experimental versions will, however, be lens and fibre coupled and this is easier with a thicker active layer. Thickness cannot be excessive as the vertical guiding must not be too strong as to become double moded vertically causing problems in the device operation. Injection of carriers will also be reduced if the thickness, d, is too large as the number of carriers, N, (ignoring diffusion) is given by $N^2 \propto J/qd$, where J is the injected current density, and q the electron charge. A thickness of 0.5μm is chosen as this gives proven coupling from lenses and fibres, but is single moded at 1.55 and 1.3μm. The structure is double moded at 1.3μm when the active layer is thicker than 0.6μm. This is partly dependent on cladding layer thickness, which will be discussed next, but this can be reviewed for any value of upper cladding thickness required.

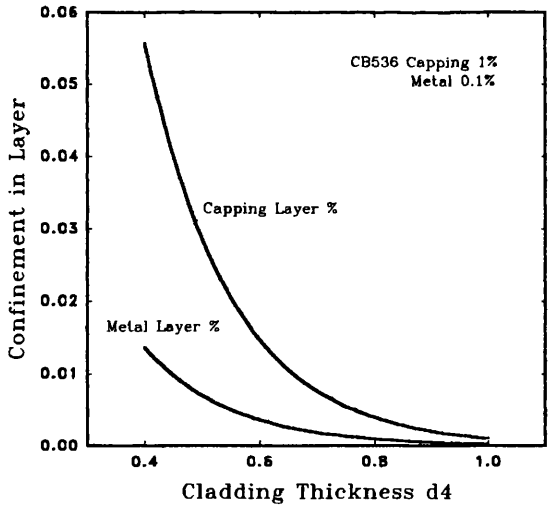

Figure 4.7. Vertical confinement factors with cladding thickness. λ=1.55μm.

The upper cladding layer thickness is very important as it affects many properties of the final device. Its use in reducing the amount of power in the capping layer has already been mentioned, but there are also the lateral guiding considerations to be taken, and the

current spreading when injected with current. With the material parameters so far fixed at capping layer 0.05μm and active layer 0.5μm, with 38% aluminium in cladding layers, the effect of the cladding layer thickness on power in the metal contact and capping layers is shown in Figure 4.7. There is a considerable reduction in modal power in the regions shown in comparison with the old material which will help with loss improvement.

The lateral guiding has to be considered, and Figure 4.8 shows the coupling lengths for twin 3μm guides 3μm apart. It is interesting to note that the cladding thickness does not seem to affect the minimum coupling length, but it is the remaining etched sides that have the main influence on the coupling. It can also be seen that a coupler can be fabricated so that the coupling lengths are equal for 1.3 and 1.55μm although the tolerances would have to be very tight. It is not the aim of this device to be insensitive to wavelength over this range, but an interesting point to note.

The minimum coupling length is set by the etch depth, and is essentially constant for a wide range of cladding thicknesses. This specifies the thickness of the cladding layer outside the rib region and also the thickness in which current spreading occurs. The total 'as supplied' cladding thickness can therefore be designed without affecting this carrier distribution effect. What is perhaps not clear from the graph is that the thicker the cladding layer, the shallower the curve in Figure 4.8, and so it is more tolerant to etch depth errors.

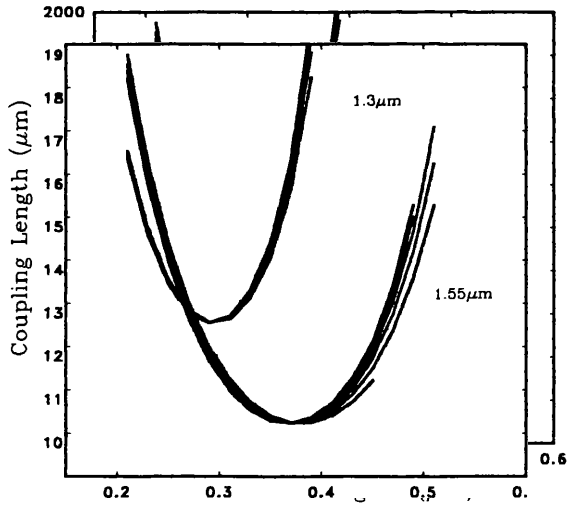

Figure 4.8. Graph of coupling length for the etched cladding distance, d3
0.55<d4<0.85μm steps of 0.06μm lambda=1.55μm, and 1.3μm
Lines only plotted where structure is double moded
Coupler metallised with SiO_2 barrier.

Having found a criterion for a minimum coupling length, d3=0.37μm, the cladding thickness can be decided upon by considering the strength of guide required. Figure 4.9 shows the lateral confinement factor of the single 3μm guide with increased cladding thickness under the rib, and etched to 0.37μm outside. The more tightly bound the lateral mode is, the better the device will be in separation of signal from the two coupler outputs.

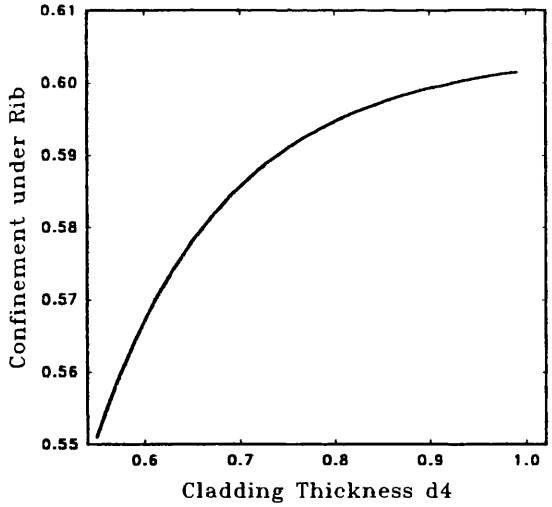

Figure 4.9. Lateral confinement factor under rib for increased cladding thickness @ 1.55μm d3=0.37μm.

Increasing the cladding layer thickness so far appears to be beneficial to all aspects, but two considerations are left that imply the opposite. The resistance of the low doped layer will affect the operation if the rib is too high, and the amount of optical power in contact with the rib side wall will also increase with rib height. The effect of this is shown in Figure 4.10, in comparison with the old material. This analysis is not ideal as it uses the EDC method over the rib wall region where it is most inaccurate, but for weak guides will be adequate for a first order approximation, and serves to give a trend. The results do however show that the rib wall loss is dependent strongly on etch depth, which is to be expected. It would be beneficial to keep the etch depth to a minimum, but operating at the optimum coupling length this requires a small cladding thickness that would increase the losses from the metal contact.

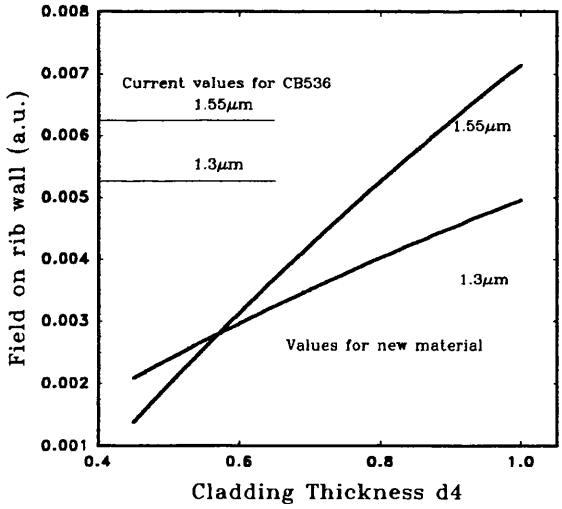

Figure 4.10. Graph of integral of normalised field over rib wall.
Given as integral (f(y))dy g(x)). $\iint E^2 dx,dy = 1$ D3=0.37 @λ=1.55μm D3=0.3@ λ=1.3μm.

It is clear that a compromise between metal losses and rib wall losses has to be made to decide on cladding thickness. The properties of the metal cannot be changed, nor can the metal be removed as it is necessary for device operation. Better device fabrication, however, can improve on the rib wall scattering, thus reducing the loss from this source. It is therefore decided that a cladding thickness of 0.7μm will be used.

To check that the device will operate with carrier injection a comparison of the change in material effective index with carriers and etch depth is made in Figure 4.11. It is clear from the graphs that the increased confinement of the mode in the active layer has made the carrier effect larger than in the other materials.

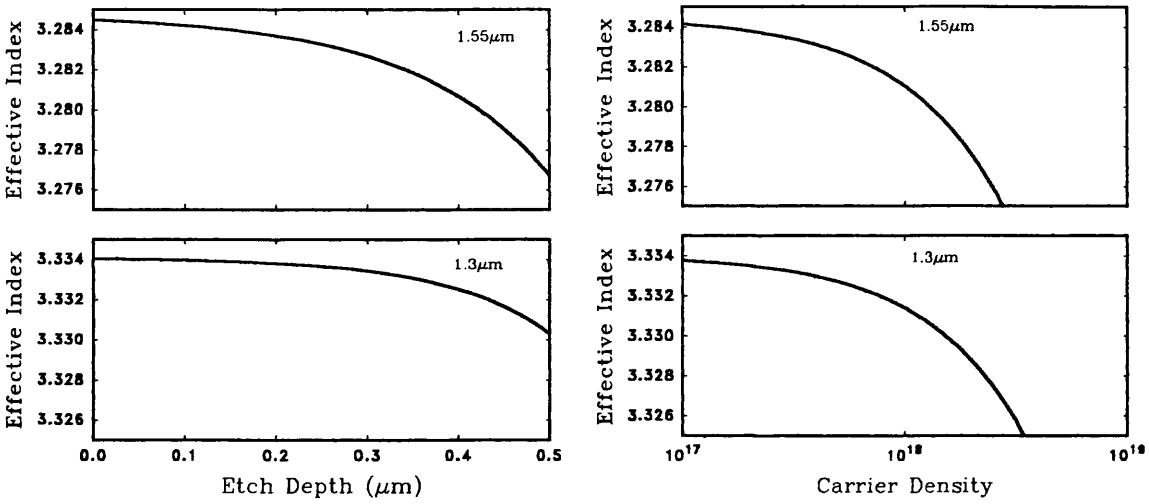

Figure 4.11. Graphs to show effect of etch depth and carrier injection on effective index. Minimum coupling length at etch depth of 0.38μm @λ=1.55μm 0.45μm @λ=1.3μm.

The parameters for the designed material are given in Table 4.1. These values give a device resistance of approximately 2 ohms, ignoring the active layer, and assuming a device contact $10\times1000\mu m^2$ and no current spreading. The active layer would introduce another 10 ohms if doped 10^{15} cm^{-3} p-type making it the most influential layer in the structure for resistance followed by the p-type cladding. These figures, however, are adequate for the injection of carriers as less than 100mA are required for operation in the last material and this new sample is hoped to improve on that.

Material	Doping cm^{-3}	Thickness
GaAs	p+ 8×10^{17}	0.05μm
GaAlAs (38% Al)	p $<10^{16}$	0.7μm
GaAs	u	0.5μm
GaAlAs (38% Al)	n $<10^{16}$	2.0μm
GaAs Substrate	n 8×10^{17}	100-150μm

Table 4.1. Final Design of Material Parameters.

For completeness, the vertically guided mode shape in the new material is shown in Figure 4.12 in comparison with that of CB536, to show the differences in modal power in the active layer, and the lossy regions of metal and capping layers.

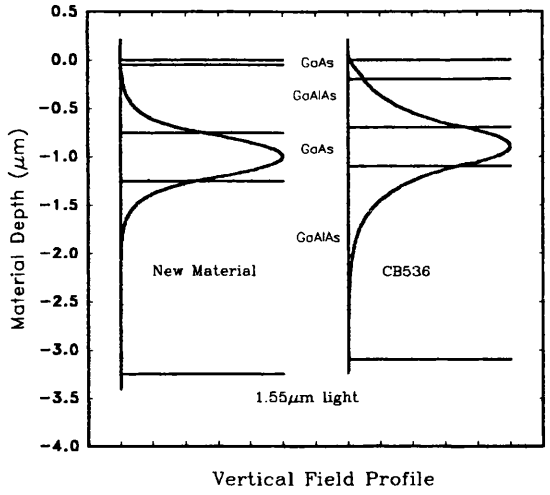

Figure 4.12. Vertical field profile for old and new materials.

4.3 Results

4.3.1 Material

The material was grown by MOVPE by the EPSRC Central Facility at Sheffield University, and because of the difficulties of compensating the background doping in such small amounts, the exact specification of doping profile could not be met. The resulting doping profile and layer structure is shown in Table 4.2. The lower cladding layer varies from p-type at the top of the wafer to n-type at the bottom, as shown in Figure 4.13. The top of the wafer then becomes a 'pip' structure that will not operate, but the lower part is useable.

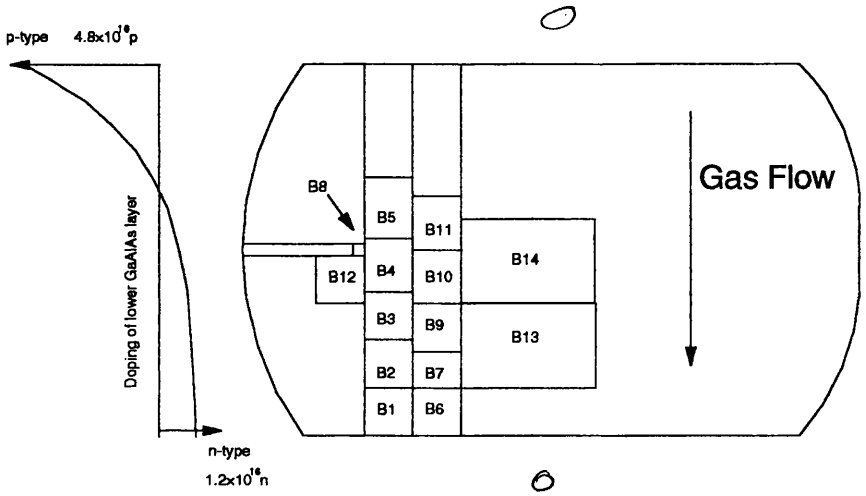

Figure 4.13. Wafer sample with doping profile of lower cladding layer and device positions.

Material QT788	design doping cm^{-3}	design thickness	Actual doping cm^{-3} (from III-V facility)	Actual thickness
GaAs	p+ 8×10^{17}	0.05μm	p+ 1×10^{18}	0.05μm
GaAlAs (38% Al)	p $<10^{16}$	0.7μm	p 4×10^{16}	0.7μm
GaAs	u	0.5μm	p 3×10^{15}	0.5μm
GaAlAs (38% Al)	n $<10^{16}$	2.0μm	p 4×10^{16} - n 2×10^{16}	2.0μm
GaAs buffer	n 8×10^{17}	-	n 2×10^{17}	0.05μm
GaAs Substrate	n 8×10^{17}	500μm	n $1.5\text{-}2\times10^{18}$	500μm

Table 4.2. Layers structure and Doping of QT788.

4.3.2 Guiding

Waveguides were fabricated from the material and tested giving good results and mode shapes that were as predicted by the theory. Vertical guiding is difficult to assess when the guiding is so strong. This is because the lens resolution dominates the shape of the measured result, and any variation in guiding from the theoretical calculation is obscured by the distortion from the lens, (Appendix 5). Horizontal (lateral) guiding, however, matches to the theory well and indicates that the material is less sensitive to the IBE damage than the previous materials. The damage will still be there, but as the vertical mode is better confined, much less of the mode will be in the damaged region. Figure 4.14 shows the theoretical profile and the measured results for IBE devices.

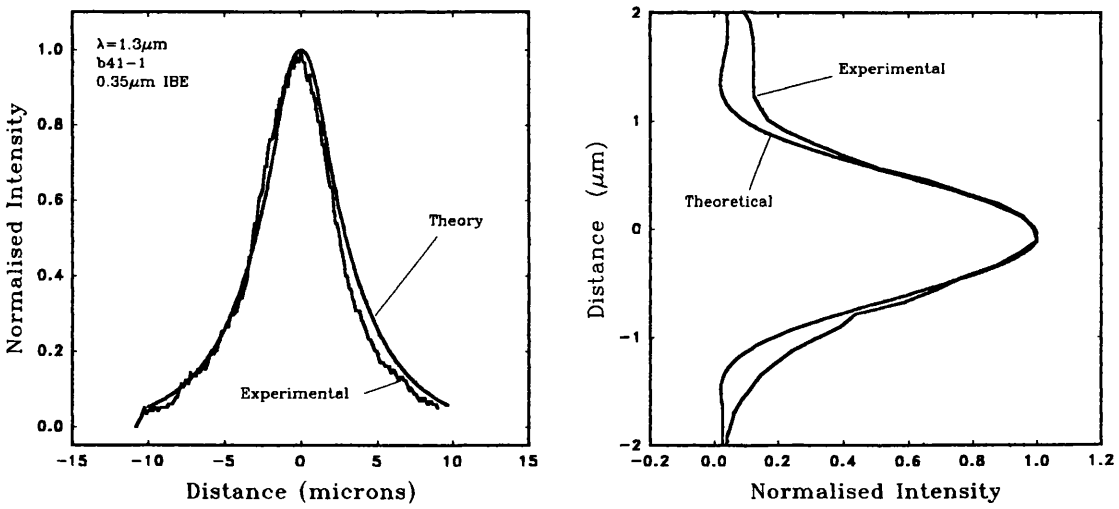

Figure 4.14. Horizontal and vertical guiding for 3μm rib in QT788.

4.3.3 Losses

Losses in the guides were measured for three types of guide. IBE, wet etch, and metal contacted with wet etch, and the results are very much lower than in previous materials. Figure 4.15 shows the results from the loss measurements are distributed, but range between 1 and 3 cm^{-1} (4.3 to 13 dB/cm) for the IBE guides, with similar results for the wet etched devices. The gold topped guides are as expected with the attenuation being

above 3 cm^{-1} (13dB/cm). The short device lengths may still introduce some error, as mentioned in Chapter 2.

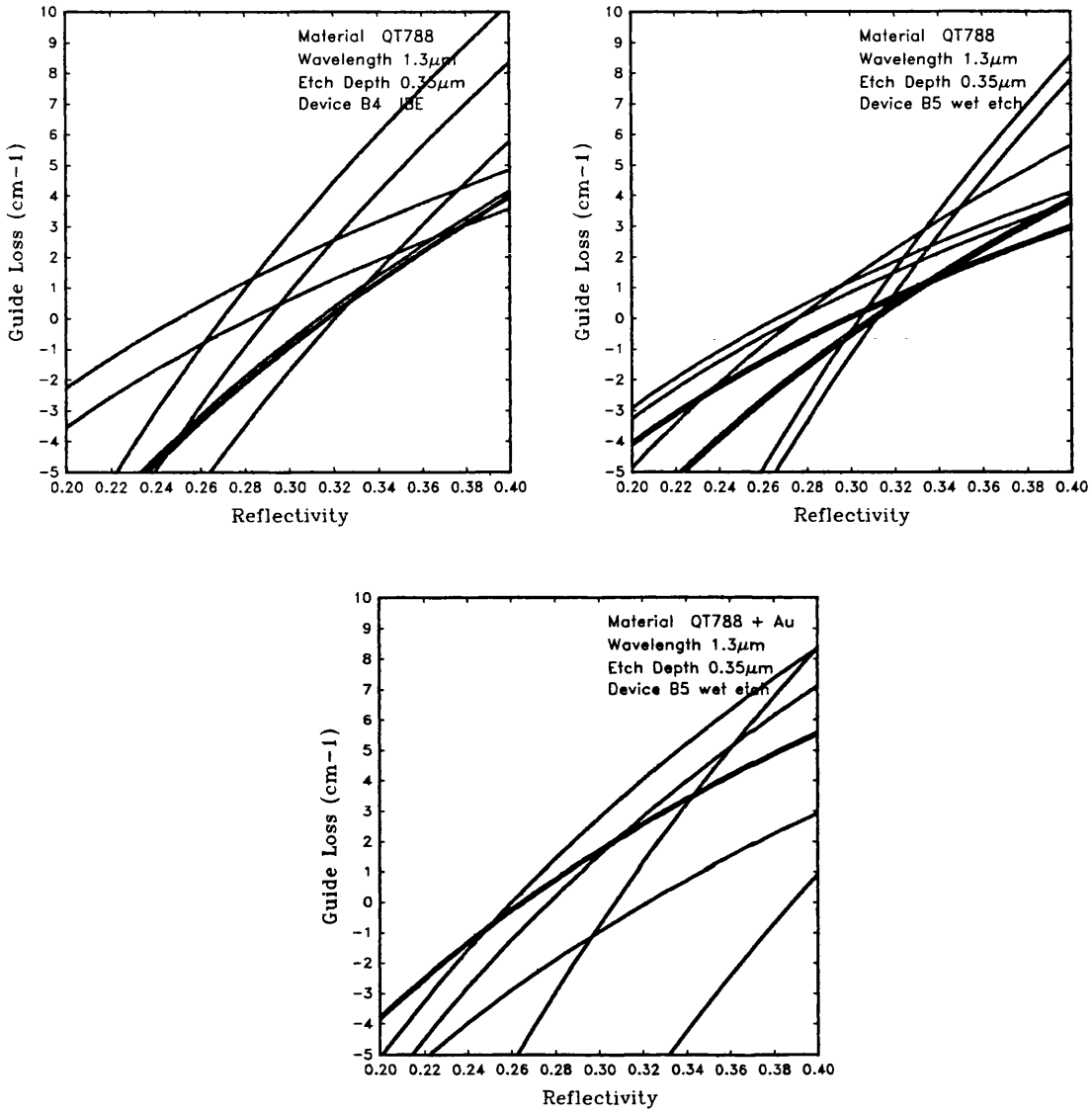

Figure 4.15. Graphs of guide loss *vs.* reflectivity for 300μm, 600μm and 1000μm long guides in QT788, showing losses measured by the Fabry-Perot method of Chapter 2.

Material	**loss in QT788**		**parameters**
Loss Mechanism	cm^{-1}	dB/cm	λ=1.3μm
Metal Contact	0.05	0.23	gold contact
Free Carrier	0.09	0.4	
Epilayer Roughness	0.12	0.5	5nm roughness
Wall Roughness	2.8	12.2	50nm roughness
Substrate Leakage	0.0006	0.0027	

Table 4.3. Theoretical losses for QT788, to compare with measured losses below 13dB/cm.

The theoretical values for optical loss in this material are given in Table 4.3, and are calculated with the same formulae as in Chapter 2. The total of the values shown is greater than the measured guide loss, which can be considered as a success in terms of loss reduction. The metallised guide does, however, cause concern in that the addition of a contact should only slightly increase the loss by 0.23dB/cm, but the measured difference is of the order of 9dB/cm. It is thought that the extra loss is caused by the rough edges of the gold on top of the rib. In fabrication of these guides the gold/Titanium layer is removed by IBE, leaving an edge roughened by etching and photoresist errors. The wet etching of the GaAs layers will smooth the rib wall, but not the metal layer, as metal is not greatly affected by the etchant. There is very little of the mode in the region of the metal, but the large difference in dielectric constant between air and metal makes it a very large scattering centre.

4.3.4 Electrical Performance

Shallow ribs were fabricated with Ti/Au contacts to test the injection of carriers into the material. As the doping varies across the wafer, a line of ribs was made in areas B1, B2, B3 shown in Figure 4.13, to assess where the lower cladding layer doping would change and the 'pip' structure would begin. No noticeable change in injection could be seen, but the amount of current and the position of the spontaneous emission were not as expected.

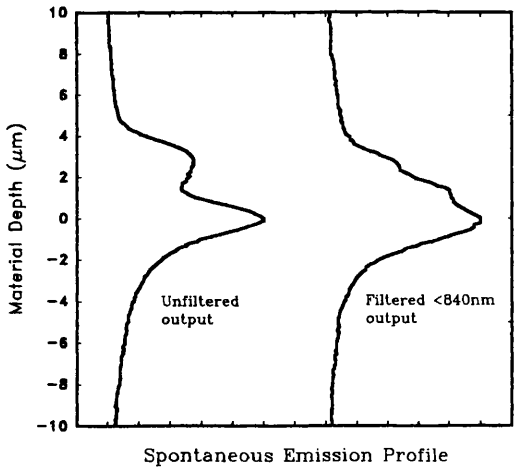

Figure 4.16. Normalised Spontaneous emission output from QT788.

The vertical spontaneous emission profile is shown in Figure 4.16, and shows two lobes of light. As before, any detail is obscured by the lens resolution, but the two areas of light are separated by a considerable distance of over 2.0μm. It is thought that the higher lobe of light is from the active layer and the lower, brighter, lobe from the substrate region. There may be two reasons for the generation of the lower area of light. The spontaneous emission, being generated in random directions, could be travelling through the GaAlAs

layer, and although there is no guiding in this layer, the band-band attenuation will be much less than in the GaAs layers and so the output will be large. The other possibility is that there is an extra layer of material that is generating spontaneous emission. This would be unfortunate as it would demonstrate that the carriers are not being confined to the active layer. The filtered output in Figure 4.16 is shown as usually the filtering of the light prevents the guided modes of light, at the spontaneous emission wavelength, being measured as they are severely attenuated. In this case, the attenuation does not happen as stray light is passing through the GaAlAs layer, while the light from the active layer is severely attenuated. This does not totally prove that the second lobe is due to light shining through the GaAlAs layer, but if the lower lobe were being generated at the facet by GaAs bandgap material, it would have been attenuated by the filter by the same amount as that in the active layer.

Layer	capping	cladding	active	cladding	buffer	substrate
Thickness (μm)	0.05	0.7	0.5	2.0	0.05	-
Doping (cm^{-3})	1e18 p	2e16 p	3e15 p	1e16 n	2e17 n	1e18 n
Resistance (Ωcm)[a]	0.03	1	7	0.15	0.009	0.002
Aluminium (%)	0	38	0	38	0	0
Bandgap (eV)	1.424	1.897	1.424	1.897	1.424	1.424
Vacuum Level* (eV)	5.44	5.40	5.288	3.841	4.0862	4.028
Conduction Level* (eV)	1.37	1.7334	1.219	0.138	0.0162	-0.0415
Valence Level* (eV)	-0.0537	-0.1645	-0.205	-1.724	-1.407	-1.4655

*Fermi level taken as zero for above figures

[a] Values from GaAs resistance tabulated in 'Physics of Semiconductor Devices' Sze

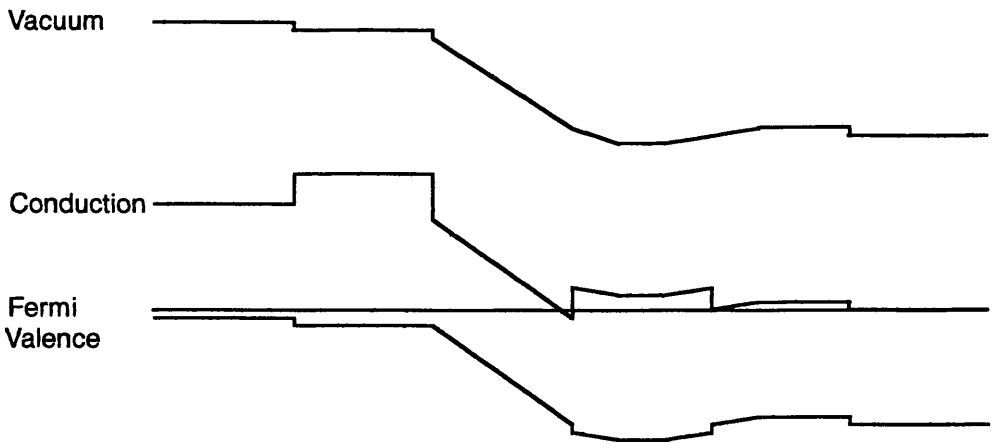

Figure 4.17. Material parameters with band diagram at zero bias.

The buffer layer that is initially grown on the substrate to smooth the growth of further layers is doped differently, and so has been analysed to check if it may generate light output. Figure 4.17 shows the material data and band profile of the full material structure. Note how the active layer bands are not flat as the depletion region between the p-type active layer and n-type GaAlAs layer extends across the whole GaAs region. From the band diagram it can be seen that there is a small discontinuity at the buffer-substrate interface, but for recombination to occur here, holes would have to travel across the whole device without recombining elsewhere. This is unlikely to happen in greater numbers that those that recombine in the active layer, so this is thought an unlikely source of light generation.

To check on spurious layers in the material that are unspecified, an electron microscope was used to view the layers. Used in backscatter mode, the microscope is sensitive to atomic number, thus making the layers clear. Figure 4.18 shows the result of this on a coupled guide structure, giving no evidence of an extra layer of differing composition.

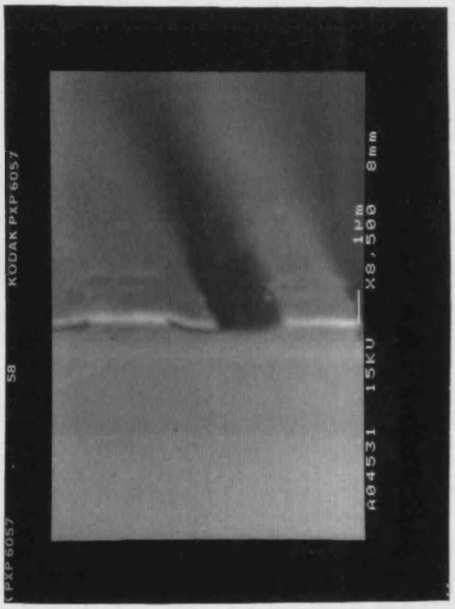

Figure 4.18. SEM of coupled guides showing layer structure to be as specified.

The current-voltage characteristic of QT778 is given in Figure 4.19 and compared with that of CB536. The amount of current that can be injected is very small in comparison and cause for concern. Bad contacts were initially suspected, but the detrimental performance is consistent over devices that have been contacted in different batches.

If the bad contacts were due to fabrication errors, the devices would not be consistent in their I-V characteristic. If the contacts were affected by the formation of a Schottky barrier at the contact, rather than ohmic contact, the I-V characteristic would show an increase in the turn on voltage compared to material CB536. From Figure 4.19 it can be

seen on the expanded scale I-V characteristic that the turn on voltage is slightly lower than that of CB536.

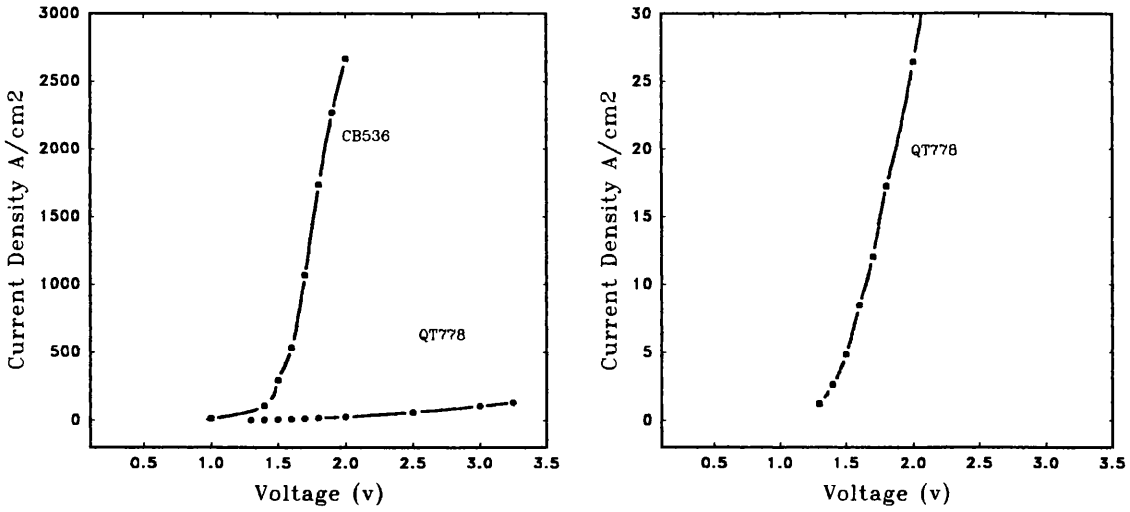

Figure 4.19. IV characteristic of CB536 and QT788, with QT788 also shown with magnified scale.

The indication is that there is a higher resistance somewhere in the device that is causing the current reduction. The doping of the top two layers has been verified by measuring their resistance using two metal probes 500μm apart and measuring the IV characteristic of the material. Lower layers will have an effect on the result, but in each case the lower layer is less doped, and so more resistive, giving a smaller margin of error.

The resistivity tests made for the top p+ GaAs and p GaAlAs cladding layers measured 0.02Ω cm and 1.82Ω cm, giving doping concentrations of $10^{18}cm^{-3}$ and $2\times10^{16}cm^{-3}$ respectively. This is in close agreement with the values measured at Sheffield.

Figure 4.20 shows the effect of time whilst driving the device hard. A 10 volt pulse was applied to a 1500μm × 3μm stripe with the duty cycles shown. The maximum current that flows increases with time to a set value. Further pumping of the device, by increasing the duty cycle increases the maximum current. This process is not reversible, in that after this treatment the devices will conduct the maximum current at any duty cycle. The effect is thought to be caused by heating which can cause diffusion of the dopants and filamentation of the current through the ohmic contact. However, as the back contacts are annealed at 430°C for 2 minutes, heating from the current pulses is unlikely to cause further diffusion of dopants or annealing of contacts, thus the effect has to come from either the top contact, or locally within the device.

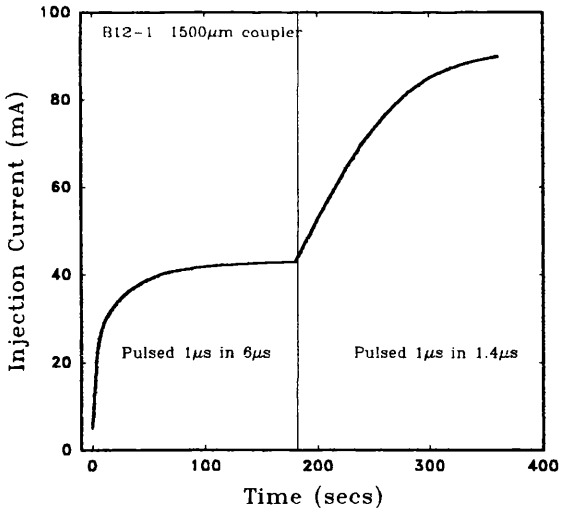

Figure 4.20. Injection current with time from a 10V pulse.

4.3.5 Couplers

Coupled guide structures were made to test the coupling length calculations in the material. The couplers were fabricated with contacts on top, so they could be used as variable devices also. Good coupling was achieved, and the devices also exhibited switching capabilities despite the electrical problems described above. The results of couplers are shown in Figure 4.21. As in Chapter 3, the light input is to the main rib, and couples across to the tap rib in the passive state. When injected the output switches to the main rib. The 1000μm coupler exhibits the most complete coupling as it is close to the expected coupling length of 1130μm.

The speed of the coupling variation was noticed to be comparatively slow and measured as 400-600ns. This is 100 times slower than the couplers in CB536 and it is therefore concluded that the mechanism by which the couplers are being varied is thermal.

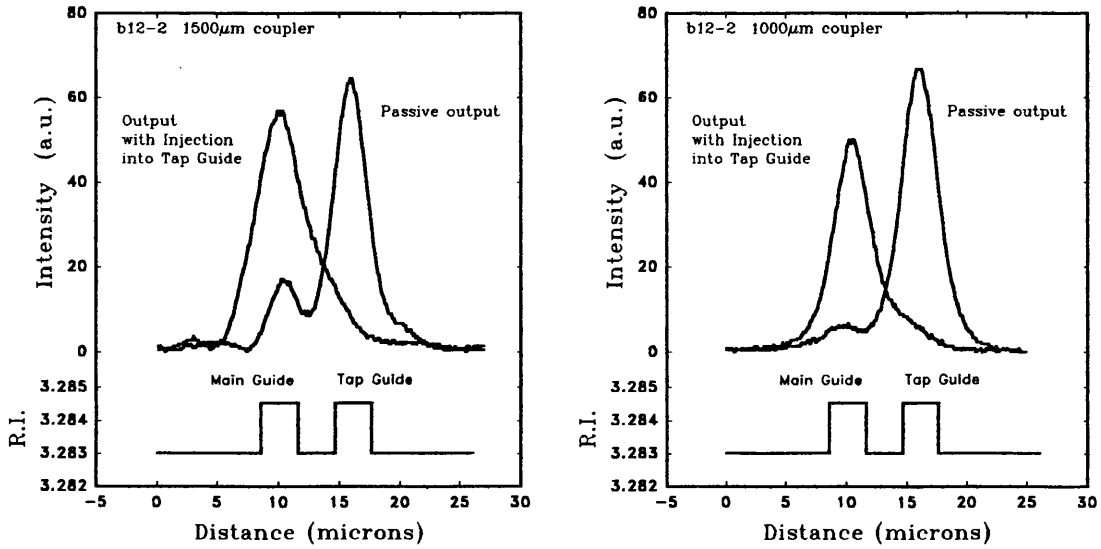

Figure 4.21. Near field patterns for injected couplers in QT788.

The program used to model the carrier effects on index can be modified to alter the refractive index due to temperature effects. The refractive index increases with temperature, as mentioned in Chapter 2, and the active layer, being the most resistive, is assumed to be the major source of heat. In this simple model, diffusion of heat will be ignored as it is only intended to demonstrate the operation of the coupler, rather than model it exactly.

Using a temperature rise of up to 20°C in the active layer, an increase of index of 0.003 is seen. A 20°C rise is easily explained from the power going into the device, but as the material is not behaving as expected, it is difficult to specify where the power is being dissipated. The spontaneous output power can be considered negligible as it could not be measured with a power meter. Assuming a 10V input resulting in 100mA current flow gives 1watt of input power.

The specific heat capacity [a]	c=0.336+0.126x j/g/K
Density[a]	D=5.36-1.63x g/cm^3
Thermal expansion coeff.[a]	6.4-1.2x $\times 10^{-6}$ °C^{-1}
Thermal Index coeff.[b]	4.5×10^{-5} °C^{-1}

a) ref[5] b) ref[6]

Table 4.4. Material parameters for $Ga_{(1-x)}Al_{(x)}As$.

An expression can be arrived at for rise in temperature per second per volume (V) of material with input power (P).

$$\Delta T = \frac{P}{cDV} \qquad °C/cm^3/s \qquad [4.13]$$

Using the above data of Table 4.4 and assuming GaAs throughout as a first approximation, with a volume of 1000μm × 1μm × 10μm to allow for current and thermal spreading, a figure of 55°C/μs is arrived at, which is not out of order for the 20°C used in the model.

Applying this calculated index increase to the tap rib waveguide gives the results shown in Figure 4.22. Again the light input is to the main rib, and comes out of the tap rib (RH rib) with no injection. Increasing the temperature of the active layer in the RH rib causes the output to change to the main LH rib. The mechanism here is very different from the desired operation of making the coupler single moded. Instead, the modes are affected in such a way as to make the coupling length change shown in Figure 4.22.

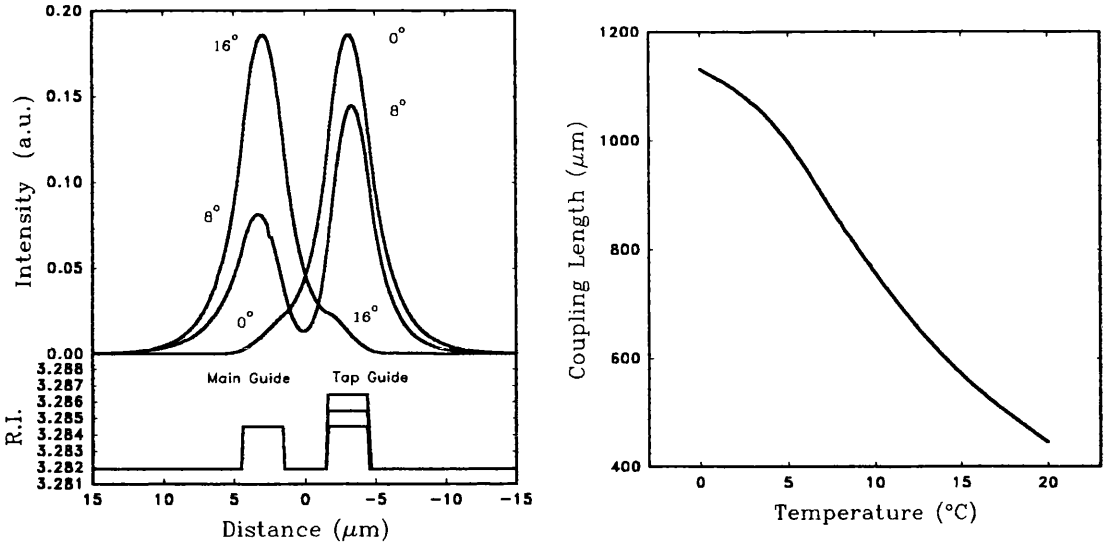

Figure 4.22. Theoretical near field output for temperature increase in RH rib, with effect on coupling length.

4.4 Material QT825

A second wafer of the material was grown to see if it had a better performance. Doping in the top cladding layer was slightly higher, together with the aluminium content. This slight change in parameters meant that QT825 wafer did not suffer from the variation of doping across the wafer to the same extent as QT788, and is 'pin' doped all the way across. The material parameters and doping are shown in Table 4.5.

Layer	Al. (%)	Thickness (μm)	doping (cm^{-3})
capping	0	0.05	p+ 10^{18}
cladding	40	0.7	p 0.93-1.05×10^{17}
active	0	0.5	p 3×10^{15}
cladding	40	2.0	n 2.9-3.4×10^{17}
buffer	0	0.5	n+
substrate	0	500	n+

Table 4.5. Material parameters for QT825

Couplers made from the above material gave excellent results, as shown in Figure 4.23 below. It can be seen that the injection efficiency has greatly improved, being almost 30% of the initial coupler devices in material CB536 shown in Chapter 3.

Current injection appears to work well in this material, despite the still high resistance shown by the voltage current curves of Figure 4.24. The curves for QT788 and QT825 are shown multiplied by 10 to give a better comparison to CB536. The new

material conducts less than one tenth the current of CB536 for the same applied voltage, but works well regardless.

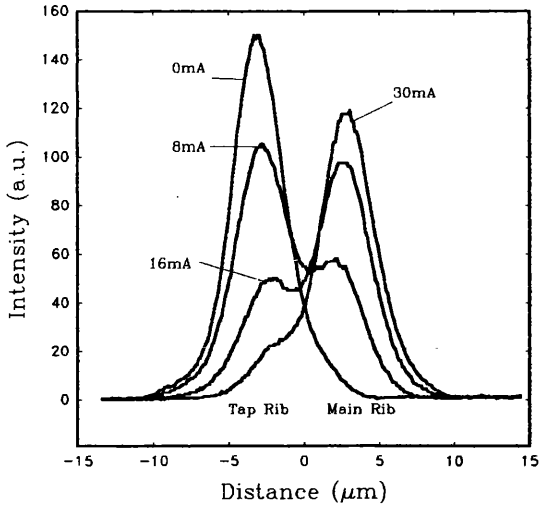

Figure 4.23. Near field patterns for 1000μm coupler in QT825.

Measurements of speed were made on the new couplers to confirm the mechanism of operation. The measurements were much easier, as with the low loss material there is more optical output power available. Following the method in Chapter 3, the speed of the switching was measured and the coupler was found to switch in 11ns and return to the passive state in 9ns. These seem to be at the larger end of the expected range of speed, but the injection current had a rise time of 7ns. Better impedance matching to the device could make the injection rise time faster, but then the speed of the device may be beyond the capabilities of the photodetector amplifier and the oscilloscope that have a 3.5ns minimum rise time.

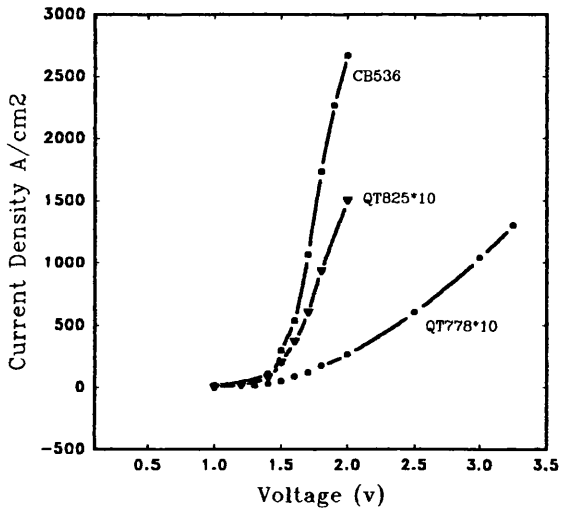

Figure 4.24. Comparisons of current density for the three materials.
NOTE QT788 and QT825 are ×10.

4.5 Conclusions

This chapter has shown the design of a new material, considering the material parameters required for low loss and short couplers. Experimental results have shown that the QT788 material is suitable for making low loss optical waveguides. Electrical performance, however, has not been as expected. Despite the anomalies in the material, guiding and coupling have been demonstrated, and switching in the couplers was achieved. The mechanism of the coupler variation is known to be due to thermal effects, and this has been modelled to prove that this is the case.

Material QT825 has shown excellent results. Couplers in this material have been demonstrated giving switching times less than 10ns with almost a factor of three improvement over the current needed to switch the couplers in the old material.

Further work continues on the material to discover why it does not perform well when injected. Independent studies and further wafers have been ordered to try and rectify the problem.

References

[1] H.C. Casey, M.B. Panish. "Heterostructure lasers, Pt A Fundamental Principles." Academic Press, p194 et seq.1978.

[2] K. Seeger "Semiconductor Physics." 3rd edn. Springer Verlag, p37. 1985.

[3] S.M. Sze. "Physics of Semiconductor Devices." 2nd edn. Wiley, p33. 1981.

[4] J.S.Roberts, "Quantax reactor Specifications." First annual users meeting, EPSRC III-V Facility. July 1994.

[5] S. Adachi. "GaAs, AlAs, and GaAlAs: Material parameters for use in research and device applications." Journal Applied Physics, Vol. 58, No. 3, pp R1-R29, August 1985.

[6] Willardson and Beer. "Semiconductors and Semimetals." Vol. 3, " Optical Properties of III-V components" Academic Press p517. 1967.

Chapter 5

Mirrors

This chapter will discuss the reasons for choosing mirrors at the crosspoint of the switch, and compare the alternatives that are currently available.

Theoretical analysis is carried out following the work of other authors to evaluate the performance of ideal facets so as to compare the effects of the fabrication process on mirror performance. The mathematical analysis is developed further in this thesis to consider the influence of a finite width mirror on the reflected power.

Results of measurements from fabricated mirrors are described and discussed to demonstrate important features of the CGCPS with the mirrors in place.

5.1 Currently available technology

To achieve the most compact design for an array of switches, the signal has to be routed into either of two guides at right angles to each other, (Figure 1.8). Orthogonal guide layouts not only improve the economic use of the substrate material, but also facilitate coupling of optical fibres, (which are typically 250μm in diameter,) to the device. Compared to the crosspoint switches mentioned in Chapter 1, which intersect at less than 1°,[1] the requirement here is for the switching element to alter the direction of propagation of the signal through 90°. There are a number of ways to do this, each having its own advantages and disadvantages. As will be shown in Chapter 7, an abrupt change of direction of a guide is very lossy, even for small angles. Methods for optimising such a bend exist,[2,3] but would only be used for angles much less than 90°.

Curved waveguides offer a better solution, but are very lossy even when the radius of curvature is increased to hundreds of wavelengths for guides that are single moded. Bends of 90° have been reported with losses of 0.7dB with a radius of 75μm at a wavelength of 632nm[4] and 0.2dB with 30μm radius at a wavelength of 1535nm[5]. These figures are, however, for deeply etched multi moded guides that are unsuitable for use in the CGCPS, as the deep etch would affect the other nearby guides, and the multimode nature would introduce unwanted effects at high data rates.

Integrated total internal reflection (TIR) mirrors offer a smaller, and less lossy solution. Measurements have been made by many authors,[6,7] by using a 90° etched mirror in a lasing cavity. Results from these techniques have yielded a best result of 0.5dB for a 90° bend[8].

Many theoretical studies have been carried out using Plane Wave Spectrum analysis at the reflecting interface,[9,10] and negligible loss can be shown for a perfect, infinitely wide mirror facet with angles above the critical angle of the medium concerned. However,

expected losses of 0.9-1.3dB are shown for typical alignment errors. Curved corner reflectors can further reduce the theoretical losses to below 0.1dB.[11]

Etched mirrors are, however, more difficult to fabricate than abrupt bends and curved guides, but it will be shown that the correctly fabricated mirror offers the solution with the least theoretical loss. Positioning of the etched facet can have a marked effect on the power lost in the "turning process". Previous studies[12] show that to achieve a loss of less than 1dB, the mirror facet error must be less than 0.6° in rotation, 2° off vertical and 0.9μm in translation. It can also be shown that, in some circumstances, it is beneficial not to have the mirror exactly at the corner point of the incoming and outgoing guides[13] to allow for the Goos-Haenchen shift. This is where the reflected beam of light from the mirror appears to be shifted from the expected position, but the shift is more prevalent when the angle of reflection is below the critical angle for total internal reflection and is therefore more important in silica guides, which have a lower refractive index, and hence a critical angle closer to the bend angle.

Not only does the fabrication process have to yield an accurately positioned facet, but also a good vertically etched surface to a depth in excess of 1-2μm. The facet roughness is also a consideration. Wet chemical etching cannot be used because it is isotropic, and therefore causes undercut, and makes a non-vertical facet. Reactive Ion Etching (RIE), and Chemically Assisted Ion Beam Etching (CAIBE) are the favoured processes, giving roughness of less than 0.1μm[14], and 15nm[15] respectively.

5.2 Theoretical study

5.2.1 Infinite Mirror

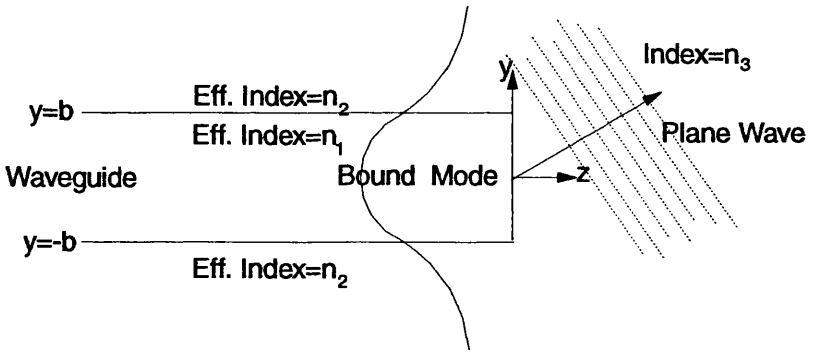

Figure 5.1. Plane Wave Deconstruction of Bound Mode.

Finding the reflectivity at the facet is achieved by a method of converting the field pattern at the end of the waveguide into a summation of plane waves, by means of Fourier transform. The mode shape is transformed from a function of y to a function of the y-direction propagation constant k_y, Equations [5.1], [5.2].

$$E_y(y) = \frac{1}{\sqrt{2\pi}} \int_{-\infty}^{\infty} A(k_y) e^{-j(k_y y + k_z z)} dk_y \qquad @\ z=0 \qquad [5.1]$$

and

$$A(k_y) = \frac{1}{\sqrt{2\pi}} \int_{-\infty}^{\infty} E(y) e^{+j(k_y y)} dy \qquad [5.2]$$

Where $A(k_y)$ is the amplitude of the plane wave, E(y) the mode shape function. The electric field of the bound mode is in this case assumed to be purely y-polarised, corresponding to the TE mode in the source laser. As the plane wave travels away from the end of the waveguide, it travels at an angle to the z axis, Figure 5.1, due to there being a z-direction propagation constant k_z governed by:-

$$k_y^2 + k_z^2 = (k_3)^2 \qquad [5.3]$$

where $k_3 = k_o n_3$ is the free space propagation constant in the region after the end of the waveguide, and n_3 the homogeneous refractive index in the region. The value of k_3 is subject to some discussion. For the calculations presented here it is taken as the propagation constant of the incident mode in the guides. Other approximations assume the region has the same effective index as the core of the guide, the cladding, or keep k_z constant at the modal propagation constant.

For completeness the transform integrals should be undertaken in x and y, (Figure 2.1) but comparison with previous work in single integral[16], and double integral studies[17] shows that the effects required for this initial study can be obtained with the integrals across y alone, thus the function $E_y(y)$ represents the lateral mode shape.

The above integral, [5.2], can be evaluated analytically for symmetric guides, giving a saving in computation time. For a mode described by:-

$$E_y(y) = \begin{cases} A\cos(k_{y1}|y|) & \text{for core} \quad |y| \le b \\ Be^{-(k_{y2}|y|)} & \text{for cladding} \quad |y| \ge b \end{cases} \qquad [5.5]$$

gives

$$A(k_y) = \frac{\sqrt{2}}{\pi} \cos(k_{y1} b) e^{-k_{y2} b} \frac{k_{y1}^2 + k_{y2}^2}{(k_{y2}^2 + k_y^2)(k_{y1}^2 - k_y^2)} \left[k_{y2} \cos(k_y b) - k_y \sin(k_y b) \right] \qquad [5.6]$$

The total field at any point after the end of the guide, z>0, can be reconstructed using the inverse transform [5.1]. The transform is not valid within the guide as the plane waves do not travel at the same phase velocity as the bound mode. Beyond the guide, however, the summation of the plane waves according to [5.1] gives the far field pattern.

In the case of the etched facet mirror, each plane wave is considered to travel toward the etched facet and reflect from it obeying the laws of the well known Fresnel reflection formula. An infinitely wide, perfectly flat mirror surface is assumed. As the device is usually to be excited from a semiconductor laser source in the same plane as the substrate, the electric field is y-polarised. The electric field vector is, therefore, parallel to the

plane of incidence to the facet, which is commonly regarded as TM polarisation for the reflection laws, but is not to be confused with the definition of the modal polarisation which in this case is TE. The reflection coefficient can be expressed in terms of the component of the propagation constant perpendicular to the facet.[18]

$$R^{TM} = \frac{k'_{zi} - \varepsilon_i / \varepsilon_t \, k'_{zt}}{k'_{zi} + \varepsilon_i / \varepsilon_t \, k'_{zt}} \qquad [5.7]$$

where k'_z is the propagation constant perpendicular to the facet, ε is the dielectric constant, and the i and t suffices are for the parameters in the incident and transmitted regions respectively, (Figure 5.2).

The values of k'_z can be found from k_y and k_z by using the transformation:

$$\begin{aligned} k'_{zi} &= k_z \cos(\phi) + k_y \sin(\phi) \\ k'_{yi} &= k_y \cos(\phi) - k_z \sin(\phi) \end{aligned} \qquad [5.8]$$

with ϕ being the angle of the plane of the mirror facet to the waveguide end, (z=0 plane). Using the boundary condition of equal phase velocity tangential to, and on either side of, the facet then $k'_{yi}=k'_{yt}$ so:

$$k'_{zt} = \sqrt{k_o^2 - k'^2_{yi}} \qquad [5.9]$$

with k_o being the propagation constant of a plane wave in the medium, the other side of the facet, which is either air or silica.

In all calculations the values of propagation constants can be real or imaginary. With the plane wave described by [5.10], the roots of equations [5.3] and [5.9] are taken as positive for k_z real such that the plane wave travels in the positive z direction with constant amplitude, and negative if k_z is imaginary, such that the wave has a decaying solution in the direction of propagation.

$$A = A_o e^{-j(k_y y + k_z z)} \qquad [5.10]$$

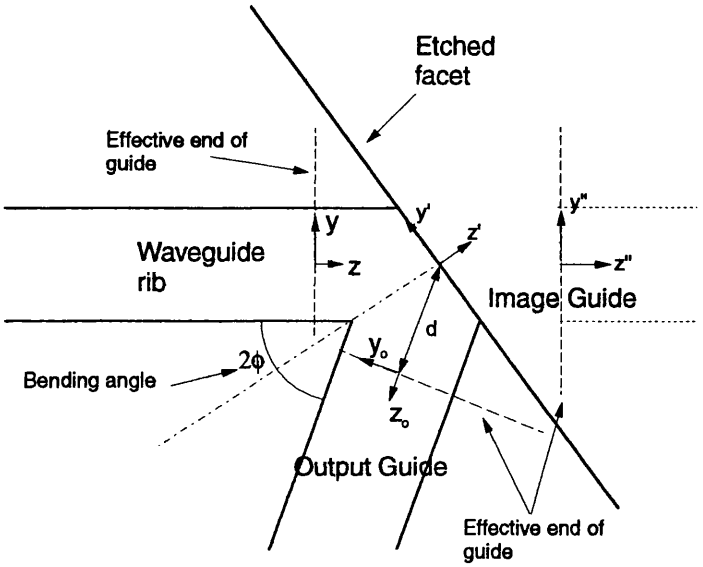

Figure 5.2. Diagram of symmetric facet case showing coordinate systems.

For angled facets, Figure 5.2, the edge of the mirror encroaches into the evanescent tail of the laterally guided mode, which affects the guiding and so should be taken into account. It is assumed, therefore, that the guide ends at the point where the facet cuts the guided mode shape where the mode field is exp(-1) of its maximum value. Appropriate values for the distance 'd' between the effective end of the guide and the facet can then be calculated for use in [5.11]. As the effect of the premature termination of the guide is assumed small, no loss is calculated due to this perturbation.

The reflected field is then reconstructed by taking the inverse fourier transform [5.11], with appropriate values for y and z due to the change in propagation direction of each plane wave from the reflection.

$$E_y(y_o) = \frac{1}{\sqrt{2\pi}} \int_{-\infty}^{\infty} A(k_y) R(k_y) e^{-j(k_y y + k_z z)} dk_y \qquad [5.11]$$

Where $R(k_y)$ is the complex reflection coefficient dependent on the angle of incidence of the plane wave. The infinite limits on the integral of [5.11] lead to k_z taking imaginary values for $k_y > k_3$.

Plane waves travelling at angles such that they propagate away from the mirror facet are not included in the summation, Figure 5.3. These should be added to the reconstructed mode shape without the effect of the mirror, but in practice, they are of such small magnitude that they are neglected.

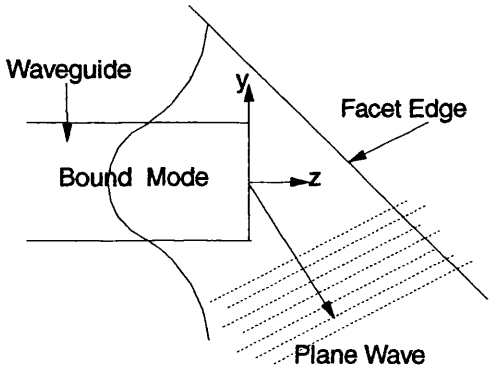

Figure 5.3. A plane wave that will not hit the front of the facet.

The reconstruction is done at the end of the output guide, (z_o=0 in Figure 5.2) and the loss caused by the waveguide bend is calculated from the overlap integral between the reconstructed reflected field from [5.11] and the guided mode shape within the output guide, $E_m(y_o)$. The loss calculation is shown in equation [5.12]. The input guides and output guides are assumed identical, thus $E_m(y_o)$ is as given in [5.5].

$$\text{Loss} = -20\log\left[\left|\frac{\int_{-\infty}^{\infty} E_y(y_o) E_m(y_o) dy_o}{\int_{-\infty}^{\infty} (E_m(y_o))^2 dy_o}\right|\right] \text{dB} \qquad [5.12]$$

5.2.1.1 Symmetric Case Evaluation

The symmetrical case is shown in Figure 5.2, where the output guide is at the same angle to the reflecting facet as the input guide. This configuration makes the analysis simpler, as the image of the output guide can be seen reflected in the mirror facet, exactly opposite the input guide. Using the reflection, it can be seen that

$$y_o=y'' \text{ and } z_o=z'' \qquad [5.13]$$

$$\text{and } y=y'' \qquad z=z''+2d \qquad [5.14]$$

(d is the distance between the effective end of guide, and the facet.)

which allows us to let the plane waves travel toward the image guide without a change in direction, but with a change in amplitude and phase from the reflection coefficients which occur in the plane of the facet.

5.2.1.2 Symmetric Case Results

Both GaAs-air, and GaAs-SiO_2 cases for the facet composition are computed, as it is likely for the etched facet to become coated in silica during fabrication.

As the structure is symmetric, it was expected that the reconstructed mode shape from the reflected plane waves would be central about the output guide, but this is not so due to Goos-Haenchen shift. Figure 5.4 illustrates the shift by showing the overlap of the reflected mode and the guided mode of the output guide for a bending half angle of 20°. Also shown in Figure 5.4 is the loss for bends of different angles. It can be seen here that the loss is very small for large angles and increases as the angle decreases due to the larger offset from Goos-Haenchen shift. For large angles, all of the plane waves impinge on the facet at angles above the critical angle, and so are fully reflected. Below the critical angle the light is not totally reflected and the loss increases dramatically. At the Brewster angle, the reflection coefficient is zero, so losses are very high. This is clearly seen in Figure 5.4b as peaks of high losses at the Brewster angles of 16° for air and 23° for silica. Critical angles for the two cases are 17.1° and 26.2° respectively. As the incident mode is split into a summation of plane waves it would be reasonable to expect the influence of the Brewster angle to only reduce a small part of the full plane wave spectrum. The angular spectrum of the guided mode is, however, very narrow, and the effect of the Brewster angle can clearly be seen in Figure 5.4b for the two cases under study, giving a peak in the loss curves.

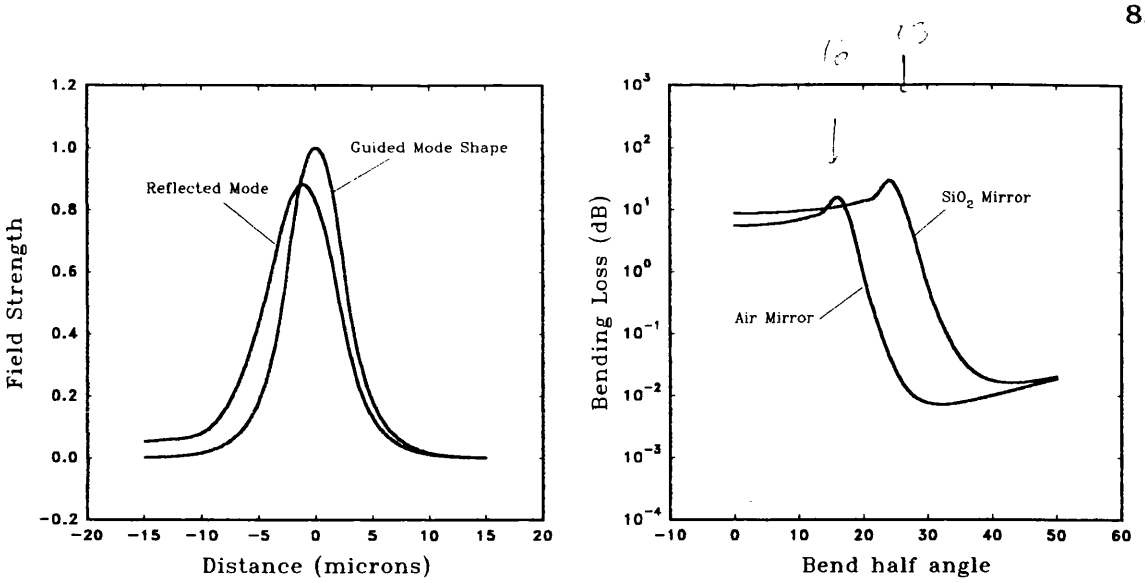

a) Effect of Goos-Haenchen Shift on reflected mode for 20° angle

b) Bending Loss for different angles

Figure 5.4.

The excess bending loss in Figure 5.4b appears to increase after 30° for the air, and 40° for the silica mirror. This is solely due to the assumption that the guide effectively ends when the mirror cuts across the guided mode at the 1/e point. As the angle increases, the effective end of the guide becomes further away from the facet, causing the increase in loss from spreading of the far field. If we assume that the etched mirror has no effect on the guide, other than reflection, then this increase is not seen.

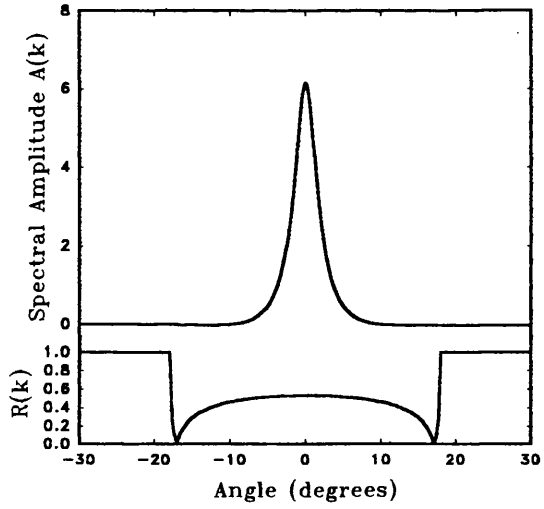

Figure 5.5. Angular spectrum of lateral mode, compared to reflection coefficient for facet angle of zero.

Figure 5.5 shows the amplitude of the plane waves together with the reflection coefficient, with which they are multiplied, for a facet angle of zero. The figure shows the narrow angular spread of the lateral mode shape plane wave spectrum. As the facet angle

is increased the relative positions of angular spectrum and reflection coefficient graphs will change, giving the reflectivity variation to the spectrum.

5.2.1.3 Orthogonal Guides Evaluation

The orthogonal layout of the guides is the more realistic configuration, as the guides would be fabricated in a different step to the mirror, and the mask would ensure that they are placed at right angles. In this case it is the alignment of the mirror that affects the device performance. The error in alignment of the mirror can be described in two ways, shown in Figure 5.6. The lateral displacement from its designed position can be represented by a shift in the mirror position normal to the facet. As the analysis considers an infinite mirror, this displacement can represent an error in the y and/or z directions. The other form of misalignment is angular.

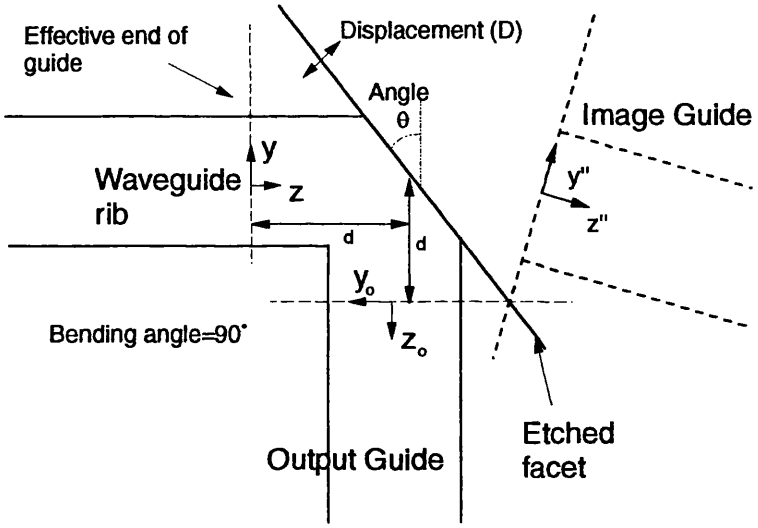

Figure 5.6. Diagram of facet showing displacement and angular movement.

Using the image guide as before, the plane waves can be allowed to propagate without any change in direction, but suffer phase and magnitude variation from their respective reflection coefficients.

The coordinate transform from the output guide to image guide is similar to before as it is purely reflected. In the case of angular alignment error the difference occurs on the image guide, as it is no longer parallel to the input. Assuming the mirror rotates about the point $z_0=z=z"=0$ then

$$z=d+d\sin(2\theta)+y"\cos(2\theta)+z"\sin(2\theta) \quad [5.15]$$

$$y=-d\cos(2\theta)+y"\sin(2\theta)-z"\cos(2\theta) \quad [5.16]$$

where d is the distance between the end of the guides and the facet at z=0

For displacement errors, assuming a facet angle of 45°, the image guide remains parallel to the input guide, but is offset by the displacement distance D×sin(θ) in the y direction. As the effective end of guide is related to the facet position, displacement of this type does not affect the distance 'd' in [5.15].

The coordinate transform then becomes:

$$y=y''+D\sin(\theta) \qquad z=z''+2d \qquad [5.17]$$

5.2.1.4 Orthogonal Guide Results

Figure 5.7 shows the effects of misalignment in both angle and displacement, assuming that the other is correctly aligned. The positional displacement is not as critical as the angular displacement, allowing over a micron of movement for a 1dB loss, compared to the half a degree of slew allowed in angular positioning. The angular alignment is not, however, that difficult to achieve as alignment marks on the substrate would be over 1000 µm apart. For 1000µm of device 0.5° of angular error would make one end of the device 8µm out of position, which would be clearly seen and corrected at the mask alignment stage. If the alignment marks are located with 1µm of error, a device this long leads to mask alignment 0.05° off line. Positioning to an accuracy of 1µm is just possible with the equipment available at Bath, implying that the major alignment loss comes from the lateral displacement, rather than angular. The sensitivities of the positioning errors are not unexpected. Since the mode has a very wide near field, there is less variation of the field overlap between the field going into the output guide and the guided mode itself with lateral translation of the facet. Conversely, the angular spectrum is very narrow, and so will be greatly affected by any angular alignment.

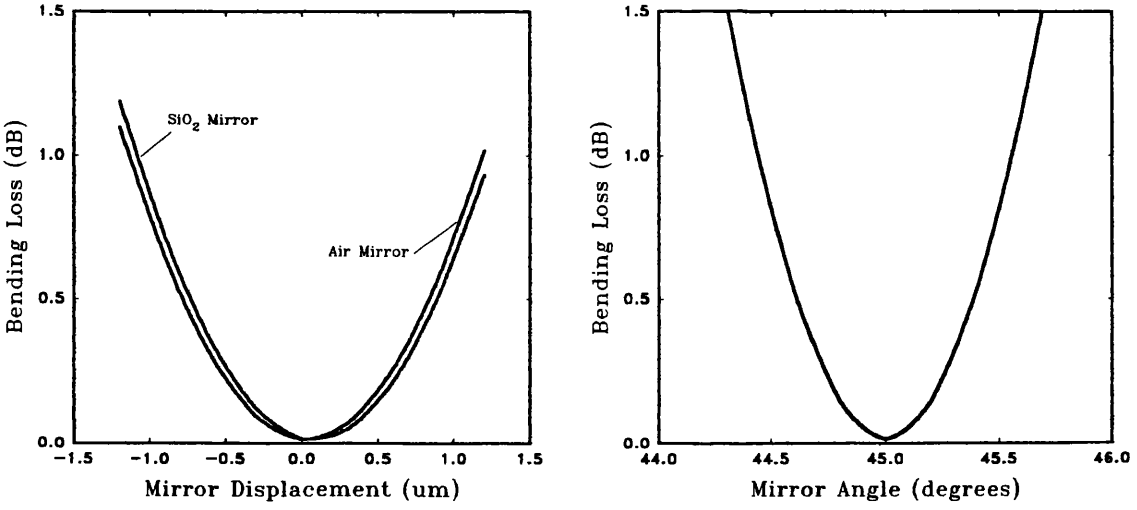

Mirror Loss for Lateral Displacement Mirror Loss for Angular Displacement

Figure 5.7.

It can be seen that the resulting loss for lateral displacement is not symmetrical, allowing the values for air mirror and silica mirror to cross over. This is due to the very slight offset from the Goos-Haenchen shift mentioned earlier. It can be seen that the optimum positioning for the mirror is not exactly at the zero displacement point, but alignment to this accuracy is not feasible. The curve for loss due to angular displacement

has only one line, as the difference between air and silica mirrors is indistinguishable at this scale.

5.2.2 Finite Mirror

The method described for the infinite mirror calculations above is only applicable to very large mirrors, and not for the small mirrors required for the CGCPS. The methods used for the infinite mirrors will now be developed in this thesis and improved to show the effect of a finite sized mirror on the reflection losses. The analysis will be restricted to a perfectly aligned mirror shown in Figure 5.8. The method for the infinite mirror allowed the set of plane waves derived from the incident mode shape to reflect from the infinite facet and be summed at the face of the output guide. If, however, the facet is finite, then a plane wave cannot be reflected as a plane wave since only a part of it will contact the facet and the resulting field will no longer be a homogeneous plane wave.

To account for the diffraction effects of the finite mirror, it is firstly assumed that the finite facet does not affect the incident plane waves, and the resultant field from all the incoming plane waves can be evaluated on the facet. From Figure 5.5 it can be seen that the plane wave spectrum of the mode shape is distributed over a narrow angle. As the facet is at 45° to the guide, the plane waves of significant magnitude are all incident on the mirror at an angle greater that the critical angle, so the reflection coefficient for each wave is taken to be unity, but the phase change due to the reflection must still be taken into account. The reflected field is reconstructed on the side of the facet of the reflected field. This is only strictly valid for an infinite mirror, but as the facet is large (~4μm) compared to the wavelength of light in the medium (~0.5μm) it is a reasonable approximation.

The reflected field, $E_r(y')$, on the facet is given by [5.11] using the appropriate transformation between coordinate systems shown in Figure 5.8, given by:-

$$\begin{aligned} y &= y'\cos\varphi + z'\sin\varphi \\ z &= d + z'\cos\varphi - y'\sin\varphi \end{aligned} \qquad [5.18]$$

φ being the facet angle, which in this case is 45°.

The resultant field constructed on the facet is now truncated to the size of the mirror, and transformed into a set of plane waves, $B(k'_y)$, as before. This method does not consider the whole field, just that reflected from the facet, but for the reasons given before it serves as a good approximation.

$$B(k'_y) = \frac{1}{\sqrt{2\pi}} \int_{-y_m}^{y_m} E_r(y') e^{+j(k'_y y')} dy' \qquad [5.19]$$

where E_r is the reflected field on the facet, and the integral is only taken over $-y_m < y < +y_m$ as $2y_m$ is the width of the mirror.

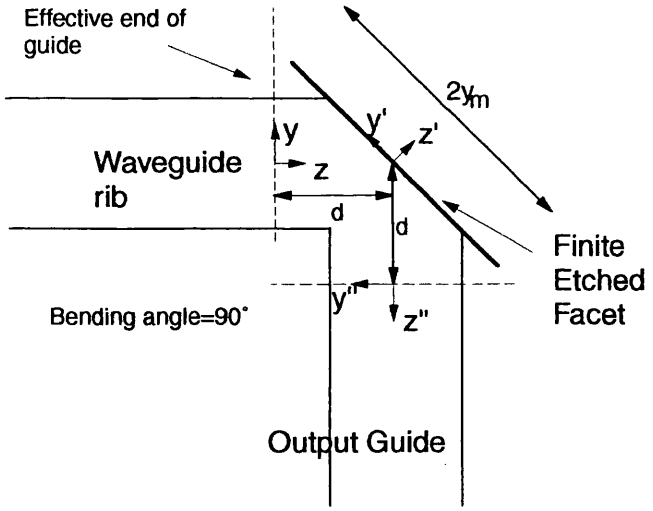

Figure 5.8. Finite Mirror Coordinate Systems.

Figure 5.9 shows the spread of the two sets of plane waves. The angular spectrum of the incident mode from the rib waveguide end is narrow compared to that of the field reflected from the mirror facet as there are no sudden transitions in mode shape as there are in the truncation of the reflected field. The peak value in the reflected field spectrum is offset, showing that the reflected field is directed away from the facet at 45° as expected.

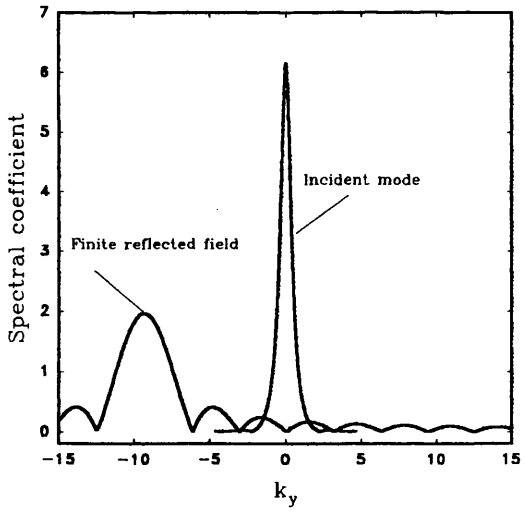

Figure 5.9. Plane Wave Spectrum of the Incident Mode Shape and Reflected Field.

The new set of plane waves is now summed at the end face of the output guide to form the field

$$E(y'') = \frac{1}{\sqrt{2\pi}} \int_{-\infty}^{\infty} B(k'_y) e^{-j(k'_y y' + k'_z z')} dk'_y \qquad [5.20]$$

using the appropriate values of y' and z' given by

$$\begin{aligned} z' &= d\cos\varphi + y''\sin\varphi + z''\cos\varphi \\ y' &= y''\cos\varphi - z''\sin\varphi - d\sin\varphi \end{aligned} \qquad [5.21]$$

Where φ is the angle of the facet normal to z.

As with the calculations for the infinite mirror, the values of k_y' become greater than the propagation constant of the medium, and the values for k_z' become imaginary. Evaluating k_z' from [5.3] the negative root is taken for imaginary k_z' so that the field decays as it travels away from the facet.

The effective end of the guide shown in Figure 5.2 is assumed to be present so as to avoid the effect on the mode shape of the infinite mirror encroaching onto the guiding region. The finite mirror does not overlap the field as far, but for consistency, the same distance, d, between the effective end of guide and the facet is kept for the finite mirror calculations. This assumption also allows the field to be found on the facet front without going into the region z<0, which would incur problems with the complex k_z giving growing solutions. The same distance is maintained between facet and output guide for a similar reason in that the output field is not reconstructed in regions z'<0.

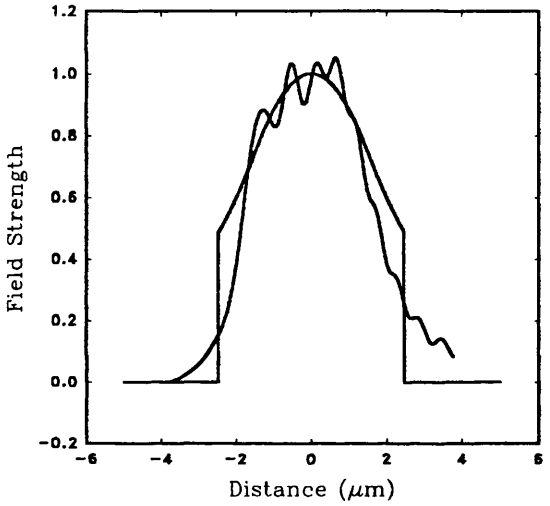

Figure 5.10. Reflected and truncated guided mode shape for 7μm wide 45° mirror.

Figure 5.10 shows the resultant field reconstructed on the front of the output guide, having been reflected from a 7μm mirror. Also shown is the truncated mode shape of the guided mode that would be expected if no diffraction occurred. The truncation is over a region less than 7μm, as the mirror is at 45°, and the apparent width will only be 7×cos(45) which is just under 5μm.

The reconstructed mode shape of Figure 5.10 is asymmetric due to the asymmetric spectrum of plane waves. Figure 5.9 shows the spectrum of the reflected field, and it appears to be symmetric about the point k_y'=9.3, but the values of k_z' will become imaginary when $k_y'>k_3$ in this case when $|k_y'|>13.2$. Above this value, when k_z' is imaginary, the plane waves decay with increasing z' and so their influence is more significant closer to the facet, which from Figure 5.8 is in the region where y'' is negative. The mode shape shown in Figure 5.10 is less oscillatory when y''<-1.5, supporting this theory.

As a comparison, the calculation for the layout shown in Figure 5.11 was evaluated. The light is free to pass through the slit, but is assumed completely absorbed by the obstruction. This is similar to the 45° mirror from which all the incident plane waves are reflected with no reduction in amplitude. In this case all the incident plane waves are used at the plane of the slit with no attenuation. The field incident on the slit is reconstructed from the plane wave spectrum. The resultant field is truncated to the slit width and a new set of plane waves evaluated.

The slit width is made to match the apparent width of the 45° mirror, in that

$$y_m' = y_m \cos(45) \qquad [5.22]$$

y_m being the half width of the mirror, and y_m' the half width of the slit. The distance between the ends of the guides and the slit are kept the same as for the mirror case.

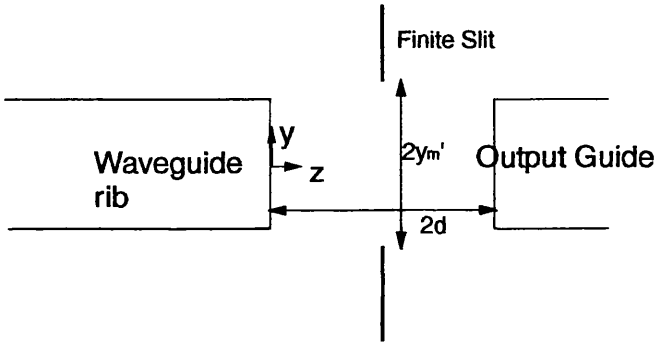

Figure 5.11. Layout for finite slit.

The resultant plane wave spectrum from the field in the slit is now symmetric about $k_y'=0$, and about $k_z'=k_3$. Reconstructing the field at the face of the output guide gives the profile shown in Figure 5.12, which is similar to both the profile from the angled facet and the truncated mode shape.

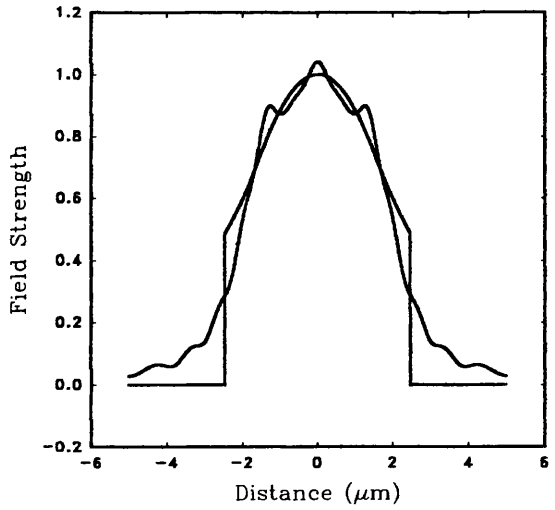

Figure 5.12. Reconstructed field from finite slit, with truncated guided mode shape.

Evaluating the amount of power coupled from the reconstructed profile into the guided mode shows the amount of loss expected from the finite mirror. The power transfer is calculated with the overlap integral as before in [5.14] and the results for a range of mirror widths are shown in Figure 5.13. The figure also shows the amount of power transmitted by the truncated mode shape as shown in Figures 5.10 and 5.12. The x-axis represents the 45° facet width, therefore, the truncation width for calculating the curve is the effective width of the guide. i.e. with a mirror width of 7μm, the truncation and slit widths are 4.94μm.

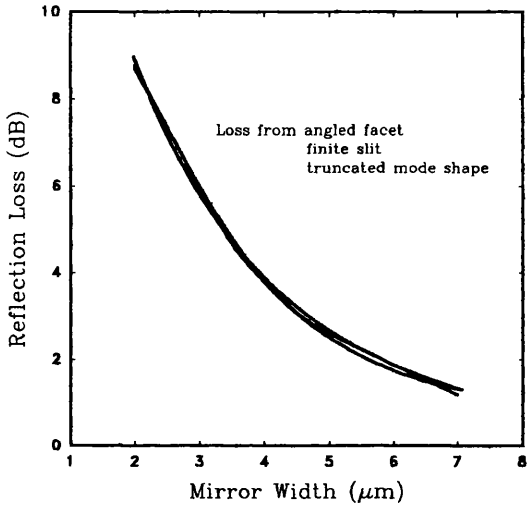

Figure 5.13. Diffraction loss from finite mirror, finite slit and mode truncation.

Figure 5.13 shows the results of the loss expected from a finite 45° mirror facet, a finite slit and a truncated mode profile. The graph illustrates that there is very little difference in result between the three methods of calculation. With this knowledge it is now far faster and easier to calculate the loss from a finite facet at 45°. At angles less than this, especially approaching the critical angle, the results for the mirror facet will differ due to the effects of the modulus of the reflection coefficient being less than unity for some of the plane waves.

The attenuation of the signal can now be broken up into three parts, namely that from the reflection, that from the finite size of the mirror, and the remainder from the irregularity of the facet, making analysis of the fabricated device easier.

5.2.3 Behind the Facet

Using the analysis for the finite slit and Babinett's theorem for complementary screens,[19] the field behind the facet can be found.

Babinett's (scalar) principle states that the field at any point remote from a source consists of the field incident at that point when there is an obstructing screen between the source and the point of interest, added to the field at the point when there is a complementary screen in the path.

With this theorem, if F_o is the field on the far facet if there is no mirror present, and F_s is the field on the far facet from a slit the size of the mirror, then the resultant field due to the blocking action of the etched mirror, F_M is:

$$F_M = F_o - F_s \qquad [5.23]$$

F_s has already been evaluated from the finite slit calculations, and F_o can be calculated from the far field of the original input guide, thus F_M can be found. Figure 5.14 shows the layout of the problem.

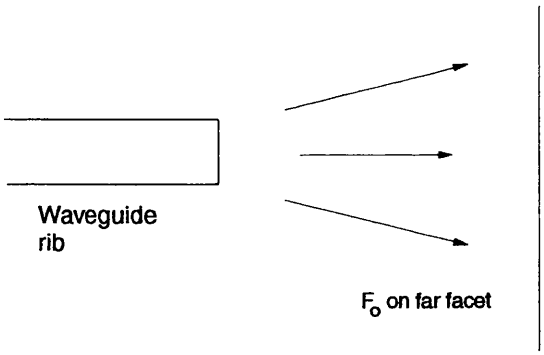

Figure 5.14a. Unobstructed far field.

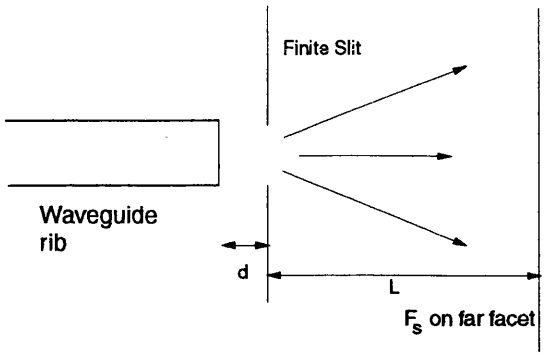

Figure 5.14b. Finite slit obstruction.

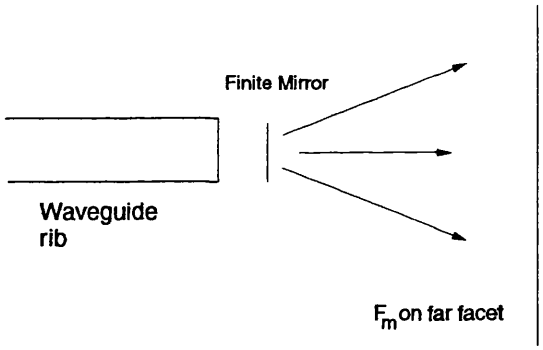

Figure 5.14c. Required field, obstructed by mirror.

The distance between the mirror and the incoming guide is kept at the same value as in all previous calculations, but the distance of the far facet is taken as 60μm, to be in line with a fabricated device. Results of this calculation are shown in Figure 5.15 for a 3μm wide mirror obstruction.

The mirror used for the experimental results of Figure 5.15 is 3μm wide, and shows a large amount of optical power incident on the device facet behind the mirror. Experiments using a 9μm mirror showed no light at the back facet, demonstrating that a larger mirror is required. This size of mirror, however, would not fit into the arrangement of the CGCPS without impinging onto the main waveguide.

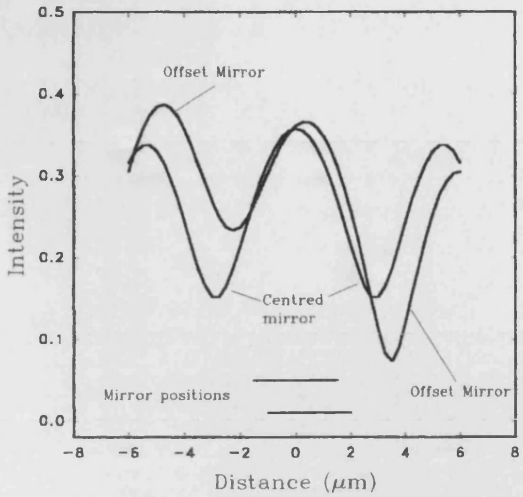

Figure 5.15a. Theoretical results for field 60μm behind mirror

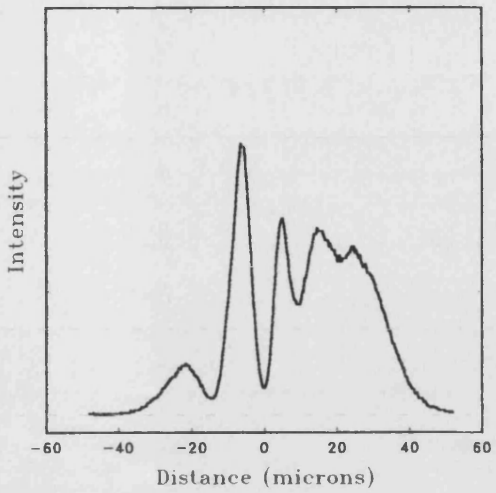

Figure 5.15b. Measured intensity at facet 60μm behind mirror.

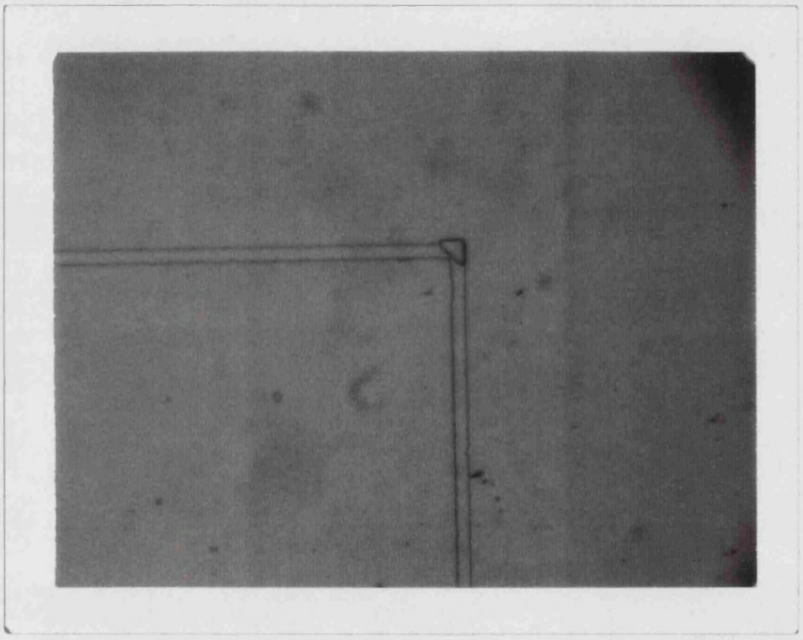

Figure 5.15c. Structure from which Figure 5.15b was measured.

These results compare well with the practical measurement of a single mirror structure also shown in Figure 5.15. It was initially thought that the dip in the intensity profile indicated the mirror position, but as the calculation shows, the region directly behind the mirror has a peak in intensity. In the case of the offset mirror, a 0.5μm offset has been used to represent the minimum offset possible in fabrication. The intensity profile is no longer symmetrical, and the fringes are more intense on the side away from the offset. The experimental measurement on Figure 5.15b shows such an offset in the fringes, albeit masked by background light.

As will be seen in Chapter 6, the comparison between the above unhindered scatter behind the facet and the CGCPS device intensity results do not compare well, as there is a

guide in the region of interest that affects the propagation of light toward the facet in the full switch device.

5.3 Measurement and Results

Mirrors were fabricated with Reactive Ion Etching (RIE) in a SiH_4 plasma at University of Sheffield. The various masking techniques are detailed in Appendix 4, but for the measurements below, the self aligned method was used throughout.

5.3.1 Measurement Technique

There are three methods for measuring the reflecting efficiency of the etched mirrors.

The first is to etch the mirrors and guides in a lasing material, such that a laser cavity is formed with a bend in it. The lasing threshold of the bent structure is then compared to that of a straight laser in the same material to judge the reflectivity. This has been used in other studies, but will not be suitable for our purposes as the material used is not designed to act as a laser at the wavelength of interest. If the material could be made to lase, the lasing wavelength would be almost half that of the signal wavelength and give a false result, as the diffraction effects would be different.

Another method is to use the Fabry-Perot technique employed earlier with the straight guides. As stated in Chapter 2, the method is only reliable when the total structure has a loss of less than 10dB, so that the resonant peaks and troughs can be seen above the noise of the measuring apparatus. From experiment, our mirror structures do not fall within this requirement, and so the method cannot be used. Using mirrors made from the self aligned technique (Figure 5.16) gives a facet that is in a different position inside and outside the guide core which could lead to phase distortion. Mode polarisation changes can also affect the technique, and arise from the facet being at an angle. Experimentation, however, has shown that any mode conversion that may be present is undetectable with the apparatus used.

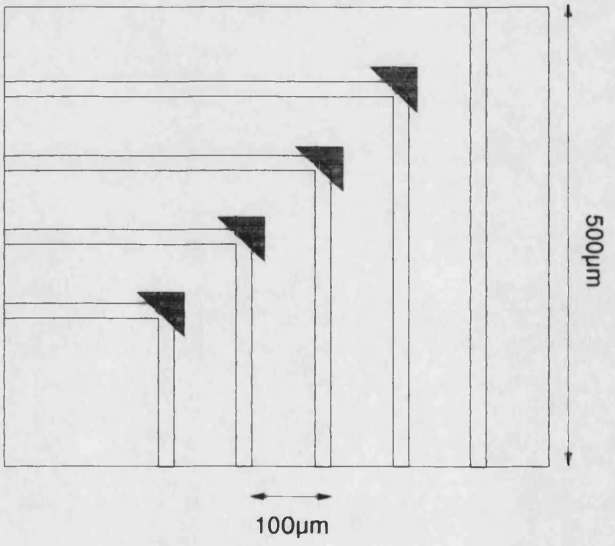

Figure 5.16a Structure for mirror loss measurement.

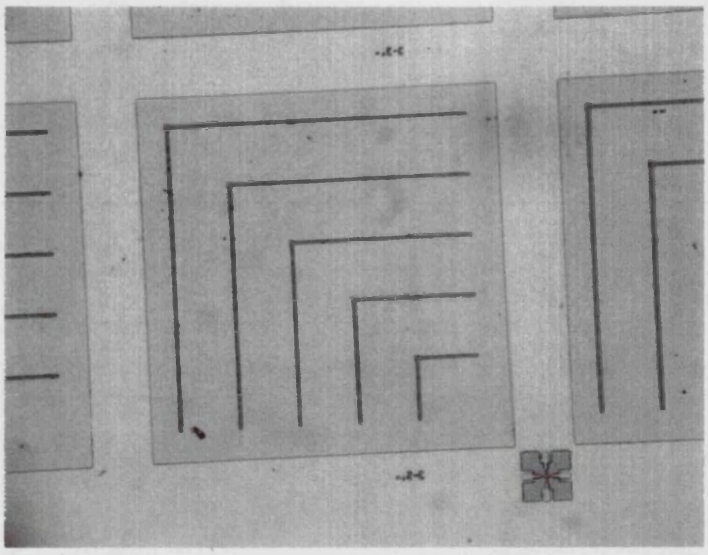

Figure 5.16b. Devices used for mirror loss measurement.

The last method is to compare the light transmission through a straight guide to that of a bent guide with a mirror facet. This is similar to the cutback technique used in Chapter 2, and has similar disadvantages, in that constant input coupling is required to each structure.

This last method is the only one available to us, and for the measurements a number of structures were made as shown in Figure 5.16. The power from the straight guide was measured and likewise the output from each of the bent guides. Taking the change in length into account is found unnecessary, as the maximum discrepancy is 0.6mm which gives a loss of 0.6dB for a metalled guide with an attenuation of 10dB/cm. Losses from the straight sections of guide were checked for these devices using the Fabry-Perot resonance technique.

The results are shown in Figure 5.17 and show an erratic spread of the data. Ideally the graphs should slope downward by 0.6dB over the full range, but other factors are contributing to the variations. Variation of input coupling is thought to be the major factor, with fabrication differences across the sample also contributing to the results. The data confirm that the Fabry-Perot technique would not be suitable as the average loss of the mirrors is in the region of 10dB.

Devices of the type in Figure 5.16 were also made with 3μm guide widths, that became wider toward the facet. The purpose of this is to increase the guide width, such that more of the mode is confined to the rib region, and thus reflected from the facet. Tapers with final widths of up to 6μm were fabricated, but the poor results prevented this.

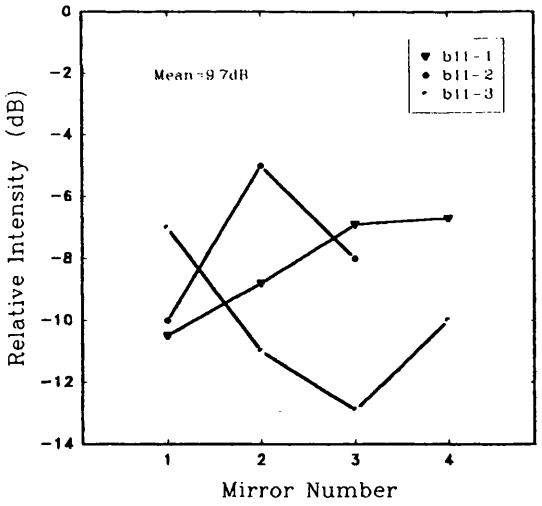

Figure 5.17 Mirror losses for three test devices

5.4 Conclusions

This chapter shows that the effects on the mirror performance, when the mirror well is filled with silica, are negligible for use in GaAs based compounds. The effect of the Goos-Haenchen shift has also been shown, and it is seen that it only needs to be considered when the reflecting angle is below the critical angle. This is more problematic for silica guides, where the critical angle is large.

The theoretical analysis has then been extended to show the effects of a mirror of finite width, and the expected results from its finite size. The loss from the finite mirror is similar to that if the mode shape had been truncated to the effective facet width. Knowing that the diffraction from a finite mirror has little effect allows us to easily calculate expected losses from the size of mirror without going to the lengths detailed in this chapter.

Experimental measurements of etched mirror facets are also made and compared to the theoretical approximations, giving a figure of loss from the real devices higher than expected. The extra scattering of light is thought to be due to the irregularity of the facet from the IBE fabrication process.

The chapter gives a quantitative illustration that for use in integrated optics the relative size of the mirror has to be as large as possible compared to the mode shape so as to reflect as much power as possible. This fact may be thought to be intuitively obvious, but has now been given formal confirmation.

References

[1] J. Nayyer, Y. Suematsu, K. Shimomura. "Analysis of reflection type optical switches with intersecting waveguides". Journal of Lightwave Technology, Vol. 6, No. 6, pp1146-1151. June 1988.

[2] K. Hirayama, M. Koshiba. "A new low loss structure of abrupt bends in dielectric waveguides." Journal of Lightwave Technology, Vol. 10, No. 5, pp563-569. May 1992.

[3] S. Safavi-Naeini, Y.L. Chow, "A Novel Design and Analysis of Low-Loss Abrupt Bends of Dielectric Slab Waveguides." Journal of Lightwave Technology, Vol 10, No. 5, pp570-580. May 1992,.

[4] E.C.M. Pennings, G.H. Manhoudt, M.K. Smit, "Low Loss Bends in Planar Optical Ridge Waveguides." Electronics Letters, Vol 24, No. 16, pp998-999. August 1988.

[5] L.H. Spiekman, et al. "Ultrasmall waveguide bends: the corner mirrors of the future." IEE Proceedings part J. Vol. 142, No. 1, pp61-65. February 1995.

[6] J.E. Johnson, C.L. Tang, "Precise Determination of Turning Mirror Loss Using GaAs/GaAlAs Lasers with Up to Ten 90° Intracavity Turning Mirrors." IEEE Photonics Technology Letters, Vol 4, No. 1, pp24-26, January 1992.

[7] H. Appelman, J. Levy, M. Pion, D. Krebs, C. Harding, M. Zediker, "Self Aligned Chemically Assisted Ion Beam Etched GaAs/GaAlAs Turning Mirrors for Photonic Applications." Journal of Lightwave Technology, Vol. 8, No. 1, pp39-41. January 1990.

[8] H. Han, D.V.Forbes, J.J.Coleman. "Self aligned high quality total internal reflection mirrors." IEEE Photonics Technology Letters, Vol. 7, No. 8, pp899-901. August 1995.

[9] K. Ogusu, "Transmission Characteristics of Optical Waveguide Corners." Optics Communications, Vol 55, No. 3, pp149-153. September 1985.

[10] P. Buchmann, H. Kaufmann, "GaAs Single Mode Rib Waveguides with Reactive Ion Etched Totally Reflecting Corner Mirrors." Journal of Lightwave Technology, Vol 3, No. 4, pp785-788. August 1985.

[11] H. Hatami-Hanza, P.L. Chu, J. Nayyer. "Low Loss Optical Bend Configuration with Curved Corner Reflector." Electronics Letters, Vol 28, No. 25, pp2283-2285. December1992.

[12] P. Buchmann, H. Kaufmann, "GaAs Single Mode Rib Waveguides with Reactive Ion Etched Totally Reflecting Corner Mirrors." Journal of Lightwave Technology, Vol 3, No. 4, pp785-788. August 1985.

[13] A. Himeno, H. Terui, M. Kobayashi, "Loss Measurement and Analysis of High Silica Reflection Bending Optical Waveguides." Journal of Lightwave Technology, Vol 6, No. 1, pp41-46. January 1988.

[14] P. Buchmann, H. Kaufmann, "GaAs Single Mode Rib Waveguides with Reactive Ion Etched Totally Reflecting Corner Mirrors." Journal of Lightwave Technology, Vol 3, No. 4, pp785-788. August 1985.

[15] J.E. Johnson, C.L. Tang, "Precise Determination of Turning Mirror Loss Using GaAs/GaAlAs Lasers with Up to Ten 90° Intracavity Turning Mirrors", IEEE Photonics Technology Letters, Vol 4, No. 1, pp24-26, January 1992.

[16] K. Ogusu, "Transmission Characteristics of Optical Waveguide Corners." Optics Communications, Vol. 55. No. 3, pp149-153. September 1985.

[17] P. Buchmann, H. Kaufmann, "GaAs Single Mode Rib Waveguides with Reactive Ion Etched Totally Reflecting Corner Mirrors." Journal of Lightwave Technology, Vol. 3, No. 4, pp785-788. August 1985.

[18] D.L.Lee. "Electromagnetic properties of integrated optics." John Wiley 1986. p61

[19] M. Born, E. Wolf. "Principles of Optics." Pergamon Press p381, p559 1986.

Chapter 6

The First Switches

This chapter gives the results for the device as a whole. The theoretical expectations of the device are evaluated, based on the measurements of the components of the CGCPS so far. Design of the mask set and fabrication are described together with the pitfalls that were encountered. Step-by-step fabrication detail is presented in Appendix 4 and only detail pertinent to the design is given here. Measurements of fabricated devices are described and the results are discussed.

6.1 Theoretical Device Performance

6.1.1 Evaluation of Performance

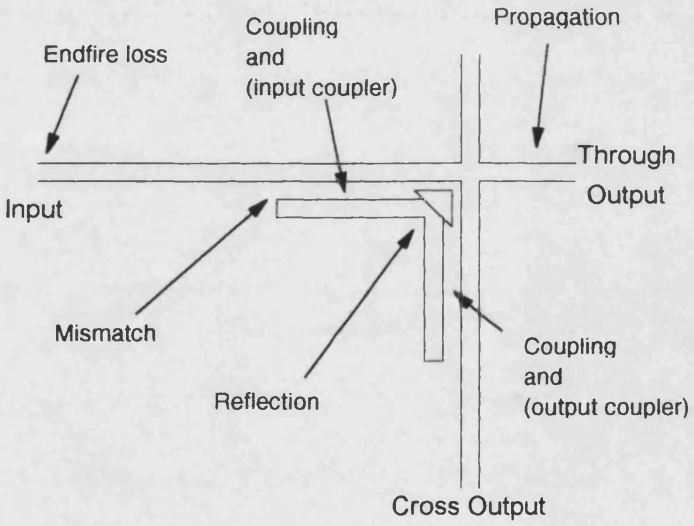

Figure 6.1. Signal reduction points in the CGCPS.

As the signal passes through the CGCPS element it encounters a number of discontinuities that can cause attenuation of the signal. These losses are shown above in Figure 6.1. The CGCPS is to be used as an array of devices so the endfire coupling will be discounted here, as we assume the signal comes from another device with similar guides.

The mismatch loss can be evaluated by using the overlap integral [6.1] between the incoming single mode F_i and the two modes of the coupler F_a, F_b which are the two modes of the complete twin ridge coupled guide structure as calculated in Chapter 3. Using equation 6.1 the magnitude of each mode in the coupler can be evaluated and the total power calculated. The equation is only valid if the β's of each mode are almost equal, which in this case they are, ranging from 13.192 rads/μm for the injected coupler, to 13.198 rads/μm for the single rib inputs.

The same is done at the end of the coupler with the total output field of the coupler and the single mode of a symmetric guide, f_o, for the injected case. [6.2] For this analysis it is assumed that the mirror is sufficiently far away from the through guide so as not to affect the mode shape of the output guide field profile, F_o.

$$F_a(y) = Af_a(y)$$
$$F_b(y) = Bf_b(y)$$
$$A = \frac{\int_{-\infty}^{\infty} F_i f_a dy}{\int_{-\infty}^{\infty} f_a^2 dy} \qquad [6.1]$$
$$B = \frac{\int_{-\infty}^{\infty} F_i f_b dy}{\int_{-\infty}^{\infty} f_b^2 dy}$$
$$F_o = Cf_o$$
$$C = \frac{\int (F_a + F_b) f_o dy}{\int_{-\infty}^{\infty} f_o^2 dy} \qquad [6.2]$$

The results of these integrals show that minimal loss is incurred at the guide coupler interfaces, as the insertion loss of the full coupler is 0.03dB in the passive state, shown in Figure 6.3a. However, it will now be shown that in the other modes of operation the power transfer is not as efficient.

Figure 6.2 shows how in the input coupler, the power is transferred to the through output guide. If the overlap integral [6.2] is taken over the whole width of the structure, the on-off ratio becomes 8.5dB which is very poor. The presence of the mirror improves this figure, as the mirror reflects the light in the tap guide away from the through guide output. The overlap integral can be taken from the edge of the mirror (shown in Figure 6.2a) reducing the amount of power in the output. The on-off ratio is 13.8dB for the figures given, but this is an optimistic calculation as the free carrier attenuation, from excessive injection, has not been considered.

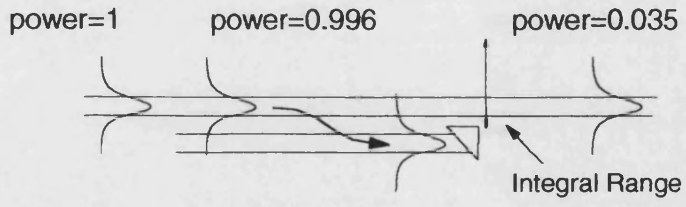

a) Passive Case

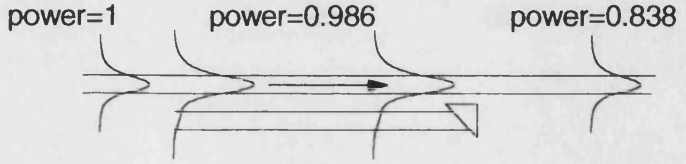

b) Injected Case

Figure 6.2. Power transfer on input coupler.

The case of the output coupler is shown in Figure 6.3. In this case the input to the coupler is into the injected guide, which when passive almost all the power is transferred across to the output guide. When the coupler is injected with carriers, there is only the injected side of the coupler mode for the incoming light to couple into, thus the power entering the coupler is reduced severely. Although the on-off ratio of the output coupler is only 7.3dB, that figure is valid for a constant input power. In the CGCPS, when the device is injected, less power will arrive at the output coupler. With carriers in the input coupler the mirror reflects only 14.6% of the input power, leaving 83% to go to the through output (Figure 6.2b). Thus the output of the second coupler is reduced to 18.5%×14.6%=2.7%. Taking a similar calculation for the non-injected case, this gives an on/off ratio of 15.5dB.

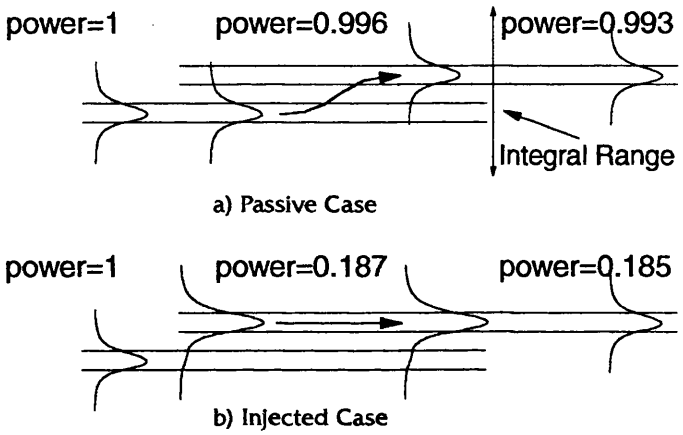

Figure 6.3. Power transfer in output coupler.

The losses of the device have not been considered so far. The propagation loss and scatter from the mirror have to be added into the above calculation to obtain the signal crosstalk and insertion loss of the device.

The incidence onto the mirror in the non-injected case has been dealt with in Chapter 5, and the fabricated devices were shown to have high losses in the region of 10dB. Other workers have made mirrors with losses as low as 0.7dB, so a figure of 1dB loss is taken as a reasonable measure. A figure of 100dB/cm is taken for the propagation loss as this is in agreement with the measured values for the material currently being used, although this loss is significantly reduced by using the material designed in Chapter 4.

Taking the passive case first, the power from the cross output will be

0.965 from 1st coupler to the mirror,

×0.1 from the 10dB propagation loss in the 1st coupler,

×0.79 from the 1dB loss at the mirror,

×0.993 due to the output coupler mismatch,

×0.1 from the 10dB propagation loss in the 2nd coupler, giving a final power throughput of $=7.5\times10^{-3}$.

For the through output, by comparison the coupling factors are,
0.035 from the 1st coupler,
×0.1 from the 10dB propagation loss in the 1st coupler
×0.56 from the 250μm output guide, to give a net power reduction factor of
$=1.96\times10^{-3}$.
These figures give a crosstalk figure of 7.5/1.96, which is 5.8dB. This crosstalk is very bad and not useable in a real device, but is greatly affected by the propagation loss, and the arbitrary choice of the through output guide length. For the same figures but a 5dB/cm waveguide propagation loss the crosstalk becomes 0.6/0.03, giving 13dB which is approaching a useful operating figure.

In the injected case the power transfer values for the through facet are:
0.838 from the first coupler
×0.1 from the propagation loss in the 1st coupler
×0.56 from the 250μm output guide, resulting in an output of:
=0.047

for the cross facet
0.145 from the 1st coupler to the mirror
×0.1 from the propagation loss in 1st coupler
×0.79 from the 1dB loss at the mirror
×0.185 from the 2nd coupler mismatch
×0.1 from the propagation loss in the 2nd coupler, giving an output of
$=2.11\times10^{-4}$

The figures above give a cross talk of $0.047/2.11\times10^{-4}$ or 23.5dB which is a very acceptable figure, but in this case aided by the propagation loss. For similar calculations with 5dB/cm propagation loss in the waveguides the crosstalk becomes 16.3dB, which is line with the passive case crosstalk. It must be noted that the extra loss in the second coupler from carrier injection has not been taken into account, and would improve the figures for the injected case.

6.1.2 Conclusions

From the introduction of Chapter 1 it was stated that an aim of 15dB for on-off ratios and crosstalk was required for a useable device. The figures above clearly do not achieve this, but are dominated by the propagation loss in the guides. Further improvement could be introduced by separating the guides, but at the expense of increasing coupling length, which in turn increases the overall propagation loss. It is clear that work has to be done to reduce the losses if this modification is used. Separation of guides is discussed further in Chapter 7. Fabricated mirrors also have to be improved to

meet the figures used here, but it is not possible for us to concentrate on this aspect of the design because of fabrication limitations.

6.2 Mask Design

6.2.1 CGCPS I

The patterns for the CGCPS fabrication are taken from the master mask which is etched onto a chromium plated sheet of glass with electron beam lithography. The fabrication of the mask is carried out at the Rutherford Labs in Chilton, but the designs are made in-house at Bath. The mask design has to take into account the various stages of fabrication, and provide a separate pattern for each step. Consideration of other steps is also necessary so that alignment marks can be made and overlaps avoided.

The CGCPS, in essence, consists of a deeply etched mirror well, a number of shallowly etched guides, and at least one contact for the current injection. The first CGCPS mask set was made as three separate patterns for the mirrors, guides, and metal contacts respectively, in the exact form as they appear in the diagram of Figure 6.1. The masks being in this form left open the option of the order of fabrication.

Further thought on the fabrication sequence centred around whether to first etch the mirror wells or the guides. Etching the guides first would leave the platform for the mirror mask uneven, resulting in bad contact, which would be detrimental for a good mirror edge. It would also be better to put the silica layer down before making the mirrors as then liftoff can be used. However, the plasma etch used for the mirrors cannot etch through silica very quickly, therefore a window in the silica would have to be made to allow the mirror etch. Liftoff for the mirror pattern is not recommended as it would leave a rough facet to reflect off.

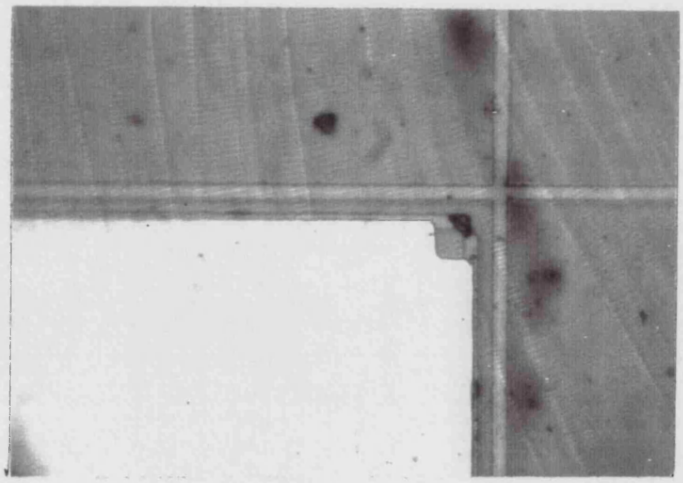

Figure 6.4 Photograph of UB622, the first CGCPS. CGCPS I

If the mirrors are etched first, then the reflecting facets have to be protected from further fabrication steps. Not only would the etching of guides affect the facet, but coating with gold would short circuit the top capping layer to the bottom cladding layer. This is the method that was chosen, and protection offered by filling the mirror well with photoresist using the negative of the mirror mask. The resist would then have to be baked hard as the process for making the guides' mask would expose and wash away the protective area.

The result achieved using the above process is shown in Figure 6.4 Clearly the alignment of the mirror is not exact, and realignment of the protective resist is to the same accuracy, and so cannot be thought of as reliable. No light was detected at the output in this device, although the coupler is known to have worked satisfactorily.

6.2.2 CGCPS II

With the experience of the first CGCPS, and the opportunity for another mask set to be made, further thought was given to the mask design. The protection of the mirror facet had to be made more reliable, and alignment accuracy increased.

To improve the mirror protection, two changes were made. The first was to fill the mirror well with silica before the photoresist had been removed, so that the bulk of the silica is lifted off, leaving only the mirror coated. This stopped the etched facet from being directly coated with metal and shorting out the device. The second improvement was to extend the guides' mask to create a protective pad to stop the etch attacking the mirror well. The disadvantage of the pad is that it has to fit between the main guide and the tap guide without shorting them together, but it must also be bigger than the mirror. To achieve these requirements, and make the pattern have a minimum linewidth greater than 1μm, the mirror has to be made quite small. The layout is shown in Figure 6.5 and results in a mirror 4μm across, which from Chapter 5 should offer a minimum reflection loss of 4dB.

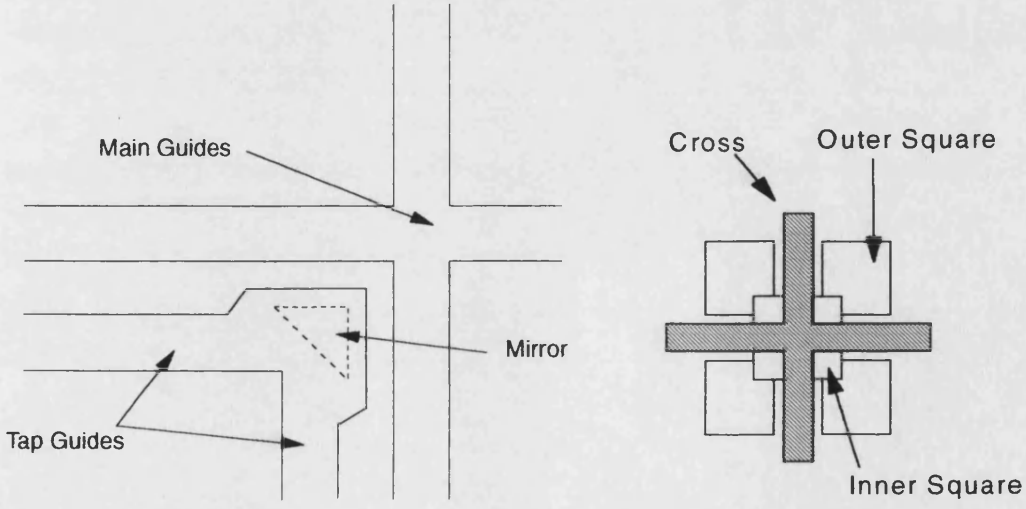

Figure 6.5 CGCPS II Guides mask with protective pad in relation to mirror, and alignment mark.

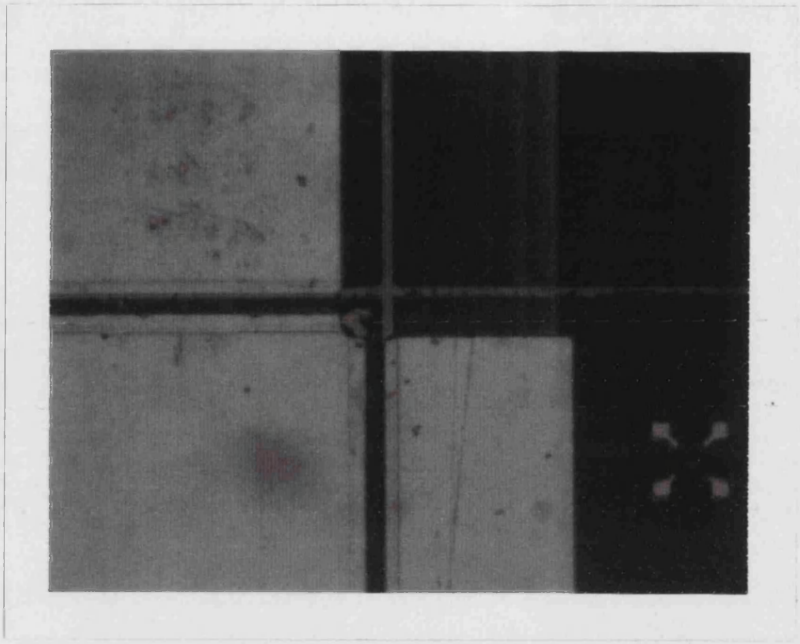

Figure 6.6 CGCPS II Photograph of a fabricated device.

A number of working devices have been made with the above fabrication configuration, and a device is shown in Figure 6.6. Although the mirror is almost 1.5μm off line, it still reflects enough of the signal to demonstrate the operation of the switching arrangement. The results will be discussed later in the chapter.

Also shown in Figure 6.5 is the registration mark for the alignment of the three mask patterns. The mark consists of a cross on one mask and the sets of squares on the guides and contact masks. The large cross is associated with the mirror pattern, and is made first. The outer squares are made on the mask with the guides and contact pad patterns. The set of registration marks is particularly useful in that the outer squares give a rough alignment with a 3μm gap between them and the inner cross. There are also inner squares on the same pattern (over developed in the picture in Figure 6.6) that give a more exact lineup with no gap between them and the cross. The different sizes of square accommodate the variation in development and wear from other etching stages. For example, the cross in the alignment mark is etched with the mirror. Further, unprotected, etching is made on the alignment mark when the guides are etched, making the cross wider. Misalignment of the guide mask also distorts the image of the cross where the patterns overlap. When aligning the contact mask, the cross is now wider than the smallest gap between the inner squares, so alignment can be achieved on the outer squares with the bigger gap. In practice, the resolution of the mask aligner does not give a sharp image of the alignment marks, so an amount of intuition and patience is required to achieve alignment better than 1μm. Ideally, however, from the results of Chapter 5, accuracy of better than 0.5μm is required.

Alignment is helped by using a spin speed in excess of 4500rpm when depositing the resist as then resist is then thin enough for the marks on the device and the marks on the mask to be in focus, through the mask aligner optics, at the same time.

6.3 Fabrication

Fabricating the devices is time consuming. Details of exact settings for the process steps used are given in Appendix 4, but this section discusses the reasons for the methods chosen and the fabrication sequence. Outlines of the fabrication processes that have been rejected are also given, which, although not contributing to the final result, reinforce the reasons for the finally chosen fabrication sequence.

6.3.1 Process order

Some of the process ordering has already been discussed in the previous section with the mask design in mind, but only considered the top surface. The supplied wafer is 500μm thick, but to get good cleaving of the crystal planes when cutting up the devices it is better to have a sample less than 150μm thick. The material therefore has to be lapped down and the contact applied to the bottom n-type surface. It is usual in industrial environments to carry out the top surface processing first, to keep the wafer as thick and robust as possible, and then thin down the substrate. However, it has been found from experience that the annealing of the bottom contact affects the top surface. The result appears to be as if the top gold layer has shrunk, leaving holes in the gold through which the titanium can be seen. Silica layers are also affected in that their adhesion to GaAs is reduced and the silica may come off in the annealing chamber.

The problem with the gold is thought to be caused by the gallium in the top semiconductor layer diffusing into the gold in large quantities. This diffusion can be prevented by using a thin layer of platinum between the semiconductor and the gold, but facilities at Bath do not allow for this, so the annealing is undertaken first, and top surface processing carried out on a 150μm thick sample. There are drawbacks in using such thin sample, but it is mounted onto a glass coverslip to give the sample rigidity and make it easier to handle.

The final ordering of fabrication is given in Appendix 4.

6.3.2 Exposure and Development

6.3.2.1 Contact

Exposure of the photoresist to transfer the pattern from the chrome mask to the resist is highly dependent on the contact between the mask and photoresist. Any gap between them gives rise to interference patterns and diffraction of the incident UV light, and so must be avoided for a good pattern. The sample, however, is quite small and does

not rotate the chuck of the mask aligner enough to ensure a flat contact between itself and the mask. Larger samples have a larger radius and therefore better leverage to ensure that the mask and sample are parallel and in contact over the whole area. The amount of material required to do this would reduce the number of trials possible from one wafer, so a compromise is reached and small samples are used to give adequate contact for most applications. For the mirror pattern, mask contact is very important, and is improved with manual adjustment of the chuck plane and a great deal of patience. Contact can be judged during the alignment stage by the distance between the interference fringes of visible light used for the microscope.

To further increase the contact between the mask and sample, the resist around the edges is removed. When spun onto the sample, a small ridge of resist forms at the edge that prevents the mask from touching the main area of the sample. The removal of resist can be done in either of two ways, and sometimes both. The first is to chamfer the edge of the device. This allows the ridge of resist that forms at the edge to fall down during the spin and not obstruct the mask. Figure 6.7a. The second method exposes the edges of the device to remove any edge ridges of resist Figure 6.7b. This is a useful backup if the first chamfering method is inadequate, but does require an extra developing stage of the resist which is open to potential contamination.

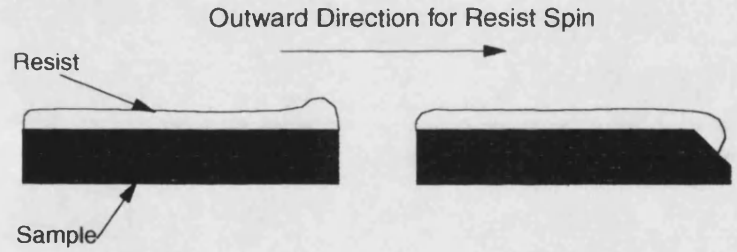

a) Chamfer Method

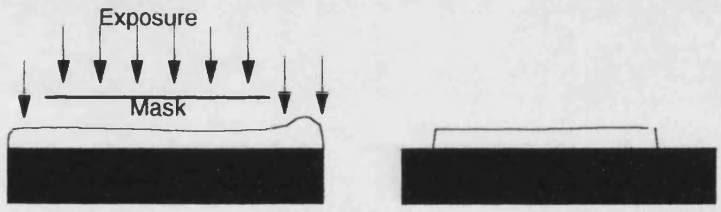

b) Exposure Method

Figure 6.7. Methods for ensuring a flat resist layer for improved mask contact.

6.3.2.2 Developer Concentration

The mirror pattern has already been mentioned as being important, and its pattern can be affected not only by the mask contact but also by the development of the resist. The resist developer is recommended to be used in 3:1 (water:developer) concentration for fast developing, or 5:1 for high contrast results. The 3:1 dilution is usually used as it gives smoother edges and requires lower exposure of the resist. The 3:1 solution does, however, slightly over develop the pattern resulting in slightly thinner guides and rounded facets on

the mirror triangles. The 5:1 solution requires the resist to be exposed for longer, and so the results are less affected by interference fringes and diffraction. The 5:1 solution is used on the mirror pattern as it gives a straighter facet for the reflection, but the facet edge can be more jagged than when the 3:1 is used. In practice the solution was made up as 55ml of 4.5:1 for the development of the edges and the weakened solution reused for the triangles themselves giving adequate results.

6.3.2.3 Postbaking

Baking of the resist reduces its sensitivity to the UV exposure and increases its adhesion to the substrate and durability to etching. Postbaking after development is usually used to increase durability, but can result in the resist running slightly, reducing the resolution of the developed pattern. This is most critical in the mirror pattern as the surface tension tends to round off the flat facet of the mirror, but for guides it is useful in smoothing the edges of the pattern. The first trial gave a combination of bad contact and postbake run, resulting in the resist shown in Figure 6.8. The plasma etch used for the mirror facet fabrication does not require hardened resist, so the postbake is now omitted for this step to reduce the resist running.

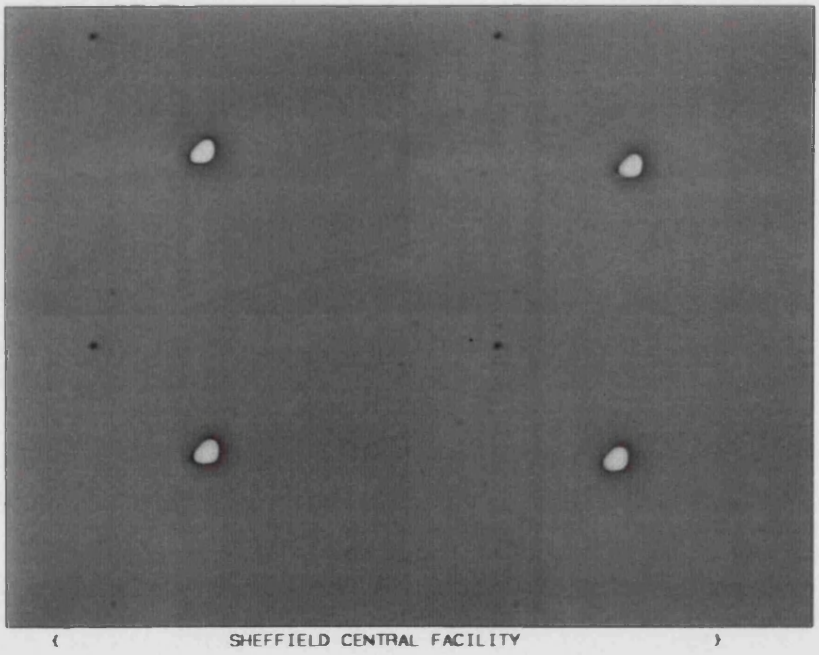

Figure 6.8. Photoresist pattern for mirrors after postbake showing rounding of facets.

6.3.2.4 Galvanic Action

Another problem encountered with the exposure of resist patterns is that when exposing a layer of resist that lies on top of a silica layer, the UV light can travel laterally through the silica, and expose masked areas from below. This is found to happen in the

final contacting stage when a 3μm strip of resist is required to separate two gold contact pads. The UV travels under the silica and exposes the bottom of the 3μm strip causing it to lose adhesion to the sample and break away. The penetration of the UV through the silica can be halted by depositing a thin (20Å) layer of aluminium over the silica, Figure 6.9a. The developer will remove the aluminium in the normal developing process, leaving areas of GaAs exposed for further layers to be deposited, Figure 6.9b. When this technique was applied, the next layer was Ti/Au which was deposited over the whole device for liftoff, Figure 6.9c. Liftoff removed the resist and areas of Ti/Au that were not required, leaving areas of GaAs with aluminium and areas with Ti/Au, Figure 6.9d. The usual developer was used to remove the unwanted aluminium, as NaOH has little effect on GaAs or Ti/Au. In this case, however, the combination of metals served to create an electrode potential that made the developer etch quickly into the device. Figure 6.9e. The results of the device are shown in Figure 6.10, and show the different etch rates of the different layers.

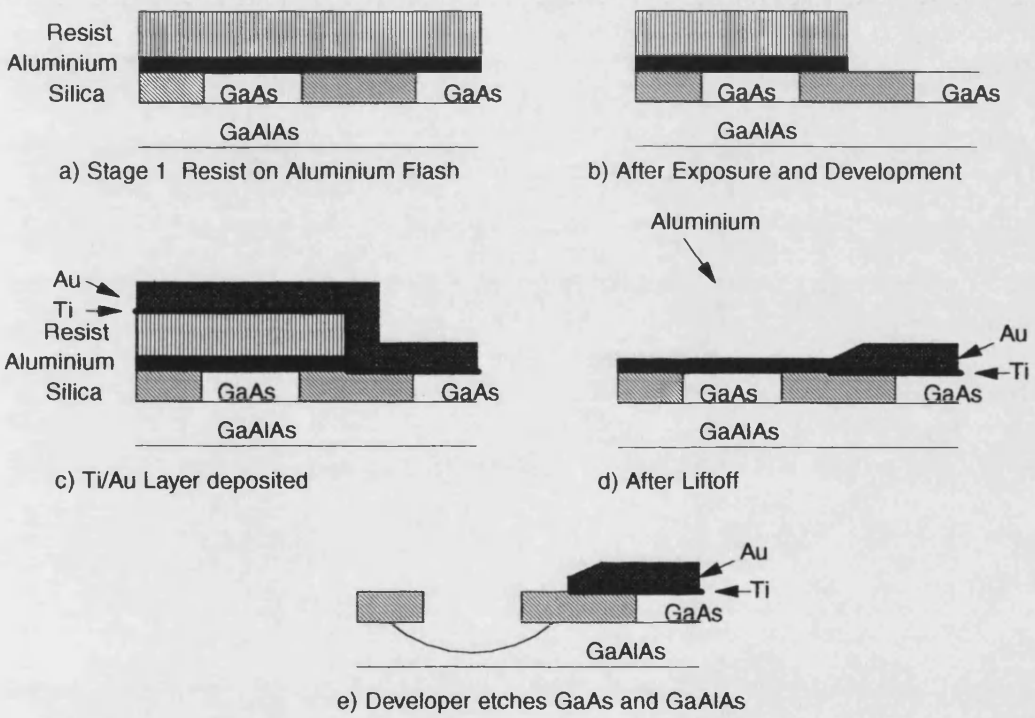

Figure 6.9. Fabrication stages leading to galvanic action.

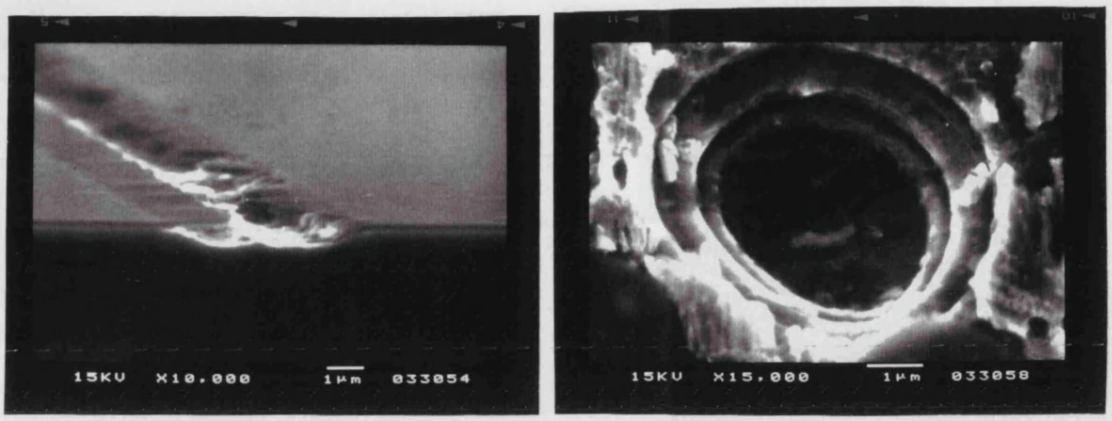

Figure 6.10 SEM of galvanic action on guide and mirror.

6.3.2.5 Etching of Resist

Because of the galvanic action described above, the contact pads are fabricated by coating the whole device with titanium and gold, and then etching away the unwanted areas of metal. By using this method, the need for the aluminium flash is removed. The method involves large areas of resist over the contact pads, with a small separation between them. (3µm). It has been found that in some cases of thick photoresist that has been postbaked at 60°C the ion beam etching causes blooming of the resist which consists of 5-10µm circles of resist that have expanded. It is thought that this is due to discharge of the charge stream from the ion gun hitting the sample. It does not adversely affect the contact pad, but the two contact pads 3µm apart become short circuited due to the expansion of the resist, thereby rendering the device useless. The effect is prevented by spinning a thinner coating of resist onto the device and postbaking at 120°C for 30 minutes, and isolating the device from the mount with another coverslip. Care must be exercised as baking the resist above 120°C makes the resist very hard to remove with the normal acetone bath.

6.4 Measurement

The measurement of the CGCPS in its single crosspoint is hindered by the size of the lenses used. The measurement apparatus is shown in Figure 6.11, and illustrates that if the lenses that focus onto the two output facets are too close to the device they will collide. This is almost always a problem as the working distances of the ×20 and×40 lenses are 3mm and 0.75mm respectively. As the diameter of the objective is almost 20mm it is easily seen that the lenses will not be able to focus on both facets at the same time. The use of ×10 lenses, with working distances of 7 or 13mm, does allow a lens to focus on each of the facets, but at the reduction in magnification and signal strength. The signal strength

is reduced because the numerical aperture (N.A.) of the ×10 lenses is much lower (0.17 and 0.25) than those of the ×20 (N.A.=0.54) and ×40 (N.A.=0.64) lenses.

With the high losses and low numerical aperture lenses that are used, the resulting signal is too low to measure with a photodiode. Using the cameras as a measuring device is only valid if the same camera is used as each camera has different sensitivity, gamma factor and lag factor. (See Appendix 5 for details of these problems.) The most sensitive of the cameras has a dynamic range of only 12dB (noise floor to saturation with fan cooling) which also limits the measuring capabilities of this setup.

Fibre coupling of the outputs has been considered, but the signal strength would still be found to be very low for photodiode measurements, and the advantages of seeing the full near field pattern at the facet have highlighted other factors of the device that will be detailed in the next section. Fibre coupling will also suffer from misalignment problems, as the microscope magnification required to see the fibre accurately requires a large lens that will have a small working distance. Unless the launching lens is also replaced with a fibre, the microscope lens will not be able to get close enough to focus. If all three signal facets are fibre coupled this creates problems with alignment, which although possible, would be very difficult to set up without guaranteeing one of the connections by, for instance, pigtailing the fibre.

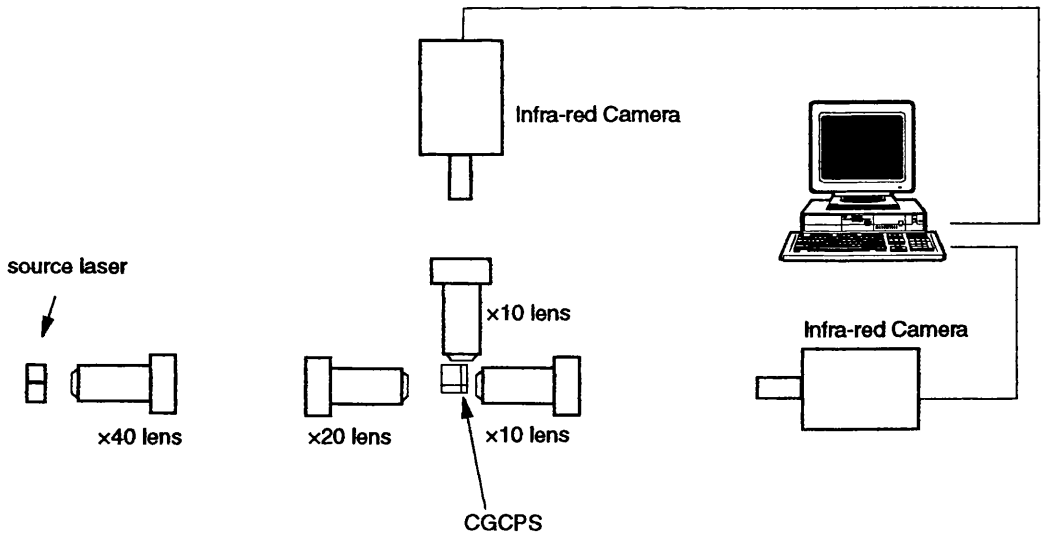

Figure 6.11. Schematic of measurement apparatus for CGCPS.

6.5 Results

CGCPS I did not give any output from either the through or cross facets and so was impossible to measure. CGCPS II, after a number of fabrication attempts gave outputs large enough to measure and exhibited switching, although, as already discussed at the beginning of the chapter, the performance would not lead to a realistic device with the material currently being used.

The outputs from a number of devices are shown below. Figure 6.12 shows the outputs from through and cross outputs for device A22-d1. Care must be taken in that the main guide appears on the left in the near field profiles.

The device in this case has been cleaved at the end of the coupler to assess the coupler performance, Figure 6.12c. Normally the tap guide would terminate here and any light remaining in the guide would be scattered into the wafer, while the main guide would continue to the next cross point element. It is interesting to note that in the cross output, Figure 6.12a, the residue of light in the tap guide can be seen. The amount of remaining light is small, but indicates that the tap guide has not been completely annihilated by the current injection. The intensity in the tap guide actually increases with injection, despite the fact that the amount of light being launched into the output coupler from the mirror is being reduced. This is indicative if the coupler being detuned rather than the coupled guide structure becoming single moded, as in the single moded case, which has been shown in Chapter 3, there should be more light in the main guide than the tap. Further injection would make the coupler single moded, but light output from the cross output in this case is so low, and close to the noise floor, that a conclusion could not be drawn.

The crossover of the cross and through outputs are shown in Figure 6.12b, and show that the through output reaches a peak at 90mA. The graphs are normalised as the power from the cross output is considerably less than that from the through facet.

The peak occurs at 90mA which is the same current found for the single coupler. In the CGCPS there are two couplers, which would imply that twice that current is needed for switching. In the single coupler, the power output also reduces above 100mA from free carrier absorption in the injected carriers. It was first thought that the injected current into this CGCPS was not evenly distributed between the two couplers, with the current mainly entering the input coupler, and little current being supplied to the output coupler, but just enough to cause detuning of the device. The total output from the cross facet will go down whether the output coupler operates or not, as it is reduced by the first coupler.

Further thought concludes that both guides are detuning, but the signal launched into the output coupler from the mirror is launched into the weakened guide. From the mode shapes of Figure 3.8 it can be seen that the power will couple more into the second order mode as it is larger in the tap guide when the device is injected. This accounts for the increase in magnitude of the tap guide output. As the input coupler is detuning past the peak in through facet output, it gives more signal to the output tap guide. The power in the output coupler does increase, but it is launched mainly into the second order mode which is lossy, and as injection increases becomes more confined to the tap guide. Thus the output from the main guide continues to fall.

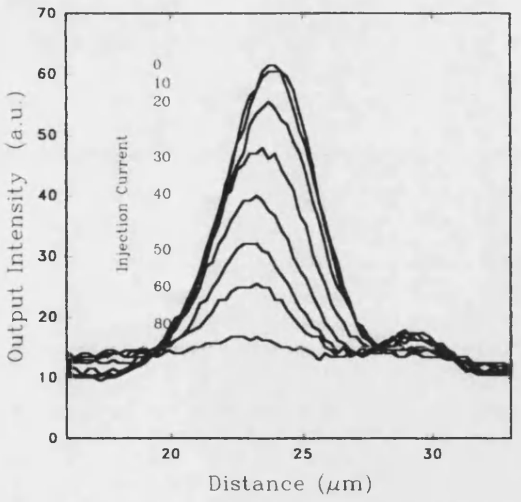

a) Near Field Pattern of Cross Output.

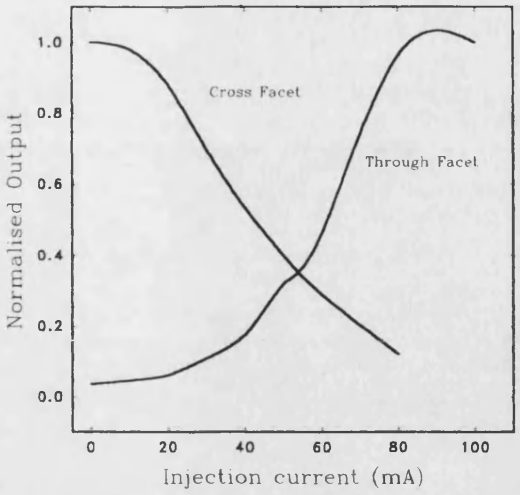

b) Normalised output of each facet

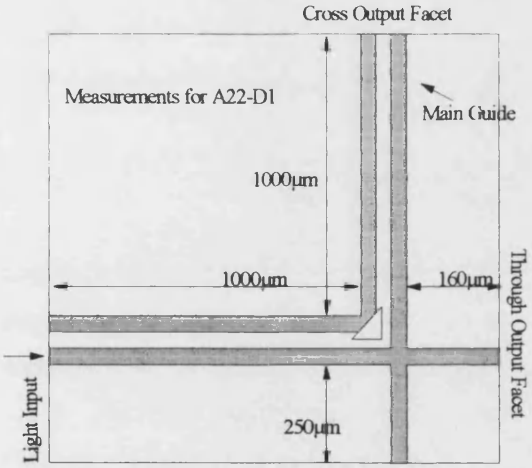

c) Schematic of device under test

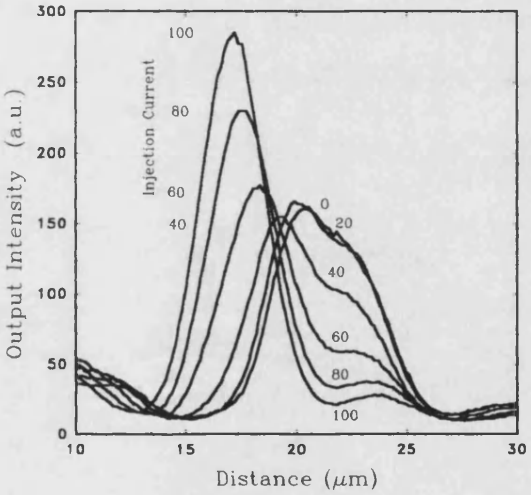

d) Near Field Patterns of Through Facet

Figure 6.12 Results from Device A22-d1.

The output of device A21-1, Figure 6.13 shows a similar result to that of Figure 6.12, but the current range has been increased. The graph clearly shows the output of the input coupler detuning and not becoming single moded. The output from the cross facet main guide shows the sharp falloff from the detuning, followed by the shallow reduction of output from the coupler structure becoming asymmetric.

Further injection of the devices fails to make the output from the through facet rise again as would be expected from the input coupler detuning, and the signal passing straight through. This is thought to be from the high injection of current making carriers diffuse into the main guide region of the input coupler, and increasing the propagation loss of the device. The output of the cross facet does not rise as the through facet output falls (injection current >100mA). The continued reduction in output with increased injection is because the light reflected from the mirror will be entering the injected tap guide, where

the free carrier absorption together with the effects of asymmetry discussed in Section 6.1 will reduce the cross facet output.

Although the operation of this device is not satisfactory, it does demonstrate the robust operation of the cross facet output.

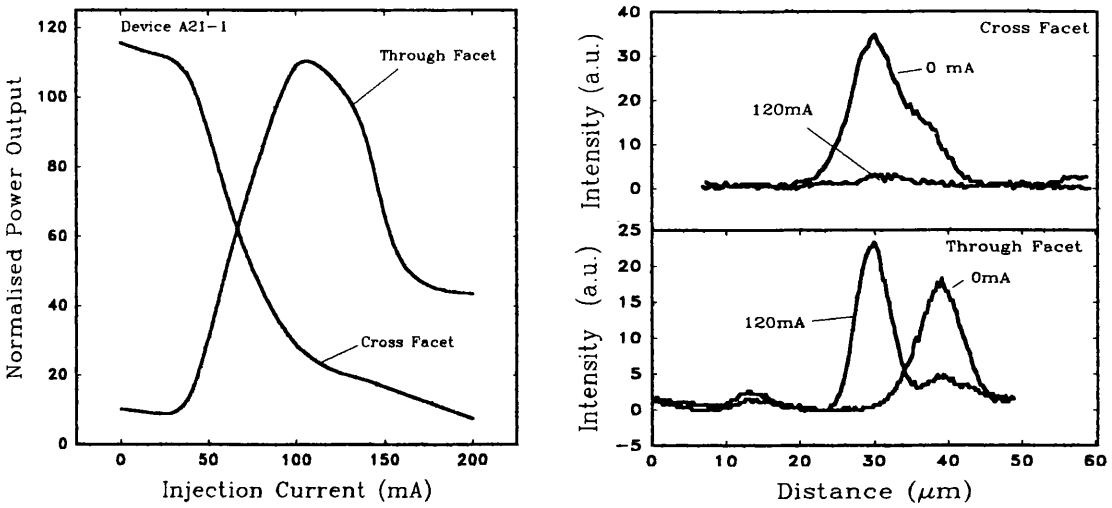

Figure 6.13 Results from device A21-1.

The output response of the switch to injection is almost flat for low injection currents. This can be explained by the non-linear change of index with carrier density proposed by Bennet *et al.*[1] which shows that there is little reduction of index until a carrier concentration of 10^{17} cm^{-3} is reached.

All the results from the through facet have shown an anomalous spot of light to the right of the main guide output. This is light that has not been reflected by the mirror, and has continued on to the through facet. This light, in a matrix of switches, would either scatter, or couple back into the main guide giving an increase in signal crosstalk. The near fields of Figure 6.14 clearly show a dip in the anomalous light where the mirror obstructs its path. This dip was originally thought to be the position of the mirror, but from the results of Chapter 5, it can be shown that an intensity peak can be found on the facet directly behind the mirror. The near field pattern on the facet behind the mirror, however, cannot be compared to those calculated in Chapter 5 due to the extra output guide interfering with the propagation of light from the back of the mirror.

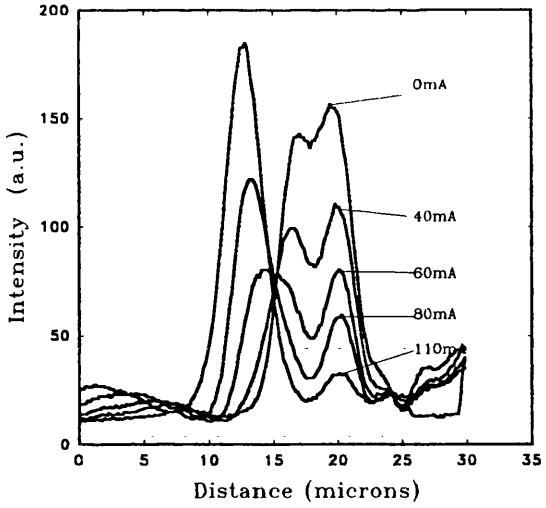

Figure 6.14 Near field pattern from through facet of A22-d3.

6.6 Conclusions

In addition to the conclusions drawn in Section 6.1.2, the device has been fabricated almost completely in-house, and demonstrated to operate. Fabrication difficulties have been overcome to produce a prototype device. The operation of the device can be explained by detuning of the couplers and eventual wipe out of the tap guides, and the devices are found to be consistent in their operation.

The cross facet output has been demonstrated to be robust in operation in that the signal always decreases with injection, unlike the through facet output.

Losses are, as expected, high in the material used for these devices and will be reduced by the use of material designed in Chapter 4.

The small size of the mirror introduces a problem that has to be removed in order to preserve the separation of signals. Larger mirrors and better alignment have to be investigated, and are discussed in Chapter 7.

Reference

[1] B.R. Bennet, R.A. Soref, J.A. del Alamo. "Carrier induced change in refractive index of InP, GaAs and InGaAsP." IEEE Journal of Quantum Electronics, Vol. 26, No.1, pp113-122. January 1990.

Chapter 7

Fabrication Improvements

The previous chapter showed that the problems associated with the design and fabrication of the CGCPS were in the mirror size, and the signal separation between the two outputs being affected by the coupler design and the guide loss. This chapter presents improvements on the design and fabrication route, giving means by which the mirror size and signal separation can be improved. Experimental results from devices fabricated in the low loss material designed in Chapter 4 show that the design improvements have been most worthwhile.

7.1 Fabrication Route

The order of fabrication for the design of CGCPS II (Chapter 6) permitted the mirror to be fabricated first and other steps made afterwards with the facet having been protected. This, in hindsight, was felt to be inefficient in two ways. Firstly, as the mirror etching is the most time consuming, but reliable step, and the process steps after the mirror fabrication are liable to error, it is more productive to carry out the lower yield steps first, and leave the mirror until as late in the process as possible. Secondly, the design of the masks, and the protection required for the mirror resulted in a smaller than ideally desired mirror being made. It was decided, therefore, that the self aligned mirror method would be used.[1] This would not only give the preferred order of fabrication, but also provide better alignment and a slightly larger mirror, with a side length of 6μm (shown in Figure 7.1), compared to the 4μm of CGCPS II.

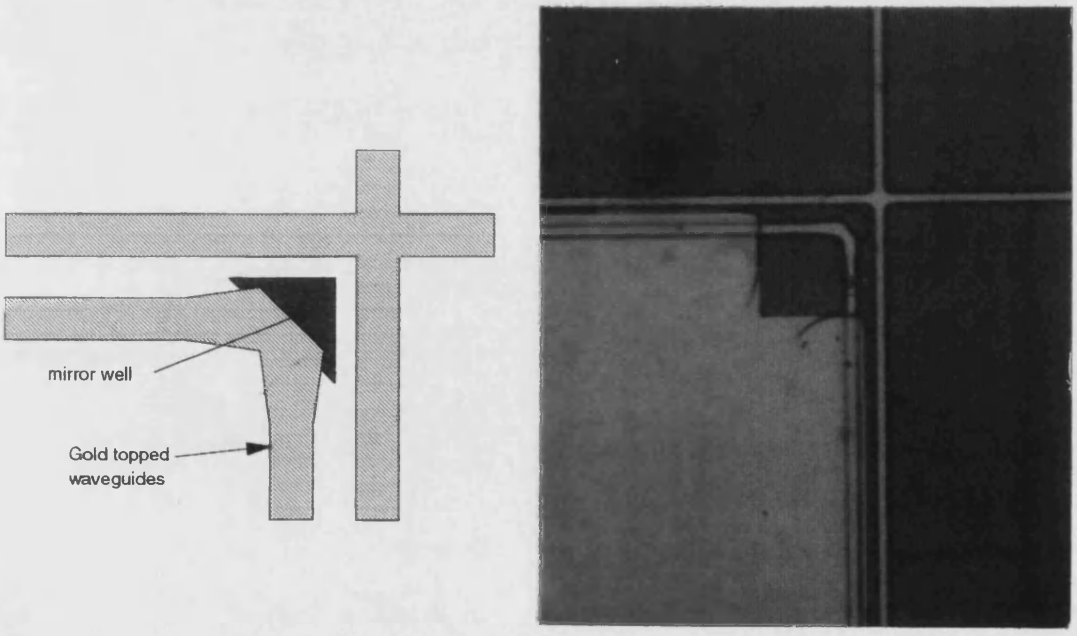

Figure 7.1. Schematic of CGCPS III layout with photograph of fabricated device.

The order of the new fabrication route is given in Appendix 4. The mirror facet edge is now defined by the gold top of the guide. The guide mask that defines this does not suffer from the round-off effects of hard postbaking, or the discharge problems of large areas of resist mentioned in Chapter 6. The facet is, however, defined by a gold edge that has been ion beam etched, and so will suffer from some edge roughness. The other sides of the mirror well are defined by the silica layer, and the edge roughness of these sides is not important.

Figure 7.1 also shows the increase in width of the tap guides as they approach the mirror. This increase in width is to increase the amount of modal power confined in the (rib loaded) core region of the guide, such that a larger amount of power is incident on, and reflected by, the mirror.

7.2 Larger Mirrors

One of the main problems seen from the results of CGCPS II is the amount of light that can go around the mirror and appear at the through facet. Ideally, a total reflection of the signal would be desirable. This is clearly seen in Figures 6.12 to 6.14. Chapter 5 has shown that some of this 'leakage' around the mirror is due to misalignment, but a significant amount is due to the mirror not being large enough to extend across the full mode shape, and some of the evanescent field not being reflected. The fabrication changes detailed in Section 7.1 should help improve the alignment and size of the mirror but the limiting factor on the size is the adjacent 'main' guides that obstruct any larger mirrors. Other methods are available for improving the reflector performance and they are illustrated in Figure 7.2.

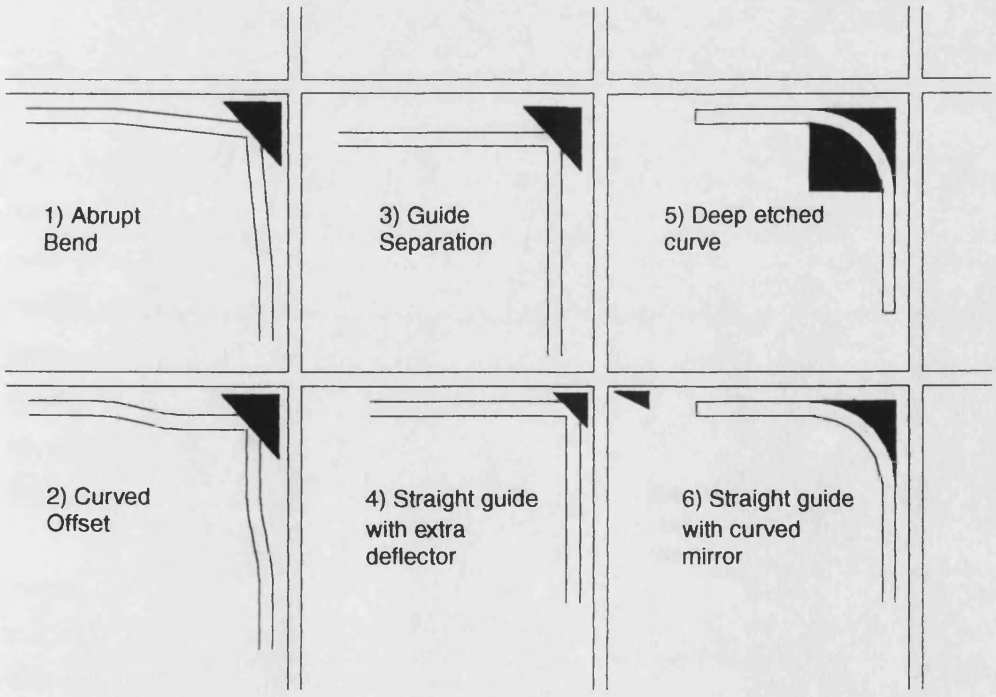

Figure 7.2. Methods for improved light reflection.

Options 5 and 6 offer a deeply etched curve and a curved mirror. The deep etched curve enables a sharp bend to be made, and this type of structure can be very low loss, 0.5dB for a 30μm radius has been reported[2]. The curved mirror offers the possibility of using whispering gallery modes, but coupling into these modes and their associated losses requires very accurate fabricational tolerances and alignment.[3] The disadvantage of these methods is that they require deep etching close to the main guide over a long distance (>30μm) whereas the first three options give the possibility of moving the mirror away from the main guides. The deep etch will make the main guide very asymmetric, and may even result in a cutoff condition for the propagating mode. If another etch is made, to make the main guide symmetric, the guide will become multimoded leading to potential problems with losses from the higher order modes. In addition, the curved guide structures only increase the 'capture area' of the light from the tap guide on one side of the guide, and leave the evanescent tails of the mode shape to travel past the curve. The options of deeply etched, curved guide structures have therefore been discarded for the present. Option 4 of Figure 7.2 is also discarded due to its inefficiency. Although the stray light is deflected away from the through guide by an extra mirror, it does not allow any improvement in the collection of the signal and so there is an undesirable loss in signal power. The deflection of the stray light can also affect other outputs depending on which direction it is sent, and so the method is not thought to be suitable. Changing the extra mirror for an absorbing region has also been considered, but again, the stray signal power is lost, so the technique inefficient.

The options of widening the gap between the tap and main guide to allow a larger mirror to be fabricated take three forms which are discussed below.

7.2.1 Guide Separation

For all the designs made so far, the guide width and separation have been 3μm. The reasons for this were detailed in Chapter 3, and were mainly for reasons of ease of fabrication and minimising coupling length. Increasing the separation between the tap and main guide along the whole length of the coupler will allow space for a larger mirror to be etched at the crosspoint, but will drastically increase the coupling length. Separation of the guides is also advantageous as it increases the on-off ratio for the output main guide. It was mentioned in Chapter 6 that for the through output guide without the mirror in place the on-off ratio would be 8.5dB. Figure 7.3 shows the effect of increased separation on both the on-off ratio and the increase in coupling length.

Clearly from Figure 7.3 it can be seen that increasing the guide separation will benefit the device by increasing the signal dynamics, and will allow a larger mirror to be placed between the guides to collect more light from the tap guide. However, the increase in coupling length is felt to be too great to be useable with the currently available materials

that exhibit high losses. The above method could be used in future devices which would use low loss material.

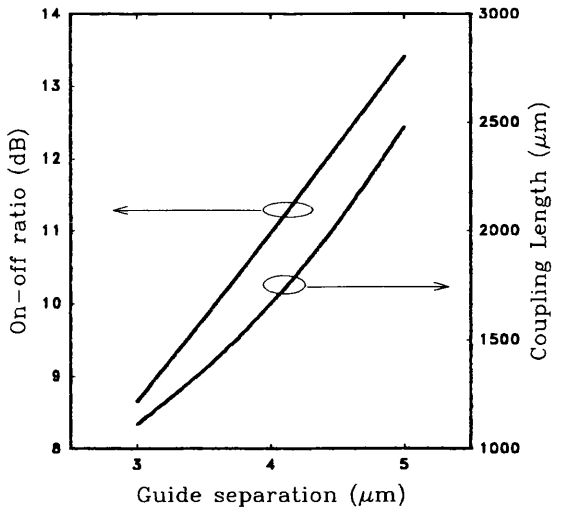

Figure 7.3. On-off and coupling length for two 3μm guides with varying separation.

7.2.2 Curves and Bends

Figure 7.2 options 1 and 2 show configurations of guide layout that allow for a larger mirror to be made within the device, while keeping the coupler sections the same. Both options show a change in the direction of the guide to allow for the larger reflector, but differ in that one uses a curved guide and the other an abrupt bend. The following sections discuss the relative merits of the two methods.

From the results of the measurements of trial mirrors presented in Chapter 5, it has been seen that an appreciable amount of light is allowed to pass the mirror when it is 3μm wide, but the 9μm mirror does not let any discernible light through. The aim is, therefore, to offset the guides so as to fit a 9μm mirror at the corner. This requires a guide offset of 3μm from the original position which is the specification used for the following analysis.

7.2.2.1 Curves

Using a simple analysis of the curved guide[4] the phase front of the guided mode travels at a constant angular velocity around the bend, and the velocity in the centre of the guide is assumed to be that of the straight guide. The power lost due to the curve can be attributed to the part of the mode tail on the outside of the curve which travels faster than a plane wave would in that medium, Figure 7.4. The power is assumed to be lost over a specific length. This length is determined by evaluating the plane wave spectrum (PWS) of the portion of the mode which is lost. The propagation length over which the power is lost is the distance the angular spread of plane waves takes to fill the initial aperture. For the

evanescent tail the aperture is taken as the reciprocal of the exponential decay constant, 1/p.

This method is only valid for very large radius bends, as it assumes that the mode profile remains unchanged, and the propagation constant β is unaffected by the curve. In practice, the peak of the mode profile shifts toward the outside of the curve, giving an increase in the scattering loss from the etched rib wall.[5]

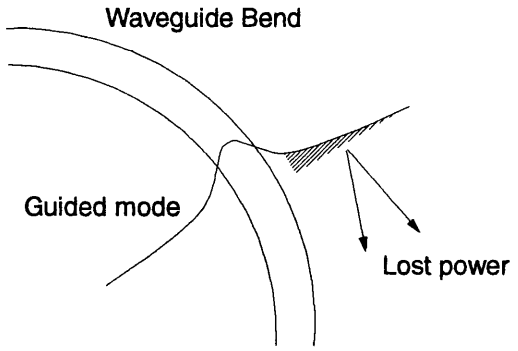

Figure 7.4. Schematic of curvature losses.

Following the calculation procedure described above, the power loss from a waveguide bend is:-

$$P_{lost} = \left(A\cos(hb)e^{-p(x_r-b)}\right)^2 p/k_1 \ \mu m^{-1} \qquad [7.1]$$

$$A^2 = 1/\left(b + \frac{\sin(2bh)}{2h} + \frac{\cos^2(hb)}{p}\right) \qquad [7.2]$$

x_r is the critical radius at which the phase velocity of the mode reaches the plane wave velocity in the medium, k_1.

$$x_r = \frac{(\beta - k_1)R}{k_1} \qquad [7.3]$$

where R is the radius of curvature, k_1 is the plane wave propagation constant of the outer cladding region and β the propagation constant of the mode in a straight guide. b,h and p have been defined in Appendix 1.

From this analysis the curved guide is found to be very lossy for the range of etch depths possible for single moded guide. The method of evaluation used here will underestimate the losses because of the aforementioned shift of the mode shape, therefore it is not considered to be worth pursuing the option of curving the waveguide with the normal single mode dimensions.

Increasing the etch depth around the guide rib increases the guide strength (normalised frequency) and has a large effect on the bending loss as shown in Figure 7.5. The loss shown here takes into account the length of the bends required to get the 3μm offset of guide. A depth of 0.4μm gives a very good result of less than 0.2dB for all radii. The length is also shown to illustrate the dominance of the radius of curvature, as the total

attenuation decreases despite the increase in length of the curved section of guide. The losses shown are excess losses, i.e. over and above those for the straight guide, and so these must also be taken into consideration for the overall design. This analysis is very simple, however, and does not consider any change in the field shape or further coupling between the two guides in the curved region.

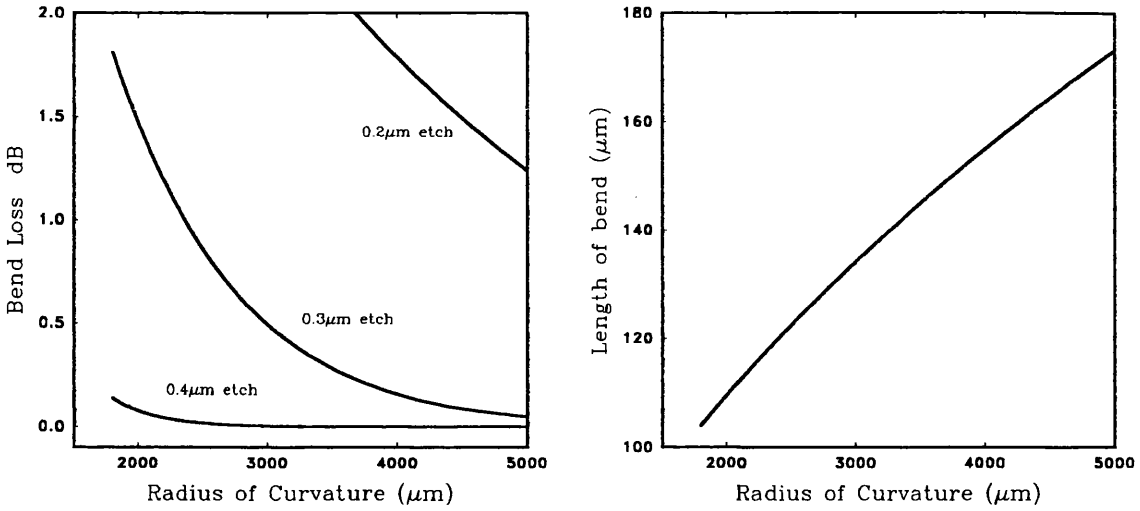

Figure 7.5. Graphs of curve loss and bend length for 3μm offset in CB536.

7.2.2.2 Abrupt Bends

The analysis of bends is done in the same way as the analysis of mirrors in Chapter 5. The guides are assumed to terminate at the intersection of the bend and the mode shape incident on the end of the guide decomposed into plane waves. The resultant field shape that appears at the end of the oblique guide is coupled into the guided mode, and the resulting reduction in amplitude is taken to be the bending loss.

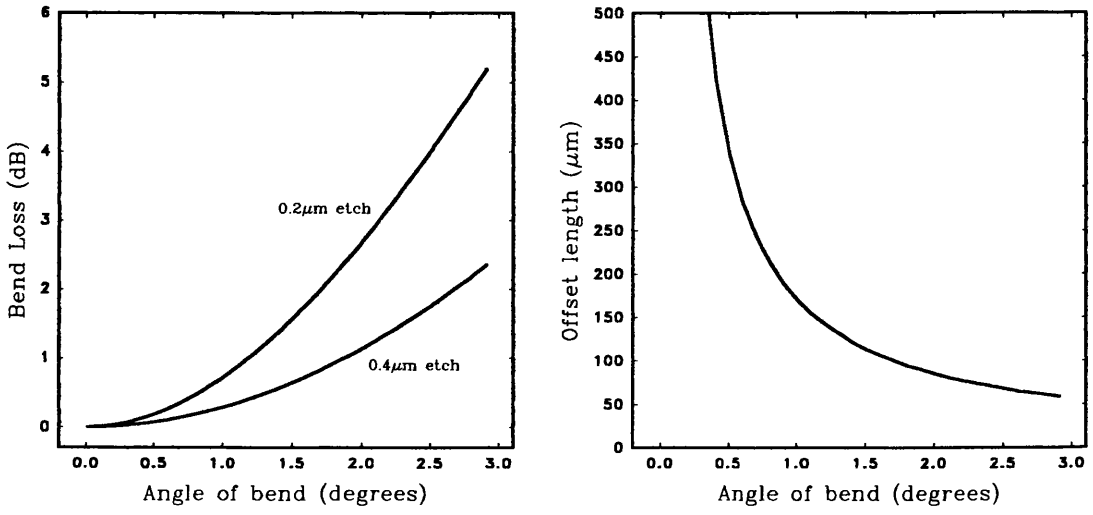

Figure 7.6. Graphs of bend loss and angled guide length for an abrupt bend giving 3μm offset.

Unlike the curvature loss shown above, the bending loss occurs at a single point and is independent of the length of the oblique guide. The losses calculated are shown in Figure 7.6 and are higher than those of the curved guide for the same length of oblique guide. The abrupt bend has, therefore, not been used.

It can be seen from Figures 7.5 and 7.6, that using the curved guides is the preferred option for improving the CGCPS structure, but it does require extra etch depth over the curved waveguide region only, in order to create a guide with sufficiently low loss.

The designs for increasing the mirror size by separating the main and tap guides, and for moving the mirror away from the main guide have been carried out as far as making masks for the fabrication, but they have not been implemented in the semiconductor material as yet.

7.3 CGCPS III

7.3.1 Results from devices fabricated in material QT788

The new mask design shown in Figure 7.1 was used to fabricate devices in the semiconductor material designed in Chapter 4. Since, in this material, the change in waveguide coupling is due to thermal effects the device performance results were not expected to be outstanding. However, they do serve to show that the improvements have been effective in the better capture of light, giving better isolation for the through output.

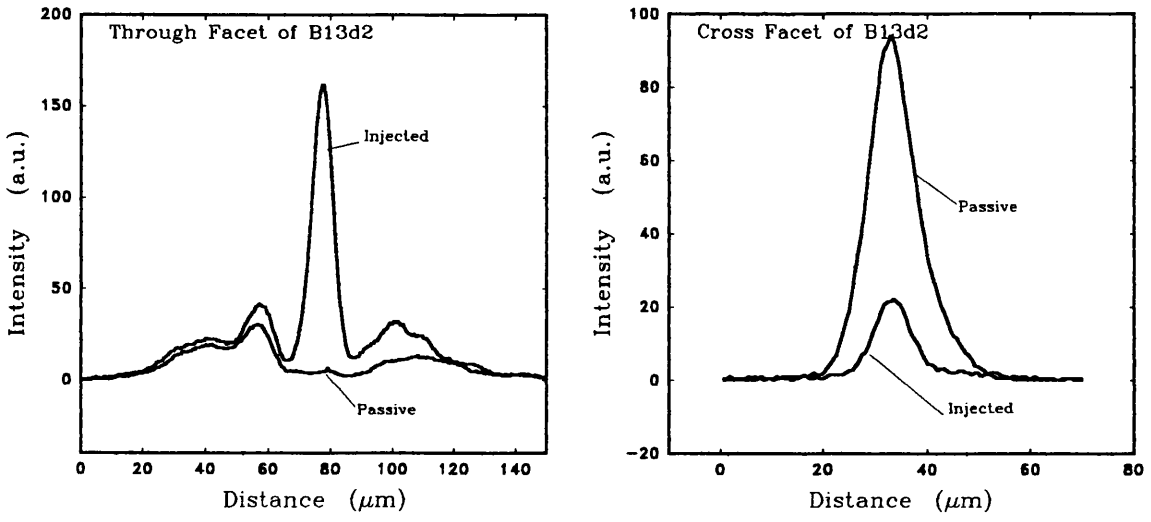

Figure 7.7. Near field pattern of through and cross facets of CGCPS. Injection current is 100mA.

Figure 7.7 shows the near field patterns from the through and cross facets of a device fabricated from the new material. Clearly, a much improved pattern from the

through output has been achieved. The through facet in the passive state has a very good off condition compared to the device measurements given in Chapter 6. In the injected state the output of the through facet rises markedly, the residual scatter being due to the launching of light into the input. Using only the mode in the guide, and ignoring the scatter, the on-off ratio is over 15dB, which is as expected from the theoretical predictions. Higher values cannot be measured with the IR camera as this is approaching its dynamic range. Appendix 5.

These results show that the improvement from the slight increase in mirror size and greater alignment are good enough so that the designs for moving the mirror further away from the crosspoint do not yet have to be implemented.

The cross facet results are not as good, but as the couplers are not being turned off, but only detuned, this is to be expected. An on-off ratio of 6.7dB is, however, still achieved.

The scatter present in the near field pattern of the through facet output makes the signal difficult to measure with the wide aperture power meter. Powers of 600nW and 10nW have been measured, however, from the through and cross outputs respectively, illustrating that the new material has significantly lower loss, enabling quantitative measurements to be taken. The power figures quoted above appear orders of magnitude apart, and even accounting for high mirror loss (10dB) and disparate lengths of waveguide to the two outputs, the cross output power still appears very low. The reason for this discrepancy is that the lenses through which they have been measured were of different Numerical Aperture and Working Distance for each output, and thus will have different efficiencies.

The faults in the semiconductor material have resulted in a device switching speed in the range of micro seconds, rather than the nanoseconds hoped for. The reasons for this slow response have been explained in Chapter 4. The results do, however, confirm that the increased mirror size has improved the output at the through facet, and the low loss material gives an output that can be easily measured.

The mirror still suffers from a high loss, (10dB) but this is expected from the results of Chapter 5.

7.3.2 Results from devices fabricated in material QT825

With the excellent results of the couplers in material QT825 shown in Chapter 4, it was expected that good devices could be made from this wafer. However, the ohmic contact to this wafer proved to be variable, and of 30 devices fabricated, only one crosspoint was found to be fully operational, with the switching occurring due to carrier injection, and not due to heating.

Figure 7.8 shows the near field outputs from this device, and are in contrast to those of Figure 7.7 in that the cross output has the better performance.

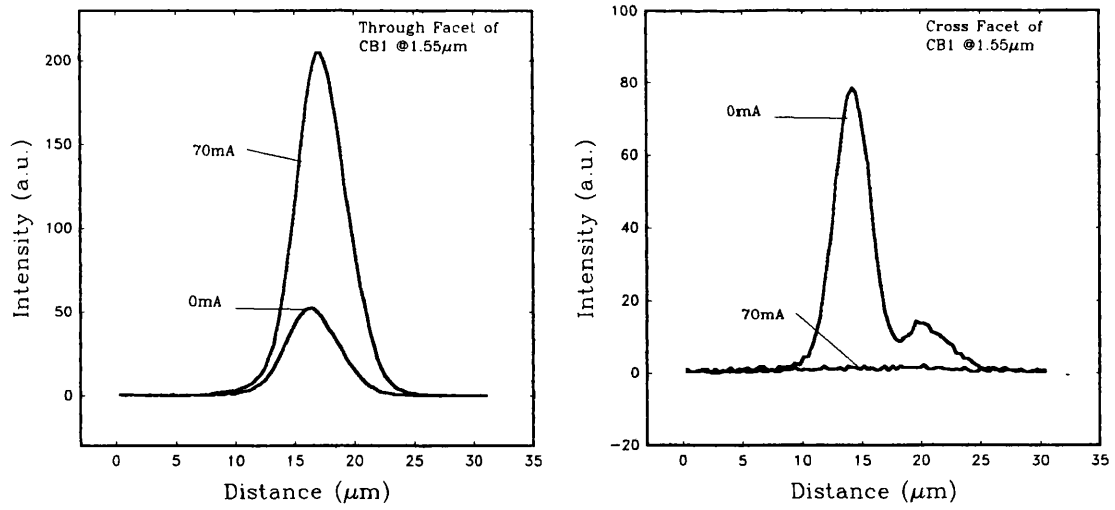

Figure 7.8. Near field profiles from device CB3. Material QT825.

The cross output from the above device has excellent on-off performance, as predicted when the couplers are being properly turned off. The device is cleaved close to the end of the cross output coupler, and in the passive state, the coupling can be seen to be incomplete. This is due to the device being on the edge of the sample, and the etch depths not being as accurate as in other regions. It is difficult to get a uniform etch over the whole sample as the ion gun used to fabricate the devices has an active beam-width of less than 5mm across, and the sample is 8×10mm. Despite constant rotation of the device whilst etching, it is difficult to achieve a uniform etch depth.

In the active (injected) state the output from the cross facet is well below the noise floor of the camera, and cannot be reliably measured, but it gives a good indication that the on-off ratio is approaching the 15dB dynamic range of the camera.

The output from the through facet has a lower dynamic range, as the coupling is not as well tailored as it could be. The output variation will be suppressed, since, in the injected state, the single mode coupler will guide the power past the mirror. In the passive state, the two moded coupler couples most of the power across to the mirror, but leaves a small amount to propagate to the through facet output, thereby giving an output intensity in the off condition, degrading the on-off ratio. This explanation is supported by the cross facet output showing that the coupling is not complete in the passive case either. An on-off ratio in excess of 6dB is seen in the through output despite the fabrication errors in the device. This proves that switching can be demonstrated even with the etch depth (hence coupling length) so far out of specification. As with the QT788 device, the slightly larger size of mirror has proved to be adequate to give a clean output at the through facet and to collect the light more efficiently.

The results of the individual couplers in this material (Chapter 4) show that the couplers require much less current to switch compared to those in the original (CB536)

material. The lower current needed to activate the switch has increased the on-off ratio, by not requiring as many carriers in the active layer for the coupler to change state. The lower carrier density for switching entails that the losses will not be much increased due to the carriers in the guide. From the results of Chapter 6, it is seen that the output from the through facet decreased with injection above 120mA, which is a similar current to that needed to get the device to operate fully. The same is true for this material, in that the output from the through facet decreases after 120mA, but this is much larger than the 70mA at which the device is fully switched across, hence any considerable carrier induced loss is avoided at the operating point.

The reduction of the injected current also serves to reduce the amount of spontaneous emission that is generated. This is highly advantageous as the filtering requirements to remove the spontaneous output can now be relaxed as the majority of the unwanted light will be absorbed by the material.

7.4 Architecture

As this chapter deals with improvements to the design of the CGCPS, it is felt that this is an appropriate place to discuss a new architecture for the switching array. So far the device that has been examined has had the tap guides that form the switching mechanism on the 'inside' of the corner of the intersection of two main guides, as in Figure 1.9. The structure illustrated has both main guide and tap guide etched into the material, so that in the passive, uninjected case, the signal can pass around the corner to the cross output. If the whole matrix is considered, however, it is clear that in the passive state, the matrix will block any signals that pass through more than the first switch element that they encounter, as the couplers will direct the signal power into a tap guide which terminates, and this is illustrated in Figure 7.9.

The array of switches shown in Figure 7.9 shows that without injection to the other cells there would be only one switch cell operating as it should. Not only does this require the majority of cells to be energised, requiring a relatively large amount of power, but this design can be considered as not being 'fail-safe' in that without injected current, only one signal (if it were to exist) would be able to pass through the array.

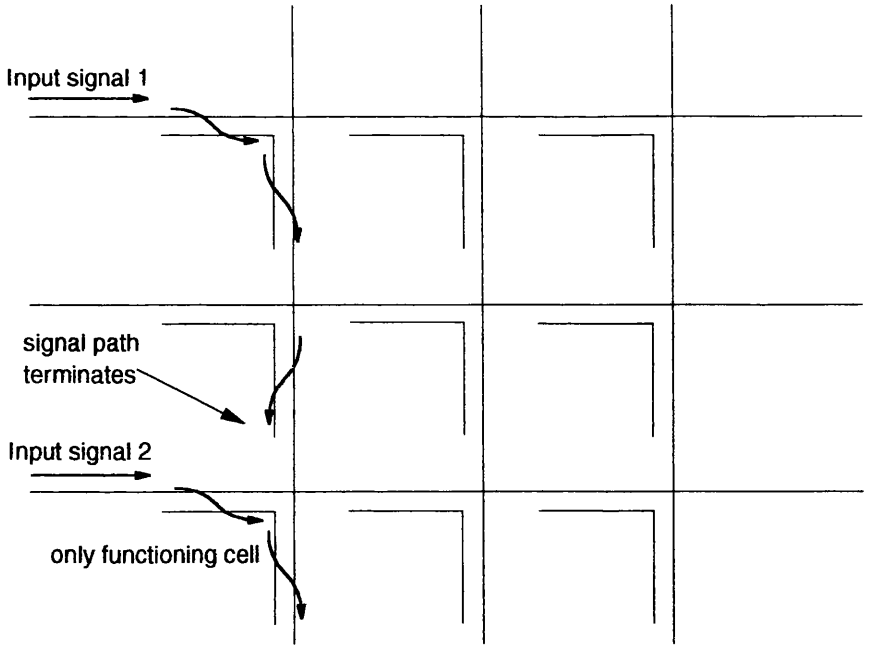

Figure 7.9. Signal routing for uninjected case.

There are two methods by which these problems can be solved. The first is to use the variable couplers in a detuning mode, such that they would normally not couple light into the tap guide, and would couple light across when retuned. The second is to arrange the device such that the existing carrier injected variable couplers, with their proven performance, are reversed, as shown in Figure 7.10.

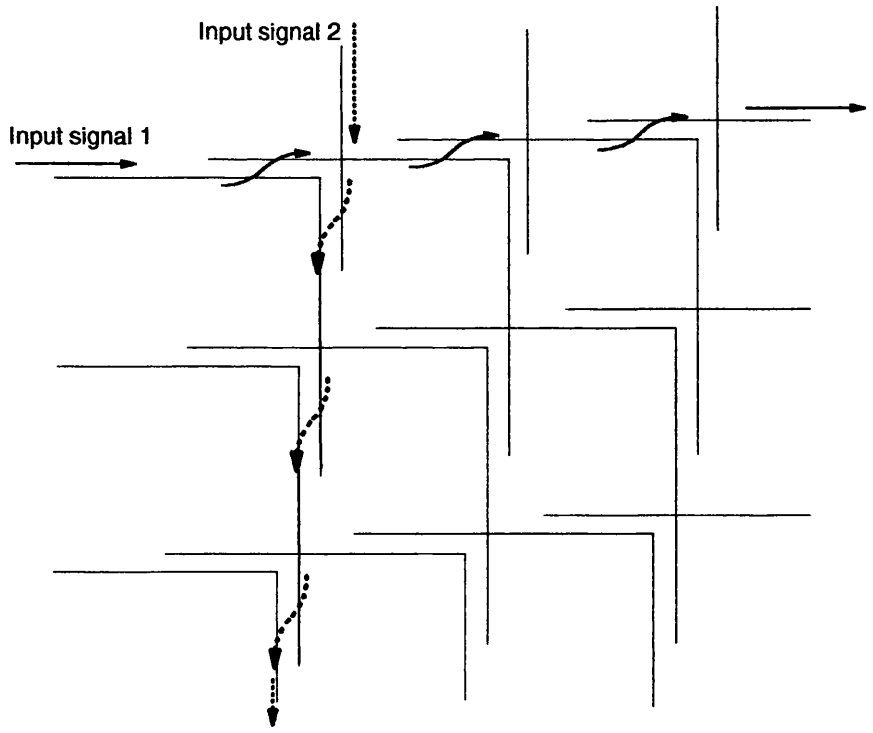

Figure 7.10. Signal routing in new architecture with no injection.

With the architecture of Figure 7.10, it is possible for a signal to pass through the array when none of the couplers are injected, thus giving a non-blocking operation in the passive state. In order for the device to switch, in this case, it would be the outer guides that are injected to allow the signal to be routed through 90°. This design retains the advantages of the injected variable couplers in that the signal always passes through an un-injected, and thus lower loss, guide, and with the array as a whole requiring less injection of carriers, the signal must suffer less loss overall. Similarly, the design does not remove the need for larger mirrors discussed in Section 7.2, but the methods put forward for implementing larger mirrors are equally applicable to this new architecture.

7.5 Conclusions

This chapter has shown that the improvements in the mask designs employing the self aligned process for the fabrication of the mirror well have been successful in giving a clean output at the through facet, and in doing so, collecting more light for reflection into the cross output.

Devices made from the initial low loss material (QT788) have been demonstrated to operate well and to give the expected results despite the switching being due to thermal effects and not from plasma effect on refractive index. This undesired means of thermally increasing the refractive index of the device serves to show that the design of the switch is capable of operating by detuning the couplers. Although this is not the required mode of operation, detuning of the directional coupler could be applied to the general concept of this type of switch in future applications and, where speed is more important, faster detuning methods are available.

The second low loss material (QT825) has demonstrated that the device can be made successfully with injected carriers locally reducing the index of the material, but the problems with ohmic contacts still persist, even if only in patches across the wafer. This is a fairly straightforward difficulty resulting from the semiconductor material deficiency which can be readily overcome, and work continues on this problem.

A new architecture has been suggested to make the device more attractive as a commercial device, in that it has lower power consumption, and a non-blocking operation. It does, however, share the design problems described in this thesis, and therefore does not detract from the work undertaken.

References

[1] H. Appleman, J. Levy, M. Pion, D. Krebbs, C. Harding, M. Zediker. "Self aligned CAIBE GaAs/AlGaAs turning mirrors for photonic applications." Journal of Lightwave Technology, Vol. 8, No. 1, pp39-41. January 1990.

[2] L.H. Spiekman, Y.S. Oei, E.G. Metaal, M.K. Smit. "Ultrasmall waveguide bends: the corner mirrors of the future." IEE Proceedings Pt J, Vol 142, No. 1, pp61-65. February 1995.

[3] J.P. Braud. "Whispering Gallery Mirrors: Fabrication tolerances and the effects of surface imperfections." Applied Optics, Vol. 31, No. 24, pp4979-1986. August 1992

[4] D.L. Lee "Electromagnetic Principles of Integrated Optics" Wiley, p135. 1986.

[5] S.J. Garth. "Modes on a bent optical waveguide." IEE Proceedings pt J, Vol. 134, No. 4, pp221-229. August 1987.

Chapter 8

Conclusions and Further Work

8.1 Conclusions

A design of semiconductor optical switch has been systematically analysed by taking each component part in order to optimise its performance when standing alone and also in conjunction with the other elements of the switching system. Devices and components have been fabricated in different materials and their performance analysed. New designs for the fabrication technique and device layout have been explored, and shown to give good improvement to the device performance.

Effects of fabrication processes on the device component parts have been analysed both experimentally and theoretically to reveal the changes in guiding parameters, such as loss and mode shape, from fabrication methods causing lattice damage and edge roughness to the guides. Fabrication tolerance has also been studied and the devices have been designed to minimise the influence of fabrication error on their performance.

Effects of material properties have also been studied, and the trade-offs between losses and functionality have been described. Methods for reducing the influence of fabrication properties have been discussed and a new material has been designed, taking into account these effects, and minimising their influence, resulting in a low propagation loss while still retaining the ability to act as a p-n junction for injection of carriers. The same material has also been designed to be optimised for the fabrication of carrier injection into electrically variable couplers, and material parameters have been modelled to show their effect on the coupling length and the sensitivity of the coupled power to tolerances in fabrication for different material designs. Compromises over coupling length and guiding loss from a number of sources have had to be made in the design of material.

Measurements of coupler performance with carrier injection have been made and theoretical models have been used to measure the diffusion of carriers in the active layer, and give a better understanding of the mechanism of coupler variation. Thermal effects have also been detected and models used to explain the unwanted method of thermal detuning of the coupler. The speed of the thermal detuning method of switching is 1000× slower than the carrier injection method, which would not make it fast enough for fast data routing, but could be applied to semi-permanent routing applications such as redundancy and backup selection. The carrier injection switching time has been measured to less than 10ns which is applicable to the lower standards of data routing.

The methods of turning the guide through 90° have been analysed and the mirror facet chosen as the best solution. Analysis of both infinite and finite reflecting facets has shown the limitations of a perfectly smooth mirror, and the effect of misalignment on the

amount of light that is not reflected. Experimental measurements have illustrated that the fabrication method of the mirror is important to its functionality from the roughness it leaves on the facet surface. The self aligned method for fabricating mirrors in the correct position has shown improvement over the older method of manual alignment, but the analysis has shown that larger mirrors are still required for optimised performance.

A number of complete devices have been fabricated, and have shown excellent results in proving the concept of the device. The new lower loss material has proven variable in its contact resistance, leading to only one working active device in this material.

8.2 Further Work

The work carried out so far has demonstrated a fully functional cross point device in a new material with reduced propagation losses. The analyses and experimental results show, however, that further improvements can be made to the design of the switch to reduce losses and signal crosstalk.

Chapter 7 shows a number of methods for increasing the mirror size, and their analyses suggest that there has to be a compromise between guide separation, to allow a larger mirror, and the coupling length. Alternative solutions of introducing curves and abrupt bends into the waveguides, allowing a larger mirror to be incorporated, have been shown to have inherent losses and are, therfore, not ideal solutions. Trial designs for these options have been made as masks, and fabrication and test still need to be carried out to verify the theoretical predictions.

The fabrication of a device array has also to be demonstrated. Variation in contact resistance over the area of the wafer has proved to be a problem at present, but once this has been resolved, a CGCPS array should be easily fabricated. The addition of extra GaAs capping to the QT826 material appears to have resolved the contact problem, and new devices will be made from the regrown wafer.

Other architectures could also be explored. The current CGCPS arrangement will block the signal in an array if the crosspoints are not energised, which is not a fail-safe mode of operation. Chapter 7 outlines a slight change to the architecture to make the CGCPS array non-blocking, but the same compromises over material and mirror designs still exist in the new architecture.

Appendix 1. Guiding

The purpose of this appendix is to set out the background theory for analysis of waveguiding in the structures under study, and to define the notation that is used throughout the thesis.

Maxwell's Equations

Given that bold type represents vector quantities, Maxwell's equations for electromagnetic waves are:-

$$\nabla \times \mathbf{E}(x,y,z,t) = -\frac{\partial}{\partial t}\mathbf{B}(x,y,z,t) \qquad [A1.1]$$

$$\nabla \times \mathbf{H}(x,y,z,t) = \mathbf{J}(x,y,z,t) + \frac{\partial}{\partial t}\mathbf{D}(x,y,z,t) \qquad [A1.2]$$

$$\nabla \cdot \mathbf{D}(x,y,z,t) = \rho(x,y,z,t) \qquad [A1.3]$$

$$\nabla \cdot \mathbf{B}(x,y,z,t) = 0 \qquad [A1.4]$$

$$\mathbf{D}(x,y,z,t) = \varepsilon\mathbf{E}(x,y,z,t) + \mathbf{p}(x,y,z,t)$$
$$\mathbf{B}(x,y,z,t) = \mu\left(\mathbf{H}(x,y,z,t) + \mathbf{m}(x,y,z,t)\right) \qquad [A1.5]$$

where **E** and **H** are the electric field and magnetic field vectors, **D** and **B** are the electric and magnetic displacement vectors, **J** and ρ are the current and charge sources, and **p** and **m** are the electric and magnetic polarisation vectors of the material. ε is the dielectric constant of the material and μ the magnetic permeability. In the cases under study here, there is no magnetic material and so $\mu=\mu_o$. Also for the purposes of this thesis, in the region of interest, it is assumed that there is no net charge, thus $\rho=0$. **p** and **m** are considered static in time and space so their differentials do not contribute to the above equations. It is also generally accepted that the functions are time harmonic, i.e.

$$F(x,y,z,t) = f(x,y,z)\,\mathrm{Re}\left[e^{j\omega t}\right] \qquad [A1.6]$$

thus $\partial/\partial t$ can be replaced by $j\omega$. The time variation exponential is usually omitted in the notation, but always assumed present. If the current density is given by $\mathbf{J}=\sigma\mathbf{E}$, these conditions, when applied to Maxwell's equations give [A1.7] and [A1.8]. The conductivity σ is small and is usually neglected, but if included, contributes to a complex propagation constant, β, by representing the material loss through the complex dielectric constant ε' shown in [A1.8].

$$\nabla \times \mathbf{E}(x,y,z) = -j\omega\mu\mathbf{H}(x,y,z) \qquad [A1.7]$$

$$\nabla \times \mathbf{H}(x,y,z) = j\omega\varepsilon'\mathbf{E}(x,y,z) \qquad \text{where} \quad \varepsilon' = \varepsilon - j\frac{\sigma}{\omega} \qquad [A1.8]$$

The above can be rearranged to eliminate **H** and give the wave equation of

$$\nabla^2\mathbf{E}(x,y,z) + \omega^2\mu\varepsilon'\mathbf{E}(x,y,z) = 0 \qquad [A1.9]$$

Bound Modes of the Slab Guide

The slab guide depicted in Figure A1.1, is to be infinite and uniform in the y and z directions. The field excitation is such that f(x,y,z)=f(x,z), i.e. $\partial/\partial y=0$. Assuming for the cases here that the dielectric constant is real, expanding equations [A1.7] and [A1.8], it can be seen that the fields fall into two sets given by:-

$$\frac{\partial H_y}{\partial z} = -j\omega\varepsilon E_x \qquad \frac{\partial H_y}{\partial x} = j\omega\varepsilon E_z \qquad \frac{\partial E_z}{\partial x} - \frac{\partial E_x}{\partial z} = j\omega\mu H_y \qquad \text{[A1.10]}$$

$$\frac{\partial E_y}{\partial z} = j\omega\mu H_x \qquad \frac{\partial E_y}{\partial x} = -j\omega\mu H_z \qquad \frac{\partial H_x}{\partial z} - \frac{\partial H_z}{\partial x} = j\omega\varepsilon E_y \qquad \text{[A1.11]}$$

where each component of the **E** and **H** vectors is considered a function of x and z. The field quantities of equation [A1.10] contribute to the $(TM)_x$ mode, and those of [A1.11] are of the $(TE)_x$ mode.

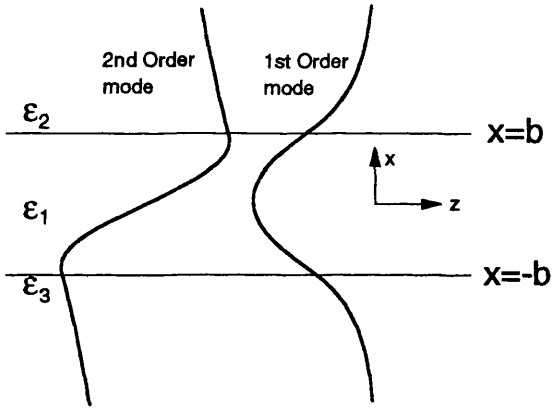

Figure A1.1 Slab Guide with the first symmetric and anti symmetric modes.

If it is further assumed that the fields travelling in the +z direction have a z dependence of exp(-jβz), then, as $\partial/\partial z=-j\beta$, the wave equation [A1.9] becomes the one dimensional equation:-

$$\frac{\partial^2 \mathbf{E}}{\partial x^2} + \left(\omega^2\mu\varepsilon - \beta^2\right)\mathbf{E} = 0 \qquad \frac{\partial^2 \mathbf{H}}{\partial x^2} + \left(\omega^2\mu\varepsilon - \beta^2\right)\mathbf{H} = 0 \qquad \text{[A1.12]}$$

For bound modes to be supported $\varepsilon_1 > \varepsilon_2, \varepsilon_3$, and the solution for the vector components of [A1.10] or [A1.11] takes the form:-

$$\mathbf{E}(x,z) = \begin{Bmatrix} B\exp(-p_2 x) \\ A\cos(hx) + C\sin(hx) \\ D\exp(p_3 x) \end{Bmatrix} e^{-j\beta z} \qquad \begin{matrix} x > b \\ -b < x < b \\ x < -b \end{matrix} \qquad \text{[A1.13]}$$

$$\text{with } h = \sqrt{k_o^2\varepsilon_1 - \beta^2}, \qquad p_{2,3} = \sqrt{\beta^2 - k_o^2\varepsilon_{2,3}} \qquad \text{[A1.14]}$$

$$k_o = \omega\sqrt{\varepsilon_o\mu_o} = \frac{2\pi}{\lambda_o} \qquad \lambda_o \text{ is the free space wavelength of the light}$$

Taking the four cases for the symmetric guide, where $\varepsilon_2 = \varepsilon_3$, and matching the components tangential to the boundary E_y, H_z, H_y, E_z the relations between p and h are:-

TE symmetric C=0	TE Antisymmetric A=0	TM symmetric C=0	TM Antisymmetric A=0
$h\tan(hb)=p$	$-h\cot(hb)=p$	$\frac{\varepsilon_2}{\varepsilon_1}h\tan(hb)=p$	$-\frac{\varepsilon_2}{\varepsilon_1}h\cot(hb)=p$

Table A1. [A1.15]

Defining w as the normalised frequency of the guide, where

$$w^2 = k_o^2 b^2(\varepsilon_1 - \varepsilon_2) = b^2\left(h^2 + p^2\right) \qquad [A1.16]$$

the quantities h, p, β can be found from [A1.15] and [A1.16]. The amplitude A, B, C and D have to be found by considering the power in the mode. It is common to normalise the amplitude such that

$$\int_{-\infty}^{\infty} E_y^2 dx = 1 \qquad [A1.17]$$

which gives for the symmetric mode,

$$A = \frac{1}{\sqrt{b + \frac{\sin(2hb)}{2h} + \frac{\cos^2(hb)}{p}}} \qquad [A1.18]$$

and $$B = \frac{A\cos(hb)}{e^{-pb}} \qquad [A1.20]$$

A plane wave travelling in a medium of refractive index n, has a phase velocity of $k_o n$. The mode in the slab guide has a phase velocity of β, and therefore an effective refractive index can be associated with the guide, given by:

$$n_{eff} = \beta / k_o \qquad [A1.21]$$

Bound Modes in Two Dimensions

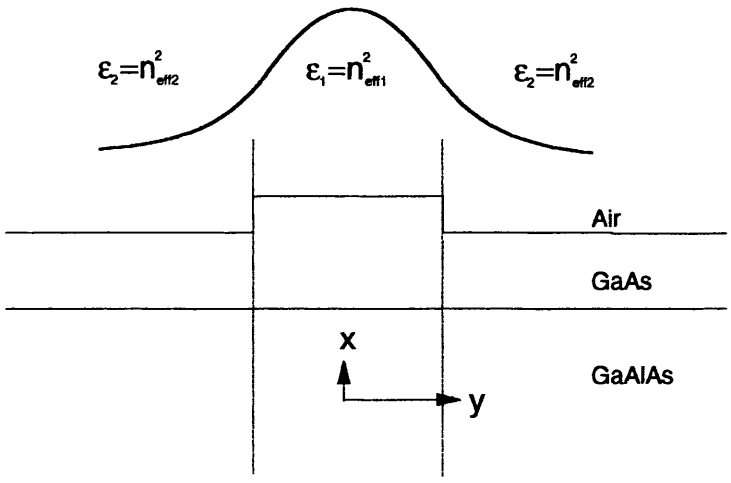

Figure A1.2 Lateral Bound Mode

In the derivation of the slab guiding formulae, the condition of $\partial/\partial y=0$ was used. To support two dimensional bound modes, there has to be a central region of high index, giving variation of the electric field in both x and y. The guides under study in this work generally have weak lateral guiding, so that although the condition of $\partial/\partial y=0$ given for the slab guide is not strictly held, it is very small compared to $\partial/\partial x$.

With this assumption it is possible to calculate the lateral mode shape using the same methods as the slab guide technique, by considering the guide to be an infinite slab in x, but with the effective indices of the vertical (x) slab guide as the refractive index of the layers in the y direction. Figure A1.2 However, if the vertical calculations have used the TE solutions to give a function in terms of E_y, then the lateral calculations take the TM mode solutions as the electric field component is now perpendicular to the guide boundaries.

Appendix 2. Transverse Resonance Method

The waveguides of Appendix 1 are of a simplified nature, consisting of three layers in each case, and symmetric in terms of the dielectric constants of the materials. More realistic structures rarely have this format, and consist of many layers of differing materials for which the condition for guiding cannot be found analytically. This appendix shows the method by which the mode shape and propagation constant, β, can be found for such guides.

The transverse resonance method uses the similarity between the transverse wave equation of [A1.12] and the wave equation of the transmission line to solve for the guiding condition. The assumptions used to derive [A1.12] still apply. By drawing the parallel between the voltage in a two conductor transmission line, with the electric field in a waveguide, and similarly for the current and the magnetic field, each layer of different dielectric constant, ε, can be represented by the equivalent transmission line matrix,

$$\begin{pmatrix} V_i \\ I_i \end{pmatrix} = \begin{pmatrix} \cos\theta & -jZ_i \sin\theta \\ -j\sin\theta / Z_i & \cos\theta \end{pmatrix} \begin{pmatrix} V_{i+1} \\ I_{i+1} \end{pmatrix} \qquad [A2.1]$$

where the electrical length θ of the 'i'th region of width d, is given by

$$\theta = d\sqrt{k_o^2 \varepsilon_i - \beta^2} \qquad [A2.2]$$

$$Z_i = \frac{1}{\sqrt{\varepsilon_i - \varepsilon_{eff}}} \text{ for TE} \qquad Z_i = \frac{\sqrt{\varepsilon_i - \varepsilon_{eff}}}{\varepsilon_i} \text{ for TM} \qquad [A2.3]$$

$$\beta^2 = k_o^2 \varepsilon_{eff} \qquad [A2.4]$$

The complete transverse structure, which can be many layers thick, can now be represented as one matrix, by multiplying all the individual layer matrices together. The matching of fields at each boundary is accounted for by the output of one matrix section always being the input for the next. The outer, infinitely thick, cladding layers are represented as a terminal impedances as shown in Figure A2.1.

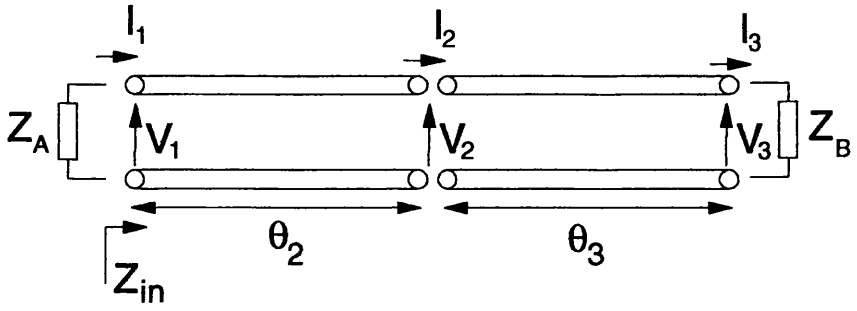

Figure A2.1. Two core layers represented as transmission lines, with outer cladding impedances.

With the whole transverse structure represented by one matrix of the form:

$$\begin{pmatrix} V_1 \\ I_1 \end{pmatrix} = \begin{pmatrix} A & B \\ C & D \end{pmatrix} \begin{pmatrix} V_2 \\ I_2 \end{pmatrix} \qquad [A2.5]$$

the resonant condition for the lateral guiding can be found by making the impedance at any point in the system be equal in either direction. In the case of figure A2.2,

$$Z_A = Z_{in} \qquad [A2.6]$$

which from equation A2.5 with the termination of Z_B gives the eigenvalue equation

$$Z_A = \left(\frac{AZ_B + B}{CZ_B + D} \right) \qquad [A2.7]$$

which is solved numerically to find ε_{eff}.

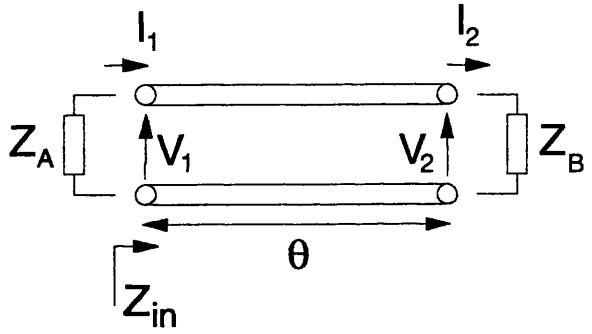

Figure A2.2 Waveguide layers represented by one transmission line terminated by outer cladding impedances.

If there is only one central region between identical cladding layers, and the matrix takes the form of equation [A2.1], then [A2.7] can be rearranged to give the solutions of Appendix 1.

This method for finding the value of β for each mode is used throughout the modelling of the waveguides in this thesis. It can be used successfully for over 300 layers of differing dielectric constants, in highly non-symmetric structures. Once the value of ε_{eff} has been found, it can be used in the layer matrices to find the value of the voltage (field) across the dielectric layer by varying the value of θ across each layer in turn.

Appendix 3. Effects on Refractive Index.

There are a number of physical processes by which optical routing can be achieved, but they all involve a change in the refractive index of the material in selected areas. This is either a change in the real part of the index, giving a change in the guiding parameters, or a change in the imaginary part of the index resulting in increased or decreased gain in specified regions. Both the real and imaginary parts of the refractive index are, however, related through the Kramers-Krönig relations, so a change in one can give rise to an appreciable effect on the other.

Changes in the refractive index can be brought about by many different mechanisms, the most important of which will be described below.

Gain is easily controllable, using direct electrical modulation as is used for semiconductor lasers. The injection of carriers into the conduction band leads to gain through stimulated emission. Depletion of carriers can have the opposite effect and produce an absorbing region. The gain is, however, restricted to wavelengths close to the bandgap.

Pockels Effect or **Linear Electro-optic Effect** affects the index by the electric field applied across the material. As the name suggests it is linear with field, but only affects TE polarised light (parallel to the <001> plane)and has a positive effect in the $<1\bar{1}0>$ crystallographic direction, and negative effect in the <110> direction. The magnitude of this effect is given by[1] :-

$$|\Delta n| = \frac{n^3 r_{41}}{2} E \qquad [A3.1]$$

where n is the refractive index, E the electric field in the <001> direction, and r_{41} the linear electro-optic coefficient for the material.

Kerr Effect or Quadratic Electro-optic Effect. Again caused by electric field and usually very small in crystal where the linear effect is present. It gives rise to birefringence in the crystal parallel and perpendicular to the applied electric field.[2]

$$n_o = n - \frac{n^3 s_{12}}{2} E^2 \qquad [A3.2]$$

$$n_e = n - \frac{n^3 s_{11}}{2} E^2 \qquad [A3.3]$$

where n_o is the index perpendicular to E and n_e is that parallel to E. s_{ij} terms are the quadratic electro-optic coefficients in the appropriate direction.

Band Filling directly affects the absorption within a crystal. As the lower conduction band states are filled, then absorbed photons will have to be of shorter wavelength to give the generated electron enough energy to fill a higher state. (Burnstein-Moss effect). Thus a

shift in the absorption edge results, and through the Kramers-Krönig relations a reduction in the real part of the index occurs with increased carriers for photon energies lower than the bandgap. This has been evaluated[3] in closed form as:-

$$\Delta n(E) = \frac{4\hbar^2 q^2 |M^2| \pi}{n m_o^2 \bar{E}(\bar{E}^2 - E^2)} N_{e,h} \qquad [A3.4]$$

where E is the energy of the incident light, and $\bar{E}$ is the bandgap energy. $|M^2|$ is the momentum matrix element, and $N_{e,h}$ is the density of carriers.

Bandgap Shrinkage or **many-body effect** also affects the absorption in the material by reducing the bandgap with increase of carriers. This gives rise to an increase of index for wavelengths longer than the bandgap energy, and has also been approximated by[4]:-

$$\Delta n(E) = \frac{b_{e,h}}{\bar{E}^2 - E^2} N_{e,h} \qquad [A3.5]$$

The values given for b in the literature are $b_e = 8.9 \times 10^{-22}$ cm^3 eV^2 and $b_h = 1.42 \times 10^{-21}$ cm^3 eV^2.

Franz-Keldysh Effect is also proportional to the square of the electric field, and affects the absorption by allowing a photon of energy lower than the bandgap to be absorbed. This is achieved by raising the generated electron to a mid-gap trap state, and using the electric field to allow the electron to tunnel into the conduction band.[5]

$$\Delta n = \frac{n^3 R(\lambda)}{2} E^2 \qquad [A3.6]$$

E here is the electric field, and R is a function of wavelength, λ.

Plasma or Free Carrier Effect is due to the presence of free carriers in the conduction or valence bands, resulting in intra-band absorption affecting the index of refraction. This is strongly wavelength dependent and dominant in the longer wavelength regions. Because of the differences of effective masses the contribution from holes is smaller than that from electrons. This effect is always negative with increase of carriers[6]. There is little difference between the carriers being from ionised dopants or carrier injection.[7]

$$\Delta n = -\frac{\lambda^2 q^2}{8 m^*_{e,h} \pi^2 c^2 \varepsilon_o n} N_{e,h} \qquad [A3.7]$$

λ is the wavelength of light, and N is the carrier density.

QCSE (Quantum Confined Stark effect) is a very large effect (≈1%) seen only in quantum well devices. It is caused by an electric field, applied perpendicular to the plane of the wells, affecting the orbits of the electrons in the crystal. It is sensitive to polarisation in that for TE light it is dependent on electron-heavy hole transition dipoles, and for TM light electron-light hole transitions[8]. The effect is very wavelength specific, and although zero at the bandgap energy, at its greatest for wavelengths 5nm each side of the bandgap energy.

This effect also affects the absorption of the material[9], and is used primarily for absorption modulators.

Speed is an important factor for a practical switch. The above effects due to field, affect the electron orbits within the lattice of the crystal, and so react very quickly. Carrier injection techniques are much slower because if the carriers are not removed by depletion or stimulated recombination, switching speed is limited to the time for the electrons to spontaneously recombine. This is typically 3-10 nano-seconds in GaAs.

Effects can be combined to work together. This is often the case in reverse biassed pn junctions, where carriers are removed from the depletion region, giving rise to the carrier effects. The electric field across the depletion region also influences the index change through the field controlled effects. This can be with or against the carrier effects depending on crystallographic direction.

Other factors can cause variation in the refractive index such as temperature, stress and fabrication techniques. These will be discussed in a later section.

Comparison of Effects

for λ=1.55μm, carrier concentration 10^{18} cm^{-3}, electric field 10^5V/cm. It is seen here that the plasma effect has the largest influence on the refractive index, although the other carrier induced effects are also quite large. The linearised equations for band filling and bandgap shrinkage are an approximation and for calculations at wavelengths far from the bandgap, and with high current densities they can be neglected.

Effect	GaAs
LEO	$\pm 2.9\times10^{-4}$
Franz-Keldysh	7.9×10^{-6}
Kerr	1×10^{-6}
Bandfilling	-1.9×10^{-3}
Bandgap Shrinkage (electrons+holes)	1.5×10^{-3}
Plasma (holes)	-1.6×10^{-3}
Plasma (electrons)	-3.5×10^{-3}

Table A3.1. Effects on Refractive Index.

References

[1] A.Yariv & P.Yeh. "Optical Waves in Crystals" Wiley Interscience 1983. p230
[2] ibid. p262
[3] J. Faist, K. K. Reinhart, Phase modulation in GaAs/GaAlAs double heterostructures. 1. Theory. J. Applied Physics, 67 (11) pp6998-7005
[4] J. Faist, K. K. Reinhart, Phase modulation in GaAs/GaAlAs double heterostructures. 1. Theory. J. Applied Physics, 67 (11) pp6998-7005
[5] D.K. Gautam, K. Ishida. Carrier induced MESFET optical switched for photonic integration. IEE proc. Part-J. 140 (5) pp317-324.

[6] B.R. Bennet, R.A. Soref, J.A. del Alamo, Carrier induced change in refractive index of InP GaAs and InGaAsP. IEEE J. Quantum Electronics 26 (1) pp113-122
[7] H.C. Huang, S. Yee. Change in refractive index for p-type GaAs at λ=1.06, 1.3 and 1.55μm due to free carriers. J. Appl. Phys. 70 (2) pp925-929
[8] T.C. Chong, H.W. Wan, S.J. Chua, Polarisation dependance of field induced refractive index variation in strained and unstrained quantum well structures. Elec. Letters. 26 (14) pp1060-1061
[9] H. Yamamoto, M. Asada, Y. Suematsu. Electric field induced refractive index variation in quantum well structure. Elec. Letters 21 (13) pp579-580

Appendix 4. Fabrication Detail

This appendix is intended as a reference for the conditions under which the devices were fabricated. The fabrication sequences are presented diagramatically for both CGCPS II and CGCPS III devices. The description of each of the steps is then given in detail. Discussion of reasons for using these fabrication techniques is given in Chapter 6.

A4.1 CGCPS II Fabrication Route

The n-side of the sample is lapped to 150μm and contacted with Ge/Ni/Au. The sample is then annealed at 430°C for 2 minutes. The top surface is then cleaned and the mirror resist pattern is then applied. Figure A4.1a. Postbaking is not done to avoid reflow of the resist and degradation of the pattern. The mirror wells are then etched using the $SiCl_4$ plasma etch. Figure A4.1b. Without removing the resist layer, the sample is coated in a thick layer of silica to half fill the mirror well. (12hr coat) shown in Figure A4.1c. The resist is now removed to leave the top surface bare so that it can be coated in Ti/Au. Figure A4.1d. The resist mask is then put on for the guides, which also contains a protective pad over the mirror well region. Figure A4.1e. Precise alignment of the guide mask is very important at this stage, and helped by a thinner layer of resist. The guides are etched to the required depth (0.2μm into GaAs for CB536), and then coated with silica (0.2μm) for electrical insulation. Figure A4.1f. The resist is now lifted off, and the device cleaned and given an ion-beam pre-etch for application of another Ti/Au layer for the contact pads. Figure A4.1h. The resist mask for the contact regions is now applied, as in Figure A4.1i, and the areas of metal that are not required are etched away. Removal of the resist leaves the device ready for cleaving. Figure A4.1j.

A4.2 CGCPS III Fabrication Route

This route for CGCPS fabrication leaves the mirror etching to the end, which ensures that all the pitfalls can be overcome before plasma etching.

As with CGCPS II, the sample is lapped to 150μm and the n-side contacted and annealed. The resist pattern for the guides is then deposited, taking care of the contact, as the edges of the guides will form the mask for the mirror facet. Figure A4.2a. A 90°C postbake can be used with no degradation to the guide edge. The sample is then ion beam etched to the required depth (0.4μm QT788) and coated in 0.2μm of silica. Figures A4.2b and c. The resist is not removed, but left intact to protect the guides from the next step. The resist mask for the mirror wells is now deposited over the silica, and exposed accordingly. Figure A4.2d. Alignment of the mirror mask is not as critical as for CGCPS II since it is the waveguide edge that forms the facet, and rounding off of the pattern due to postbaking of the resist pattern does not affect the facet either. Thus 120°C postbake of the

resist for 30minutes is used. Etching of the pattern is done to remove the silica layer, but not the GaAs, as this is left to be etched by the plasma etch. Figure A4.2e.

At this stage the resist layers can be removed. This is more difficult than usual since the lower layer of resist on the guides has been baked many times at high temperatures. Removal with cotton bud causes scratching of the gold surface, so a forced jet of acetone from a syringe is used to good effect along the line of the guides. Figure A4.2f.

The negative mask for the contact pads is now put onto the device as shown in Figure A4.2g. The area is then coated in Ti/Au, Figure A4.2h, and liftoff of the resist leaves the contacts in place. Figure A4.2i. At this stage the device is ready to be etched with the plasma etch with no resist pattern as the mask for the mirrors is formed from the silica layers around one edge of the mirror, and the gold capping from the guides giving the mask for the reflecting facet. Once etched through the active layer with the plasma etch, in Figure A4.2j, the device is ready for cleaving.

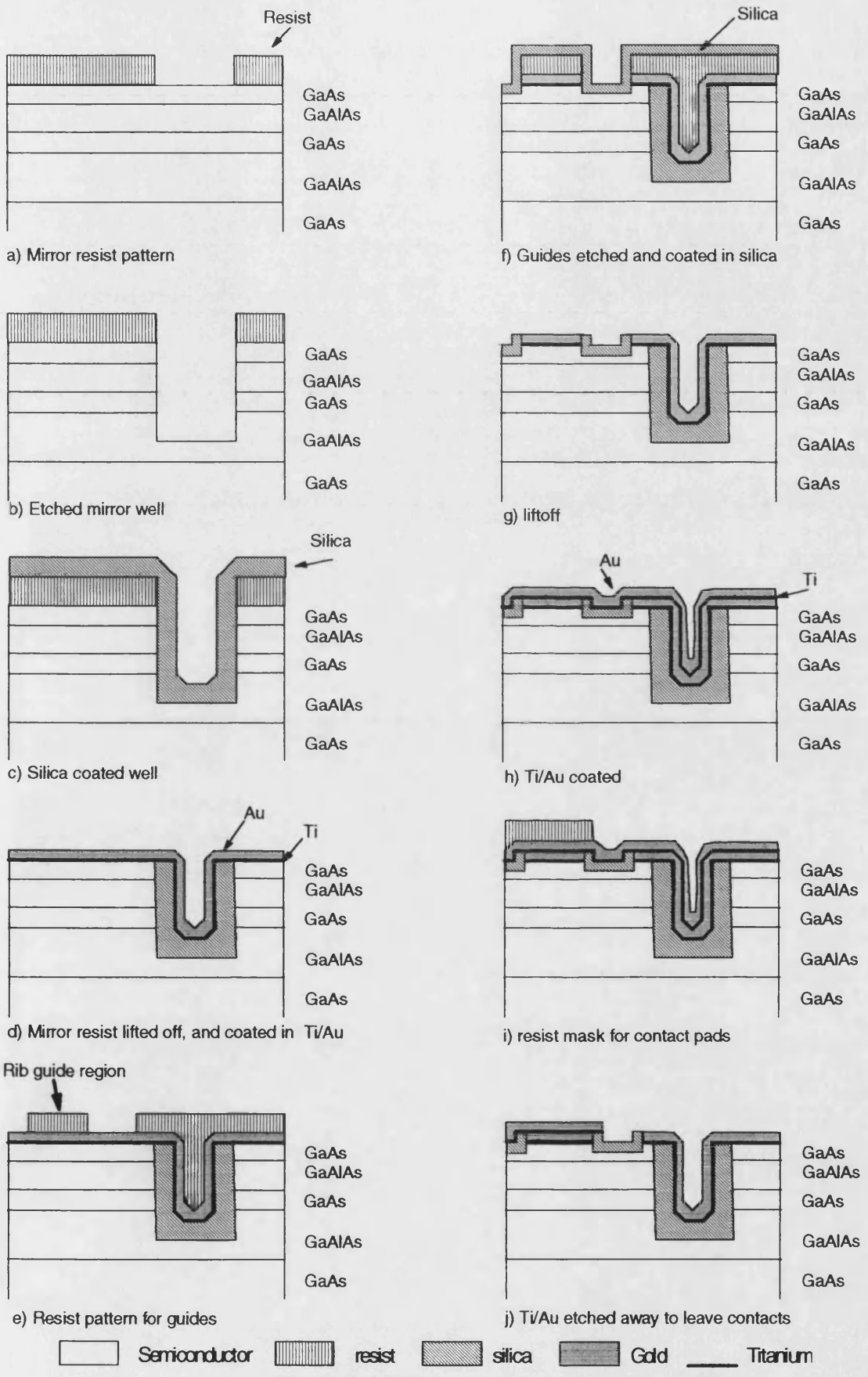

Figure A4.1. Fabrication order for CGCPS II

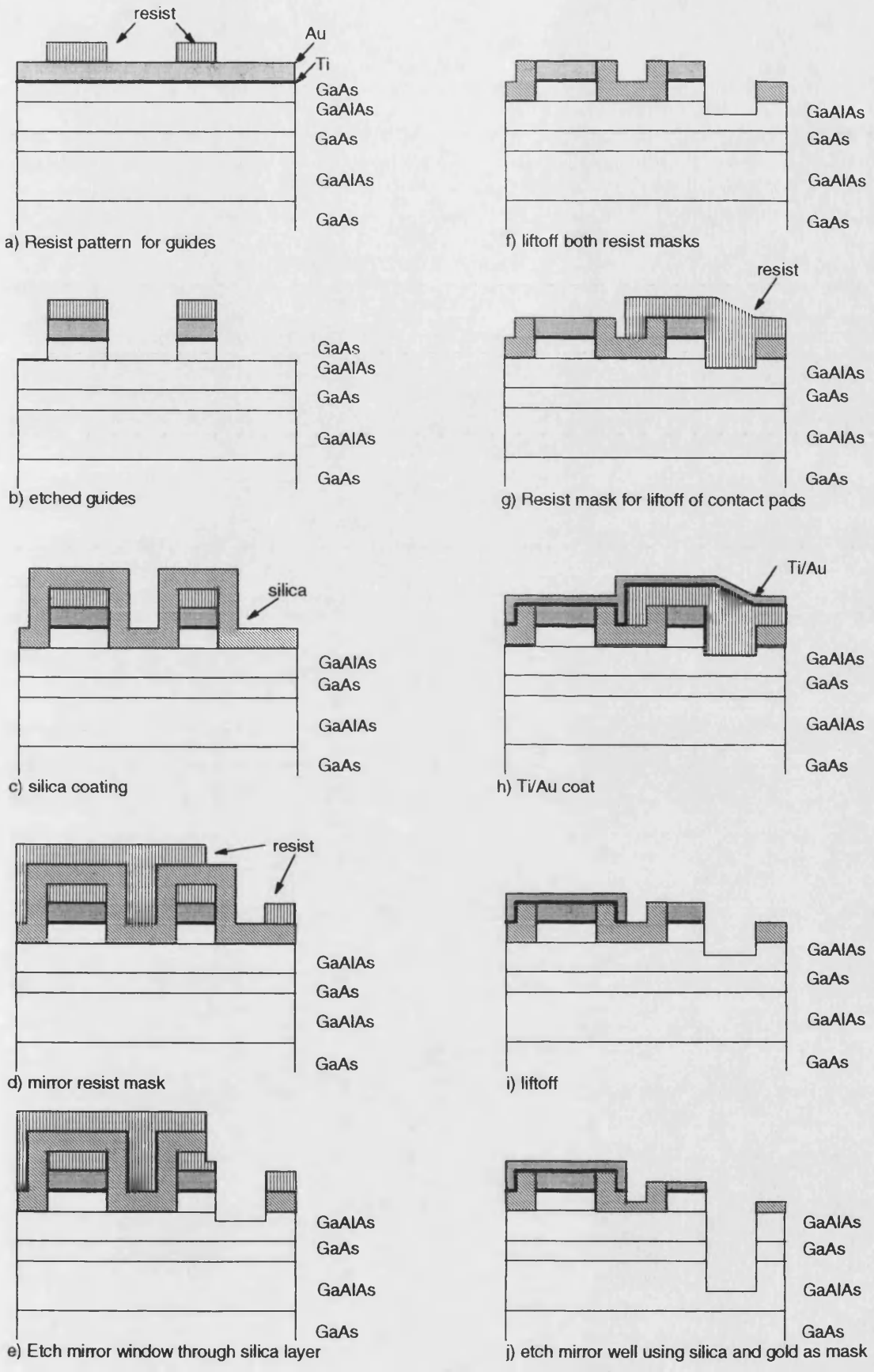

Figure A4.2. Fabrication order for CGCPS III

A4.3 Preparation

Sample preparation consists of cleaving the required amount from the source wafer and filing the chamfer on one or two ends of the sample top side for the resist to flow over. The sample is wax mounted to the edge of a cover slip to give support while the filing is done with a small piece of emery cloth stuck to a metal blade.
The substrate side of the sample is then lapped down to approximately 150μm. The lapping is done firstly with emery cloth by hand to approximately 200μm followed by machine lapping of the last 50μm with 40μm diamond paste. The lapping machine is cleaned every 5 minutes to ensure no build up of the waste products which jam the mounting block. The waste products are disposed of carefully as they contain a high proportion of arsenic. (24%)

A4.4 Contacts

A4.4.1 N-type

The substrate side, after lapping, is washed with trichloromethane, followed by cotton bud scrubbing with trichloromethane, then acetone, followed by detergent solution which is washed off with distilled water. The remaining water is blown off with forced air, and a final cotton bud scrub with propanol is then used.

The cleaned sample is now placed in the evaporation chamber which is evacuated down to 10^{-6}mbar. Coatings of Ge/Ni/Au alloy and then Au alone are evaporated onto the n-side of the sample. Pure gold will not adhere to GaAs so an alloy has to be used. Molybdenum boats are used to evaporate the alloys. One boat contains 34mg of Ni, with 200mg of Ge/Au alloy (12% Ge). The other contains 114mg of Au. All metals are in the form of wire or ribbon which is cut into small pieces. The boats are placed approximately 10cm from the sample and heated by passing 80A of current through them until all the alloy has evaporated. As the boats are metal, the current decreases as the metal heats up, so the current has to be monitored during warm-up. Initially the evaporation boats are hidden from the sample to be coated until the solid metals used to form the applied alloy have melted and mixed well.

The sample is now removed from the chamber, and the alloy coating annealed by heating the sample to 430°C for 2 minutes in hydrogen gas. The hydrogen is used to prevent oxidation, and the time limit is imposed to prevent the Ge diffusing too far into the sample. The annealer is slow and 15 minutes is required for it and the device to reach temperature. Temperature is measured with a J-type thermocouple on the metallised surface of the device. Diffusion of the Germanium gives the outer gold layer a noticeably silvery look after annealing, thus the sample is placed alloy side up so the colour change can be monitored.

A4.4.2 P-type

P-type contact application is similar to that of the n-type but Ti is used instead of the Ge/Ni/Au alloy to adhere to the top surface as Ge would diffuse into the active area of the device.

The device is cleaned as for the n-contact, but given a pre-etch in NaOH developer to remove any oxidised GaAs on the surface. Approximately 100Å of Ti is applied by evaporating 18mg of Ti wire from a Tungsten filament running at 40A. The Ti layer is under a great deal of stress when it cools and a thicker layer will curl up at the edges and fall off. The thickness of the Ti layer is too small to measure, and so a rule of thumb is used to gauge its thickness: The evaporating filament is exposed for long enough to just make the supporting glass slide have a perceivable grey tint. The exposure time may be as short as 10 seconds. A gold layer is applied as before using 114mg of gold wire giving approximately 0.2μm of Au on the device surface. Exposure time of the gold evaporator is a few minutes.

The p-type contact does not require annealing.

A4.4.3 Liftoff or Etchoff

Contacts in the form of the metal coatings described above, are rarely needed across the whole sample, and so have to be placed in selective areas, which can be achieved in two ways. The first is done by coating the whole sample in metal and etching away the unwanted regions, and the other is to put down a resist mask first. The device is then coated in metal, and the resist washed away in acetone, taking away the metal that laid on top of it.

Each method has its advantages, and has to be selected on application. The first, etchoff, method is a reliable route to take, but may etch lower layers once the required gold/Ti areas have been removed, causing unwanted damage. The liftoff technique has to be used with care as the areas of the device where the resist has been developed away, may be contaminated with resist solution and cause bad contact of the Titanium.

In removing the resist from underneath the metal, the metal is torn away from that which is to remain, leaving a jagged edge. In some cases this is an important disadvantage if the gold is to be used as a mask for further etching.

A4.5 Photoresist and patterning

A4.5.1 Resist

For all processing Shipley AZ1470 positive resist is used. The resist is spun onto the sample at speed of 4000-4500rpm giving a coating between 1.1 and 1.2μm thick.

The coated sample is baked at 90°C for 30 minutes before exposure and after developing unless otherwise stated. If large areas of resist are present 120°C is used for a

postbake. A cooling time of 10 minutes is recommended, but as it usually takes longer than this to align the mask, the cooling period is not formally allowed for.

A4.5.2 Exposure

Exposure of the resist is from a mercury lamp through the MJB3 mask aligner. Exposure times of 2×22 seconds is used for all patterns except when exposing the outer perimeter of the device when maximum exposure is used *twice*. (5 minutes)

A4.5.3 Developing

Resist developing is done with AZ 351 developer initially diluted in the ratio of 4:1, making approximately 50ml of solution. This is used to develop the outer perimeter of the samples as well as following steps, so will progressively become weaker. Weaker solutions of 5:1 are recommended for high contrast developing. The solution is divided into 2 parts and the samples developed for 30 seconds in each part.

The developing solution degrades with exposure to air, forming a film on the surface after 5-6 hours which contaminates the device. Care must be taken when mixing the solution to avoid skin contamination as skin flakes stick to the device and are difficult to remove without destroying the resist pattern.

A4.6 Wet Etching

Trials to find an effective diffusion limited etchant resulted in the use of a solution of H_2SO_4:H_2O: H_2O_2 in the ratio of 20:1:1. The solution of H_2SO_4 is 98% by weight and H_2O_2 is 30% by weight initially, but the peroxide is not fresh and may have deteriorated.

Mixture technique of the solution will affect the final concentrations as temperature of the solution influences the peroxide. The solutions are mixed in a running water bath at 17°C. The H_2SO_4 is slowly added to the water and reaches over 40°C very rapidly. This is allowed to cool before the peroxide is slowly added while constantly stirring. The solution is allowed to cool again before it is used for etching.

The etch rate of the above mixture varies depending on the agitation of the solution while in use. With gentle stirring the first 15 seconds produces a 0.1µm etch, slowing to a 0.3µm etch after 60 seconds at 17°C.

Care must be exercised in that the etchant affects the photoresist, causing it to shrink and lose adhesion. This is more prevalent on larger areas of resist and less of a problem for 3µm waveguide strips. It is more reliable to use a Titanium/gold coating for a mask.

A4.7 Ion Beam Etching

Ion beam etching is carried out using a B21 saddle field source operating at an accelerator voltage of nominally 5KV with an ion monitor current of 50µA. The chamber is

pumped down to a pressure of $<10^{-5}$ mbar, before the argon is let into the chamber to a pressure of between $2\text{-}4\times10^{-4}$mbar.

The device is rotated during etching about an axis normal to the plane of the substrate. Rotation speed is approximately 40 rpm and the ion beam is aimed at 45° to the plane of rotation.

Etch rate of GaAs is 150Å/min with the gun positioned 10cm from the sample. The Ti layer takes approximately 5 minutes to etch through. Gold varies in thickness, but can be seen to etch as the grey underneath of Titanium is exposed.

The device may be set up to rotate off centre to ensure an even spread of the <1cm diameter ion beam. This reduces the overall etch rate, as each area of the device is not being etched at all times.

The device is usually mounted on a glass coverslip with wax, and possibly another layer of glass below it before the metal rotating mount. The device is not cooled during etching.

A4.8 Plasma Etching

Plasma etching is used for the mirror wells as it gives a vertical sidewall compared to the IBE and wet etching techniques that give sloped walls. It uses $SiCl_4$ as the reactive gas, and etched at a rate of 1000 Å/min. Silica masks can be used as the etch rate for silica is 100 Å/min.

A4.9 Silica Insulation Layers

Deposition of the silica layers is done by sputtering silica onto the sample. The ion beam gun is used for this in the same setup as for etching except that the gun is aimed at a silica target, not at the device. The ion beam is at 45° to the plane of the target and only 5cm away from it. The sputter yield is maximum at about 70-80° to the plane of the target, and not the 45° that is expected, so the rotating device is placed accordingly, as close as is possible, but out of the ion beam.

Sputter yield is 500 Å/hour, there fore the normal 0.2µm thickness takes approximately 4 hours to deposit.

Appendix 5. Calibration of Measuring Equipment

In taking the measurements for the experiments undertaken during the work for this thesis, the apparatus used has to be calibrated in order to preserve the accuracy, and thus validity of the measurement. The detail of the calibration techniques used and the limitations are discussed below.

A5.1. Vidicon Camera Linearity.

The Infra-red vidicon camera tube used for measuring the near field intensity suffers from a non-linear light intensity to video signal response. The problem is compounded by the dark current variation with temperature, which varies the dynamic range, and the burn-in of the camera, which limits the saturation level. Circuitry inside the camera is designed to reduce the non-linearity, but it cannot overcome the temperature variation, or the change in response with wavelength.

The non-linearity (or gamma factor) can be removed by measuring the response of the camera, and correcting the experimental near field measurements afterwards. As the semiconductor laser source used in the experiments does not give a linear intensity with current, it is inconvenient to use the laser without complex measurement of the intensity with both photodiode and vidicon simultaneously. The camera time response is of the order of 3 seconds, and so the light intensity focussed onto the tube in effectively integrated over this time. This lag of the camera can be used to simplify the calibration, in that instead of having to measure the input light intensity to linearise the laser current response, the duty cycle of the laser can be varied with constant laser drive current, giving an intensity proportional to laser pulse frequency. Suitable duty cycles can be used to make this assumption valid (on-time << off time) and this also avoids heating variation in the laser. Care must also be taken to avoid the laser pulse rate beating with the camera frame rate. Typical use is a laser pulse of 500ns, with a repetition rate between 2-100kHz. A wide range of frequencies is required to vary the integrated intensity over the 12-15dB dynamic range of the camera.

When taking measurements for experimental results and calibration, the spot of light to be measured should not be allowed to fall onto the vidicon tube for long periods of time as this will affect the results from burn-in. In this case the signal from the camera slowly rises over a number of minutes until saturation occurs. To avoid this, measurements are taken in one region of the camera view, and setup operations in another, and the shutter is closed between each measurement.

A curve in fitted to the data of video output, and laser pulse rate using the least squares method and typically a 5th order polynomial. This curve is used to correct the experimental data for near field profile measurement. The calibration has to be done for each wavelength to be measured, and before each critical experiment as the data varies

with temperature. Figure A5.1. shows the transfer curves for different wavelengths at different times illustrating the output variation possible from the camera.

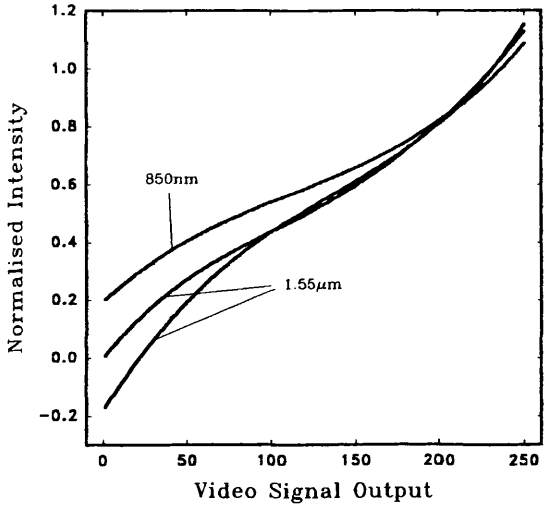

Figure A5.1. Graph of actual intensity against camera response.

A5.2. Lens resolution.

The resolution of the microscope is limited by the size of the lens, the wavelength and any aberrations in the lens system. The theoretical size, d, of the smallest resolvable object is given by:-

$$d = 0.61\lambda / N.A. \qquad [A5.1]$$

where the N.A. is the Numerical Aperture of the lens.

For the highest magnification lens used in the experiments here, ×40, 0.65 NA, the resolution limit, d, is 1.45μm with light of wavelength 1.55μm. As the active guiding layer of the material used is of the order of 0.5μm, the poor resolution causes much degradation of the image. Even in the horizontal (y) direction, the resolution affects the measured profile of the guided light and must be corrected for.

The diffraction of light from a slit results in an intensity distribution, $\phi(x)$, given by [A5.2].

$$\phi(x) = A\left\{\frac{\sin(kx)}{x}\right\}^2 \qquad [A5.2]$$

where A and k are constants.

The poor image created by the lens cannot be corrected, therefore the theoretical profiles that are calculated have to be degraded to match the results obtained through the lens. To achieve this, each point of the theoretical profile, f(x), is considered to give a distribution given by the lens function [A5.2], where now the constant A, is the intensity of the point in the theoretical profile. Thus the resultant intensity after lens degradation is given by:-

$$I(x) = \int_{-\infty}^{\infty} f(\rho)\phi(x-\rho)d\rho \qquad [A5.3]$$

The value of k, in [A5.2] is found by matching the fringes of an experimental profile to those of the sinc function.

The effect of the lens resolution is most noticeable in the vertical (x) direction, but its affect has to be taken into account for accurate measurements of lateral profile too, but apart from in the analysis of damaged regions in Chapter 2, the application of lens resolution degradation has not been applied to lateral profiles.

A5.3. Photodiode Linearity.

The photodiode used for measuring the light intensity can be considered linear over its operating range, but when used in conjunction with transimpedance amplifier for the Fabry-Perot loss measurements, care has to be taken to ensure that the amplifier is linear and has no DC offset as this would affect the results of contrast ratio.

As the intensity of the laser is not linear with current, it is difficult to measure the system linearity directly. However, by measuring the laser's light-current characteristic with different attenuators in the optical path, a set of curves is obtained. The ratio of intensity for the same current should be the same along the length of the curve for a linear amplifier.

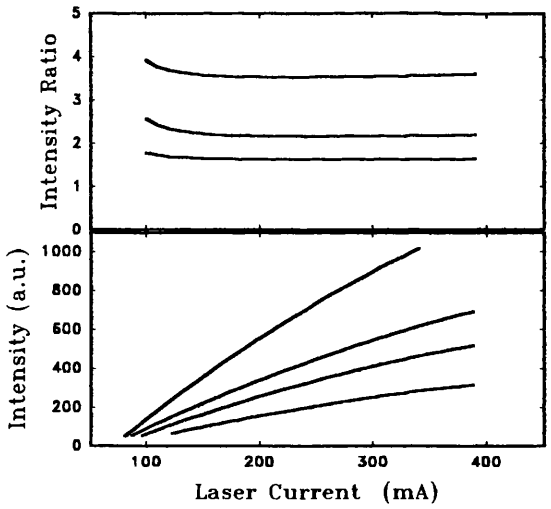

Figure A5.3. Laser light current characteristic with various attenuators, and the ratio of the responses.

The curves are shown in figure A5.3 with their ratios, and show that the measurement system is not completely linear, with the ratios in the low light region being up to 8% from the mean value. In the higher intensity region the ratios are flatter, and thus in this region the amplifier is more linear.

The 8% variation in ratio does not imply that the whole signal will be 8% in error, but will introduce a small offset from the absolute intensity value, as the signal is compressed at

the low intensity region. To overcome this offset, and any other DC offset from the amplifier, an artificial DC offset is added to the signal by means of a background incandescent light. This offset can be measured when there is no laser signal and removed from the final calculations, but allows the important signals to be measured in the linear region of the amplifier response.

Appendix 6. Material Parameters

Below are the wafer structures of the materials used in this study.

	CB34			
layer	Alloy	thickness (μm)	doping (cm^{-3})	index @ 1.55μm
capping	GaAs	0.2	8×10^{17} p	3.3772
cladding	$Ga_{0.72}Al_{0.28}As$	0.17	8×10^{17} p	3.2352
active	GaAs	0.5	u	3.3772
cladding	$Ga_{0.72}Al_{0.28}As$	2.0	8×10^{17} n	3.2352
buffer				
substrate	GaAs	500		3.3772

	CB536			
layer	Alloy	thickness (μm)	doping (cm^{-3})	index @ 1.55μm
capping	GaAs	0.2	5×10^{18} p	3.3772
cladding	$Ga_{0.71}Al_{0.29}As$	0.5	1×10^{18} p	3.2352
active	$Ga_{0.91}Al_{0.09}As$	0.4	u	3.3772
cladding	$Ga_{0.71}Al_{0.29}As$	2.0	6×10^{17} n	3.2352
buffer				
substrate	GaAs	500		3.3772

	QT788			
layer	Alloy	thickness (μm)	doping (cm^{-3})	index @ 1.55μm
capping	GaAs	0.05	1×10^{18} p	3.3772
cladding	$Ga_{0.72}Al_{0.28}As$	0.7	4×10^{16} p	3.2352
active	GaAs	0.5	3×10^{15} p	3.3772
cladding	$Ga_{0.72}Al_{0.28}As$	2.0	see text	3.2352
buffer	GaAs	0.05	2×10^{17} n	3.3772
substrate	GaAs	500	2×10^{18} n	3.3772

Because of the low doping in QT788 there is a variation across the wafer. The lower cladding layer is doped p-type at the top of the wafer, and n-type near the bottom. The transition from one to the other is exponential, so it is assumed that the majority of the wafer is n-type doped in the GaAlAs layer. Figure A6.1 illustrates the doping profile.

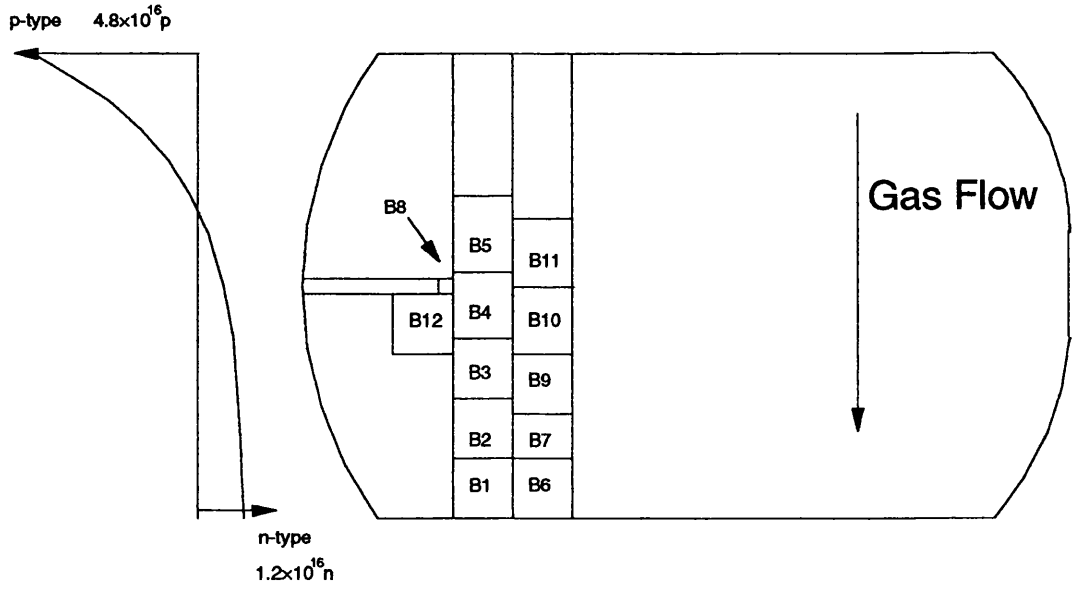

Figure A6.1. Lower GaAlAs layer Doping level relative to device positions on wafer.

	QT825			
layer	Alloy	thickness (μm)	doping (cm^{-3})	index @ 1.55μm
capping	GaAs	0.05	1×10^{18} p	3.3772
cladding	$Ga_{0.60}Al_{0.40}As$	0.7	$.93\text{-}1.05\times10^{17}$ p	3.0789
active	GaAs	0.5	3×10^{15} p	3.3772
cladding	$Ga_{0.60}Al_{0.40}As$	2.0	$2.9\text{-}3.4\times10^{17}$ n	3.0789
buffer	GaAs	0.05	2×10^{17} n	3.3772
substrate	GaAs	500	2×10^{18} n	3.3772

The material, QT825, as described above was found to be variable in its conductivity. This is thought to be the thin layer of capping GaAs being rubbed off with mechanical cleaning of the material surface.
To overcome this an extra 0.05μm of GaAs was regrown on top of this wafer. Brief conductivity experiments have shown that this has improved the situation.

Appendix 7. Solution Methods for Current Spreading Equations

A7.1 Laplace's Equation

The solution of Laplace's equation in the cladding layer of the semiconductor material, Figure 3.11, is undertaken numerically, by representing Laplace's equation [A7.1], by a numerical equivalent. The numerical equivalent takes values of the potential distribution, $\varphi(x,y)$, at discrete intervals to evaluate the second order derivative, as shown in Figure A7.1. The Laplace equation is then represented by [A7.2]'.

$$\nabla^2\varphi(x,y) = 0 \qquad [A7.1]$$

where is the distribution of potential through the cladding layer.

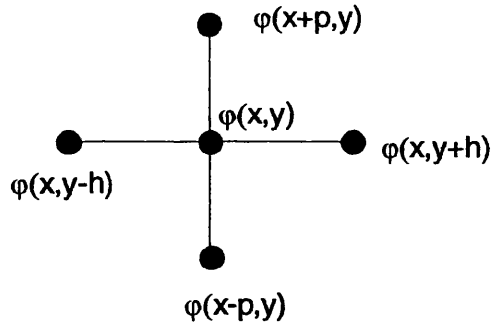

Figure A7.1. The five points required for numerical approximation of Laplace's Equation

$$\varphi(x+p,y)+ \varphi(x-p,y)+ \varphi(x,y+h)+\varphi(x,y-h)-4\varphi(x,y)=0 \qquad [A7.2]$$

To find the distribution of potential across the layer, an initial estimate for φ is made . As the initial estimate of the potential will not be the required solution of Laplace equation, then equation [A7.2] will be non-zero, and given by [A7.3]. The error, e(x,y), is subtracted from the value of $\varphi(x,y)$ to make a better estimate for the potential function, shown in equation [A7.4]. The process is iterated over all x, and y until the error distribution is sufficiently low. In the cases studied here the criterion was for $\Sigma\, e(x,y)<10^{-6}$.

$$\varphi(x+p,y)+ \varphi(x-p,y)+ \varphi(x,y+h)+\varphi(x,y-h)-4\,\varphi(x,y)=e(x,y) \qquad [A7.3]$$

$$\varphi(x,y)^{k+1}= \varphi(x,y)^{k}-e(x,y) \qquad [A7.4]$$

where k is the iteration number.

At the boundaries, either the potential is known, in which case that value is used in [A7.3] at the boundary, or the current density is zero. In the latter case the potential gradient is, therefore, zero giving $\varphi(x,y+h)=\varphi(x,y-h)$. Equation [A7.3] can therefore be replaced by [A7.5] for zero current in the y direction, at the right hand boundary.

$$\varphi(x+p,y)+ \varphi(x-p,y)+ 2\varphi(x,y-h)-4\,\varphi(x,y)=e(x,y) \qquad [A7.3]$$

A7.2 Solution of Diffusion Equation

The following describes the method by which the diffusion equation for injected carriers is solved in the active layer of the semiconductor material. The full diffusion equation is reduced to a 1 dimensional system, assuming that the distribution of carriers across the active layer is linear.

$$D\frac{d^2N(y)}{dy^2} - B_r(N(y)+N_o)N(y) - gP + \frac{j(y)}{qd} = 0 \qquad [A7.4]$$

D, is the diffusion coefficient,

B_r is the spontaneous recombination term,

N(y) is the carrier distribution,

j(y) the current density,

g, P are the gain and Photon Density in the active region,

N_o the background carrier concentration

q, the electron charge and d, the active layer thickness.

The program is written for light of lower energy than the band gap, thus the gP term, giving the stimulated recombination rate, is zero. The equation is rearranged into a more standard form, so that a solution is more forthcoming:-

$$\frac{d^2N}{dy^2} + \frac{B_r}{D}(N+N_o)N = \frac{j}{qdD} \qquad [A7.5]$$

As this is a non-linear equation in N, it is linearised by assuming that for a small region in y, dy, the $N+N_o$ term in the spontaneous recombination part of equation [2] is constant N_c, giving the standard solution in each small region of:-

$$N = Ae^{ky} + Be^{-ky} + c$$

$$\text{where} \quad k = \sqrt{\frac{B_rN_c}{D}} \qquad [A7.6]$$

$$c = \frac{j}{qdB_rN_c}$$

which is shown in Figure A7.2. For this solution a local value for j(y) is taken from the solution of the Laplace equation in the cladding layer above.

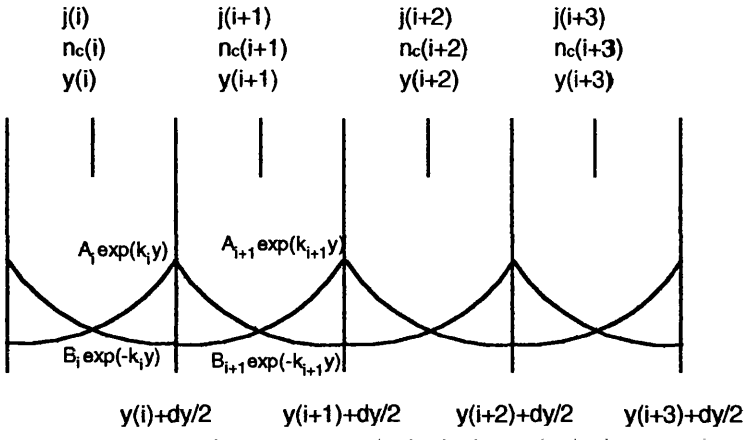

Figure A7.2. Solutions of linearised diffusion equation in regions of width dy.

To find the solution over the whole region of interest, each of these small region solutions has to be matched at each boundary, with the boundary conditions at the outer regions of N→0 as y→±∞ and dN/dy→0 as y→±∞. These outer conditions are satisfied by taking the decaying solution only in each case, thus either A or B is zero. Matching at each boundary gives:-

$$A_i e^{k_i\left(y(i)+\frac{dy}{2}\right)} + B_i e^{-k_i\left(y(i)+\frac{dy}{2}\right)} + c_i = A_{i+1} e^{k_{i+1}\left(y(i)+\frac{dy}{2}\right)} + B_{i+1} e^{-k_{i+1}\left(y(i)+\frac{dy}{2}\right)} + c_{i+1}$$
$$k_i A_i e^{k_i\left(y(i)+\frac{dy}{2}\right)} + k_i B_i e^{-k_i\left(y(i)+\frac{dy}{2}\right)} = k_{i+1} A_{i+1} e^{k_{i+1}\left(y(i)+\frac{dy}{2}\right)} - k_{i+1} B_{i+1} e^{-k_{i+1}\left(y(i)+\frac{dy}{2}\right)} \qquad [A7.7]$$

Rearranging gives:-

$$A_i = \left(\frac{k_i + k_{i+1}}{2k_i}\right) A_{i+1} e^{-(k_i - k_{i+1})(y_i + dy/2)} + \left(\frac{k_i - k_{i+1}}{2k_i}\right) B_{i+1} e^{-(k_i + k_{i+1})(y_i + dy/2)} + \frac{c_{i+1} - c_i}{2} e^{-k_m (y_i + dy/2)}$$
$$B_i = \left(\frac{k_i - k_{i+1}}{2k_i}\right) A_{i+1} e^{(k_i + k_{i+1})(y_i + dy/2)} + \left(\frac{k_i + k_{i+1}}{2k_i}\right) B_{i+1} e^{(k_i - k_{i+1})(y_i + dy/2)} + \frac{c_{i+1} - c_i}{2} e^{+k_m (y_i + dy/2)} \qquad [A7.8]$$

Which can be represented as:-

$$\begin{bmatrix} A_i \\ B_i \end{bmatrix} = \begin{bmatrix} a & b \\ c & d \end{bmatrix} \begin{bmatrix} A_{i+1} \\ B_{i+1} \end{bmatrix} + \begin{bmatrix} C_i^- \\ C_i^+ \end{bmatrix} \qquad [A7.9]$$

At the far boundary, where i=I, we know that a decaying solution is required so A_I=0, and the same is required at the other boundary, thus B_0=0. From this all other A, and B can be found to give a full solution. The values for N are then placed into N_c, and the process starts again until adequate convergence has been reached.

---

[1] E. Kreyszig. "Advanced Engineering Mathematics" Wiley 1988 Sixth Edn. p1085.